Novel Opto-Electronic and Plastic Optical Fibre Sensors

Nicos Ioannides

A thesis submitted in partial fulfilment
of the requirements of the University of North London
for the Degree of Doctor of Philosophy

January 1998

Abstract

The design and performance of a novel displacement sensor is investigated both theoretically and experimentally. This is an optical, extrinsic and differential sensor based on the inverse square law and is insensitive to source intensity variations. It can, in principle, be implemented using only opto-electronic components or it can incorporate optical fibres to allow for EMI free and remote operation. The sensor is implemented using Plastic Optical Fibres (POF) as these offer considerable advantages over glass fibres or glass fibre bundles. The sensor head consists of three POFs positioned side by side and displaced from each other parallel to the axis of the sensor head by a separation X_0 (mm). The middle POF is coupled to a red LED and emits light onto a flat target with the two outer fibres receiving the reflected light from the target and guiding it to two silicon PIN photodiodes.

Theoretical investigations on the behaviour of the sensor are presented for ranges between 0 mm and 100 mm, and for targets with different reflectivities. Non-linearities in the form of a spike are shown to exist in the very short ranges resulting in a minimum operational range of about 15 mm. Beyond this minimum range the sensor response is linear and depends on the reflectivity of the target, the accuracy of calibration between the two detectors, any offset voltage present in any of the detectors, possible errors on the detected signals and the X_0 separation which in principle can be used to scale the sensor.

Experimental results obtained confirm the long and linear operational range of the sensor (between 15 mm and 90 mm for a mirror target and between 20 mm and 100 mm for a matt white paper target). Likely variations in the source light intensity do not affect the performance and accuracy of the sensor. Measurements performed with various X_0 separations verify the scalability feature of the sensor in that by increasing X_0 one can achieve longer operational ranges. Temperature variations up to 40 ^{0}C do not affect the linearity of response. Effects arising from angular misalignment of the target and/or the ends of the three POFs are also investigated and could be minimised by rotating the emitting POF. Matt white paper is concluded as the preferred type of target since it offers a longer linear operational range with less stringent alignment requirements as opposed to reflective targets.

Operation of the sensor under ambient illumination conditions is demonstrated using suitable electronic circuitry with filtering facilities. The result is a linear operational range of 60 mm with 1 % accuracy with a matt white paper target.

An automated version of the sensor under software control is also demonstrated for monitoring large amplitude (0.15 mm - 6 mm), single degree vibrations. The maximum determined frequency of the vibrating surface is about 150 Hz and this is only limited by the target displacement which is close to the resolution limits of this version of the sensor (0.15 mm).

This novel sensor offers considerable advantages over other sensors reported in the literature. It is shown to offer a very long and linear operational range in excess of 100 mm, with accuracy better than 1 % and resolution better than 0.2 % of range, and currently this performance is only limited by the electronic circuitry used. Overall, the proposed sensor offers a superior sensor head arrangement and performance combination and its cost is expected to be very low. Suggestions for improvements and other applications are offered.

Contents

Where: **F:** Foreword Section
A: Appendix Section

List of Figures

CHAPTER 2

CHAPTER 3

CHAPTER 4

CHAPTER 5

CHAPTER 6

CHAPTER 7

CHAPTER 8

CHAPTER 9

List of Tables

CHAPTER 6

CHAPTER 7

CHAPTER 8

Acknowledgements

During the course of this study many people have given help and support to me. They are far too many to list. However, their contribution to the completion of this study was not unnoticed and I would like to thank them for their contribution - Thank you.

I would more specifically like to thank my supervisors: Dr Demetri Kalymnios for suggesting this topic and for his supervision, advice, assistance, criticism, encouragement and friendship, and Dr Ian Rogers for his constructive criticism, advice and the plenty "WHYs ?".

My thanks are also due to Professor Andy Palmer of City University for advise and suggestions offered to me after reading my transfer report.

I would also like to thank Dr David Faulkner for his advice on electronic matters, Marisa Mezzacapo for her help in the laboratory, Robert Harley at the University Workshop for constructing the sensor head and polishing jigs, Professor John Charalambous for his friendly advice and financial support and Mr Patrick Prigmore, the school secretary, for his help.

A special thanks to Dr Mark Rümmeli for his friendship and encouragement, and for allowing the use of his PC to produce this Thesis.

Dedication

This Thesis is dedicated to:

my parents Yiannis and Demetra, and my sister Maria.

And to:

my uncle Lavithakis, my aunt Maria and my cousins Chris, Elena and Lauren.

Thank you all for the love, the support, the understanding and the patience you have shown over this long period. I couldn't have done it without you.

Thank you.

Definition of Some Terms

Accuracy:	The highest deviation of a measured value from the ideal or true value (*).
Calibration:	The degree of similarity in the operation of the two detecting circuits.
Drift:	A usually gradual and undesirable change in a quantity, such as current or voltage, as a result of a disturbing factor, such as temperature or age (**).
Dynamic Range (electrical):	20 log (Voltage Output / Voltage Input).
Dynamic Range (optical):	10 log (Voltage Output / Voltage Input).
Error:	The deviation (difference or ratio) of a measurement from its true value.
Frequency Range:	A range of frequencies where the sensor performs to the required level of accuracy and linearity.
Linearity:	The degree to which the performance or response of a system approaches the condition of being linear, expressed in percent (**).
Measurand:	The quantity, property or condition that is sensed and converted into electrical signal with stress on the quantitative characteristic of sensing (*).
Noise:	A random-frequency current or voltage signal extending over a considerable frequency spectrum and having no useful purpose (**).
Operational Range:	The range where the sensor can perform measurements to the required level of accuracy.
Reliability:	The ability of a sensor to perform a required function under stated conditions for a stated period (*).
Repeatability:	The closeness of agreement between successive measurements carried out under the same conditions.
Reproducibility:	The closeness of agreement between measurements of the same quantity carried out with a stated change in conditions.

Resolution: The smallest portion of the signal that can be detected.

Sensitivity: The ability of a circuit or device to respond to a low level applied stimulus (**).

Sensor: A device which receives and responds to a signal or measurand and converts this into electrical energy.

Signal to Noise Ratio (electrical): 20 log (Voltage Signal / Voltage Noise).

Signal to Noise Ratio (optical): 10 log (Voltage Signal / Voltage Noise).

(*) Fraden (1997).

(**) Turner and Gibilisco (1991).

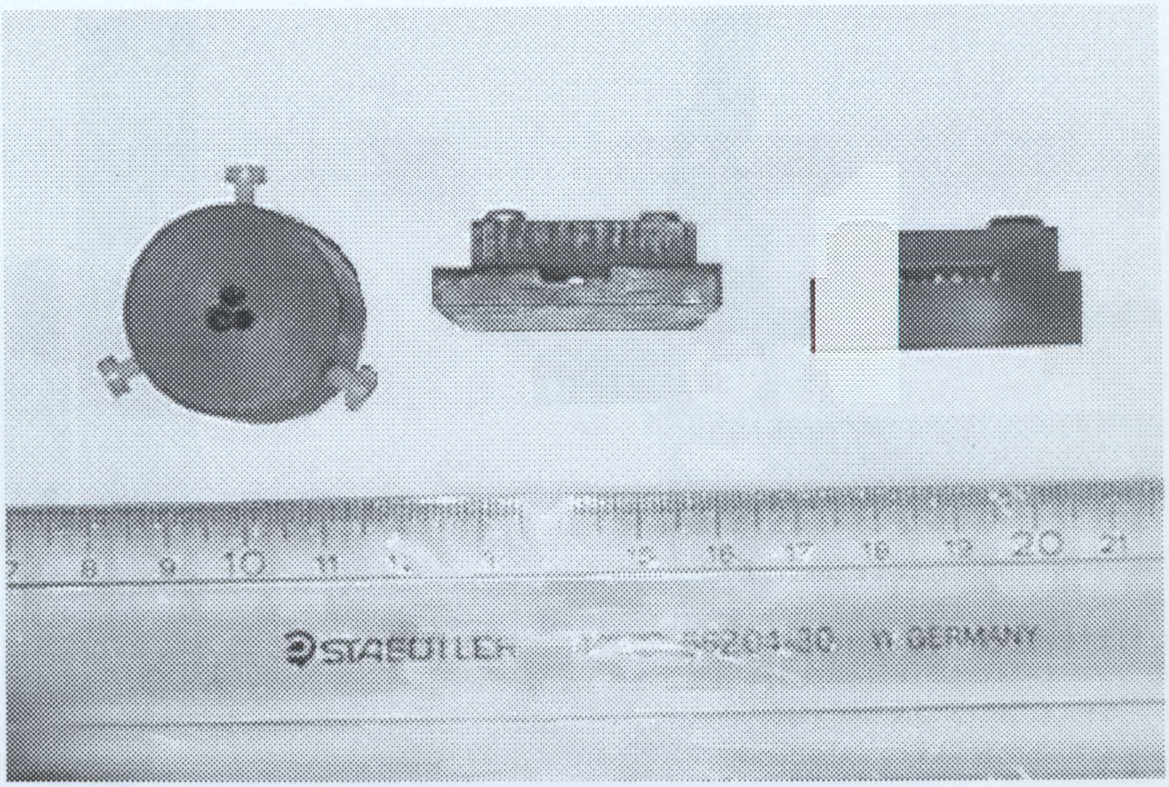

Front View of the Sensor Head Jigs - Refer to Section 6.1

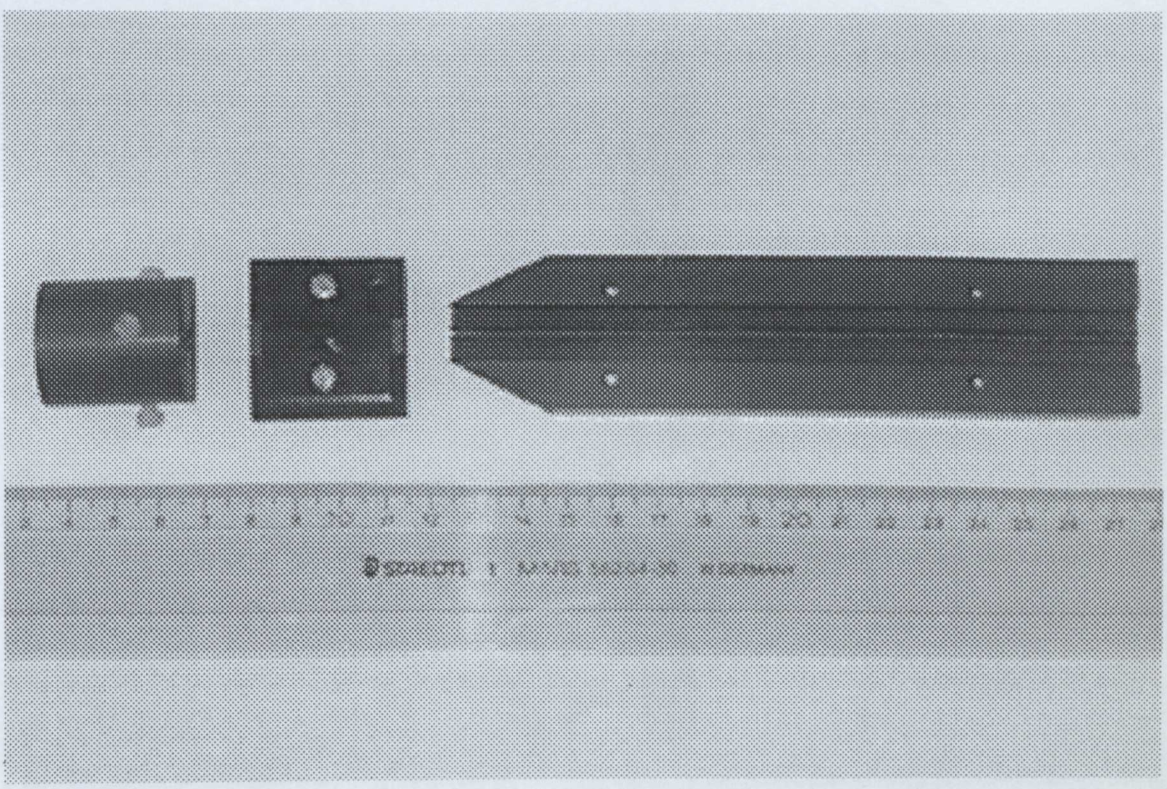

Top View of the Sensor Head Jigs - Refer to Section 6.1

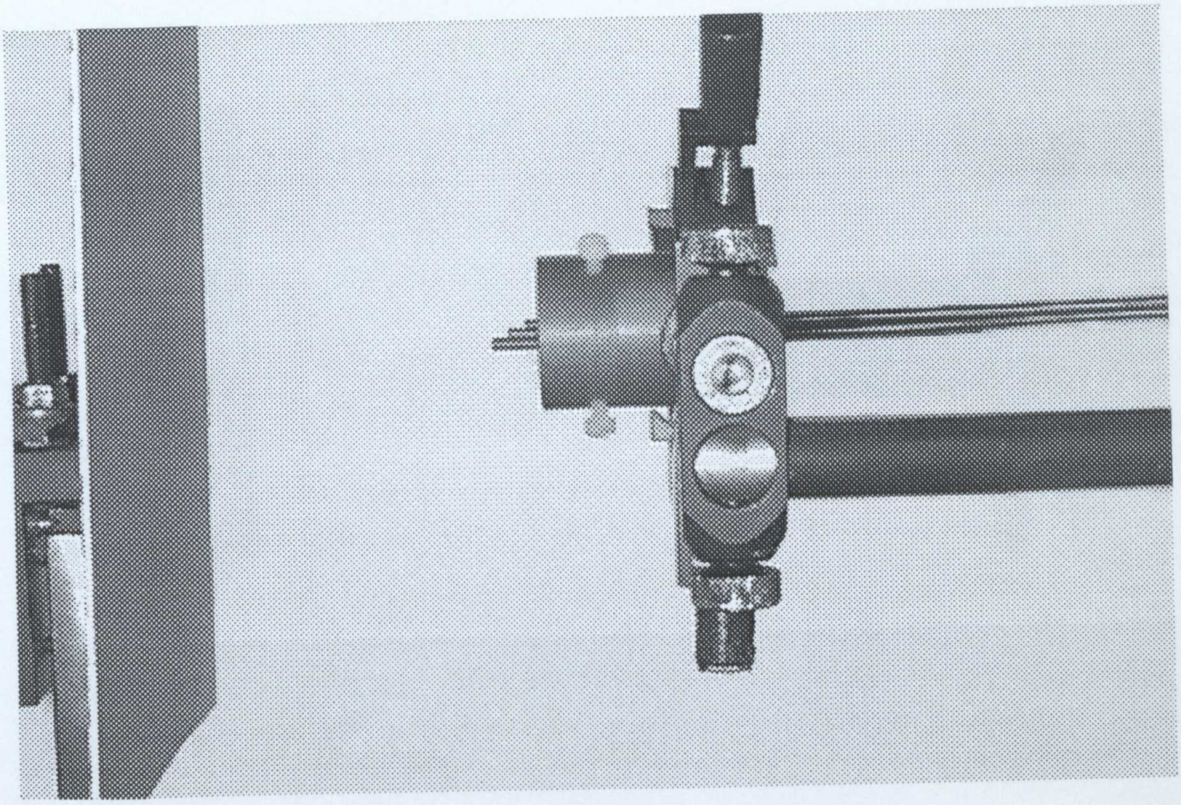

Displacement Measurements using the Cylindrical Sensor Head Jig

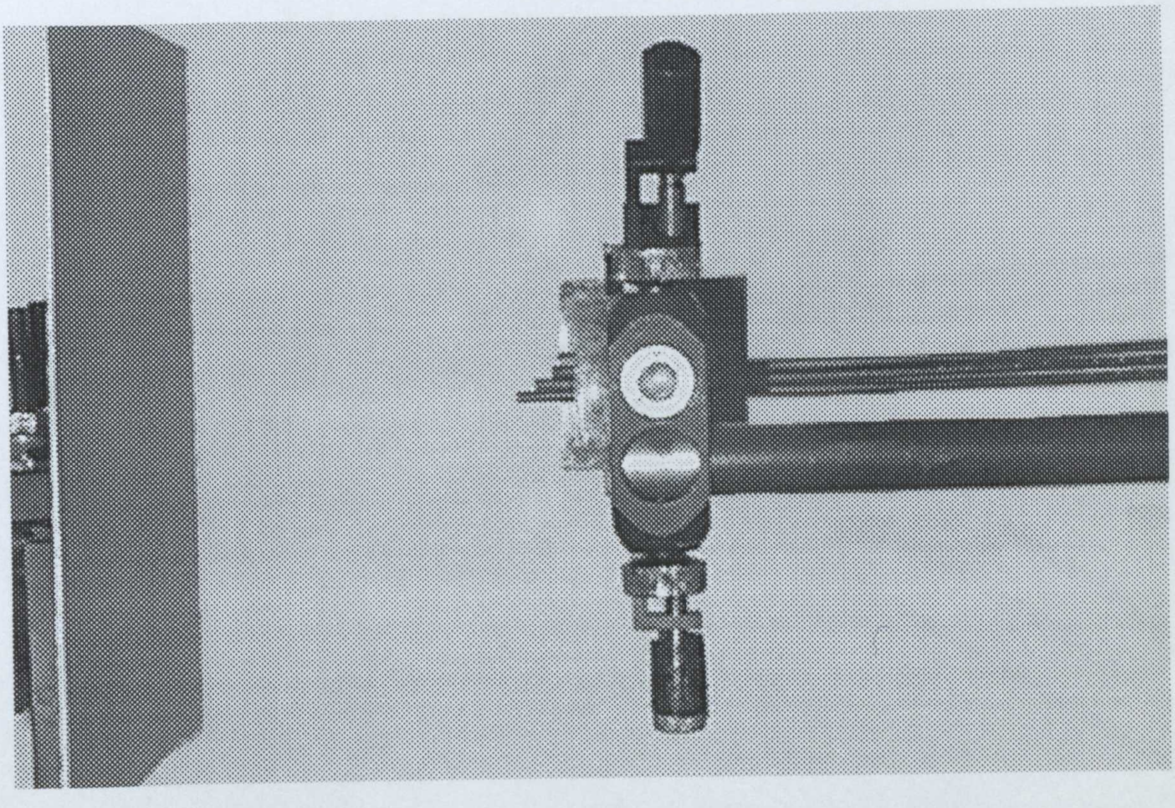

Displacement Measurements using the Flat Sensor Head Jig

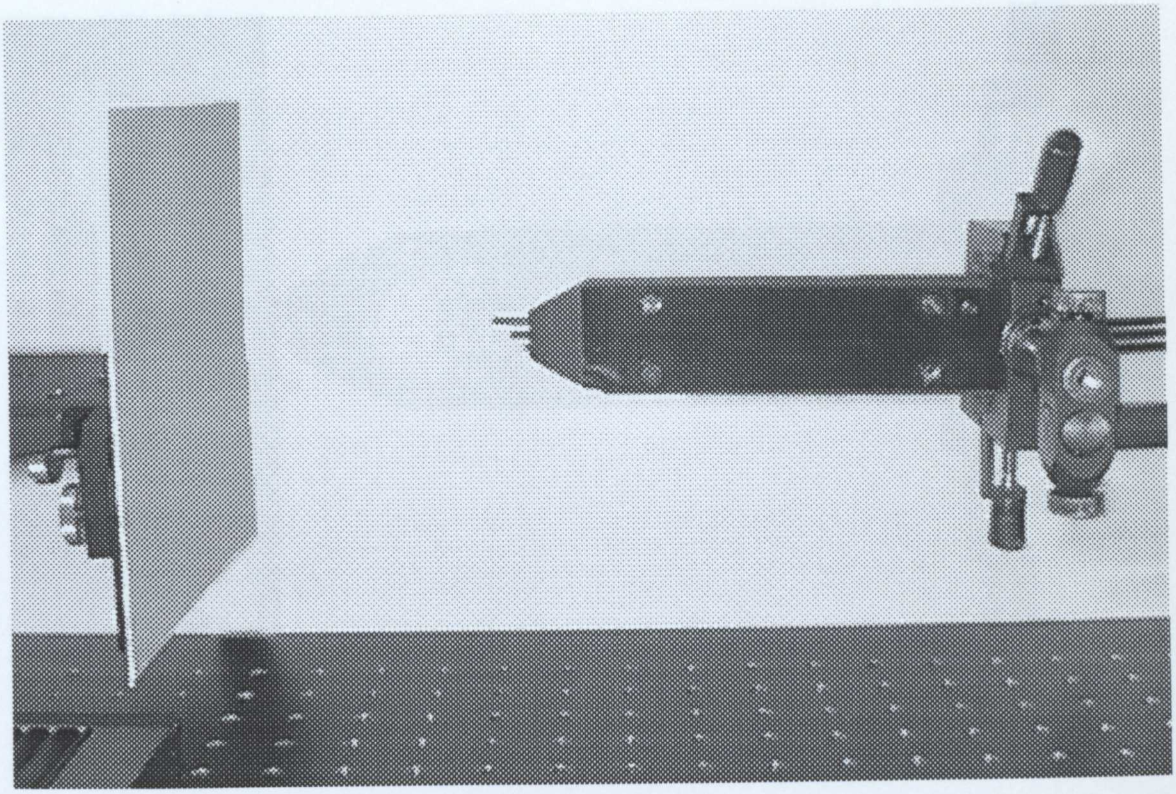

Displacement Measurements using the Sensor Head Jig with the V-Grooves

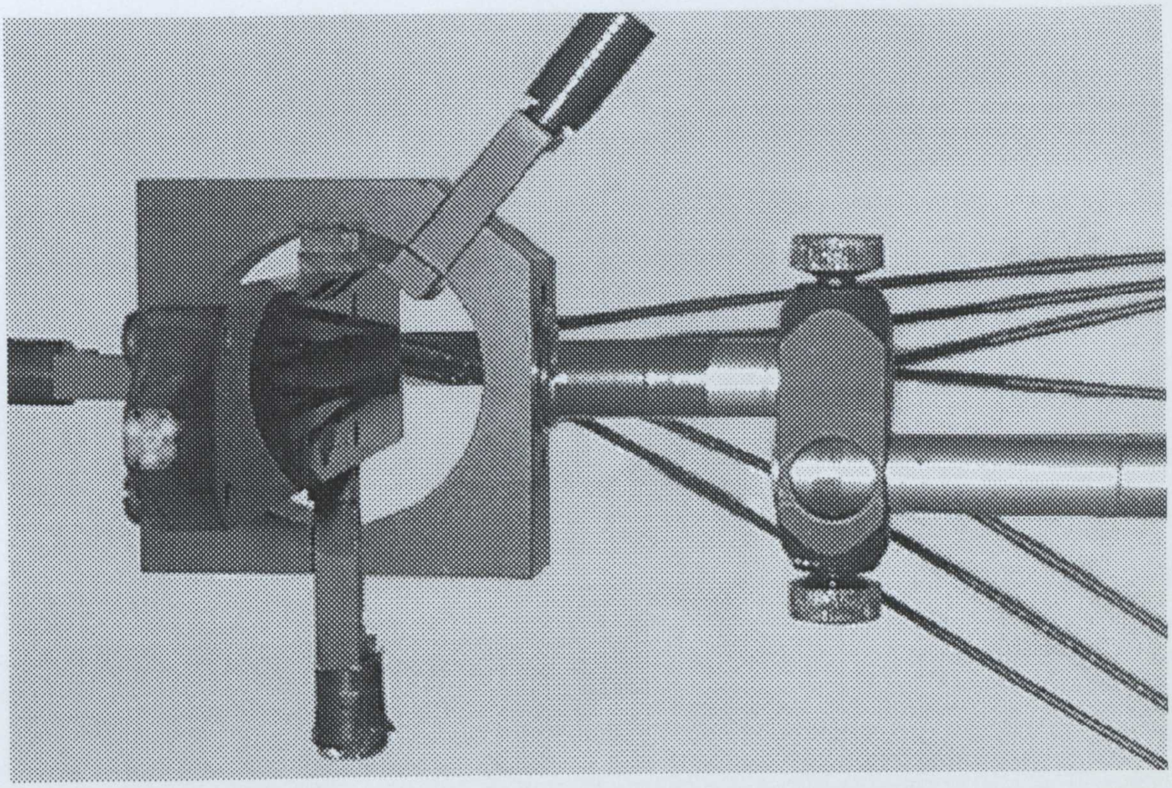

The Sensor Head Jig using Seven (7) POFs - Refer to Section 7.8

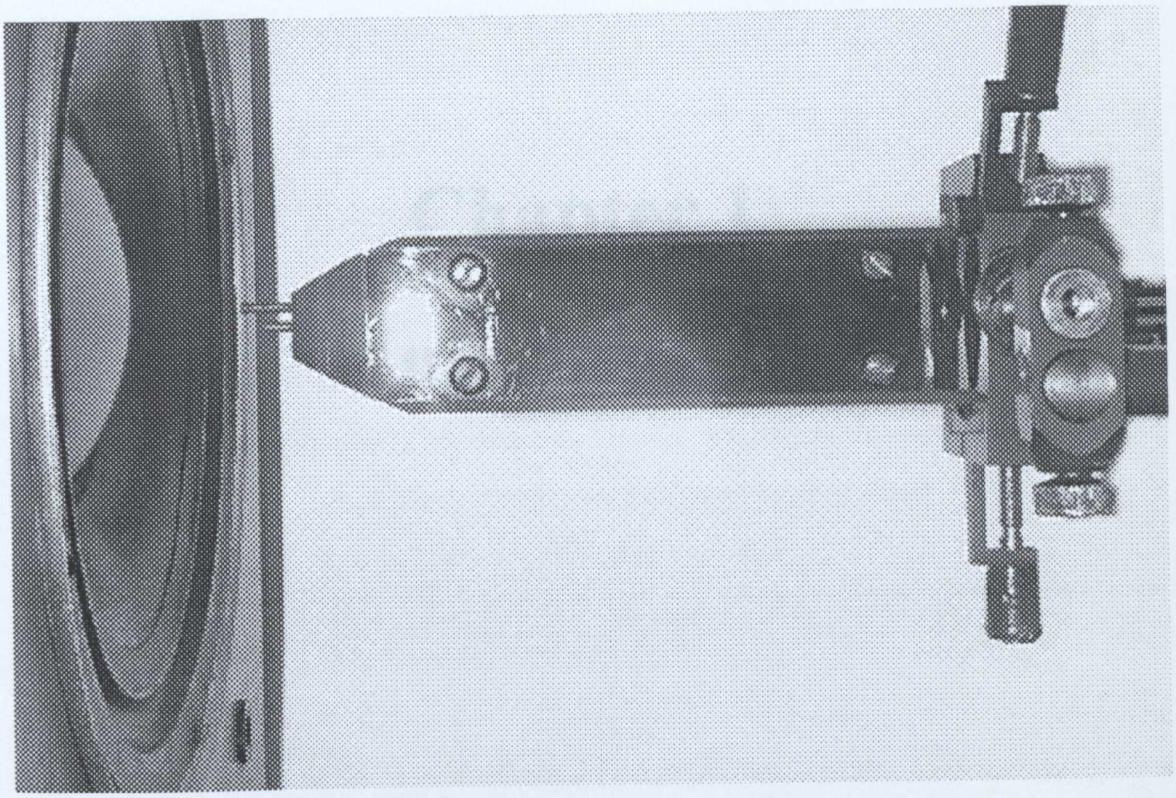

Vibration Measurements using the Sensor Head Jig with the V-Grooves

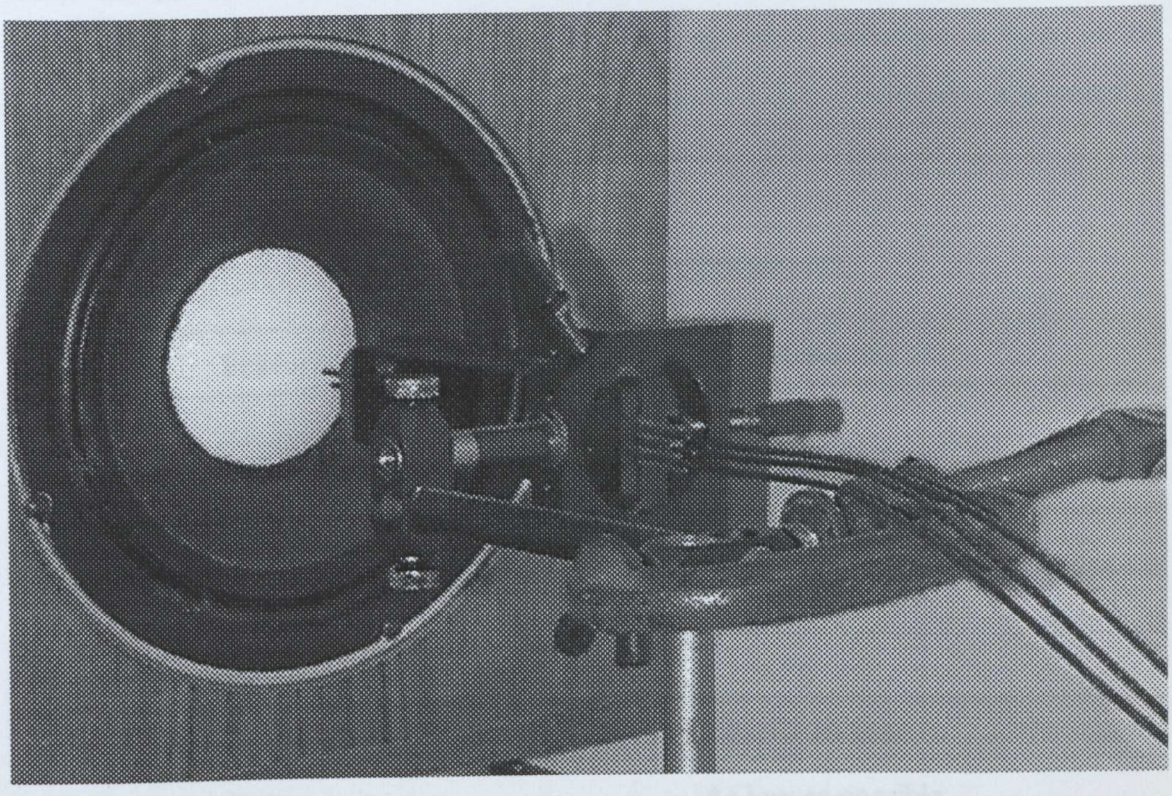

Vibration Measurements - Refer to Chapter 8

Chapter 1

Introduction

1.1. BACKGROUND

An industrial requirement for a non contact and non destructive sensor which could monitor piston movement over tens of millimetres in a clean environment has resulted in a simple displacement sensing technique being proposed. This is an optical technique, is based on the inverse square law and has a linear response (Kalymnios, 1993). The initial requirements / specifications are shown in Table 1.1.

Table 1.1: Initial sensor requirements

Features	Specifications
Response	Linear
Operational Range	10 mm - 100 mm
Accuracy	1 %
Resolution	< 1 %
Temperature Stability	0.1 %/^{0}C
Operating Frequency	5 kHz - 10 kHz
Cost	As low as possible

1.2. AIMS AND OBJECTIVES

The aims and objectives of this work were to:

- Further develop the proposed technique (Kalymnios, 1993) including the first principles (theoretical and experimental analysis) for a non contact and non destructive optical displacement sensor which will employ optical fibres to allow for electromagnetic interference (EMI) free and remote operation ;
- Design and construct the necessary analogue and digital electronic circuitry;
- Automate the sensor, and use software to control its operation;
- Application of the sensor to vibration measurements;
- Suggest further applications where the sensor could be implemented.

1.3. STRUCTURE OF THESIS

The structure of the thesis is outlined briefly in this Section. Initially, a survey on the field is performed which is followed by theoretical investigation on the behaviour of the sensor and then experimental work.

A survey of sensors with emphasis paid on those able to monitor static and/or dynamic (vibration) displacements was performed (see Chapter 2) prior to developing the proposed technique further. A more detailed survey of optical sensors utilising optical fibres (see Chapter 3) was performed in order to determine whether a suitable sensor already existed that could monitor displacements (static and/or dynamic) with the requirements shown in Table 1.1. Some optical fibre sensors could monitor static displacements covering the required range but they were either not implemented into dynamic displacement or could not meet the requirements.

It was therefore decided that the proposed technique should be taken forward and developed further in order to establish whether it could meet the specified requirements. In the initial stage a decision is made on which optical components would be the best to use for the sensor (see Chapter 4). It was decided to use Plastic Optical Fibre (POF) with active opto-electronic components operating in the visible range of the electromagnetic spectrum.

The theoretical behaviour of the sensor had originally been investigated using a simple mathematical analysis. In this thesis it is analysed in more depth using computer simulation, considering all the factors which could affect the sensor behaviour under ideal and under adverse conditions (see Chapter 5). Linear response was determined for the longer ranges but non-linear effects in the form of a spike occurred at the shorter ranges.

Initial experimental results were taken under dark room conditions. Operation under ambient illumination conditions was subsequently achieved by modifying the control electronics. Ultimately, complete automation of the control electronics was also accomplished (see Chapter 6).

The experimental work undertaken verifies the theoretical predictions of long linear operational ranges and spikes occurring at the shorter ranges. Factors which might affect the performance of the sensor were identified and suggestions/solutions were given (see Chapter 7).

Since the initial requirement was for a sensor which would be able to monitor motion, the automated version of the sensor was appropriately modified in order to monitor single degree vibrations using the dust cap of the cone of the bass driver of a loudspeaker as target. The successful monitoring of vibration under such conditions is described in Chapter 8.

Finally, a summary and conclusions of the work done with suggestions for further work incorporating improvements and other applications are presented in Chapter 9.

Chapter 2
Survey of Sensors

Industrial processes have always been (and always will be) dependent on measuring instruments to monitor physical or chemical variables, otherwise known as measurands, and thus provide information about a particular process, control it and assure its quality.

In the early days of industrial process control bulb thermometers, hydrometers and pressure meters were used as the measuring instruments . These are still used in many simple systems. Although they provided information in a form which could be easily quantified their output had to be monitored by an observer. Such systems are known as open loop systems.

Towards the middle of this century developments in semiconductor technology enabled through the use of electronic circuitry the conversion of the information provided by the measuring instruments (also known as sensors) into electronic compatible signals. The combined system, sensor and electronic conversion circuitry, were called transducers. In recent years, the sensor and transducer terms are used synonymously. In this thesis the term sensor will be used instead of transducer.

Sensors were intensively developed during the 1970s allowing for monitoring of many measurands. Automatic correction to the process when necessary was achieved by developing sensors which would incorporate a microcontroller or would allow for connection to a computer system. Such systems are known as closed loop systems.

The International Electro-Technical Commission (IEC) considers sensors to be "devices able to convert a physical or chemical variable into a signal suitable for measurement" (Grandke and Ko, 1989). The fundamental function of a sensor is thus to measure the appropriate signal affected by the measurand and convert it into a form understood by either an observer or by an electronic information processing system.

Important characteristics which should be featured by sensors are:

- High fidelity between the output of the sensor and the determination of the measurand;
- Minimum interference of the sensor with the measurand;
- Minimum sensitivity to external effects such as electro-magnetic interference (EMI), vibration, temperature and in the case of optical sensors background illumination;
- Separation of the natural frequency of the sensor and the frequency and harmonics of the measurand, where appropriate, since this will cause instability effects due to resonance;
- Small size so that the sensor can be positioned exactly where it is needed.

Other requirements that should be optimised by sensors are their operational range, accuracy, resolution, temperature stability, reliability, maintainability and life cycle cost. Linear relationship between the measurand and the sensor output signal, although desirable is not essential.

The increasing number of sensors emerging to monitor various measurands called for some kind of classification. Lion (1969) proposed six types of sensor which are listed in Table 2.1 together with their most common input signals according to the form of energy in which the signals were generated. In a similar way classification can be performed considering not the form of energy in which the signals were generated but the form in which the measurand, whether physical or chemical, is converted by the sensor for measuring purposes, i.e. output signal.

Table 2.1: Types of sensor and their most common input signals

Sensors	Most Common Input Signals
Thermal	Temperature, heat and heat flow.
Mechanical	Force, pressure, velocity, acceleration, displacement, position.
Chemical	The internal quantities of the matter such as concentration of a certain material, composition or reaction rate.
Magnetic	Magnetic field intensity, flux density and magnetization.
Radiant	The quantities of the electromagnetic waves such as intensity, wavelength, polarization and phase.
Electrical	Voltage, current and charge.

This thesis is concerned with electrical, mechanical and radiant sensors. In particular the thesis reviews and considers sensors which can measure displacement and some related applications such as vibration. In order to do this the sensors reviewed are classified by their output signal.

2.1. DISPLACEMENT

Displacement is the most widely measured physical quantity and can be defined as the distance that an object travels from a reference position which is usually its equilibrium or rest position. This distance may have a translational or a rotational character or even a combination of both. The monitoring of displacement not only provides information on this quantity as such, but also on variables such as vibration, pressure, force, acceleration, tension or liquid level.

The investigation on displacement sensors presented in the survey that follows has been based on the specifications / requirements outlined in Table 1.1. Their fundamental characteristics, i.e. mode of construction and operation, operational range, accuracy, resolution, advantages and disadvantages are outlined.

2.1.1. Electrical Displacement Sensors

Electrical sensors capable of measuring displacement fall into three main categories, potentiometric, capacitive and piezo-electric and are described below.

Potentiometric sensors consist of a resistive element and a movable wiper as shown in Figure 2.1. They operate by measuring changes in the voltage across the resistive element. The measurand forces the wiper to move along the resistive element thus varying the effective potential divider ratio of the potentiometer. The output is taken between one end of the resistive element and the wiper (Dally *et al*, 1993 and Alloca and Stuart, 1984).

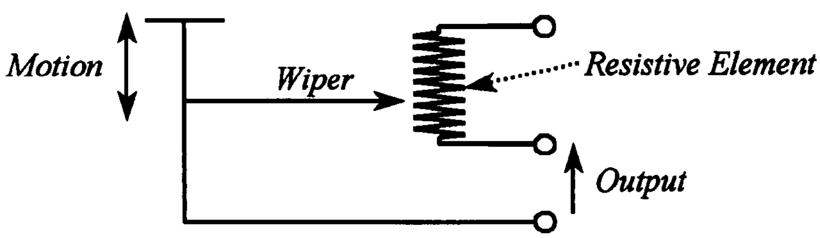

Fig. 2.1: A potentiometric sensor

The resistive element is usually a high resistance wire wound around an insulating core. In wire-wound potentiometers the resolution (between 0.05 % and 1 %) depends on the number of turns that the resistive wire has along the insulating core. In potentiometers such as these the wiper may, while moving across the winding, make contact with either one or two wires resulting in variable resolution. Potentiometers that utilize thin films with controlled resistivity have also been introduced in order to improve resolution.

Potentiometric sensors can be adjusted to measure rectilinear and angular motion. They are relatively inexpensive and can operate under dc or ac voltage supply conditions. A maximum operational range of 1 m for linear potentiometers is possible.

Several disadvantages characterise potentiometric sensors. Physical coupling with the measurand is necessary in order to perform their task which may require insulation at the point of contact to avoid errors. Frequency response is limited which is caused by the inertia of the shaft and the wiper assembly thus precluding their use for dynamic measurements. EMI can affect their performance. Mechanical wear limits their life, which depends on the material which they are made of. They are highly sensitive to loading effects (Haslam *et al*, 1981) and uneven wear of the track will result in degradation of linearity.

Poor brush contact of the wiper will also result in noise generation. Any variations of the supply voltage will result in error.

Capacitive sensors consist of two conductive plates positioned next to each other without touching, as shown in Figure 2.2. They operate by measuring the charge stored on the conductive plates. The measurand can vary the electric charge stored by changing one of two variables which are the distance separating the two conducting plates, Figure 2.2.a, effective for very small displacements (microns) and the effective area, Figure 2.2.b, effective for displacements up to a few millimetres (Morris, 1991 and Alloca and Stuart, 1984).

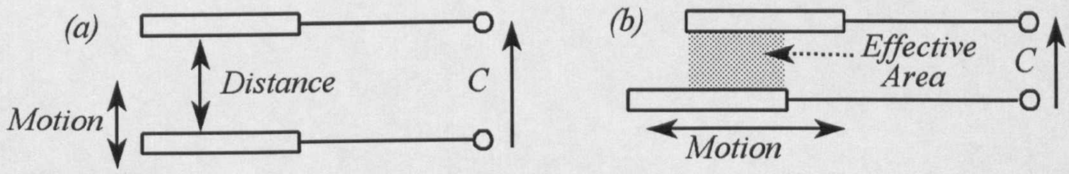

Fig. 2.2: Capacitive sensors

The capacitive sensor can have very high resolution which depends on its set up (Haslam *et al*, 1981). It is non-contact, rugged, can be subjected to very high shock loads (5000 g) and intense vibratory environments (Dally *et al*, 1993). It can be constructed to withstand temperatures up to 1090 ^{0}C and can have constant sensitivity over a very wide temperature range (23 ^{0}C - 870 ^{0}C).

The performance of a capacitive sensor can be affected by EMI, temperature variations which change the dielectric constant and fringes in the electrostatic field which can limit the range of the sensor making the need for a linearizing circuit a necessity.

Piezo-electric sensors consist of a crystal whose sides are cut parallel with respect to each other and is sandwiched between two metal plate electrodes as shown in Figure 2.3.

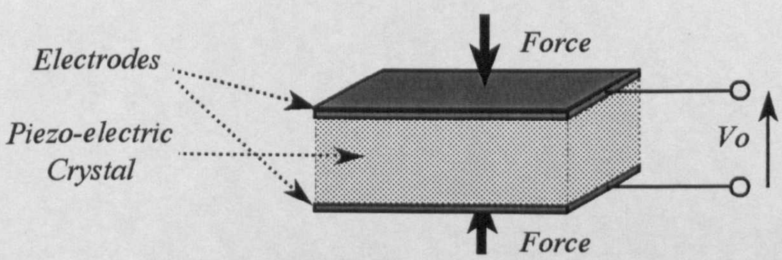

Fig. 2.3: A piezo-electric sensor

The crystals are cut relative to their crystallographic axes which would determine the voltage sensitivity of the sensor. Usually single crystal quartz, Rochelle salt or lithium sulphate crystals are used which contain molecules with asymmetrical charge distributions.

When the crystal is pressurised by the measurand it deforms and a relative displacement of the positive and negative charges within the crystal takes place producing an electric charge which appears on the faces of the crystals with opposite polarity. The amount of charge is linearly proportional to the force applied on the crystal over a certain range. The two metal plate electrodes serve to spread the pressure evenly over the crystal and to make electrical connections to it (Dally *et* al, 1993 and Alloca and Stuart, 1984).

Piezo-electric sensors do not require electrical supply, have very high frequency response, their displacement range is in the order of a few tens of microns, are accurate (1 %) and can operate at very high temperatures (< 350 °C). Their capacitance is very small (tens of picofarads) and so the lead capacitance has to be considered very carefully. The amplifier used to measure the output voltage from the sensor has to have very high input impedance (> 10^{15} Ω) since any other measuring system will short-circuit the sensor. Its performance can be affected by EMI. Piezo-electric sensors are used to measure displacement only when the system which causes the displacement is not affected by the material stiffness of the sensor. Also, if the pressure applied to the sensor is maintained for some time, the charge developed by the crystal will leak off as a small current through the amplifier and crystal internal resistances (Dally *et al*, 1993).

2.1.2. Magnetic Displacement Sensors

Magnetic sensors capable of measuring displacement fall into three main categories, inductive, linear variable differential transformer and eddy current and are described below.

Inductive sensors consist of an inductor and a permeable core as shown in Figure 2.4. They operate by measuring inductance changes across the inductor. The insertion of a permeable core into the inductor will increase its net inductance. Depending on the influence of the measurand on the position of the core with respect to the inductor windings a different inductance can be produced (Johnson, 1993). Inductive sensors feature very high resolution and accuracy and have a displacement range which varies from microns to tens of centimetres.

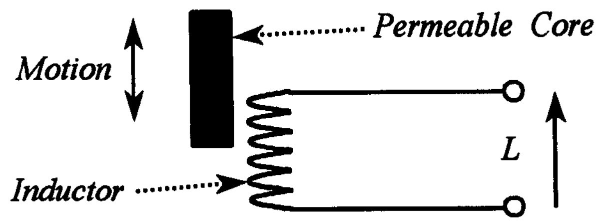

Fig. 2.4: An inductive sensor

The core used has some properties that cause error (Hughes, 1977). The circulating currents, also known as eddy currents, induced in the iron core due to the varying magnetic field cause loss of power and heating due to the very low resistance of the iron core. Eddy currents can be reduced if the iron core is made of laminations insulated from each other confining the eddy currents to their respective sheaths. Alternatively, other kinds of cores such as silicon-iron alloy can be used which have higher resistivity. Another source of error is the hysteresis effect, which depends on the quality of the iron core. This is the tendency of the core to saturate and retain some of its magnetism after the magnetic field to which is subjected changes its magnetic field strength causing losses of energy and heating limiting high frequency operation. The inductive sensor is also prone to EMI.

Linear variable differential transformers (LVDT) consist of a single primary inductor and a pair of secondary inductors arranged relative to a ferrite core as shown in Figure 2.5. They operate by comparing the inductance of the secondary inductors. They are based on the variable inductance principle in which a moving core is used to vary the magnetic flux between two or more cores.

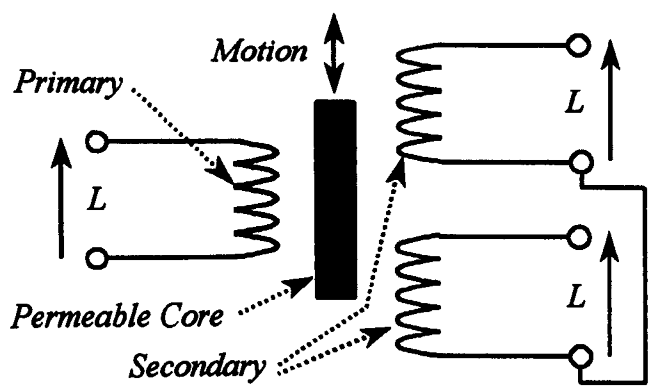

Fig. 2.5: A linear variable differential transformer (LVDT) sensor

The measurand will change the position of the core with respect to the three inductors thus the initial coupling between the primary and the two secondary windings will change leading to a change in the amplitudes of the induced secondary voltages. The output of the LVDT is bipolar and is linearly proportional to the displacement of the core (Haslam *et al*, 1981). The direction of the motion can be determined from the phase of the output voltage relative to the input voltage. Ideally, the two secondary voltages should be 180^0 out of phase when the core is at the central position and their reading should be zero. This is very difficult to achieve and so a small null voltage is always present. This sensor is also prone to EMI.

The LVDT features very high resolution, accuracy and linearity. There is no contact between the core and the coils so friction is eliminated. However, physical contact with the measurand is necessary in order to perform measurements which may require insulation at the point of contact to avoid errors. The displacement range can vary from millimetres up to half a metre. Overtravel of the core does not damage the sensor. The maximum displacement frequency has to be 10 times smaller than the excitation frequency (< 25 kHz) in order to measure the motion of the measurand accurately (Dally *et al*, 1993 and Alloca and Stuart, 1984).

Eddy current sensors consist of two coils, one active and one inactive, and a conductive surface as shown in Figure 2.6. They operate by observing the eddy currents induced by the conductive surface. The active coil generates magnetic flux lines driven at high frequency (1 MHz) which when they intersect with the surface of the conductive material induce eddy currents at the conductive surface producing a magnetic field which opposes that of the active coil resulting in an imbalance with the inactive coil. The inactive coil is used as a reference in order to compensate for variations in temperature which can affect the behaviour of the sensor. Changes in the eddy currents are sensed with an impedance bridge demodulator. Their magnitude is a function of the distance between the active coil and the surface (Dally *et al*, 1993).

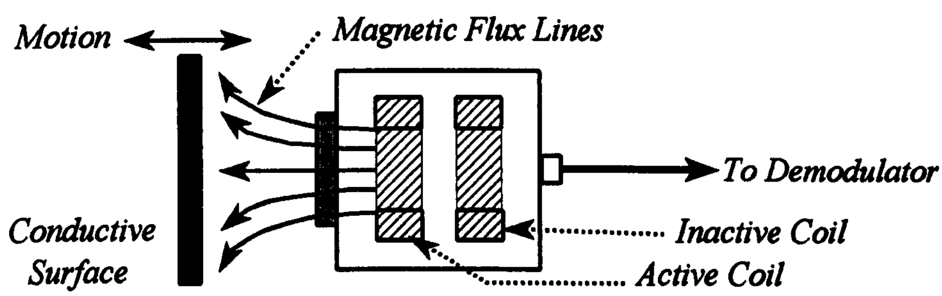

Fig. 2.6: An eddy current sensor (Dally *et al*, 1993)

The sensor which is non-contact requires highly conductive target materials for best case sensitivity. Poor or non conductive or magnetic materials decrease the sensitivity of the sensor quite significantly. The range of the sensor is controlled by the diameter of the coil with a range to coil diameter ratio of 1:4. The largest coil diameter used does not exceed 25 mm. The frequency response of the sensor depends on the diameter of the coils with a best case of 50 kHz achieved when using very small diameter coils. Linearity, accuracy and resolution are very high but EMI affects its performance.

2.1.3. Radiant Displacement Sensors

Radiant sensors capable of measuring displacement fall into three main categories, ultrasonic and microwave which are described below, and optical which are described in more detail in Chapter 3.

Ultrasonic sensors consist of a transmitter and a receiver or a combination of both, known as transceiver, emitting ultrasonic frequency pulses (Loughlin, 1989 and Alloca and Stuart, 1984). They operate by measuring the time delay between the emission of the pulse, and the reception of its reflection or echo by the sensor as shown in Figure 2.7.

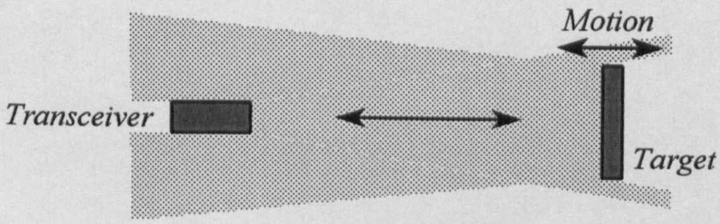

Fig. 2.7: An ultrasonic sensor

The characteristics of the electronic equipment and the properties of the acoustic path will determine the frequency of the pulse which lies in the range 20 kHz up to 225 kHz. Resolution is determined by the frequency of the sound with the higher frequencies giving the best resolution. The acoustic wave at these frequencies is directional becoming more so as the frequency increases.

Apart from the fact that the sensor is prone to EMI, the received signals are also prone to interference from both ghost reflections of the transmitted pulse and from background noise. The sensor can operate with any sort of surface but the very absorbing ones. It can have an operational range which depends on the target size and target surface reflectivity starting from a few millimetres up to a few metres with an approximate accuracy of 1 %. Temperature affects the performance of the sensor by altering the velocity, attenuation and spread of the sound signals. The sensor does not operate in vacuum since sound waves cannot travel through a vacuum.

Microwave sensors consist of antennas which transmit and receive microwave signals. The antennas can be of many different kinds such as dipole, horn and parabolic. The operation of microwave sensors is determined by the electromagnetic energy propagation laws. When the object to be detected enters the microwave field, it either absorbs or reflects enough energy to cause a significant change in the signal level at the receiver. The amount of energy that travels in each direction is a function of the angle of incidence, polarization and wavelength of the energy. It is also a function of the target electrical properties such as conductivity, permittivity and permeability of the materials involved.

Nyfors and Vainikainen (1989) classify microwave sensors in five categories: Transmission, reflection and radar, resonator, radiometer and active imaging.

Displacement is measured using reflection or radar sensors where the signal reflected from an object is monitored. Continuous wave or pulsed signals may be used as well as signals of fixed or swept frequency. The sensor can measure the time of flight of the signal, a change in its frequency (Doppler Effect) or any amplitude variations.

Microwave sensors are non-contact, insensitive to environmental conditions and have fast response. Low energy level microwaves are used so as not to cause displacement in atomic structures although minor heating may be caused. EMI affects the performance of the sensor which is also sensitive to more than one variable, such as moisture, density or temperature, thus needing other extra measurements for compensation. Due to the relatively long wavelengths used the achievable spatial resolution is limited. The higher the frequency of operation, the more expensive they are.

The displacement sensors reviewed in Sections 2.1.1 to 2.1.3 belong to the electrical, magnetic and radiant output signal domains. The investigation was based on the specifications / requirements outlined in Table 1.1. Their fundamental characteristics, i.e. mode of construction and operation, operational range, accuracy, resolution, advantages and disadvantages were outlined. Their main characteristics are summarised in Table 2.2.

Table 2.2: Important characteristics of displacement sensors

Displacement Sensors	Operational Range (mm)	Accuracy (%)	Coupling with Measurand
Potentiometric	< 1000	1	Contact
Capacitive	0.01 - 10	< 1	Non-Contact
Piezo-electric	< 0.05	1	Contact
Inductive	< 500	1	Contact
LVDT	< 500	1	Contact
Eddy Current	< 6	< 1	Non-Contact
Ultrasonic	10 - 10000	1	Non-Contact

Considering the requirements outlined in Table 1.1 where non-contact operation is necessary then it is obvious that only three types of sensor can be considered. These are the capacitive, eddy current and ultrasonic sensors. But capacitive and eddy current sensors do not offer the required operational range. Ultrasonic sensors seem to be the best option. However, ultrasonic sensors along with all the other types of sensors summarised in Table 2.2 are sensitive to external effects such as EMI. Insensitivity to EMI can be achieved to a certain degree by employing various techniques although their effectiveness is greatly depended on the amount of money spent towards achieving this goal. The sensor investigated in this Thesis employs optical fibres which are immune to EMI. The electronic circuitry can be positioned in an EMI free area and the signals can be transferred to the sensing location using the optical fibres thus achieving EMI free operation of the sensor. In this way an overall lower cost level is achieved.

2.2. VIBRATION

The survey for vibration sensors was aimed towards sensors which could monitor vibration of frequency around a few hundreds of Hertz over an operational range of a few tens of millimetres with an accuracy of around 1 %, as defined by the requirements outlined in Table 1.1.

Vibration is a term used to define dynamic motion. This is the periodic forward and backward motion, or oscillation, from rest or static position of an object (Seippel, 1983). Although it can be used to advantage in certain areas it is often an undesirable effect.

Vibration can be desirously used to produce music through the excitation of various musical instruments or through the controlled electrical excitation of the cone of a loudspeaker. It is also desirously used in cleaning and mixing machines.

Vibration is an undesired effect encountered with machines in motion or machines that have rotating members. If vibration remains uncontrolled it can degrade the performance and safety of such machines. Periodic monitoring of the machines to ensure that they do not vibrate beyond allowable limits, thus preventing fatigue failures and faulty operation, is necessary. Through vibration monitoring, information about the state of a machine, its calibration stability and analysis of its structural points (loose screws, faulty interconnections and broken components) can be obtained.

Acoustic noise is another effect resulting from unwanted vibration. In industrial environments where heavy machinery is used it can cause annoyance and inefficiency to the workers and at worst cause deafness. In areas such as these vibration must be controlled and contained (Anderson and Bratos-Anderson, 1993).

Vibrations can be free, forced or self-excited. Free vibrations occur if a system is set in motion and then allowed to continue moving under the action of its own internal forces (i.e. weight). The system which will be vibrating at its own natural frequency will eventually come to rest under the influence of various internal or external influences. This opposing action is called damping. Forced vibration occurs by the fluctuating excitation of a system in motion using an external force. Initially, the forced and natural frequencies will control the vibration but the natural frequency will soon die away depending on the damping used leaving the forced frequency to control the vibration. When the forcing frequency is equal to the natural one the system will be vibrating at its resonant frequency and will always vibrate periodically. The amplitude of vibration can build up to a very high value if the system is at resonance. Self-excited vibrations are produced by the motion of the system itself and take place at a natural frequency of the system (Ryder and Bennett, 1992).

Vibrations caused by a periodic forcing function are characterised by their amplitude, frequency and phase. In phase characterisation the frequency of vibration is compared with a reference frequency to give a phase difference. A system can vibrate in one or more directions, known as modes or degrees of freedom, at the same time each having its own natural frequency.

2.2.1. Vibration Sensors

Measurements of vibration may be made using two different approaches (Dally *et al*, 1993). The first involves a fixed reference plane which is the vibrating surface when stationary. The base of the sensor here is separated from the vibrating surface and does not move. Examples are versions of the displacement sensors described in Sections 2.1.1 and 2.1.2. In the second approach the use of a fixed reference plane is not possible thus the sensor has to be attached to the vibrating surface experiencing the motion that is to be measured. This is known as a seismic sensor.

The seismic sensor consists of three basic elements. These are the spring-mass-damper system, a protective housing and an output displacement sensor, as shown in Figure 2.8. When the measurand vibrates the force (F) required to move the seismic mass (m) will be transmitted from the housing through to the spring which will deflect by an amount proportional to the force required to displace the mass. This will be dependant on the force constant for the spring (k). Displacement (d) of the mass will thus be measured and the resulting acceleration (a) could also be determined, as shown in equation 2.1:

$$F = k\,d = m\,a \qquad \textbf{Eq. (2.1)}$$

Ideally, the mass should remain stationary in an absolute frame of reference and the housing and output transducer should move with the vibrating object (Figliola and Beasly, 1991).

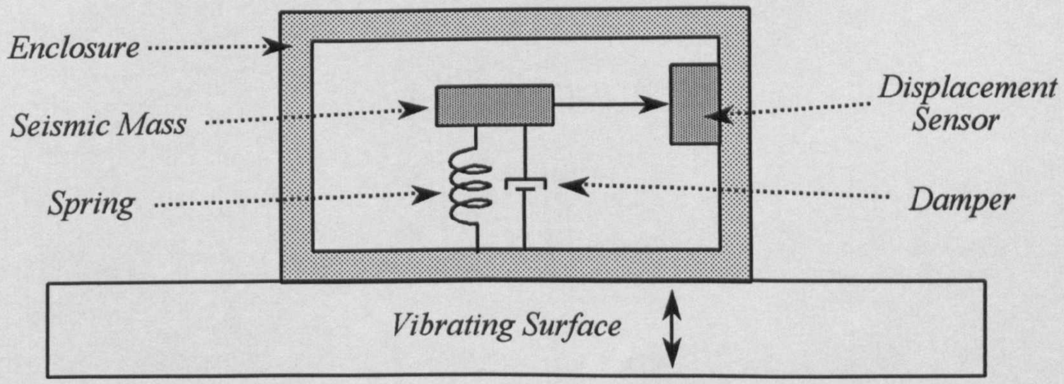

Fig. 2.8: A seismic sensor (Figliola and Beasly, 1991)

The spring-mass type of seismic sensor has a characteristic that complicates its analysis. A system such as this will always exhibit oscillations at some characteristic natural frequency which depends on the structure of the sensor. Vibration at this frequency will result in continuous oscillations of the spring-mass mechanism which will come to rest under the influence of the damper employed. If the applied frequency of vibration is similar to the natural frequency of the sensor then non-linearities will occur in the output due to the resulting resonant frequency. As a general rule, the applied frequency (f) with respect to the natural frequency (f_N) of the sensor must be either $f < 0.4\ f_N$ or $f > 2.5\ f_N$ (Johnson, 1993). A typical frequency response plot for vibration sensors is shown in Figure 2.9.

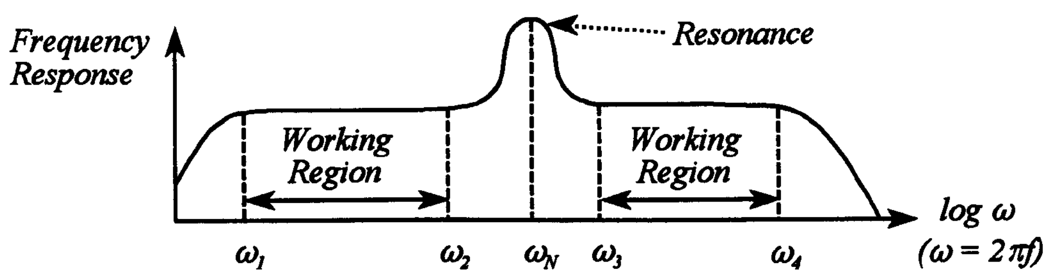

Fig. 2.9: Typical frequency response for vibration sensors

As seen in Figure 2.9 the frequency range close to the natural frequency of a sensor is always avoided since this is the area where resonance occurs. The figure shows working regions on both sides of the resonant peak. Vibration sensors are always calibrated to operate in only one rather than both working regions with the one enclosed by ω_1 and ω_2 being the region most frequently used. The working region enclosed by ω_3 and ω_4 is used mostly when a specific vibrational frequency is necessary to be monitored which is in that particular region. The factors affecting the choice of working region (range) are:

- The natural frequency of the sensor;
- The frequency range of the measurand that needs monitoring;
- The range which offers the necessary operational frequency range.

The displacement sensors used in vibration measurements can be electrical, magnetic or radiant (see Sections 2.1.1, 2.1.2 and 2.1.3) and some can be used in seismic as well as in fixed referenced plane sensors. In the case of the seismic sensor they are fixed on the enclosure of the seismic sensor and use the mass at rest as their fixed reference plane.

Two types of displacement sensor used in vibration measurements which are not presented in Sections 2.1.1, 2.1.2 and 2.1.3 are the strain gauge and the piezoresistive ones.

These two techniques, which are mostly used when vibration is needed to be monitored and not when static (i.e. when the measurand is not moving) displacement measurements need to be taken, are briefly presented below.

Strain gauge sensors operate by the principle that if an electrical wire is stretched (not beyond its elastic limit) then its length will increase and its cross sectional area will decrease resulting in an increase in its resistivity. The wire has to be attached to the measurand via an elastic carrier (referred to as backing) in order to be electrically isolated. The temperature coefficients of the backing and wire must be matched. Standard gauge resistivities are 120 Ω, 350 Ω, 500 Ω, 1000 Ω and 5000 Ω (Dally *et al*, 1993). For good sensitivity the sensor should have long longitudinal and short transverse segments so that the transverse sensitivity will be very small (1:50) compared to the longitudinal. The size of the gauges may vary between 0.2 mm and 100 mm. Typically the strain gauges are connected to wheatstone bridge circuits. EMI affects the performance of the sensor and so do temperature effects due to contraction/expansion of the metals used (Fraden, 1997).

Piezoresistive sensors are made from materials (crystals) that exhibit a change in resistance when subjected to stress. Semiconductor materials are used such as silicon with either boron for a P-type or arsenic for a N-type material. The resistivity of the material can be adjusted to any specified value by controlling the impurity concentration. When the piezoresistive crystal is stressed it becomes electrically anisotropic and its resistivity changes. The voltage drop across the sensor depends on the current density through it, the level of stress and the piezoresistive coefficients (adjusted by controlling the impurity concentration and optimizing the direction of the axis of the sensor with respect to the crystal axes) of the materials used. Vibration sensors employing the piezoresistive technique have the largest frequency of vibration response (Dally *et al*, 1993).

Table 2.3 summarises the most important characteristics of vibration sensors and presents general figures of their performance.

Table 2.3: Important characteristics of vibration sensors

Vibration Sensors	Natural Frequency, f_N, (Hz)	Applied Frequency, f, (Hz)	Cross-Sensitivity, (%)	Accuracy, (%)
Potentiometric	10 - 100	$< 0.4 f_N$	1	1
Strain Gauges	20 - 800	$< 0.4 f_N$	2	1
LVDT	20 - 2000	$< 0.4 f_N$	1	1
Capacitive	3000	< 2000	1	< 1
Piezoelectric	6000 - 7000	< 5000	2 - 4	1
Piezoresistive	25000 - 65000	< 13000	2	1

Note: The data in Table 2.3 have been taken from Bolton (1996) and Fraden (1997).

It is obvious from the Table above that the natural frequency of the sensor is the one which controls the applied frequency range able to be monitored. Another factor is the construction of the sensors themselves which if composed of relatively large mechanical components, such as the potentiometric and LVDT, will affect their frequency range. The sensors which can measure high frequencies of vibration are the capacitive, piezoelectric and piezoresistive. The size of these sensors is relatively small and they have a natural frequency which is much higher than the others. Their displacement range rarely exceeds a few tens of microns which limits them to monitoring measurands which vibrate with a maximum displacement span of only a few tens of microns. The piezoelectric sensor suffers from the fact that it can only produce the necessary electric charge if the pressure applied is continually changing, resulting in a minimum frequency of response of a few Hertz. All sensors shown in Table 2.3 can be affected by EMI.

The sensor investigated in this Thesis can be EMI free due to the use of optical fibres and positioning of the electronic circuitry in an EMI free environment. It can also be arranged to measure large displacements which can be in the order of a few tens of millimetres if required.

2.3. SUMMARY AND CONCLUSIONS

In process industries displacement is the most widely measured physical quantity. As noted in the introduction through the monitoring of displacement, information on variables like distance, vibration, pressure, force, acceleration, tension and liquid level can be determined.

In the first half of this chapter sensors able to measure displacement with an operational range in the region of a few centimetres have been reviewed. These sensors belong in the electrical (potentiometric, capacitive and piezoelectric), magnetic (inductive, LVDT and eddy current) or radiant (ultrasonic and microwave) signal domains.

In the second half of this chapter sensors able to measure vibration have been reviewed. Vibrations can be measured in two ways. In the first a fixed reference plane is involved and the sensor is separated from the vibrating surface. In the second their is no fixed reference thus the sensor has to be attached to the vibrating object (seismic sensor). The displacement sensors used in vibration measurements can be electrical, magnetic or radiant. The most widely used vibration sensors are the potentiometric, strain gauges, LVDT, capacitive, piezoelectric and piezoresistive. The frequency range that these sensors monitor is determined by their natural frequency and by their size. Sensors such as the potentiometric and LVDT have a bulky construction which lowers their frequency range. The piezoelectric and piezoresistive sensors have the largest frequency range.

Some of these sensors, whether for displacement or vibration measurements, offer non-contact and non-destructive operation whereas others depend on coming in contact with the measurand in order to perform their task. Important requirements, however, such as being non contact, non destructive, lightweight, compact, have low power requirements and environmental ruggedness are difficult to be met. Most importantly these techniques are susceptible to EMI and although they do have a form of EMI protection its effectiveness can depend on the location in which they must operate. EMI protection is a factor greatly dependant on the amount of money spent towards this goal. These sensors, however, have stood the test of time, have been adjusted to the various requirements of production and are at present very highly developed. Investing in alternative sensing techniques would not be justified unless the benefits are well clear.

Chapter 3

Survey of Fibre Optic Sensors

Optical sensors is another class of sensors which belong in the radiant signal domain and are reviewed in more detail in this chapter. They consist of three essential components which are the light source, the photodetector and light guidance devices such as lenses, prisms, splitters, reflectors, diffusers, filters and polarisers. These will guide the light emitted from the light source (very often modulated) to the measurand by performing their appropriate function and from there to the photodiode. The measurand will change the characteristics of the light in one or more ways and examination of these changes will determine the state of the measurand. The attributes of optical sensors are simplicity, relatively long operational ranges (several millimetres), insensitivity to loading effects, non contact and non destructive operation, lightweight, compact and have low power requirements. These are factors that distinguish optical sensors and benefits that the sensors described in Chapter 2 seldom have.

But these benefits, however, cannot tempt the process industry to invest in these new techniques since the problem of immunity to EMI may still exist. Positioning active opto-electronic components in an electrically noisy environment affects their performance. Another reason for this reluctance is the highly developed, practical sensors described in Chapter 2 which have stood the test of time and are well suited to the requirements of production.

What will give optical sensors an advantage over all the other sensors is the adoption of optical fibres into the system as light guidance devices. Active opto-electronic components can be positioned in an EMI free environment and the light can be guided to the measuring location via optical fibres where the measurand will change its characteristics. Optical fibres as a propagating medium are not vulnerable to many forms of interference thus minimizing noise problems. The optical fibre is non conductive and the absence of an electrical signal means that optical fibre sensors are well suited to operation in many hazardous environments.

Some important requirements also exist when using optical fibres. The most important is the need for insensitivity to external factors since these may interfere with the sensed signal along the fibre path. Also, compatibility between the properties of individual components is necessary.

3.1. OPTICAL FIBRES

The most widely used structure in optical fibres is the single solid dielectric cylinder, the core, which is surrounded by a solid dielectric, the cladding. Most fibres are encapsulated in an elastic, abrasion-resistant plastic material known as jacket, as shown in Figure 3.1. In low and medium loss optical fibres the core material is glass and is surrounded by either a glass or a plastic cladding. Higher loss plastic-core fibres with plastic claddings are also widely in use.

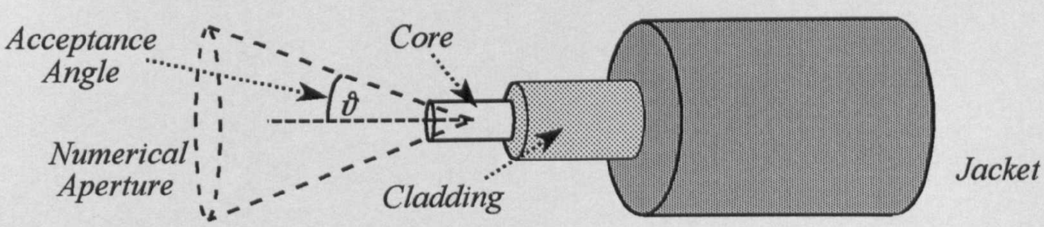

Fig. 3.1: Optical fibre structure

Light can be injected in the core up to a maximum angle, known as the acceptance angle, within a cone shaped zone, known as numerical aperture (NA = $n_0 \sin \vartheta$, where n_0 for air), in order to propagate (Figure 3.1). Total internal reflection of the light propagating inside the core at the interface between core and cladding is achieved if the refractive index of the core is slightly higher than that of the cladding. The refractive indices of the core (n_1) and cladding (n_2) define the numerical aperture of the fibre, i.e. $NA = (n_1^2 - n_2^2)^{1/2}$. The cladding also serves to reduce scattering losses resulting from dielectric discontinuities at the core surface, adds mechanical strength to the fibre and protects the core from absorbing surface contaminants with which it could come in contact. The jacket adds further strength to the fibre and mechanically isolates or buffers the fibre from small geometrical irregularities, distortions or roughnesses of near by surfaces that could cause scattering losses (Keiser, 1991).

Variations in the material composition of the core give rise to two commonly used fibre types, the step index and the graded index types. In the step index type the refractive index of the core is uniform throughout and undergoes an abrupt change at the cladding boundary. In the graded index type the core refractive index is made to vary as a function of the radial distance from its centre. The step index fibre can be further divided into single-mode and multimode fibres. A single-mode fibre has a much smaller core diameter (5 μm) than the other two types of fibre (50 μm) and can only sustain one mode of light, whereas multimode fibres can contain many hundreds of modes.

Multimode fibres offer several advantages compared to single-mode fibres. The larger core radii of multimode fibres make it easier to launch optical power into the fibre and facilitate the connecting together of similar fibres. Also, light can be launched into a multimode fibre using a light emitting diode (LED) source, whereas single-mode fibres must generally be excited with laser diodes.

A disadvantage of step index multimode fibres is that they suffer from intermodal dispersion. This effect is reduced when the graded-index core profile is used which also allows for much larger bandwidths. Even higher bandwidths are possible in single-mode fibres where intermodal dispersion effects are not present.

3.2. ADVANTAGES AND DISADVANTAGES OF OPTICAL FIBRE SENSORS

Optical fibres possess a number of significant advantages which make them suitable for use as the basis for a wide range of optical sensors. The main advantages of optical fibre sensors are summarised below:

- Optical fibres are made from dielectric materials thus have no electrical conduction paths and are free from EMI;
- They can perform non-contact, non destructive and remote measurements;
- They suffer very low signal transmission losses;
- They respond very rapidly to signal changes, have large dynamic range and large bandwidth;
- Have low operating power requirements;
- They are mechanically rugged and flexible, frequently there is no need for moving parts, are highly compact in size and have high tensile strength;
- They can withstand high temperatures in the order of a few hundred degrees Celsius (in the case of some glass optical fibres), shocks, mechanical vibrations and adverse environments;
- They can be chemically inert (cladding and jacket specifically selected for this purpose) and can be used in explosive environments without danger;
- Passive mode of operation for extrinsic sensors is possible and signal multiplexing for most intrinsic and interferometric sensors is generally simple.

There are also some disadvantages when using optical fibres and careful consideration of these is advised in order to achieve the best possible performance from the sensor. The main disadvantages are summarised below:

- The introduction of new technology, i.e. the precision and stability required as well as the high costs associated with new technologies.
- Careful selection of the materials used to construct any optical fibre sensor system is essential in determining the ultimate performance in terms of sensitivity, cost benefit and suitability for use in the operating environment;
- The choice of optical fibre used, the nature of any specialized sensing mechanism and the overall sensor construction components are governed by material considerations;
- Matching of the properties of the individual components both within the sensor and to the operating environment is essential;
- The fact that the fibre itself can respond to an external influence immediately indicates that the optical fibre that leads to and from the sensing region may also

accidentally respond to such external influences. This gives rise to the possibility of interference with the sensed signal along the fibre path. The need for insensitivity of the fibres to external factors is very important.

3.3. MODULATION TECHNIQUES USED IN OPTICAL FIBRE SENSORS

The five modulating techniques most widely employed in optical fibre sensors are intensity, wavelength, polarization, phase and time duration modulation (Medlock, 1986).

Optical detectors, also known as photodiodes, respond mainly to changes in optical intensity and are strongly dependant upon both temperature and ageing. These dependencies may also be a function of wavelength and in many cases the simplest coding mechanism could be digital (on/off). Analogue sensors require a different and more critical approach to their design and use.

Intensity modulation is the simplest and most cost effective modulation technique employed by optical sensors. Variation in the intensity of the detected light indicates a change in the state of the measurand. Low cost active opto-electronic components such as light emitting diodes (LEDs) and PIN photodiodes can be employed, along with very simple circuitry and multimode, step index optical fibres.

Factors that affect intensity modulation are various forms of electronic noise, temperature effects, stray illumination and varying signal to noise ratio (Jones *et al*, 1989).

Intensity-based sensors are very successfully employed for switching/digital applications (Usher and Keating, 1996). Where good accuracy (< 1 %) and long term stability is required, a form of compensation (reference) has to be provided (Murtaza and Senior, 1995).

Wavelength modulation offers sensing of the state of a measurand without having to depend on the intensity of the detected signal if all intensity modulating effects are minimized at the point of sensing. It is not as widely used as intensity modulation for the simple reason that it requires complex demodulation circuitry. A broadband source, a colour modulator and a form of a spectrometer are usually required. A minimum power level of received power is often necessary. In narrow band systems this may be difficult to achieve, resulting in long integration times. An easier approach to this problem is based on optical filtering and two wavelength detection (Murtaza and Senior, 1995).

Wavelength detection has the advantage that it is inherently less susceptible to instabilities caused by system components which may affect the behaviour of fibres or connectors.

Polarization modulation involves the use of a specific monomode type of fibre such as polarization maintaining, single polarization or birefringent types and offers great sensitivity. Wilson and Hawkes (1989) state that usually two orthogonally polarized modes are launched into the same fibre at 45^0 to the polarization maintaining direction of the fibre in order to excite the two modes equally. The measurand will affect one of the two modes and will cause an increasing phase difference between them as they travel down the fibre. The modes are then separated at the end of the fibre and are detected by two detectors.

Another way would be to launch light having the same initial phase in both ends, instead of one, of a single mode fibre arranged in an interferometer loop rotating in an inertial frame reference and detect it from both ends of the fibre (Sagnac effect). Although the two beams will have travelled the same distance they will be detected with different phases due to the Doppler effect. The phase of the two signals is then compared. This approach is mainly used as the basis of a gyroscope (Billings, 1993).

Phase modulation offers better noise performance and higher sensitivity than intensity modulation depending on the application. This type of sensor demands single mode optical fibres. In order to obtain these parameters it is usually necessary to employ a high quality phase discriminator, coherent light sources and single mode fibres. The fibres to be used are typically expensive polarization maintaining or low linear birefringent fibres. Comparison between continuous referencing of a standard input condition and the measuring phase through a quadrature relationship is necessary for maximum sensitivity. Temperature variations and wavelength instability can jeopardise the performance of the sensor. These requirements and limitations add to the complexity of the sensor and tend to make the cost prohibitive for industrial requirements.

Time duration modulation is based on the time elapsed between the transmission of a short pulse and the reception of its echo by the sensor. It is an accurate and cheap way of performing measurements. Drift in measurement systems is greatly reduced, reference is not necessary, the transmission of data suffers little from degradation of the signal and linear relationships exist. In the case where short distances are to be measured, due to the speed of light, high frequency modulation is necessary, typically in the order of hundreds of MHz.

Sensors employing time duration modulation are used as rangefinders employing lasers as light sources. Their use as position sensing sensors in the ranges relevant to this work, i.e. several centimetres is impractical and expensive due to the very high frequency equipment necessary to perform the measurement.

The benefits and problems of each modulating technique are summarised in Table 3.1 for comparison purposes.

Table 3.1: The benefits and problems of each modulation technique.

Class	Benefits	Problems
Intensity	Simplest, most cost effective and cheap.	Affected by electronic noise, stray illumination and varying signal to noise ratio. Requires referencing for high accuracy and long term stability.
Wavelength	Less susceptible to instabilities caused by system components. Does not depend on intensity of detected signal.	Requires complex demodulation circuitry. Minimum received power level often necessary. Long integration times in narrow band systems.
Polarization	Highest sensitivity.	Requires specific monomode fibres (polarization, etc.).
Phase	Better noise performance than intensity modulation.	Requires polarization maintaining fibres, discriminators, coherent light sources and continuous referencing between a standard input condition and the measuring phase.
Time Duration	Accurate, cheap, reduced drift in measurements. No need for reference.	High frequency modulation necessary for short distance measurements.

It can be seen from Table 3.1 and Section 3.3 that the five modulation techniques follow a different approach with different benefits and problems. The choice of technique, however, will be determined by the application and its requirements and specifications. If sensitivity is of paramount importance then polarisation modulation will be the best choice. If cost effectiveness with relatively high accuracy is important then intensity modulation would be the best choice.

3.4. CLASSIFICATION OF OPTICAL FIBRE SENSORS

Optical fibre sensors are classified into four main groups by the way in which the measurand is measured. The groups are interferometric, intrinsic, evanescent and extrinsic (Udd, 1992). Interferometric and evanescent sensors are essentially intrinsic and extrinsic sensors respectively but they are usually treated as independent groups.

Interferometric sensors are the most sensitive optical fibre sensors to date. Coherent monochromatic light (usually polarized) is used propagating in a single mode fibre under stress or varying temperature and interferes with light either directly from the source or guided by a reference fibre isolated from the external influence. The effects of strain, pressure or temperature change lead to differential optical paths by changing the optical fibre length, core diameter or refractive index with respect to the reference fibre. Interferometric sensors have been very successfully employed as gyroscopes (Billings, 1993).

In intrinsic optical fibre sensors, the fibre itself is the active element. Propagation of light through the fibre is used not only for signal transmission, but also for quantifying the parameter to be measured. The parameter to be quantified must influence the fibre characteristics in some way so that the light flux transmitted by the fibre will be altered in some manner.

In evanescent sensors the measurand changes the characteristics of the evanescent wave around and within the optical fibre core. This is usually achieved by stripping a length of fibre of its cladding. The sensor is then composed of the naked fibre core and whatever sensing layer is positioned on, or close to, the surface of the fibre. In another way, a longitudinal, precise, aperture inside the fibre at a controlled distance from the core can be produced into which suitable liquids or gases can be made to flow.

Evanescent field sensors are highly sensitive to unwanted effects. Any material absorbed by or bound to the surface of the guide may give rise to absorption, scattering or fluorescence signals which can be erroneously interpreted.

Extrinsic optical fibre sensors offer simplicity, low cost, ability to use established opto-electronic components as well as non-contact and non-destructive operation. In extrinsic sensors sensing results from external to fibre related effects such as reflected or scattered light, intensity of light and interruption of a light beam. The fibre itself is passive and is used only to transmit light from the light source to the sensing location and/or from the sensing location to a detector. The fibre plays no role in the actual sensing and any influence of the fibre itself on such sensing is undesirable and leads to inaccurate sensor response. Extrinsic optical fibre displacement sensing techniques are presented in detail in Section 3.5. The novel displacement sensing technique investigated in this thesis belongs to this class of optical fibre sensors.

The most widely investigated intrinsic displacement fibre optic sensor is the microbend sensor shown in Figure 3.2 (Berthold, 1994). Here, an optical fibre is clamped between a pair of corrugated platforms. When the separation between the platforms changes, the amplitude of the signal transmitted through the fibre changes accordingly. A maximum operational range in the order of tens of microns and accuracy of 1 % is possible.

Microbend sensors enjoy the usual advantages that fibre optic sensors offer and also mechanical and optical efficiency that leads to low parts count, low cost and easy mechanical assembly. It can also avoid differential thermal expansion problems since it does not require fibre bonding to other components. It is a fail-safe sensor which either produces a calibrated output signal or fails to a state of no light output.

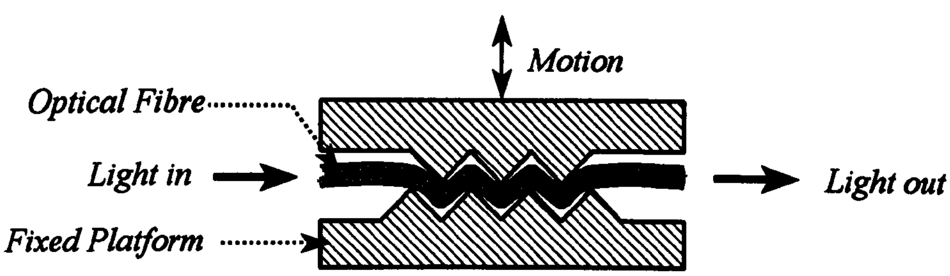

Fig. 3.2: A microbend sensor

The microbend sensor is sensitive to optical power level changes and light direction (modes). The modal sensitivity of the sensor makes it also a modal filter thus any modal filtering action by other components in the multimode fibre optic link is a potential source of error. In order to avoid this source of error some form of self referencing is necessary.

Frustrated total internal reflection (FTIR) and attenuated total reflection (ATR) are two examples of evanescent type optical fibre sensors where the evanescent wave can be used to measure displacement. Light guided through a fibre is coupled into a prism, as shown in Figure 3.3, where it undergoes internal reflection on the large side of the prism and is then coupled to another fibre. Their operational displacement range is in the region of approximately 1 micron.

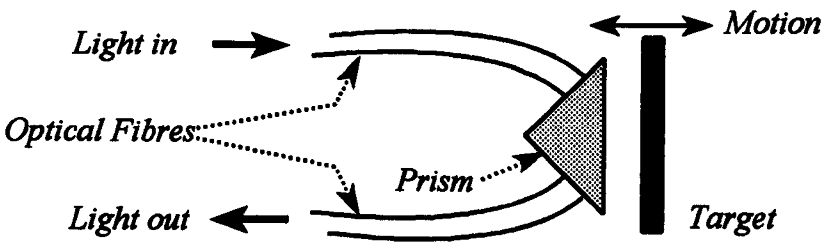

Fig. 3.3: An FTIR/ATR evanescent sensor

FTIR sensing (Jones *et al*, 1989) involves the extraction of energy from the evanescent wave which exists near the external surface of the prism when light undergoes internal reflection at the prism-air interface. Light absorber materials are used as targets.

ATR (Sincerbox and Gordon, 1981) is similar to FTIR but operates on a different principle. The modulation is brought about by varying the distance between a reflecting surface such as silver and the prism face. When polarized light enters the prism and is internally reflected at the critical angle of incidence the reflectivity which is a function of polarization can vary from almost zero to about 96 % for a zero gap.

Optical fibre sensors can be classified into four categories interferometric, intrinsic, evanescent and extrinsic. The benefits and problems of each class of sensors are summarised in Table 3.2. Extrinsic sensors offer clear advantages over the other categories such as simplicity, low cost, etc. But its the application which will determine which class of optical sensors would be the best option.

Table 3.2: The benefits and problems of each class of optical fibre sensor

Class	Benefits	Problems
Interferometric	Most sensitive.	Requires coherent monochromatic light and single mode fibres.
Intrinsic	Simplicity and low cost.	Sensitive to optical power level changes and modes.
Evanescent	Sensitive.	Highly sensitive to unwanted effects.
Extrinsic	Simplicity, low cost, non-contact and non-destructive.	External influences on the fibre can cause inaccuracies.

3.5. EXTRINSIC, INTENSITY BASED SENSORS

Extrinsic optical fibre sensors can detect changes in the intensity of the light caused by the measurand. They have very important advantages over intrinsic, interferometric or evanescent sensors. Features such as simplicity, low cost, ability to use established opto-electronic components and adaptability to various environments and applications make them very attractive. They also offer non-contact and non-destructive operation.

The main drawback of these sensors is the requirement for a reference signal which may be used to compensate for intensity variations of the signal caused by factors other than variations in the measurand. The signal may be affected by noise originating from the transmitter/receiver and effects caused by the transmission optics. The removal of such effects is necessary in order to provide an output which is solely related to the state of the measurand. Many examples of referencing techniques exist such as differential, optical balanced bridge, triangulation and wavelength. Their effectiveness depends upon the system configuration and sensor head arrangement, as will be shown in the following pages of this chapter. Systems offering the greatest level of reliance on referencing tend to be complicated and expensive to implement.

3.5.1. Non-Referenced Displacement Sensors

Non-referenced extrinsic optical fibre sensors depend on the measurement of optical intensity and can be configured to be either transmissive or reflective as shown in Figure 3.4. They tend to have a non-linear response (such as an inverse square law) and small range (< 2 mm). The efficiency with which light is collected by the detecting fibre depends on the distance that the light has to travel from the emitting to the receiving fibre, the effects of any intermediate material and, in the reflective configuration, on the quality of the reflective surface.

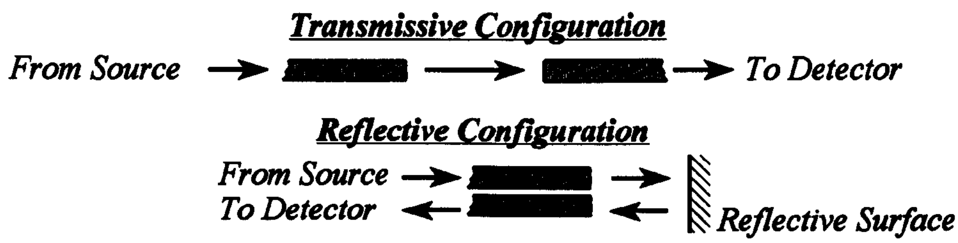

Fig. 3.4: Sensor configurations

This kind of sensor is the one most likely to suffer from influences unrelated to the sensing operation (Jones *et al*, 1989). Electronic noise such as excess noise, generated by the source itself (considerable if a laser is used but usually not significant if an LED is used), fluctuations in the electronics supplying the source, 1/f noise in the receiver circuit (insignificant above 1 kHz modulating frequency), shot noise, thermal noise and dark current will affect the behaviour of the sensor. Temperature changes will affect the intensity output ($\approx$ -0.7 %/^{o}C in the case of an LED) and the spectral emission of the source, the responsivity of the photodiode ($\approx$ 0.4 %/^{o}C in the case of a PIN photodiode, also a function of wavelength), link attenuation and mechanical changes in components, and optical transmission through connectors. The signal-to-noise ratio (SNR) varies depending on the level of illumination (signal). Ambient illumination also affects the detected signal and the SNR. For these reasons non-referenced, intensity based, extrinsic fibre optic sensors like the ones shown in various configurations in Figure 3.5 are used for short term measurements at modest accuracies. Their response is determined by their configuration and arrangement.

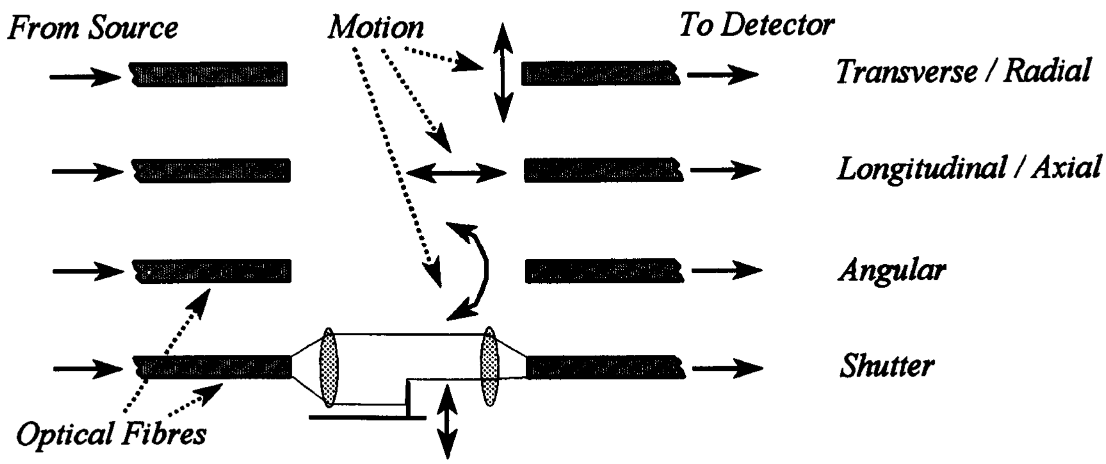

Fig. 3.5: Simple, intensity based, non-referenced extrinsic displacement sensors

In the transverse arrangement the detected signal will be at maximum in the middle of the range and will decrease due to solid angle effects and the angular emission involved as the detecting fibre moves away from the middle position.

In the longitudinal arrangement the detected signal will be at maximum at minimum range decreasing as the range increases following an inverse square law relationship.

In the angular arrangement the detected signal will be at maximum in the middle of the range. It will decrease as the detecting fibre starts rotating from the middle position due to the angular emission involved towards the detecting fibre.

In the case of the shutter the maximum detected signal will be at maximum range, and at minimum when the shutter blocks all the light, i.e. at minimum range. The inverse square law does not hold in this example.

In the case where the fibres are positioned in a reflective way, the behaviour/ magnitude of the detected signal will be different at close ranges. Looking at Figure 3.6, when the reflecting surface is at the closest position to the fibres the light does not illuminate the receiving fibre. As the reflecting surface moves further away it illuminates more of the receiving area of the receiving fibre and at the point where the total area of the receiving fibre is illuminated, and assuming broad angle of emission, the intensity of the light detected will reach its maximum value. Beyond this point the intensity of the light will decrease in an inverse square law fashion.

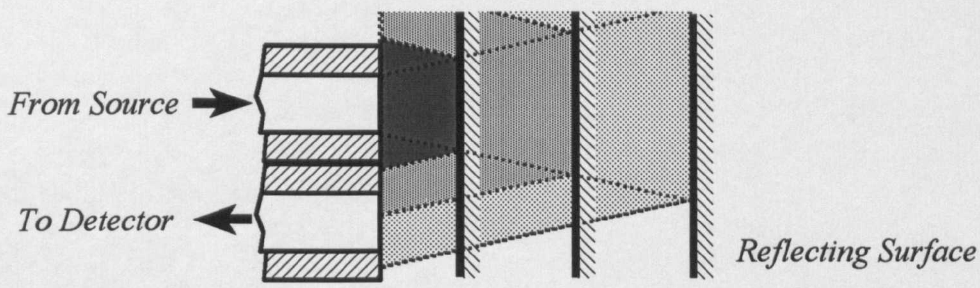

Fig. 3.6: Detection of light in a sensor with reflective configuration

If bundles of optical fibres are used just one bundle will be enough to transmit the light to and from the target with a coupler separating the two channels just before the point of connection to the active opto-electronic components. A bundle can have any number of fibres from a very few up to a few hundreds. Depending on the way that the individual fibres are arranged in the bundle the response of the detected signal will vary as shown in Figure 3.7 (Krohn, 1986). The fibres can be arranged randomly, hemispherically or coaxially (the black circles represent the receiving and the white ones the emitting fibres in the bundle).

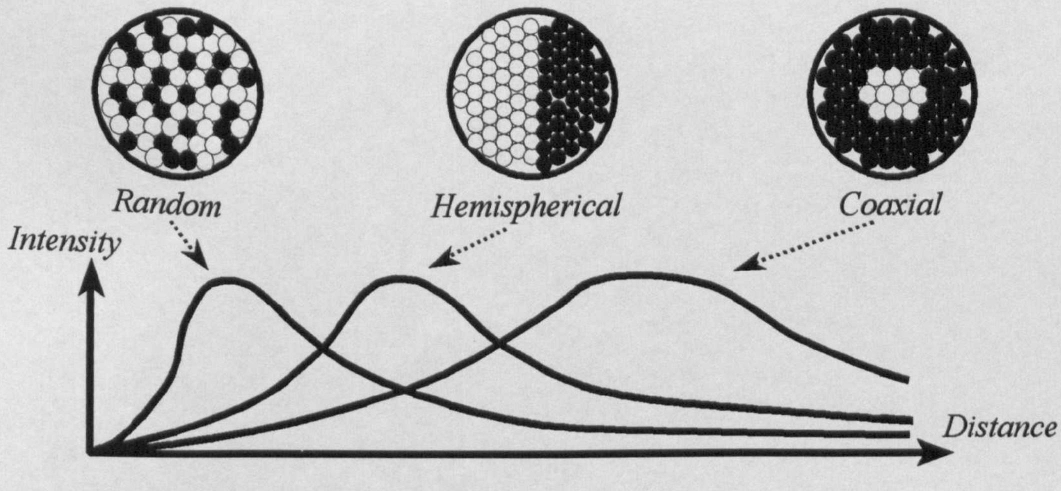

Fig. 3.7: Optical fibre bundle arrangement and response

The adoption of various kinds of lenses whether simple collimating or graded index (GRIN) can improve the operational range of these sensors up to a few millimetres.

These simple, intensity based sensors are most successfully applied to switching (digital, on/off) applications, i.e. to detect the existence or not of objects in their sensing area. A binary or Gray coded disk can be employed in this technique to produce a digital encoder (Usher and Keating, 1996). The code is arranged in tracks to provide rectilinear or rotary displacement. It can be read by individual fibres in a transmissive (Figure 3.8) or reflective way. The resolution of the technique will depend on the number of fibres used with the higher number of fibres resulting in higher resolution but increased sensor size.

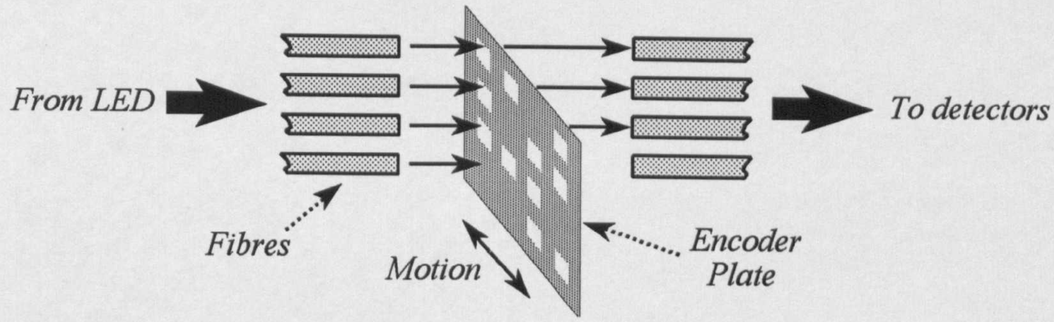

Fig. 3.8: A digital encoder

3.5.2. Referenced Displacement Sensors

For applications where the quantitative status of a measurand is required with good accuracy and stability, a form of compensation has to be provided which will allow rejection of common mode variations of noise such as those outlined in the beginning of Section 3.5. This compensation can take the form of a reference signal which will follow a similar length and conditions of optical path as the measurand signal but not at the point of measurement. Here, the common mode variations will be extracted from the two signals with only the effects of the measurand remaining. Another compensating technique would be to have both signals monitoring the measurand, like the one investigated in this thesis, with some form of mathematical manipulation determining the state of the measurand. The improvements from employing referencing techniques are in terms of reliability, reproducibility, accuracy, resolution (submicron possible) and large operational range although they unavoidably add to the complexity and cost of the sensor.

The referencing techniques for extrinsic, fibre optic, displacement sensors surveyed in this section are the differential, optical bridge balancing, triangulation and wavelength.

In differential techniques, one source (LED, laser, tungsten filament lamp) illuminates a surface via an optical fibre and two or more optical fibres detect the reflected, transmitted or scattered light affected by the measurand. Signal processing and interrelation of the detected signals will determine the quantity measured.

Libo *et al* (1993) described one of the simplest principles for a referenced fibre optic displacement sensor. The emitting fibre is positioned at a fixed distance from two receiving fibres and is made to move vertically with respect to its axis directing light onto the ends of the receiving fibres, as shown in Figure 3.9. Depending on the position of the emitting fibre with respect to the two receiving fibres, differing amounts of light can be received from each fibre thus changing the ratio of the signals from the two receiving fibres. This signal ratio remained constant when the intensity of the source was varied and also when the two receiving fibres were coiled on a rod. In both cases the intensity of the signal varied considerably. The operational range of the sensor was 0.6 mm.

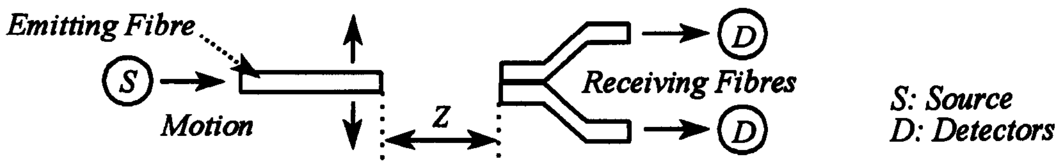

Fig. 3.9: The sensor arrangement of Libo *et al*, 1993

Cockshott and Pacaud (1989) used a different fibre arrangement where an optical fibre was emitting onto a reflective surface and the reflected light was detected by either one (Figure 3.10.a) or two (Figure 3.10.b) detecting fibres positioned next to the emitting fibre but with different separations from it. In the case where two receiving fibres were used, the detected intensity was expressed as the ratio of the two detected signals. All fibres were positioned equidistantly from the target. The sensor was tested under conditions of varying intensities of illumination and different reflectivity targets. The arrangement shown in Figure 3.10.a was immediately affected by any variation in these conditions. The set up of Figure 3.10.b was not affected and the ratio of the two signals remained the same. The displacement operational range of the sensor was 4 mm and its accuracy was 1 %. The response of the sensor was not, however, a linear one.

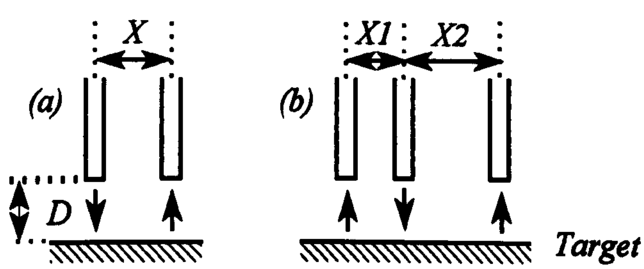

Fig. 3.10: The sensor arrangement of Cockshot and Pacaud, 1989

Libo and Anping (1991) followed a different approach, closely related to the one taken in this thesis. Three fibres were used positioned parallel to each other with the middle one emitting white light onto a surface as shown in Figure 3.11. The other two fibres, positioned one ahead and the other behind the emitting fibre, collected the reflected light and guided it to two power meters. The separation between the two detecting fibres and the emitting one was not equal (0.8 mm and 0.6 mm). The final signal, which was the ratio between the signal detected by the front fibre to that detected by the rear one, was a function only of the fibre to target surface separation and the axial separation between the fibres. It resulted in a linear response with a negative slope coefficient. Reflectivity measurements did not affect the sensor response. An overall displacement range of 0.2 mm with an accuracy of 1.1 % was reported. This sensor was configured to measure pressure in the range 0 - 20 kPa and a diaphragm was used as target.

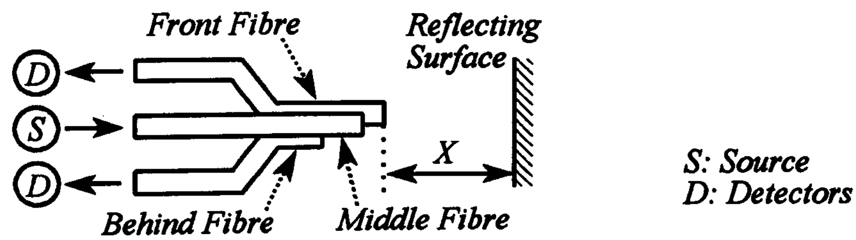

Fig. 3.11: The sensor arrangement of Libo and Anping, 1991

Regtien (1990) used a similar configuration but with the front fibre positioned at an angle (30^0) to the axis of emission rather than parallel to it as was the case with the rear detecting fibre (Figure 3.12). The separation between the two detecting fibres and the emitting one was 10 mm and the axial separation between the two detecting fibres was set at 16 mm. The surfaces used for the experimental measurements were white and black paper sheets. The response of the sensor, shown in Figure 3.13, shows that the variations in the reflectivity of the target do not affect the relative response of the sensor which clearly is not a linear one. The displacement operational range obtained was 60 mm. In another experiment the front angled fibre was positioned in parallel with the other two. The surfaces used were white paper and aluminium. The displacement range obtained was 100 mm and the relative responses were similar to those shown in Figure 3.13. In both cases the transfer function was obtained by dividing the difference between the two signals with either one of the outputs or with their sum.

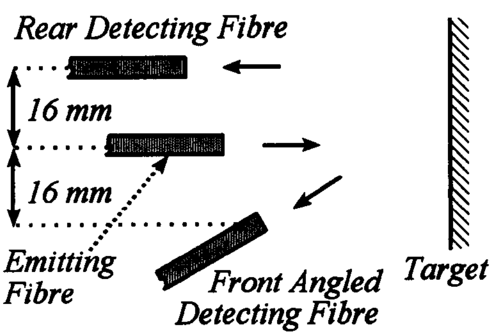

Fig. 3.12: The sensor arrangement of Regtien, 1990

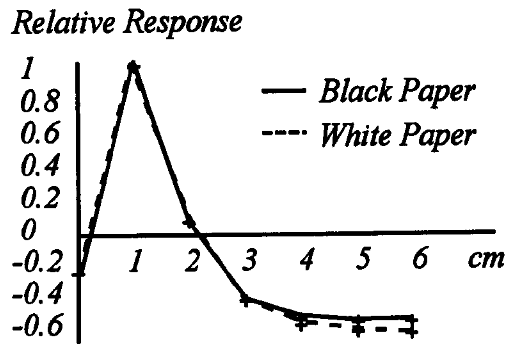

Fig. 3.13: The sensor response (Regtien, 1990)

The displacement sensor investigated in this thesis is also a differential one. It employs three 5 m long, 1 mm core diameter POF complete with their protective sheaths as shown in Figure 5.1. The middle POF, coupled to a red LED, emits light onto a target and the two outer fibres receive the reflected light from the target and guide it to two silicon PIN photodiodes with transimpedance amplifiers connected to a digital multimeter each. Experimental results under dark room conditions (see Chapter 7.2) resulted in a linear and scalable operational range of 75 mm when using a mirror as target and in excess of 85 mm when using matt white paper. Accuracy in the range of 1 % and resolution of 0.1 % at short and < 0.5 % at long ranges for both types of target was achieved.

Giles *et al* (1985) tried to solve the problems associated with intensity modulation with a technique called Optical Bridge Balancing. This technique is based on a configuration which employs four ports, two as input and two as output, as shown in Figure 3.14. Two identical LEDs emit in each of the two input ports and two identical photodetectors are connected to the two output ports. Couplers divide and combine each of the two input signals into two similar signals which feed both photodetectors introducing spatial separation between the output signals before they reach the detectors. In this arrangement, the two detectors would receive two similar signals separated by electrical time division multiplexing (TDM) or frequency division multiplexing (FDM) operation of the LED. Each signal channel would be common to two different signals which were then divided to remove any common mode variations. Accuracy of 1 % was achieved.

The drawbacks of this technique emerge from the fact that it uses two sets of identical LEDs and photodetectors. Obtaining two identical LEDs and two identical

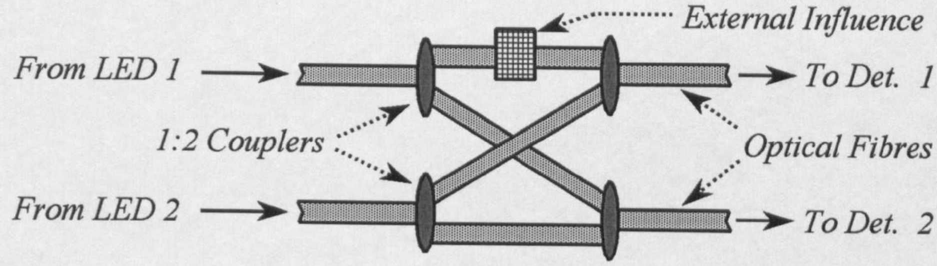

Fig. 3.14: Optical bridge balancing

photodetectors is very difficult. Identical operation is also very difficult to be ensured for various environmental conditions. Any offset voltages caused by the detectors or the associated electronics cannot be compensated. The necessity of using several fibres and couplers makes this a rather costly method for referencing.

Triangulation is another measurement method which can employ referencing. It involves a collimated source (laser) or an optical fibre with a focusing lens which would emit towards a diffuse target and a detecting element positioned at an angle to the target which would detect the reflected/scattered light, as shown in Figure 3.15. Preferably, the source should emit normally to the surface being measured. If the source and detectors are positioned on either side of the normal of the surface, the illuminated spot on the target will move horizontally as well as in the direction of the displacement causing ambiguity.

Loughlin (1989) described two ways for detector positioning in triangulation. In the first way, the detector is positioned normal to the line joining the centre of the detector with the centre of the measuring range of the sensor as shown in Figure 3.16.a. In the second way, the detector is positioned parallel to the light source with the beam reflected from the central position of the target illuminating the centre of the detector as shown in Figure 3.16.b. In the first case, non-linearity exists to the spot displacement on either side of the centre of the measuring range of the sensor. In the second case, the non-linearity effect is removed but the light is out of focus for the ends of the displacement range.

Various drawbacks characterise this technique (Clarke, 1998). The returned light beam can be easily blocked by an extension of the body of the target, an effect known as occlusion. Depending on the nature of the target (surface texture or colour), differing levels of illumination are reflected towards the detector thus degrading the attainable level of accuracy which makes the use of automatic gain control an important factor in the overall performance of this sensor. Laser speckle degrades the accuracy of the location of the light

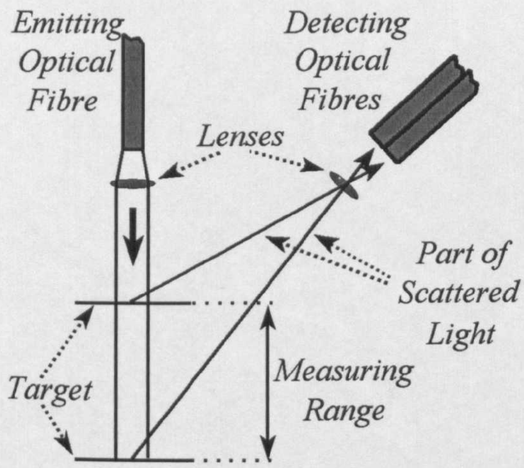

Fig. 3.15: Triangulation detection

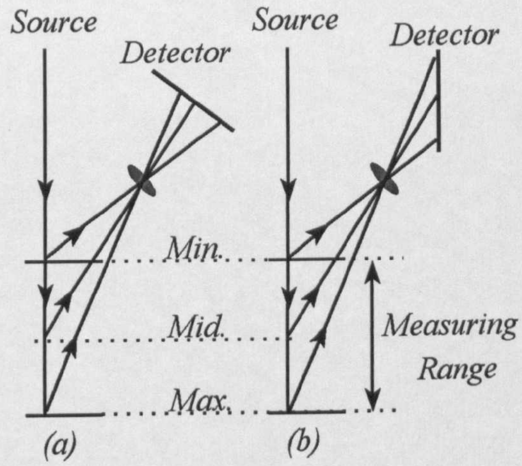

Fig. 3.16: Detector positioning in triangulation sensing

spot and therefore the accuracy of the instrument. Diffuse surfaced targets are always preferred since specular surfaced targets do not scatter but reflect the light incident on them right back towards the emitting element.

Other spacial measurements by triangulation have been performed by Brenci *et al* (1988) using a matrix arrangement. Four GRIN lens ended fibres were positioned at an angle of 30^0 from the normal of a diffuse surface. The two emitting ones were positioned on one side of the normal of the surface and the two detecting on the other side as shown in Figure 3.17. They provided information about the presence of an object in one or more out of four sensing zones. A maximum detected signal shown in a particular sensing zone would show the distance of the object from the optical head. A reference signal is not a necessity. An approximate displacement operational range of 90 mm was possible. An

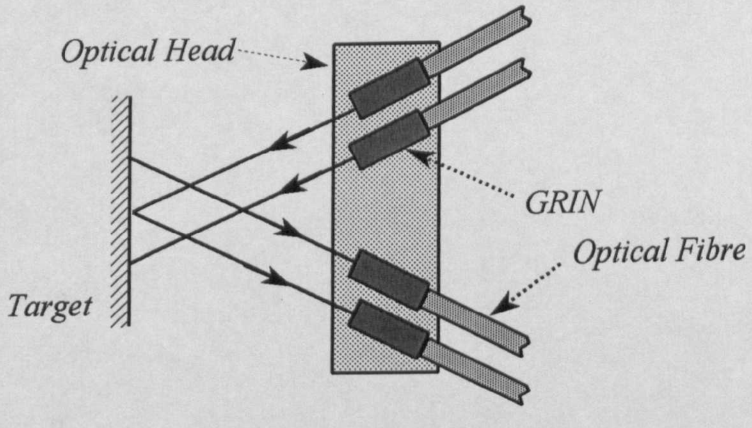

Fig. 3.17: Matrix arrangement from Brenci *et al*, 1988

M x N matrix can be realized but the increasing number of GRIN lens ended fibres to achieve a large matrix makes the cost of this technique prohibitive.

Lahteenmaki *et al* (1989) used a fibre emitting through a collimating microlens to hit the diffused surfaced target at an angle. The reflected light was received by two fibre bundles positioned equidistantly from the diffuse target as was the emitting fibre (Figure 3.18). Provided that the reflection pattern remained stable and the object homogeneous, a relative measurement could be achieved. At a specific angle of the emitting fibre to the normal of the object surface (white typing paper), the response of the sensor is linear. An operational range of 100 mm, accuracy of 1 % of the linear range, resolution of 0.1 % and temperature variation for the range from 0 ^{0}C up to 50 ^{0}C of 2 % for white typing paper as object surface were reported. Different performance was obtained for object surfaces of different reflectivity suggesting that calibration of the sensor for each specific object surface would be required for accurate measurements.

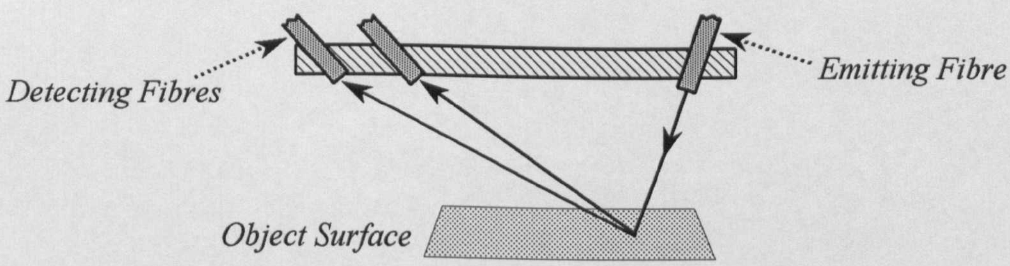

Fig. 3.18: The sensor arrangement of Lahteenmaki *et al*, 1989

Felgenhauer *et al* (1993) used plastic optical fibres (POF) with triangulation sensing (Figure 3.19). The emitting fibre emitted normally via a focusing lens onto the diffuse reflecting target. The diameter of the reflected beam falling onto the detecting POFs through another focusing lens was similar to the diameter of the POFs. The position of the target could be determined by the difference in the optical power received by the two detecting POFs. Linear response and an operational range of 9 mm were reported.

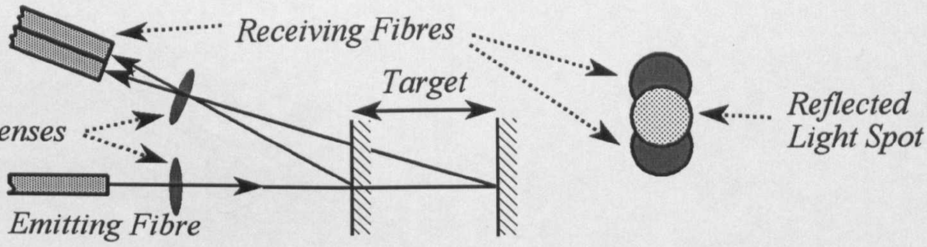

Fig. 3.19: The sensor arrangement of Felgenhauer *et al*, 1993

Table 3.3 summarises important characteristics of referenced sensors for comparison purposes.

Table 3.3: Important characteristics of referenced displacement sensors

Authors	Technique	Operational Range (mm)	Accuracy (%)	Resolution (%)
Libo *et al* (1993)	Differential	0.6	-	-
Cockshott and Pacaud (1989)	Differential	4	1	-
Libo and Anping (1991)	Differential	0.2	1.1	-
Regtien *et al* (1990)	Differential	60 / 100	-	-
Ioannides *et al* (1998)	Differential	75 / 85	1	0.1
Giles *et al* (1985)	Optical Bridge	-	1	-
Brenci *et al* (1988)	Triangulation	90	-	-
Lahteenmaki *et al* (1989)	Triangulation	100	1	-
Felgenhauer *et al* (1993)	Triangulation	9	-	-

From the above Table it can be seen that the largest operational range is offered by the technique followed by Lahteenmaki *et al* (1989) which follows a triangulation approach. But triangulation is a technique which suffers from various disadvantages such as the problem of occlusion, the necessity of a laser light source or use of collimating lenses and the limits to the physical size of the sensor arrangement (Clarke, 1998). The disadvantage of large physical size is also an issue for the techniques followed by Brenci *et al* (1988), which also follows a triangulation approach, and by Regtien *et al* (1990) which follows a differential approach similar to the one investigated in this Thesis. It seems that the only technique which does not suffer from all these problems is the one investigated in this Thesis since it offers a large linear operational range and relatively small sensor physical size.

3.6. EXTRINSIC, WAVELENGTH REFERENCED SENSORS

Wavelength referencing means that two wavelength bands will have to be chosen for use in the sensor. Senior *et al* (1992) state that differential measurements using two wavelength bands offer adequate referencing against errors from the transmission optics if all intensity modulating effects are minimized at the point of sensing (the response of the system between the sensor head and the processing electronics must be similar at these selected wavelength bands). But this technique cannot compensate for errors due to the instability of the optical source. Additional measures are required for this purpose.

Culshaw and Dakin (1989) state that if losses in a fibre optic system are not wavelength dependent, the relative output of the colour source(s) can be maintained at a constant ratio and the relative sensitivity of the detection system at the two wavelengths remains constant then the system may be compensated for losses in the fibre, connectors and other optical components.

It is also not necessary to use two separate channels of transmission optics to transmit the signals to the measuring location and back. Using wavelength division multiplexing (WDM) the two wavelengths can be transmitted along the same fibre. Although this would suggest identical behaviour of the two signals under an external unwanted condition, this is not the case. The uncertainty may still exist that the two signals will not behave in the same manner to all factors that may affect the transmission channel.

Selection of the two wavelengths is of primary importance since unequal spectral effects may affect the differential intensity variations of the two signals in a different way. The separation between the two centre wavelengths should be small to ensure minimal differential spectral effects. But if it is too small interchannel crosstalk will occur. The accuracy of the sensor is thus dictated by the spacing between the two wavelengths and the similarity in spectral effects at the two chosen wavelengths.

Senior *et al* (1992) stated that a major factor that affects the accuracy of the sensor is the temperature stability of the components used and in particular that of the source. Intensity variations are usually caused by upsetting the thermal equilibrium of the source which is affected by thermal variations, power supply fluctuations and ageing. An increase in temperature will result in a decrease of the optical power output of the source, a shift of its spectral emission towards longer wavelengths, and a widening of its spectral bandwidth. In a system where one LED source with a relatively broadband emission is used, the wavelength bands can be chosen to be at the low and high wavelength ends of the spectral emission of the optical power output with an adequate gap between the two wavelengths. A shift of the spectral emission will result in a significant decrease in the accuracy of the sensor. In the case where two narrowband LEDs are used the errors may be caused because the two sources do not change their behaviour identically with thermal variations. They also fluctuate differently due to power source fluctuations. Choosing two LEDs that have exactly the same behaviour in terms of intensity and thermal variation is very difficult since LEDs emitting at different peak wavelengths exhibit different optical characteristics.

Several attempts had been made to overcome the problems associated with wavelength based extrinsic optical fibre sensors. Senior *et al* (1992) used two thermally matched wavelength signals, by employing spectral slicing, selected from a single broadband LED source to develop a referenced dual wavelength (850 nm and 900 nm) optical fibre sensor. The sensor head (Figure 3.20) comprised a GRIN lens and a filter which separated the two wavelengths. The reference signal (850 nm) was reflected back to the processing electronics from the filter. The measurand signal (900 nm) was transmitted through towards a fully reflective target and was then reflected back to the sensor head through the same filter. Once the two signals were detected filtering occurred again to separate the reference from the measurand signal and two PIN photodiodes measured each of them and processing took place. A maximum linear displacement range of 20 mm with an accuracy of 0.8 % was

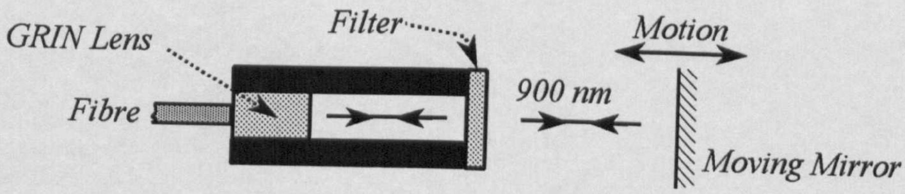

Fig. 3.20: The sensor arrangement of Senior *et al*, 1992

obtained. The displacement characteristics of the sensor were retained to an accuracy of 1 % of full scale when coiling and bending of the fibre took place.

Fuhr *et al* (1989) used matched interference filters to encode linear position. The arrangement of his sensor is shown in Figure 3.21. A collimated broadband optical source (LED) illuminated a pair of interference filters via an optical fibre. The filters were round and positioned edge to edge in a holder which moved perpendicular to the orientation of the filters. The transmitted light was directed towards another pair of filters, matched with the previous pair, via another optical fibre. PIN photodiodes would detect the intensity of the detected light for each individual wavelength and the positional information would be determined by examining the amount of light that passed through each matched filter pair. Linear response and operational range of 20 mm with an accuracy of 1.2 % was obtained. The accuracy became 2.45 % when the light level decreased by 12 dB. The authors did not say whether temperature effects were expected to affect the matching of the interference filters.

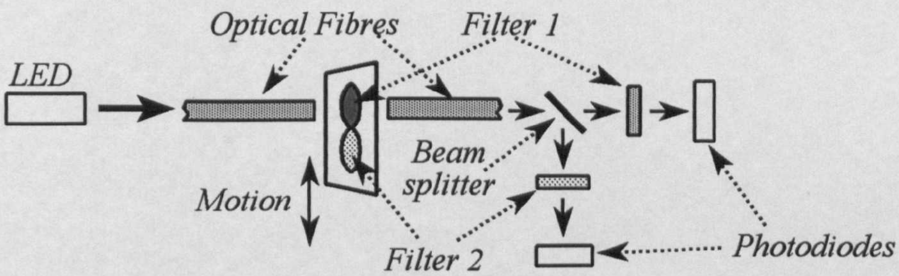

Fig. 3.21: The sensor arrangement of Fuhr *et al*, 1989

Pinnock *et al* (1987) employed two triangularly shaped filters positioned side by side to form a rectangle. Bundles of 1 mm fibres were used as source and detection fibres with the ends spread out into a rectangular configuration. The sensor can be configured in a transmissive (Figure 3.22) or reflective configuration. Two methods to obtain sensitivity changes in transmitted colours were tried. The first method combined a white light source and a colour sensitive detector with the transfer function being the ratio of the two detected signals which varied as the average wavelength of the received light changed. The other used a standard PIN photodiode and a bi-colour (red-green) LED pulsed in antiphase with the transfer function being the ratio of the filter transmissivity at the two wavelengths. Depending on the length of the filters, different displacement ranges were obtained, varying from 5 mm up to 50 mm with an accuracy of 2 % and resolution of 1 %. Possible constrains are the finite diameter of the fibres and the uniform distribution of the fibre bundles at their ends which face the filter since the sensor relies upon the gradual passage of the filter across them and the accuracy with which the filters are cut and shaped.

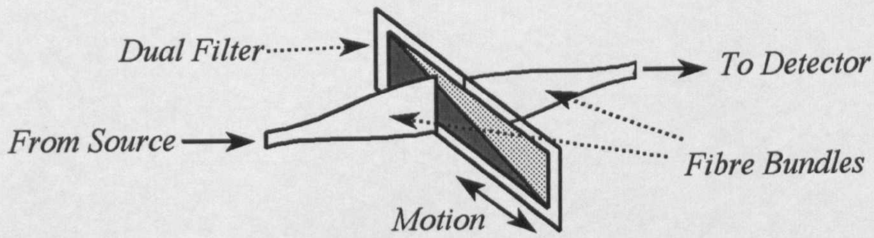

Fig. 3.22: The sensor arrangement of Pinnock *et al*, 1987

Murphy and Jones (1994) used polarized light propagating through an optically transparent material (photoelastic coating) under strain positioned on a reflective surface. This resulted in the orthogonal electric field components of the polarized light becoming phase shifted by a retardation factor. A broad band source was used which in conjunction with the increasing value of retardation resulted in a complementary colour. The resulting colour occurred in continuous bands which were directly related to the retardation of the electric field and increased linearly. In order to detect the colour changes a twin detector was used with different spectral responsivities for each detector. The transfer function was the ratio of the detected signals from each detector.

The optical fibres in the sensor arrangement, shown in Figure 3.23, were positioned at a fixed distance of 3 mm from the monitoring stress field (photoelastic coating). A variable retardation factor was induced into the photoelastic coated cantilever using the load

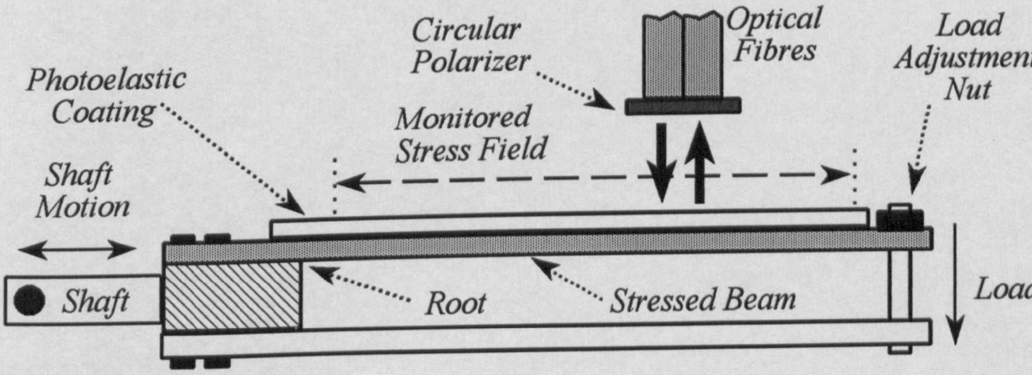

Fig. 3.23: The sensor arrangement of Murphy and Jones (1994)

adjustment nut to a suitable value. The shaft which was fixed on the sensor was displaced horizontally depending on the displacement of the measurand.

The experimental response of the sensor (Figure 3.24) followed a similar distribution with the theoretical response but their slopes did not agree. The signal-to-noise ratio was constant at ~ 65 dB over the whole of the operational range achieved which was in the order of 60 mm with a resolution of 0.05 %. Improvements in sensitivity would be achieved by the use of either lower numerical aperture and diameter fibre and/or collimating optics to avoid averaging of the received signal. The polarizer used exhibited poor thermal stability which contributed an error of ~0.5 %/^{0}C on the operational range of the sensor.

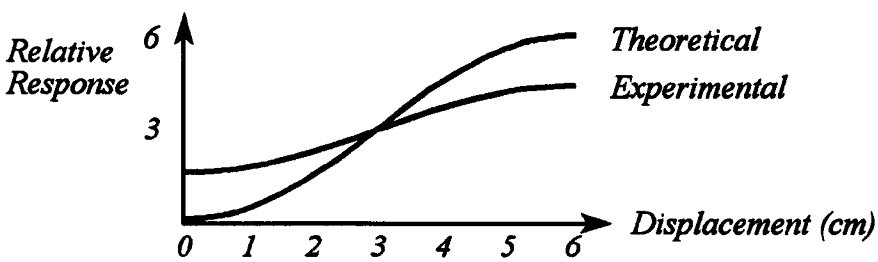

Fig. 3.24: The sensor response (Murphy and Jones, 1994)

The important characteristics of wavelength referencing displacement sensors surveyed in Section 3.6 are summarised in Table 3.4.

Table 3.4: Important characteristics of wavelength displacement sensors

Authors	Operational Range (mm)	Accuracy (%)	Resolution (%)
Senior et al (1992)	20	0.8	-
Fuhr et al (1989)	20	1.2	-
Pinnock et al (1987)	50	2	1
Murphy and Jones (1994)	60	-	0.05

From the above Table it can be seen that the longest operational range obtained is that of Murphy and Jones (1994) which is 60 mm. The accuracy of this technique has not been quoted by the authors although they state the resolution of the technique. The fact is, however, that referencing techniques which employ two wavelengths have the disadvantage that temperature variation and unequal spectral effects may affect the differential intensity variations of the two signals in a different way. Thus a very careful selection of the two wavelengths to be used in the sensor is required.

Overall the best option of sensor seems to be the one investigated in this Thesis since it offers the best arrangement/performance combination amongst the sensors surveyed (see Table 3.3).

3.7. FIBRE OPTIC VIBRATION SENSORS

Vibration sensors employing fibre optics take advantage of the usual benefits that this technology offers (see Section 3.2). Various techniques have been reported and some are surveyed below.

Nelson *et al* (1977) in an intrinsic configuration, used a fibre bend in a U-shape, as shown in Figure 3.25, to investigate what effect an acoustically vibrated membrane would have on the bending loss of the attached fibre. When the membrane was vibrated the transmitted light was modulated by a considerable amount only at certain resonant frequencies of the flexural vibrations of the fibre. The response of a "few-modes" fibre to vibrations was found to be linear with the vibration amplitude. Modulation of 5.4 % for amplitudes of vibration of a few tens of microns at the resonant frequency of 688 Hz was observed. Although the reason for the effects observed was attributed to the power loss mechanism due to bending, the analysis performed by Inoue (1990) suggested that the reason was due to the power redistribution of light inside the fibre resulting from the vibrations. He observed a linear response to dynamic disturbances in a multimode fibre but without bending.

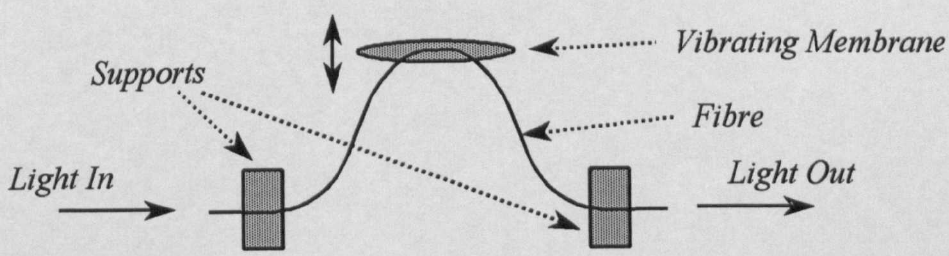

Fig. 3.25: The sensor arrangement of Nelson *et al*, 1977

Extrinsic vibration sensors are preferred when compared to other fibre optic and conventional sensors (see Chapter 2.2.1) due to the usual advantages that they offer, among them being the non-contact and non-destructive operation. The non-contact nature of extrinsic sensors eliminates problems such as structure loading and modification of natural frequencies of the measurands due to the requirement of contact to perform the necessary measurements. A number of extrinsic vibration sensors are described below.

A two fibre sensor arranged in a triangulation configuration, one transmitting and the other receiving light as shown in Figure 3.26, was used by Conforti *et al* (1989) to measure the displacement amplitude of a vibrating elastic cantilever at the fixed frequency of 100 Hz in order to monitor the effects of the 50 Hz line frequency on a vibrating machine. The cantilever was chosen so as to have a resonant frequency of 80 Hz. Measurements at the resonant frequency of the cantilever were not performed since at this frequency the cantilever vibrates unstably and with high amplitude. The detected signal is separated into dc and ac components and their ratio is taken to allow for evaluation of the vibration amplitude. Linear response for an operational range of 250 μm accurate to 3 % with a resolution of 0.1 μm was achieved. The working frequency can be changed to 120 Hz if there is need to monitor 60 Hz line frequency. Referencing was not employed in this experiment and the authors did not make any comments on how the sensor would behave if the light intensity varied.

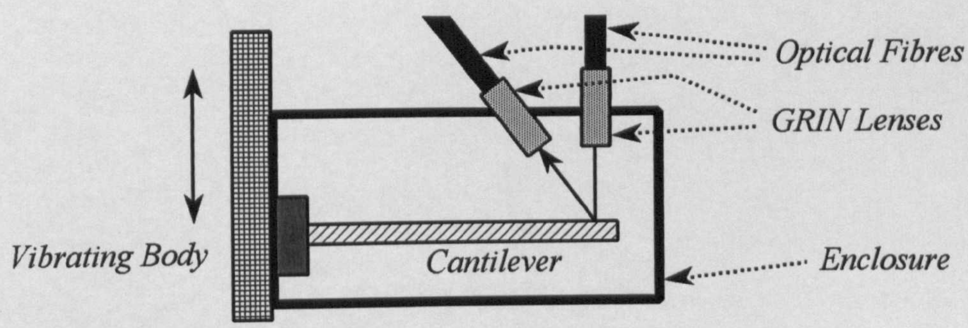

Fig. 3.26: The sensor arrangement of Conforti *et al*, 1989

In another experiment employing a cantilever Philp *et al* (1992) investigated the modal resonant frequencies of vibrating objects. An 820 nm LED was used, square wave modulated at the frequency of 1 MHz, to launch light into an optical fibre which would illuminate the side of the vibrating cantilever, as shown in Figure 3.27. As the cantilever vibrated it caused changes in the intensity of the light re-entering the fibre which produced amplitude modulation of the optical square wave signal at the oscillation frequencies of the structure. The first five resonant frequencies detected, which ranged from 26 Hz to 1482 Hz, were extremely close to the calculated ones. The amplitude of vibrations detected depended on the nature of the surface of the cantilever, with the polished surface returning a range of 1 μm and the unpolished one a range of 4 μm.

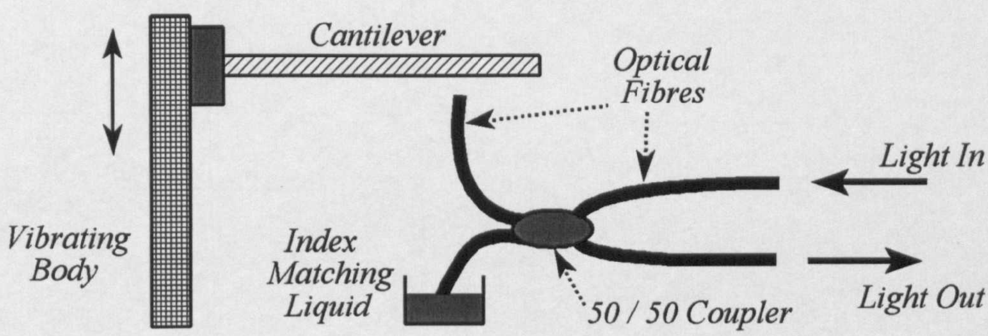

Fig. 3.27: The sensor arrangement of Philp, 1992

Toba *et al* (1991) used a fibre bundle in a coaxial arrangement (see Figure 3.7) to measure microscopic displacement and vibration in a tympanic membrane. The inner section of the fibre bundle transmitted the emitted light and the outer one received the reflected light from the target. The sensor operated on the linear part of the front (rising) slope of the detected light intensity (see Figure 3.7). A speaker was used as target with a very small, thin aluminium foil attached to it to offer the necessary reflectivity to assist in the measurements. Experimental tests resulted in a linear displacement range of 5 μm and measurable vibrational frequencies in the range between 100 Hz and 8 kHz. The lack of referencing, however, questions the ability of this technique to overcome variations in the light intensity of the source which may affect the response of the sensor.

Chitnis *et al* (1989) used a single fixed POF to illuminate a position sensitive detector (PSD) which was mounted on a vibrator, as shown in Figure 3.28. The PSD contained two photodiodes positioned next to each other facing the emitting fibre. If the illuminated areas of the two photodiodes were equal then the differential output would be zero. The motion of the illuminating spot on the vibrating PSD was monitored through an oscilloscope and a lock-in amplifier thus enabling the determination of the vibrating frequency. The amplitude of vibration obtained was between 0.1 μm and 1 mm and the frequency of vibration was between 0.5 Hz and 100 kHz. The sensor is limited by the requirement of a known reference signal for the lock-in amplifier. If the sensor is required to monitor an unknown signal then alternative signal processing must be used.

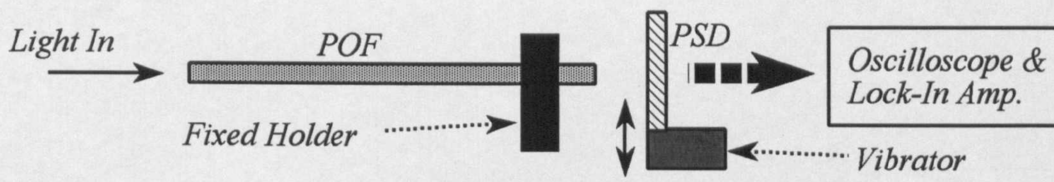

Fig. 3.28: The sensor arrangement of Chitnis *et al*, 1989

Lin and Chang (1994) used a Polarized Beam Splitter (PBS) to split a laser beam into a reference beam and a measurand signal. On reflection from the target, the PBS split the signal again and the polarised component was detected by another detector, as shown in Figure 3.29. The two signals were then used to extract the source noise content and deduce the characteristics of the measurand through a Fast-Fourier transform system. Experimental results obtained resulted in a vibrational operational range between 150 Hz and 4 kHz, amplitude of vibration between 1 μm and 2 mm, non-linearity between 0.5 % and 5 % and resolution between 0.2 μm and 5 μm.

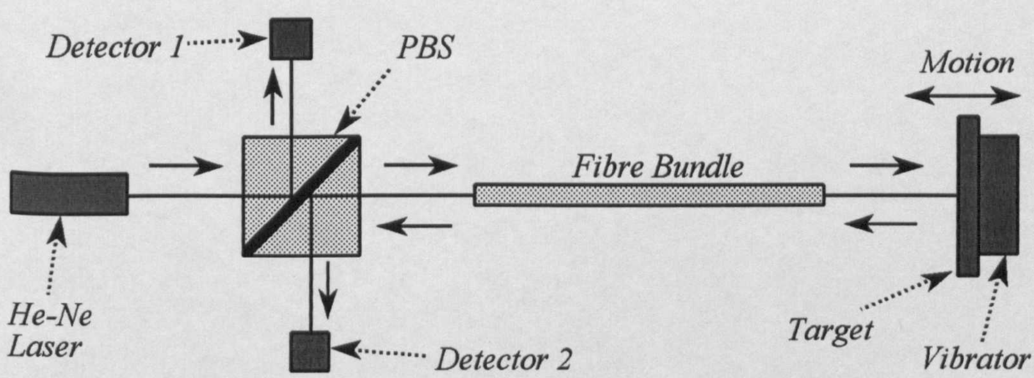

Fig. 3.29: The sensor arrangement of Lin and Chang, 1994

Dinev (1995) developed a sensor which could monitor two-dimensional vibrational amplitudes and frequencies simultaneously. The sensor arrangement is shown in Figure 3.30. The emitting fibre was fixed on a base plate 35 mm from its end and behaved like a uniform elastic cantilever with a small cylindrical mass attached to its end. Any deflection of the cantilever end will result in a light beam displacement sensed by a dual axis linear position photosensor. A maximum amplitude of 800 μm, limited by the size of the photodetectors active area, resolution of 0.5 μm, linearity of 0.1 %, a dynamic range of 64 dB and -42 dB crosstalk between the two directions was reported. The tests were performed with a 260 Hz vibration.

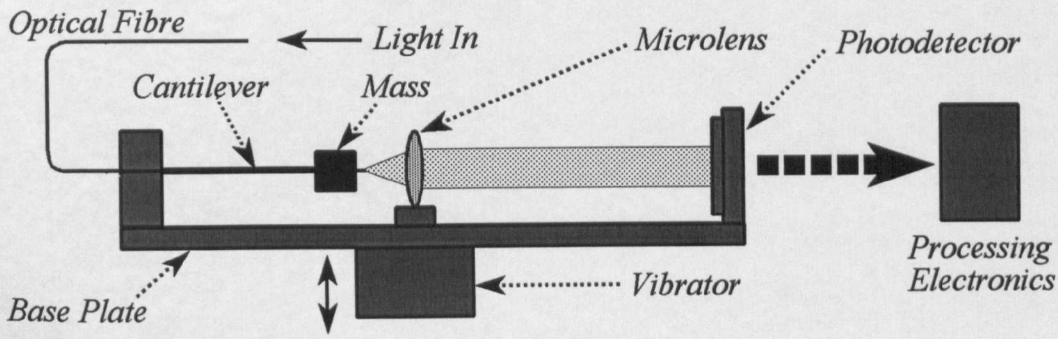

Fig. 3.30: The two-dimensional sensor arrangement of Dinev, 1995

Another technique used in extrinsic sensors to measure vibration is laser Doppler velocimetry. Here, two fibres are used, one as a reference and the other to transmit the light to and from the measurand. Laser Doppler velocimetry is based on the detection of the Doppler frequency shift in coherent light which occurs when it is scattered from a moving object. Thus, by measuring and tracking the change in frequency it is possible to produce a time resolved measurement of the object's velocity. The problem that exists, however, is the fact that the direction of the motion cannot be determined unless the reference beam is frequency pre-shifted. This will provide a carrier frequency which the target surface velocity will frequency modulate thus providing amplitude and phase information. Important points to consider with laser Doppler velocimeters are the possibility of back reflections from the ends of the fibres and any optics involved which may introduce interference with the frequency shifted reference beam due to the production of a persistent carrier frequency from the photodetector. Remote measurements will only be reliable if the lengths of the two fibres, i.e. reference and measurand, are the same. Any environmental disturbance to the measurand fibre will result in spurious noise in the detector output. Noise, vibration, heat and EMI will result in an increase in the noise contribution to the sensor (Halliwell, 1993).

An automated version of the displacement sensor investigated in this thesis has been employed to measure single degree vibrations (see Chapter 8). In order to perform vibration measurements the sensor head was positioned in front of and facing the dust cap of the cone of the bass driver of a loudspeaker which was sprayed white to increase its diffuse reflectivity coefficient. Peak to peak displacements of 6 mm (considered adequate for the requirements of this test) have been measured with a worst case accuracy of 4 %. Frequencies could be monitored with an accuracy of 0.5 %. The accuracy with which displacement and frequency could be determined depended on the target vibrating above a minimum level of displacement consistent with the resolution of the sensor (estimated to be better than 1 % of range). The target used was able to vibrate above this minimum displacement up to the frequency of 150 Hz. However, if the cone could vibrate with a higher displacement amplitude then one would be able to determine vibrations accurately up to around 650 Hz with the present arrangement.

Table 3.5 summarises the important characteristics of the vibration sensors surveyed in Section 3.7.

Table 3.5: Important characteristics of vibration sensors

Authors	Operational Range (μm)	Frequency Range (Hz)	Accuracy of Frequency (%)
Conforti et al (1989)	< 250	100	3
Philp et al (1992)	< 4	26 - 1482	-
Toba et al (1991)	< 5	100 - 8 k	-
Chitnis et al (1989)	0.1 - 1000	0.5 - 100 k	-
Lin and Chang (1994)	1 - 2000	150 - 4 k	-
Dinev (1995)	< 800	260	-
Ioannides *et al* (1998)	< 6000	< 150	0.5

The vibration sensors summarised in Table 3.5 offer several advantages which make them attractive to implement in dynamic measurements such as their non-contact and non-destructive operation which allows them to monitor vibrations without affecting the structure loading or modifying the natural frequencies of the measurand.

But some authors claim the accurate monitoring of some parameters of vibration, mainly frequency and displacement, yet they have a non-referenced arrangement which will surely suffer from any intensity fluctuations and ageing of the source used with regard to the long term accuracy in monitoring the amplitude of these vibrations. The maximum displacement range achieved is the one claimed by Lin and Chang (1994) which is around 2 mm. The sensor investigated in this Thesis has been arranged to monitor vibrations in an application which required a maximum displacement range of 6 mm with an accuracy of

4 % although it can be arranged to monitor vibrations with displacements of much larger amplitude. As it stood it could monitor single degree vibrations up to 150 Hz with an accuracy of 0.5 % limited only by the ability of the target used to vibrate above a minimum level of displacement (0.15 mm).

3.8. SUMMARY AND CONCLUSIONS

Optical sensors utilising optical fibres as light guidance devices become free from many forms of noise which would otherwise hinder their performance. Optical fibre sensors have attributes such as immunity to EMI, fast response, accuracy, simplicity, relatively long operational ranges, lightweight, compact and have low power requirements. They can be arranged in an extrinsic, intrinsic, interferometric or evanescent configuration depending on the way by which they operate. Light can be modulated in many ways, usually intensity, phase, wavelength, polarization and time duration. The measurand will change the characteristics of the light whether it is allowed to exit the fibre or not.

Extrinsic sensors offer further attributes such as non contact and non destructive operation, insensitivity to loading effects and ability to use established opto-electronic components. Simple extrinsic sensors operate by sensing changes in the intensity of the light caused by the measurand. They are extremely successful in switching applications (digital, on/off). In analog form, however, they suffer from intensity variations of the signal caused by unrelated factors to the measurand. Also, any influence of the fibre itself is undesirable and leads to inaccurate sensor response. But these drawbacks can be overcome by adding a reference signal. Various referencing techniques such as differential, optical balanced bridge, triangulation and dual wavelength show promising results with an acceptable operational range and high accuracy. Mathematical manipulation of the measurand and reference signals will remove any common mode variations of the signals but will not, however, compensate for unwanted variations not affecting both signals equally.

The survey on referenced displacement sensors presented various sensor arrangements which succeeded in delivering a long and accurate operational range which varied between 0.2 mm and 100 mm. Most of them had a linear response whereas others didn't. The sensor with the longest linear operational range (100 mm) is the one by

Lahteenmaki *et al* (1989) which uses a triangulation arrangement which consequently makes the sensor size relatively large resulting in the sensor not being flexible enough when is required to operate in difficult locations. The same holds for the arrangement by Brenci *et al* (1988) which has a non linear operational range of 90 mm. This arrangement requires expensive GRIN lenses as well. The arrangement employed by Regtien (1990) has an operational range of 100 mm and although similar to the one investigated in this thesis it does not have a linear response resulting in two ranges having the same value of relative response and the overall dimensions involved in the fibre positioning result again in a large size (a minimum of 35 mm transverse dimension). The sensor investigated in this Thesis has a transverse size which can vary between 6.6 mm and 10 mm, depending on the arrangement used, which is indeed a very compact size offering great flexibility. It can have a linear operational range in excess of 85 mm when used with matt white paper with 1 % accuracy and better than 0.5 % resolution. Overall this sensor results in the best arrangement/performance combination amongst all the sensors surveyed.

Extrinsic optical fibre sensors employed to measure vibrations have also been surveyed in this Chapter. These sensors offer several advantages which make them attractive to implement in dynamic measurements such as their non-contact and non-destructive operation which allows them to monitor vibrations without affecting the structure loading or modifying the natural frequencies of the measurand.

It is, however, noticed that some authors claim the accurate monitoring of some parameters of vibration, mainly frequency and displacement, yet they have a non-referenced arrangement which will surely suffer from any intensity fluctuations and ageing of the source used. These sensors can still be useful in measuring the frequency of vibration but their long term accuracy in monitoring the amplitude of these vibrations could be in doubt. Another important point to note relates to the maximum displacement range achieved. Lin and Chang (1994) reported 2 mm maximum displacement. The fact is that not all amplitudes of vibration that need monitoring are in the sub-millimetric region. The sensor investigated in this thesis has been arranged to monitor vibrations in an application which required a maximum displacement range of 6 mm with an accuracy of 4 %. Indeed, it can be arranged to monitor vibrations with displacements of much larger amplitude. As it stood it could monitor single degree vibrations up to 150 Hz with an accuracy of 0.5 % limited only by the ability of the target used to vibrate above a minimum level of displacement (0.15 mm).

Although optical fibre sensing is a fairly new technology, sensors employing these techniques are already finding their way to the market. These sensors can obtain information about distance, size, depth, vibration amplitude and frequency, pressure, number of goods on a conveyor belt as well as two- or even three-dimensional surfaces. As the technology matures and reliability levels are improving fibre optic sensors will substitute the existing sensing techniques and it is reckoned that they will take the lion's share of the market.

Chapter 4

Selection of Optical Components

The optical components that were selected for use with the sensor described in this Thesis are presented in this Chapter and the choices made are justified. These components relate mainly to optical fibre, light sources and photodetectors. The targets chosen are also briefly presented.

The choice of optical fibre was influenced by its physical dimensions, ease of handling, acceptance angle, termination and interconnection needs and overall cost.

The active components chosen had to be compatible with the selected type of optical fibre, be reliable, have low noise, low power requirements and have a reasonable cost.

Overall the important factors which influenced the selection of optical components were availability, compatibility amongst them, ease of handling, reliability, low noise and low power requirements, small size and low cost.

4.1. SELECTION OF OPTICAL FIBRE

Three types of commercially available optical fibre were considered for use with the sensor, the Glass Optical Fibre (GOF), Plastic Optical Fibre (POF) and GOF Bundles.

GOF remains unsurpassed in terms of data transmission due to its very low attenuation compared with the other two types of fibre considered. A typical spectral attenuation for GOF is shown in Figure 4.1. However, the low elastic limits of glass dictate that the remarkable flexibility of GOF, a necessity in industrial applications, can only be accomplished in those having a very small diameter, a typical maximum of 125 µm. Because of the brittleness that GOF has, it requires that a more elastic polymer coating be applied to the fibre to prevent the growth of cracks and fractures. A small diameter size creates handling problems in some applications and renders fibre interconnection relatively complex, time consuming and costly. Furthermore, in environments where fibres are vulnerable to impact and abrasion damage additional protective sheathing would be required. For these reasons GOF is not considered as the best choice for use with the proposed sensor. It is not, however, dismissed altogether since GOF could be used with the sensor.

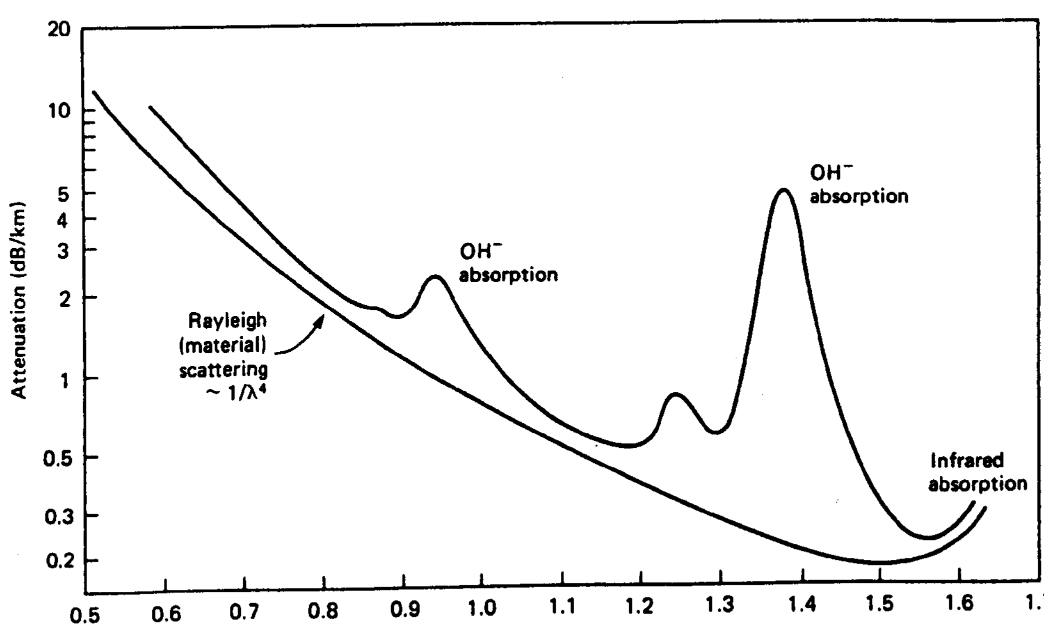

Fig. 4.1: Spectral attenuation of glass optical fibres (Young, 1991)

POF on the other hand has high elastic limits. POF made from Polymethyl Methacrylate (PMMA) polymers can withstand and recover from strains up to 13 %. This inherent elasticity and toughness of polymer materials allows POF with diameters of typically 1 mm to have much easier alignment, interconnection and handling than GOF, and be less susceptible to transmission variations arising from vibrations although the power distribution inside the fibre will be affected by these vibrations, as will with GOF and with GOF bundles. The large core diameter of POF enables enough light to be collected without the need for any additional lenses. Interconnection is also aided by the large numerical aperture that POF has (typically 0.47) which in turn eases the alignment tolerances of the connectors and their complexity thus lowering their cost. A more efficient coupling from active devices is also a major advantage. An LED with half angle emission similar to the numerical aperture (NA) of the POF can couple over 90 % more light into a 1 mm POF than in a 250 μm GOF (Farnell, 1996/7).

GOF Bundles could be considered favourably against POF since their actual diameter size of 1 mm is similar to that of POF. They also have a NA of 0.66 (acceptance angle of 83^0) and a minimum bending radius of 5 mm which are superior to POF's. But their attenuation (200 dB/km at 850 nm) is higher than that of POFs (150 dB/km at 660 nm) and what is more important than that is their price which is considerably higher than POF's (ten times). This results from the sophisticated procedures required when drawing GOF and then arranging it in a bundle.

Whitaker and Zarian (1995) reported on various other factors that favour POF against GOF Bundles. Bundles suffer from packing fraction losses since the spaces between the outer periphery of the individual glass fibres in a glass bundle do not contribute to light transmission. A bundle consisting of approximately 300 GOFs in order to obtain a diameter of 1 mm will have a 21.5 % less light receptive area than a POF with 1 mm diameter core. If bundling of the fibres is not performed properly it can cause misalignment of the fibres resulting in inefficient coupling since when cutting the bundles some fibres will not cut squarely at a 90^0 angle (an effect known as skewing). In cases where splicing is necessary gross misalignment of the fibres exists resulting in a very lossy splice. When GOF is produced for bundles, the ratio of cladding to core area for each fibre is minimized but when many fibres are put together in a bundle the surface area covered by the cladding becomes significant and counterproductive. Once light enters the bundle, the core-cladding interactions are much more frequent than in POF resulting in increased scattering losses. All these reasons suggest that GOF bundles can not be considered favourably for use with the sensor. GOF bundles could, however, be used if certain considerations are taken into account.

From what has been reported in this section the use of POF with the proposed sensor is by far the best option. In order to summarise and compare the characteristics and performance of these three types of optical fibre, Table 4.1 has been compiled. Also, the structure of these fibres is shown in Figure 4.2.

The three types of optical fibre are:

- TORAY POF PF Series, Step Index (SI) PMMA;
- BICC Brand-Rex Ltd SI GOF;
- SCHOTT GOF Bundle, MK 1.220 S Series (300 GOF).

Table 4.1: Details on the three types of optical fibre considered

OPTICAL FIBRE CHARACTERISTICS	POF (SI - PMMA)	GOF SI	GOF SI - BUNDLES
Diameter, Core:	960 μm	50 μm	50 μm
inc. Cladding:	1000 μm	125 μm	52 μm
inc. Primary Coating:	-	250 μm	-
inc. Buffer:	-	900 μm	-
inc. Jacket:	2200 μm	2500 μm	2350 μm
Attenuation, dB/km:	75 @ 570 nm 150 @ 660 nm 2000 @ 850 nm	3 @ 850 nm 1.3 @ 1300 nm	260 @ 560 nm 200 @ 850 nm 220 @ 940 nm
Bandwidth, MHz * km:	5 @ 514.5 nm	400 @ 850 nm 600 @ 1300 nm	2 @ 940 nm
Temperature Range, T, ^{0}C:	$-40 < T < +80$	$-10 < T < +70$	$-50 < T < +120$
Numerical Aperture:	0.46	0.2	0.66
Acceptance Angle:	55^0	23^0	83^0
Maximum Tension:	35 N	300 N	100 N
Minimum Bending Radius:	17 mm	30 mm	5 mm
Elastic Limits:	High	Low	Low
Termination Procedure:	Lapping Film, Hot Blade, Melting	Lapping Film, Cleaving	Lapping Film
Interconnection:	Simple, Cheap	Complex, Costly	Complex, Costly
Problems:	None	Tolerances	Misalignment, Skewing
Applications:	LAN, Sensor, Illumination, Automotive	Data Transmission	LAN, Sensor
Price, £ /m:	0.58	0.65	4.54

BICC Brand-Rex Ltd SI GOF

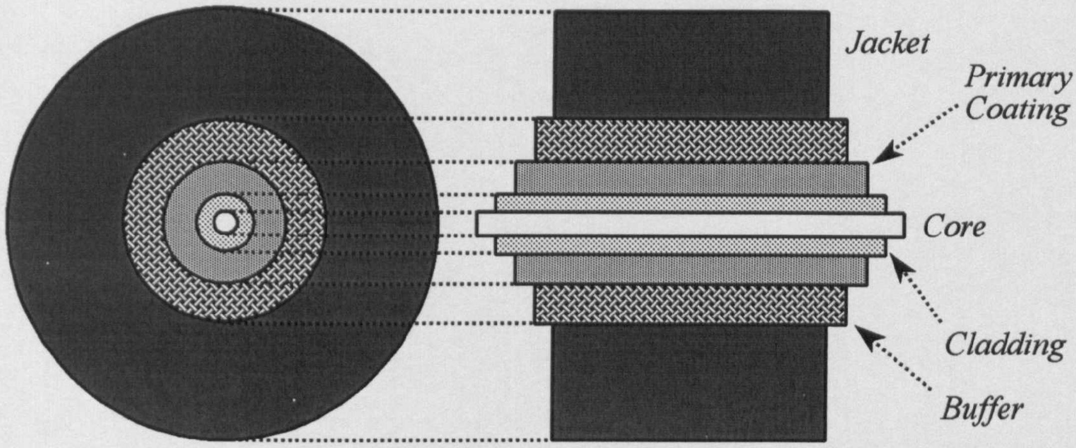

TORAY POF PF Series, Step Index (SI) PMMA

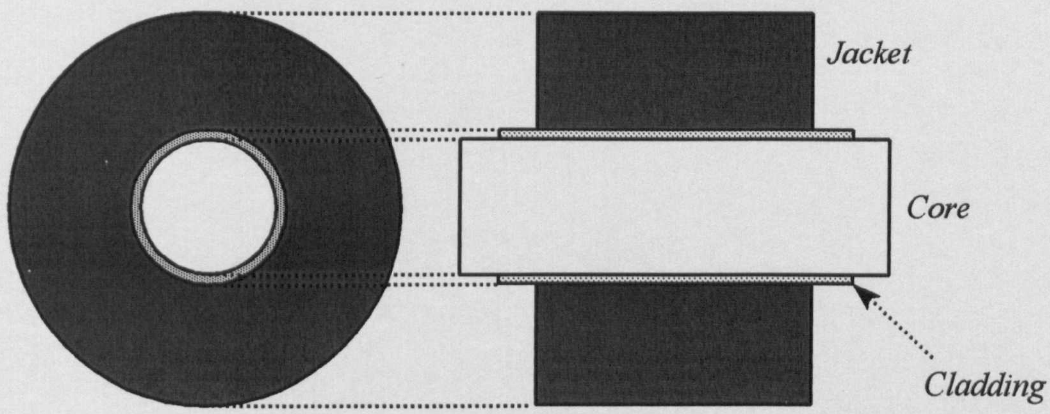

SCHOTT GOF Bundle, Mk 1.220 S Series (300 GOF)

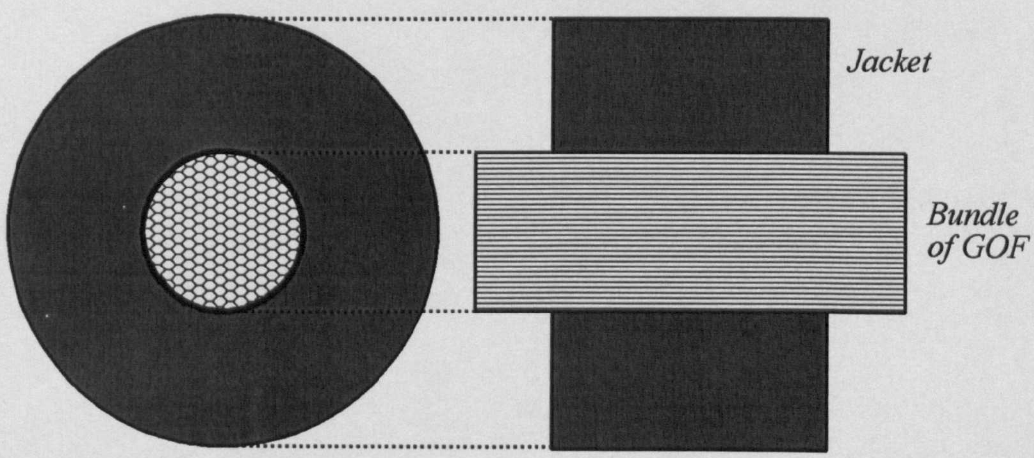

Fig. 4.2: The structures of the three types of optical fibre compared in section 4.1

4.2. PLASTIC OPTICAL FIBRE CHARACTERISTICS

Plastic Optical Fibre is made from polymeric materials. The superior mechanical properties of materials consisting of polymers are unrivalled in terms of processibility, cost and durability. The core is made from polymethyl methacrylate (PMMA) and the cladding from fluorinated polymer. The core diameter is 960 μm, the thickness of the cladding is 20 μm and the thickness of the jacket is 600 μm. POF with other core diameters is also available. It is a multimode, step index fibre.

The high refractive index difference that can be achieved between the core and cladding materials yields numerical apertures as high as 0.6 and large acceptance angles of up to 70^0. Care must be taken to ensure that the refractive indices of the core and cladding have the same temperature coefficient, because if they do not the numerical aperture of the POF will vary with temperature variations. The mechanical flexibility of polymer materials allows these fibres to have large cores with typical diameters ranging from 250 μm to 3000 μm. Whitaker and Zarian (1995) reported on a POF with core diameter of 20 mm for illumination purposes.

The production procedure of POF is basically the same as that of GOF, i.e. preform drawing, with the difference that it is performed at much lower temperatures since polymers have lower glass-transition temperatures (115 ^{0}C for PMMA) than glass (Ashpole *et al*, 1990). This is the reason for the relatively low maximum operating temperature for POF which is a limitation in high temperature applications. During the manufacturing process POF is stretched in order to orient the polymer and improve its mechanical toughness and flexibility (Marcou *et al*, 1995). Tests performed at elevated temperatures (up to 150 ^{0}C) showed that once the POF is heated the orientation of the polymer relaxes and shrinkage of POF occurs affecting the fibre characteristics and degrading its performance. However, the POF can withstand thermal and mechanical variations more or less successfully depending on the glass-transition temperature of the polymer material used. A major factor affecting the behaviour of the fibre is the material that the jacket is made of with the polyethylene (PE) type jacket being the best in protecting the core and cladding from elevations of temperature.

POF can be terminated using polishing in a similar way to GOF. Polishing the POF ends with various grades of lapping film can produce a very smooth surface, but this procedure is fairly time consuming. Instead, cutting the POF with a hot sharp blade can produce a satisfactory smooth surface very quickly. Kalymnios (1994) reviewed cases where termination was made by melting the POF on a heated polished metallic plate. The POF was positioned in specially developed metallic SMA connectors. Melting of the POF end eliminated effects of pistoning (movement) of the core inside the connector.

Performance figures for PMMA POF are summarised in Table 4.1. The spectral attenuation of the PMMA POF is shown in Figure 4.3. The factors affecting light transmission in POF are the intrinsic bulk losses due to absorption and scattering, and also the extrinsic losses arising from structural imperfections.

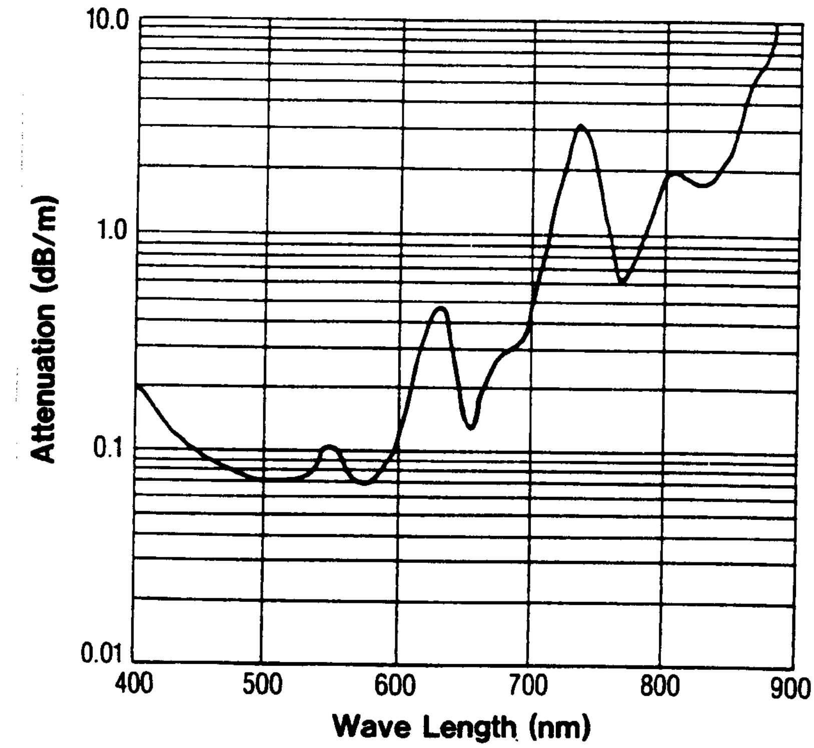

Fig. 4.3: Spectral attenuation of a PMMA POF

Daum *et al* (1992) showed that mechanical stress factors such as bending, vibration, loading and torsion, climatic stress factors such as temperature and humidity and the combination of all kinds of environmental stressing (extrinsic loss factors) over extended periods of time cause degradation of the POF properties and performance. Depending on the type of PMMA POF and more specifically its jacket, the fibre can withstand mechanical stresses with a different level of success. Absorption losses increase with increase in temperature. By comparing the results he obtained with requirements for industrial applications he concluded that POF can be employed in industrial environments.

Graded Index (GI) POF was developed by Ishigure *et al* (1995) which offered much higher data transmission rates (2.5 Gbit/s 100 m) than SI POF at 650 nm although its attenuation figure (~200 dB/km at 650 nm) was similar to that of SI POF. The GI POF was not available when this work was initiated and it would not have offered any advantages over the SI POF to this sensor since the operating frequency of the sensor is unlikely to exceed 10 kHz. A higher price should be expected once the GI POF goes on sale.

4.3. ACTIVE OPTO-ELECTRONIC COMPONENTS

The active opto-electronic components that were to operate with POF had to be able to operate in the transmission window of POF (Figure 4.3), i.e. in the visible region of the electromagnetic spectrum (380 nm to 720 nm). The opto-electronic components operating in this region are cheaply and readily available since they were the first ones developed when glass optical fibres first appeared during the early 70s. They offer a mature, reliable and low cost technological solution.

Three light sources were considered for use with the sensor. These were the Light Emitting Diode (LED), Laser diode and Tungsten filament lamp.

The LED was preferred since it is much cheaper than any of the other two light sources, is more reliable, requires simpler circuitry, offers ease of coupling, has no stringent alignment tolerances and offers various patterns of emission (from very broad to very narrow) to suit any requirement. A LED with a half angle emission similar to the acceptance angle of POF will ensure that the fibre is filled with light and that the far field radiation of an emitting POF is fairly broad and as close to a Lambertian as possible. From the attenuation characteristics of POF (Figure 4.3) a LED operating at 570 nm (75 dB/km) would seem to be the best one to use. However, a LED operating at 660 nm (150 dB/km) was chosen since at this wavelength LEDs have a much higher power output and are much faster than those operating at 570 nm resulting in higher bandwidth capabilities where necessary. Although temperature variations are expected to affect the power output of the LED, the operation of the sensor is expected to be marginally affected, because of a ratiometric method for analysing the signals.

A Tungsten filament lamp is a broadband (white light) source. It was rejected because it has a large size, high power requirements (12 V, 2 A) and the high level of heat that it produces may affect the POF when at close proximity.

Laser diodes (LD) although competitive in price with LEDs were also eliminated primarily for reasons of overall cost, complex circuitry and alignment tolerances. In order to fill the POF with light which would result in a near Lambertian far field emission distribution it would be required to use lenses between the LD and the POF to open the beam. This would result in increasing costs and very stringent alignment tolerances. Laser diodes are also very sensitive to temperature effects making the lasing threshold of the laser drift thus requiring active feedback and cooling in order to stabilize and prolong their life. Another reason for rejecting the laser diodes is that the if used without lenses the collimated beam which they emit must be launched parallel to the axis of the POF in order to obtain a Gaussian far field emission. Even when succeeding to do so, the far field emission of the POF would have a fairly narrow Gaussian distribution while by theory, the sensor assumes a fairly broad almost near Lambertian emission. In addition, due to different modes of the laser, the output far field pattern may exhibit a broadened ring structure which would most probably vary depending on the fibre length used and possible fibre bends (Karim, 1991).

The most typical photodiodes used in optoelectronic applications are the Silicon, Germanium, InGaAsP and InGaAs. These four types of photodiode are available with internal gain (Avalanche photodiodes, APD) or without. Germanium, InGaAsP and InGaAs photodiodes are clearly not suitable because their wavelength regions are not compatible with the transmission window of POF (see Figure 4.3). Typical photodetector responsivity curves are shown in Figure 4.4.

Silicon photodiodes are compatible with the required wavelength region since they detect from 400 nm up to 1100 nm. Silicon PIN photodiodes (without internal gain) were chosen as best for the sensor since they have the lowest dark current (< 1 nA) of all photodiode types, their responsivity shifts by less than 0.5 % over the temperature range between 15 ^{0}C and 35 ^{0}C and they are the cheapest ones to buy. The internal resistance of a PIN photodiode is high due to a wide intrinsic semiconductor layer which is incorporated between the p and n regions and where most of the diode voltage appears. When reverse biased, the diode operates in the photoconductive mode and the output current is proportional to the optic power incident on the detector. From Figure 4.4 it is seen that a typical PIN photodiode has a maximum quantum efficiency of 0.8 and its responsivity covers the wavelength region over which POF transmits.

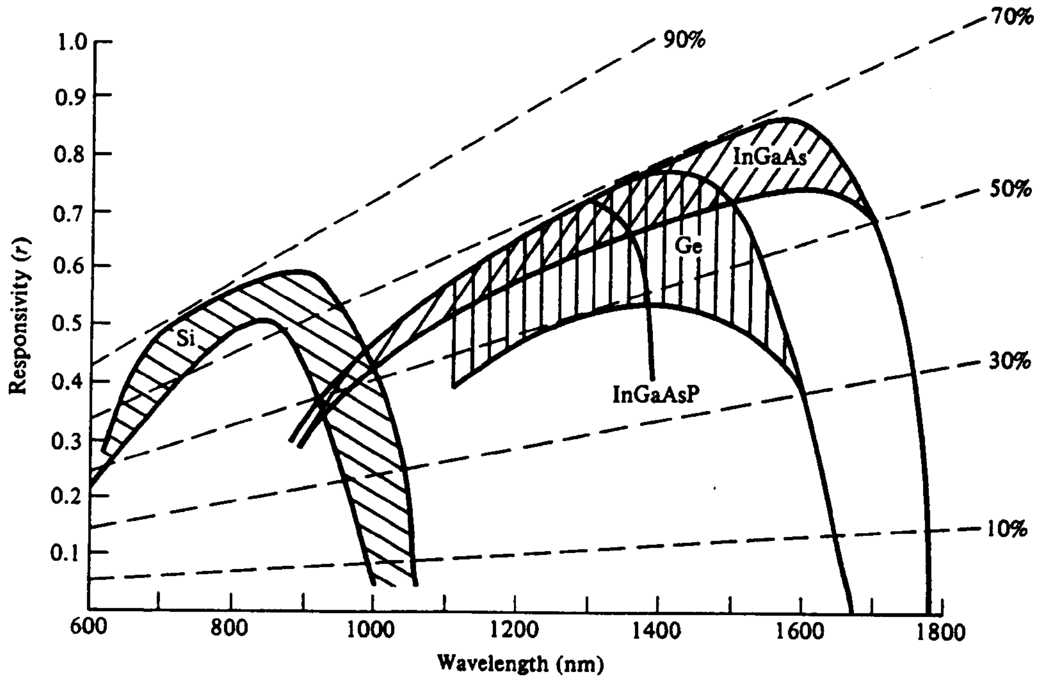

Fig. 4.4: Typical photodetector responsivity and quantum efficiency characteristics (Hoss, 1990)

Silicon APDs were rejected because they require high bias voltages ranging from 100 V up to 400 V (depending on wavelength), and require temperature compensation since the gain of the diode changes with thermal variations. Also, the random nature of their gain mechanism increases the noise. Their more complex structure makes them very expensive.

4.4. TARGETS

Various factors influenced the choice of targets which were to be used with the sensor in order to verify the theoretical predictions (see Chapter 5). These were the relation of target to theory, availability and cost effectiveness. Considerations were also paid to the arrangement of the sensor in industrial applications. And although the sensor is very unlikely to be used with a front surfaced reflective mirror in industrial applications due to its high cost (~ £ 100) it was used to enable the evaluation of the behaviour of the sensor when used with targets of very high reflectivity coefficient. Diffuse reflective targets are more likely to be encountered in industry and white matt paper is used to represent such a target.

When performing vibration measurements the target used was the dust cap of the cone of the bass driver of a loudspeaker. This target was not a flat one as were the ones mentioned above but was curved. Although not ideal, it enabled the evaluation of the sensor performance when used with non flat targets.

The targets used are summarised below:

- Square front surface reflecting flat mirror of dimensions 100 * 100 mm^2 (h*w) with a reflectivity coefficient of 0.94 at $\lambda = 660$ nm (Melles Griot, 1990);
- Matt white paper to act as a diffuse reflecting target, with a diffuse reflectivity coefficient of 0.82 at $\lambda = 660$ nm (Fraden, 1997);
- The dust cap of the cone of the bass driver of a loudspeaker (see Figure 8.1). This is a curved target with cross-sectional diameter of 70 mm and radius of curvature of 35 mm which was sprayed with white paint to increase its diffuse reflectivity coefficient.

The targets were positioned on a translation stage (Appendix B1) with a translational range of 100 mm and resolution of 1 µm.

4.5. SUMMARY AND CONCLUSIONS

In the selection of optical components for this displacement sensor three types of optical fibre and various types of light sources and photodetectors were considered.

The three types of optical fibre were GOF, POF and GOF bundles. POF offers the best option since it has considerable advantages over the other types of fibre such as very efficient coupling from active devices, much easier alignment, interconnection and handling and high elastic limits. The large core diameter eases interconnections, alignment tolerances of the connectors and their complexity and does not require additional optics to assist in the collection of light affected by the measurand. POF is less susceptible to transmission variations at the connector interface due to vibrations than GOF.

A LED was chosen as the light source for the sensor due to its reliability, simple circuitry requirements and ease of coupling. It has no stringent alignment tolerances and can offer the closest to Lambertian broad pattern of emission required by the sensor. A red LED operating at 660 nm especially recommended for use with POF with high power output

(900 μW) was selected.

Silicon PIN photodiodes (without internal gain) were chosen as they offer good spectral match to POF transmission characteristics. These have the lowest dark current (< 1 nA) of all photodiode types and their responsivity shifts less than 0.5 % over the temperature range between 15 ^{0}C and 35 ^{0}C. When reverse biased, the diode operates in the photoconductive mode and the output current is proportional to the optic power incident on the detector.

The targets selected were a front reflecting surface flat mirror, matt white paper and the dust cap of the cone of the bass driver of a loudspeaker. They were all to be positioned on a very accurate translation stage.

Selection of the optical components for the sensor was based on issues such as cost, compatibility, reliability, ease of handling, low noise, low power requirements, etc. The fact that these components operate in the visible region of the electromagnetic spectrum is also an advantage. Active optical components operating in this region belong to an established reliable and mature technology which today is very cheap compared to the latest developed technology for using GOF at 1300 nm and 1550 nm thus significantly lowering the overall cost of the sensor.

Chapter 5

Analytical Considerations on the Proposed Displacement Sensor

The proposed displacement sensor is presented in this Chapter. The sensor head arrangement and the surface of the targets used are initially described and are followed by analytical considerations on the behaviour of the sensor for ideal as well as for non-ideal conditions of operation. This process will allow for optimisation of the sensor design.

Simplified mathematical analysis performed for 100 % reflective and 100 % diffusive targets and preliminary experimental results showed that a linear response is realizable (Kalymnios, 1993). This analysis is reproduced and further elaborated in Section 5.3.

A computer program was also developed to verify the results expected under ideal conditions. It was based on the simplified mathematical analysis and allowed consideration of other parameters which were expected to affect the behaviour of the sensor. These parameters were the physical positioning of the POFs with respect to each other, their structure and solid angles subtended. Also, the polar distribution of radiation from the light source was assumed to be Lambertian taking into consideration the numerical aperture of the POF when coupled to a broad angle of emission LED. The linear response of the sensor was verified over longer ranges but important effects at the very short ranges were predicted.

The data obtained from the computer analysis were modified using a spreadsheet (Quattro Pro V5) to allow investigation of the behaviour of the sensor under non ideal conditions. Unwanted effects that could affect the performance of the detectors were thus fully investigated. Factors such as errors on the detected signals, mis-calibration between the two detectors, the presence of offset voltages on the detectors and fibre end separation variations were investigated.

In analysing the sensor response a least squares fit (LSF) line was always calculated for a range of data points obtained and the resulting equation (calibration curve) was used to determine the relationship between the sensor response and the range, and possible errors evident from the scattering of the theoretical/experimental points.

The analytical considerations on the sensor behaviour were performed for the range between 0 mm and 100 mm with the maximum range and maximum difference between true and calculated / computed / measured range (1 %) set in line with the initial specifications. Experimentally, the maximum range was also limited to 100 mm by the translation stage (Appendix B.1) upon which the targets would be positioned.

5.1. THE SENSOR HEAD ARRANGEMENT

The arrangement of the sensor head in this proposed displacement sensor is shown in Figure 5.1. It was based on the argument that if a signal is detected by two different detectors where one is positioned a few millimetres behind the other, it will result in two signals with different amplitudes. By using a transfer function of the form of that shown in equation 5.6 which includes the sum over the difference of the squares of the two signals then a linear response will result, which is one of the requirements outlined in Table 1.1.

Three, 5 m length POFs with core diameter of 1 mm (including the 20 μm thick cladding) complete with their protective jackets (2.2 mm) are considered. They are positioned side by side in the same plane with their ends displaced relative to each other by a distance X_0 along the axes of the POFs. The central fibre (emitter) is connected to an LED and is emitting towards a flat surface (target). The two outer ones (Det. 1 and Det. 2) are receiving the light reflected from the target and guide it to two PIN photodiodes. The range (R) is measured from the edge of the front detecting fibre (Det. 1) to the target.

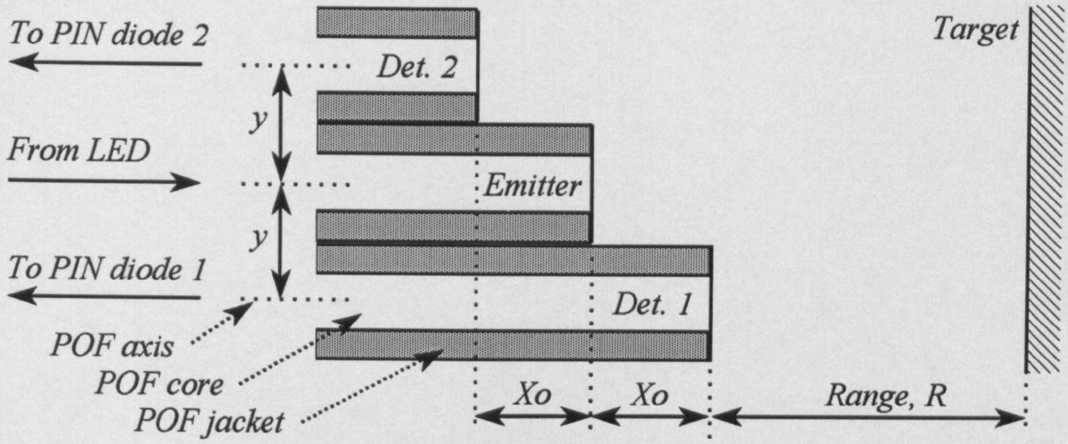

Fig. 5.1: The sensor head arrangement

5.2. SURFACES OF TARGETS

In the theoretical simulation of the sensor behaviour the surfaces used as targets were assumed to be 100 % reflective, 100 % diffusive or partly reflective/partly diffusive. It was also assumed that the targets did not absorb any light, i.e. zero absorption.

A 100 % reflective target has a reflectivity coefficient $\rho = 1$ (Fraden, 1997). It has a very smooth, polished surface that reflects all the light incident on it for the range of interest of wavelengths. The reflected ray and the normal of the reflective surface at the point of incidence lie in the same plane. Also, the angle of incidence is equal to the angle of reflection with respect to the normal of the surface.

A 100 % diffusive target has a reflectivity coefficient $\rho = 0$ (Fraden, 1997). It has a surface which is not smooth as is that of a 100 % reflective target but is rough, scattering the incident light in all directions. The laws of reflection are still obeyed at each particular point on the diffuse surface but the angle of incidence of a ray is different for each point on the target. Once a beam hits a diffuse surfaced target it will be reflected in a Lambertian fashion.

A partly reflective/partly diffusive target has a reflectivity coefficient $1 > \rho > 0$. Consider a beam incident on such a surface (assuming no transparency) as shown in Figure 5.2. The result will be a diffuse reflection which will include both the reflective and diffusive components. Matt white paper, which is also considered in the theoretical analysis, has a reflectivity coefficient of around $\rho = 0.82$ at 660 nm.

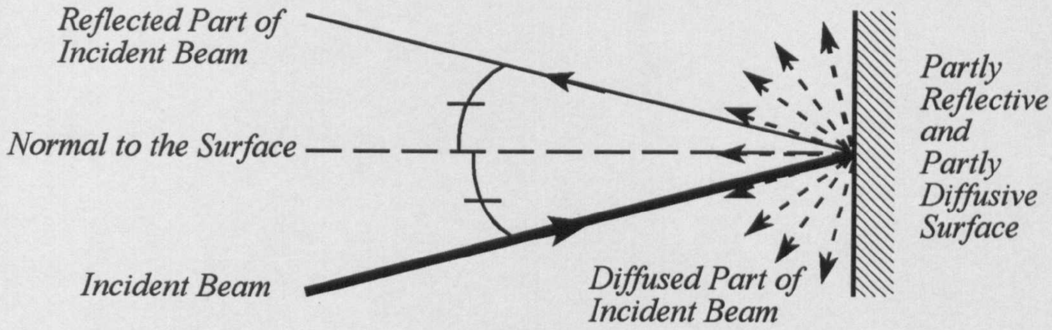

Fig. 5.2: Diffuse reflection

5.3. SIMPLIFIED MATHEMATICAL ANALYSIS

The elements comprising the sensor arrangement for the simplified mathematical approach are considered to be a point source and two point detectors positioned on the same axis. According to the inverse square law, a point source with radiant intensity I_0 (W/sr) emitted in all directions will deliver an intensity P_0 (W) at a unit cross sectional area surface at a distance d from the source, given by:

$$P_0 = \frac{I_0}{d^2} \qquad \textbf{Eq. (5.1)}$$

If the receiving surface is not perpendicular to the rays emitted by the source towards it, as shown in Figure 5.3, then the intensity at the receiving surface is proportional to the cosine of the angle ϑ involved as shown in equation 5.2.

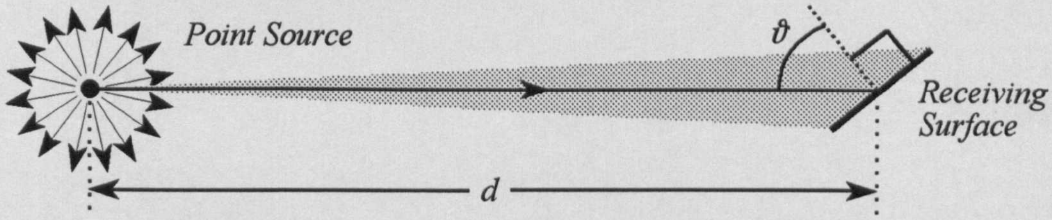

Fig. 5.3: The receiving surface is at an angle ϑ to the source emitted rays

$$P_\vartheta = \frac{I_0 \cos\vartheta}{d^2} \qquad \textbf{Eq. (5.2)}$$

Real light sources do not necessarily obey this assumption. They do, however, come very close to obeying the inverse square law if they have a broad and symmetrical polar distribution around their axis of emission. And although the end of the emitting POF cannot be a point source, the inverse square law for radiation was assumed to hold when analysing the behaviour of the sensor since the LED which will be used will have a broad emission distribution in order to ensure that the emitting POF is filled with light so that the far field radiation of the POF is fairly broad and near Lambertian.

The elements of the sensor are positioned in front of a 100 % reflective target, as shown in Figure 5.4, in such a way so as to allow for simple mathematical modelling with as few factors to be considered as possible. The two detectors are the images of the true detectors as seen through the reflective surface. It must be emphasized here that this is an unfolded version of the sensor arrangement and that the target is not transmissive.

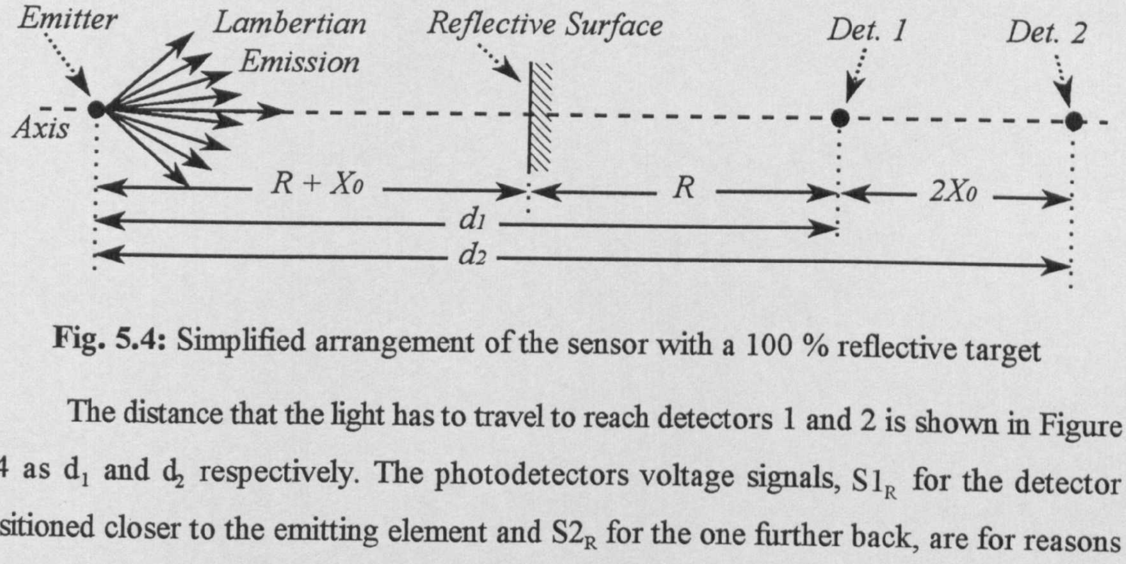

Fig. 5.4: Simplified arrangement of the sensor with a 100 % reflective target

The distance that the light has to travel to reach detectors 1 and 2 is shown in Figure 5.4 as d_1 and d_2 respectively. The photodetectors voltage signals, $S1_R$ for the detector positioned closer to the emitting element and $S2_R$ for the one further back, are for reasons of simplified analysis approximated to be of the following form:

$$S1_R = \frac{K_1 I_0}{d_1^2} = \frac{K_1 I_0}{(2R+X_0)^2} \qquad \textbf{Eq. (5.3)}$$

$$S2_R = \frac{K_2 I_0}{d_2^2} = \frac{K_2 I_0}{(2R+3X_0)^2} \qquad \textbf{Eq. (5.4)}$$

I_0 is the radiant intensity emitted by the source on its optical axis (W/sr) and K_i is a generalised constant for each detector which takes into consideration the detector responsivity r (A/W), the detector active area A (mm^2), a transmission parameter t and the detector gain G(R), and is of the form:

$$K_i = r_i A_i t_i G(R_i) \qquad \textbf{Eq. (5.5)}$$

K_1 and K_2 will in general be different because any of the three parameters r, A or t could be different. By keeping $G(R_1)$ fixed and varying $G(R_2)$, K_2 could be made equal to K_1 and so $S1_R$ and $S2_R$ could become the same when both detectors have the same light radiant intensity incident on them. This in fact is the calibration procedure which should be performed prior to arranging the three fibres as shown in Figure 5.1.

If equations 5.3 and 5.4 are substituted in the following expression, which is the transfer function S of the sensor, with $X_0 > 0$ (S_R is the S value due to a reflective target):

$$S_R = \frac{(S1_R + S2_R)}{(S1_R - S2_R)} \qquad \textbf{Eq. (5.6)}$$

and assuming that K_1 and K_2 are equal, the result is the following expression:

$$S_R = \frac{R+X_0}{X_0} + \frac{X_0}{4(R+X_0)} \qquad \textbf{Eq. (5.7)}$$

If the range is measured in multiples of X_0 with k being a constant:

$$R = kX_0 \quad \therefore \quad k = \frac{R}{X_0} \qquad \textbf{Eq. (5.8)}$$

then:

$$S_R = (k+1) + \frac{1}{4(k+1)} \qquad \textbf{Eq. (5.9)}$$

A similar approach to the one followed for the 100 % reflective target is followed for the arrangement where a 100 % diffusive target is used. But here only the beam which is emitted from the emitting POF on its optical axis is considered and not the whole emission distribution (lambertian) for simplification purposes (the complete lambertian emission is considered in Section 5.4 which calculates the sensor response using computer simulation). A simplified arrangement of the sensor under these conditions is shown in Figure 5.5.

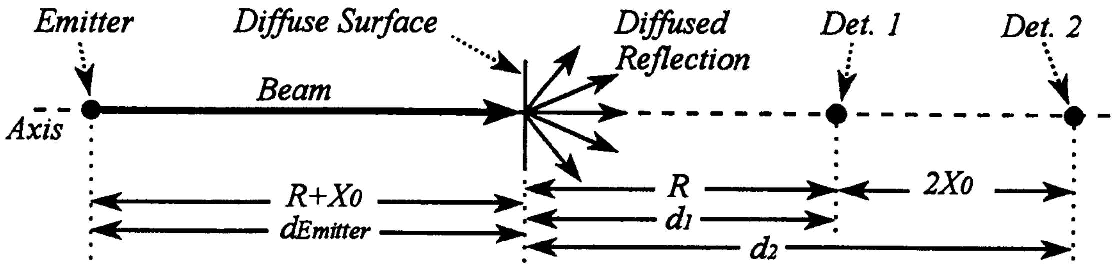

Fig. 5.5: Simplified arrangement of the sensor with a 100 % diffusive target

The beam will change into a Lambertian distributed emission once it hits the target. The point where the beam hits the target will thus be considered the source of emission and will act as a point source. The photodetectors voltage signals, $S1_D$ for the detector positioned closer to the target and $S2_D$ for the one further back, are for reasons of simplified analysis approximated to be of the form shown in equations 5.10 and 5.11.

$$S1_D = \frac{K_1 I_0}{d_1^2} = \frac{K_1 I_0}{R^2} \qquad \textbf{Eq. (5.10)}$$

$$S2_D = \frac{K_2 I_0}{d_2^2} = \frac{K_2 I_0}{(R+2X_0)^2} \qquad \textbf{Eq. (5.11)}$$

If equations 5.10 and 5.11 are now substituted into the transfer function of equation 5.6 with $X_0 > 0$ and assuming again that K_1 is equal to K_2 the result is the following expression (S_D is the S value due to a 100 % diffusive target):

$$S_D = \frac{R+X_0}{2X_0} + \frac{X_0}{2(R+X_0)} \qquad \textbf{Eq. (5.12)}$$

Considering equation 5.8, then:

$$S_D = \frac{1}{2}[(k+1) + \frac{1}{(k+1)}] \qquad \textbf{Eq. (5.13)}$$

By considering equations 5.9 (S_R) and 5.13 (S_D) we can see that their first term is linear giving a response closely equal to $(X_0)^{-1}$ and $(2X_0)^{-1}$ respectively. The second term follows a reciprocal distribution which contributes to non-linearity. As k increases the effect that the second term has on the sensor response decreases making the response more linear.

The second term of equation 5.13 has twice the effect that the one of equation 5.9 has and, in conjunction with its lower slope, will delay the sensor response from achieving acceptable levels of linearity and acceptable percentage difference between true and calculated range. S_R and S_D are shown in Figures 5.6 and 5.7 respectively with the X_0 separation set from 1 mm to 5 mm and suggests that the sensor response is linear for both types of target.

The calculated range R_{Calc} is deduced from S_R and S_D once a LSF routine has been applied over a certain range of points by considering the interception point C on the S-axis and the slope (dS / dR) of the points due to the application of LSF. The points from S_R and S_D considered for the application of the LSF are those points which lie neatly on a straight or near straight line. If points are not positioned as required, they will affect the application of the LSF resulting in a less linear response. The minimum range R_{min} where the LSF is applied is dictated by the required accuracy and the effect that the second term of equations 5.9 and 5.13 has on the sensor response.

$$R_{Calc} = \frac{(S-C)}{(dS/dR)} \qquad \textbf{Eq. (5.14)}$$

Deviation from linearity $\alpha_{(L)}$ can be obtained by taking the percentage difference between the slope of the response taken for two groups of points at two parts in the range, i.e. at short ranges $(dS / dR)_{R2}$ and at long ranges $(dS / dR)_{R1}$. The short range considered for this purpose is very important since the response at short ranges is not as linear as at longer ranges resulting in a less linear response. In the following analysis the slopes for the deviation from linearity were taken between 20 mm and 21 mm at the short ranges and between 99 mm and 100 mm at the long ranges (11 points for each range).

$$\alpha_{(L)} = \frac{(dS/dR)_{R1} - (dS/dR)_{R2}}{(dS/dR)_{R1}} \, 100\% \qquad \textbf{Eq. (5.15)}$$

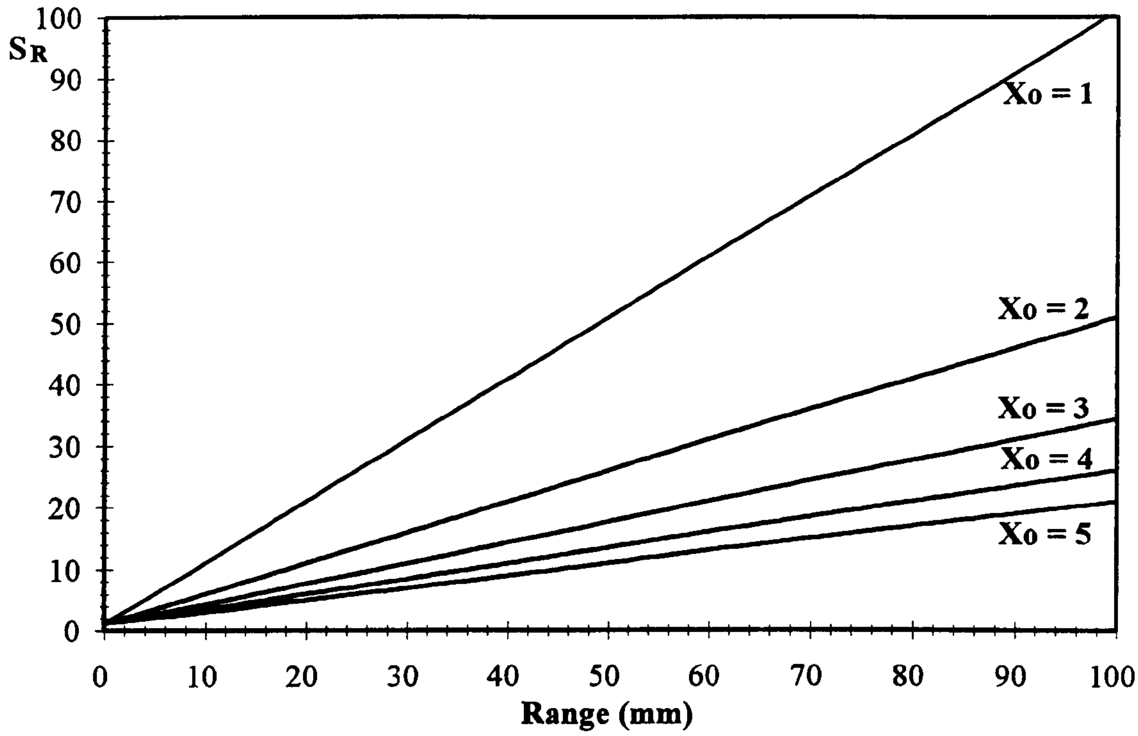

Fig. 5.6: The sensor response with a 100 % reflective target

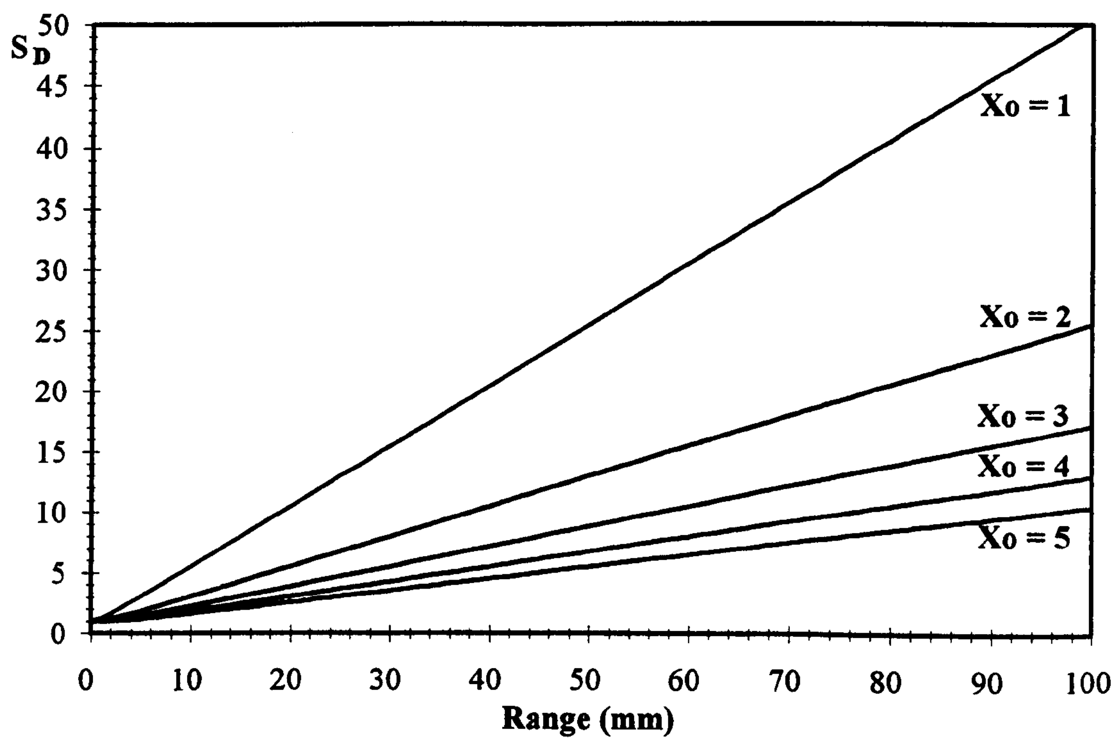

Fig. 5.7: The sensor response with a 100 % diffusive target

Tables 5.1 and 5.2 describe numerically the sensor response for the two types of target considered and for various X_0 separations, assuming a maximum of 1 % difference between true and calculated range, as defined from the initial requirements (Table 1.1).

Table 5.1: Sensor response with 1 % difference between true and calculated range for a 100 % reflective target

POF Separation (mm)	$X_0 = 1$	$X_0 = 2$	$X_0 = 3$	$X_0 = 4$	$X_0 = 5$
LSF Range, (mm)	0 - 100	0 - 100	0 - 100	0 - 100	0 - 100
R_{min}, (mm)	3	5	6	7	8
X_0^{-1}	1.0000	0.5000	0.3333	0.2500	0.2000
(dS / dR), LSF	0.9995	0.4993	0.3325	0.2490	0.1989
C, LSF (0 - 100 mm)	1.037	1.055	1.070	1.082	1.092
Effect of 2nd term on S_R at R_{min}, (%)	1.563	2.041	2.778	3.306	3.698
R_{Calc} vs R, at R = 1 mm (%)	-8.877	-22.477	-35.733	-47.973	-59.145
$\alpha_{(L)}$, (%)	0.052	0.188	0.386	0.629	0.905

Table 5.2: Sensor response with 1 % difference between true and calculated range for a 100 % diffusive target

POF Separation (mm)	$X_0 = 1$	$X_0 = 2$	$X_0 = 3$	$X_0 = 4$	$X_0 = 5$
LSF Range, (mm)	0 - 100	1 - 100	2 - 100	3 - 100	4 - 100
R_{min}, (mm)	4.5	7.5	9.5	11.5	13.0
$(2X_0)^{-1}$	0.5000	0.2500	0.1666	0.1250	0.1000
(dS / dR), LSF	0.4990	0.2489	0.1654	0.1236	0.0985
C, LSF	0.574	0.594	0.614	0.630	0.644
Effect of 2nd term on S_D at R_{min}, (%)	3.200	4.244	5.445	6.244	7.163
R_{Calc} vs R, at R = 1 mm (%)	-35.56	-96.46	-158.68	-219.39	-278.01
$\alpha_{(L)}$, (%)	0.206	0.752	1.546	2.521	3.625

From the above Tables it can be seen that the slope of the graphs (dS / dR) resulting from the application of the LSF is closely equal to $(X_0)^{-1}$ and $(2X_0)^{-1}$ for the 100 % reflective and 100 % diffusive targets respectively. The effect that the second term of equations 5.9 and 5.13 has on the response of the sensor is between 1.5 % and 3.7 % for the reflective target, and between 3.2 % and 7.2 % for the diffusive one at minimum range (the larger X_0 separations have the bigger difference). The effect that the second term of S_R has on the sensor response is smaller than that of S_D thus allowing for the LSF to be applied from R_{min} = 0 mm whereas for S_D it has to start from a selected minimum range between 0 mm and 4 mm. The maximum range where the LSF was applied was 100 mm for both targets and all X_0 separations. The start of the operational range for the diffusive target is approximately 1.5 times that for the reflective target. The percentage difference between true and calculated range at R = 1 mm, although large for both types of target, is more than four times as large for a diffusive target. The highest percentage deviation from linearity is found at X_0 = 5 mm. For the reflective target is 0.9 % and for the diffusive is 3.6 %. The short range where the LSF is applied for linearity purposes is very important. If it is chosen to be applied at the very beginning of the operational range, i.e. R = 1 mm, then the deviation from linearity will be much larger due to the effect that the second term of equations 5.9 and 5.13 has on the response of the sensor. Linearity of response for the sensor is suggested to be wholly determined by the choice of minimum range and by the X_0 separation.

If an even lower percentage difference between true and calculated range is desirable, i.e. less than 1 %, then a similar approach must be followed but the LSF will have to be applied to start from a later point on the range (where the effect of the second term becomes negligible and the response becomes almost linear) to produce the lowest percentage difference value. In this way the slopes of the responses will come even closer to $(X_0)^{-1}$ or $(2X_0)^{-1}$, depending on the target, and the effect that the second term of equations 5.9 and 5.13 will have on the response will be very small indeed at minimum range. The operational ranges will start at a later point but the achieved theoretical difference between true and calculated range will be more accurate. The minimum range for the operational range and the LSF for each X_0 separation will also be closer, if not the same.

By using this simplified mathematical approach the sensor has been predicted to give a linear response when used with 100 % reflective or 100 % diffusive targets for any X_0

separation. The linearity of response of the sensor is controlled by the second term of equations 5.9 and 5.13. The degree of linearity of operation and percentage difference between true and calculated range will determine the start of the operational range of the sensor and vice versa. Of course linearity of response of less than 1 % is not a necessity since the use of a correction factor for each specific range can return the required level of linearity.

5.4. COMPUTER SIMULATION

Computer simulation assisted in determining a more accurate analytical description of the expected behaviour of the sensor. A computer program (Appendix A1) has been developed using TurboC which calculates by numerical integration the light incident upon each of the detectors allowing for a 100 % reflective (R), 100 % diffusive (D) or diffuse reflective (DR) surfaced targets. It takes into account the following factors:

- The orientation of the detecting POFs, X_0 and y separations with respect to the emitting POF (Figure 5.1);
- The shape of the core of the detecting POFs (circular);
- The size of the detecting POF ends, dividing their light receptive area into elements of area a = 0.01 mm^2, considering solid angle effects for each individual element;
- The size of the targets, dividing their light receptive area into elements of area A_t = 1 mm^2, considering solid angle effects for each individual element;
- The numerical aperture of the POFs (emitting and receiving);
- The emitting source considered was Lambertian.

The orientation of the three POFs in the sensor arrangement is shown in Figure 5.8 with the two detectors shown being the images of the true detectors as seen through the target. The way that the detecting POFs are divided into small elements is shown in Figure 5.9 and the areas on the target considered in the simulation are shown in Figure 5.10.

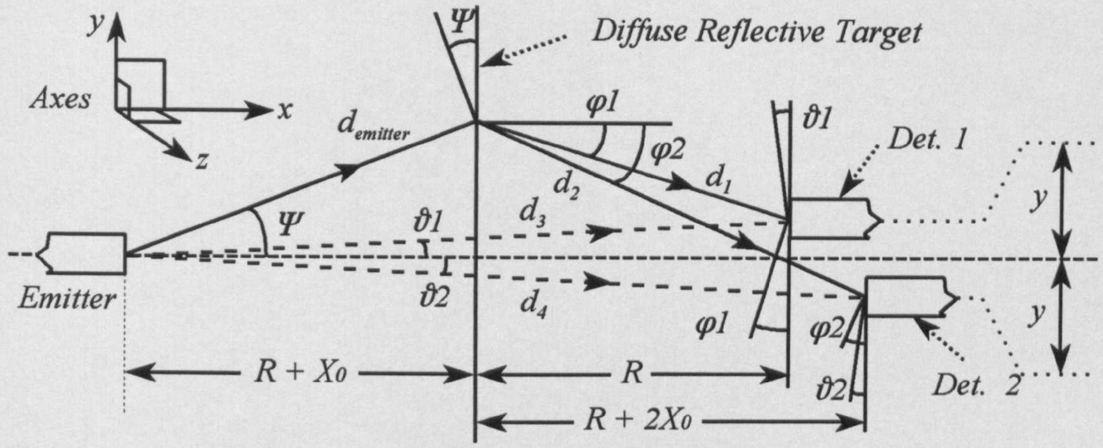

Fig. 5.8: The simplified (unfolded) arrangement of the sensor with diffuse reflective targets and lambertian emission

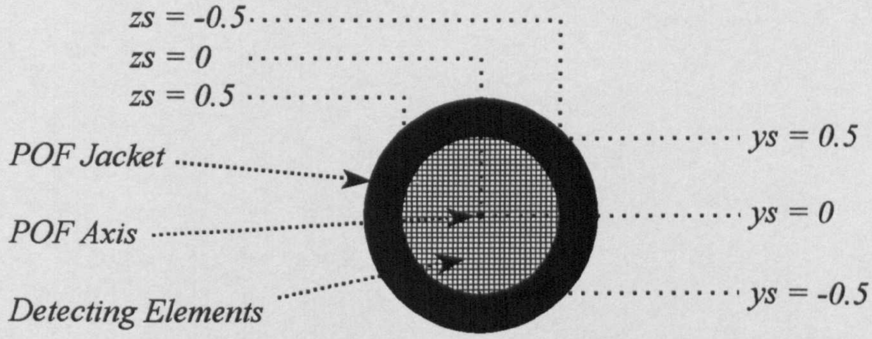

Fig. 5.9: Front view of the detecting POFs

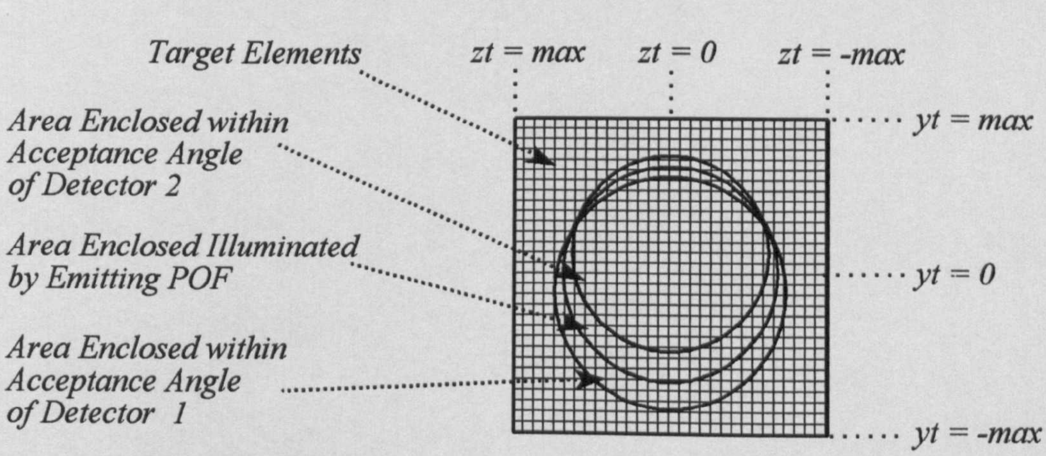

Fig. 5.10: The areas of the target considered in the program

The relative positions of each element on the target, denoted as yt and zt, are considered with respect to the y and z axial separations from the centre of the target (y = 0 mm and z = 0 mm). Similarly, ys and zs are the relative positions of each element on the detecting POFs with respect to the initial y and z separations (y ≥ 2.2 mm and z = 0 mm).

The light directed towards the detecting fibres will be a function of the intensity from the emitting fibre at each particular angle towards the target (for $\rho < 1$) which will direct a part of the light towards the detecting fibres. The photodetectors voltage signals, $S1_{DR}$ for the detector positioned closer to the target and $S2_{DR}$ for the one positioned further back, due to a diffuse reflective (DR) target are accurately defined as:

$$S1_{DR} = \frac{(1-\rho)K_1 I_0 A_t \cos^2\psi a \cos^2\varphi 1}{d^2_{emitter}\, d_1^2} + \frac{\rho K_1 I_0\, a \cos^2\vartheta 1}{d_3^2} \qquad \textbf{Eq. (5.16)}$$

$$S2_{DR} = \frac{(1-\rho)K_2 I_0 A_t \cos^2\psi a \cos^2\varphi 2}{d^2_{emitter}\, d_2^2} + \frac{\rho K_2 I_0\, a \cos^2\vartheta 2}{d_4^2} \qquad \textbf{Eq. (5.17)}$$

where:

$$d^2_{emitter} = (R+X_0)^2 + yt^2 + zt^2 \qquad \textbf{Eq. (5.18)}$$

$$d_1^2 = R^2 + (yt - y - ys)^2 + (zt - zs)^2 \qquad \textbf{Eq. (5.19)}$$

$$d_2^2 = (R+2X_0)^2 + (yt + y - ys)^2 + (zt - zs)^2 \qquad \textbf{Eq. (5.20)}$$

$$d_3^2 = (2R+X_0)^2 + (y - ys)^2 - zs^2 \qquad \textbf{Eq. (5.21)}$$

$$d_4^2 = (2R+3X_0)^2 - (y + ys)^2 - zs^2 \qquad \textbf{Eq. (5.22)}$$

By arranging ρ to a suitable value from 1 to 0 it is possible to simulate the behaviour of a target for various coefficients of reflectivity. In the case where the target is 100 % reflective then $\rho = 1$ cancelling the first term of equations 5.16 and 5.17. When the target is 100 % diffusive then $\rho = 0$ cancelling the second term of these equations.

The physical dimension values chosen to be used in the program were 1 mm ≤ X_0 ≤ 5 mm, y = 2.2 mm (equal to the total diameter of a POF) if $\rho = 1$ increasing for $\rho < 1$, and z = 0 mm (the axes of the three POFs were positioned lying in the same plane).

When $\rho < 1$ the y separation of the three POFs should be increased to a suitable value since with large X_0 separations the front detecting POF will be blocking part of the light emitted from the emitting POF. Assuming acceptance angles of $\pm 28^0$ then the minimum y separations shown in Table 5.3 must be accommodated in the sensor head arrangement.

Table 5.3: The minimum y separation depends on the X_0 separation when $\rho < 1$

POF Separation (mm)	$X_0 = 1$	$X_0 = 2$	$X_0 = 3$	$X_0 = 4$	$X_0 = 5$
y separation (min., mm)	2.132	2.663	3.195	3.727	4.259

From the Table above it can be seen that only $X_0 = 1$ mm will not need readjustment to its y separation when $\rho < 1$. When $X_0 = 5$ mm then y = 4.259 mm.

Some important effects were noted with this approach compared to the simplified mathematical analysis. These effects were concentrated at the short ranges as shown in Figure 5.11 for $\rho = 1$. Linearity of response was obtained for the longer ranges.

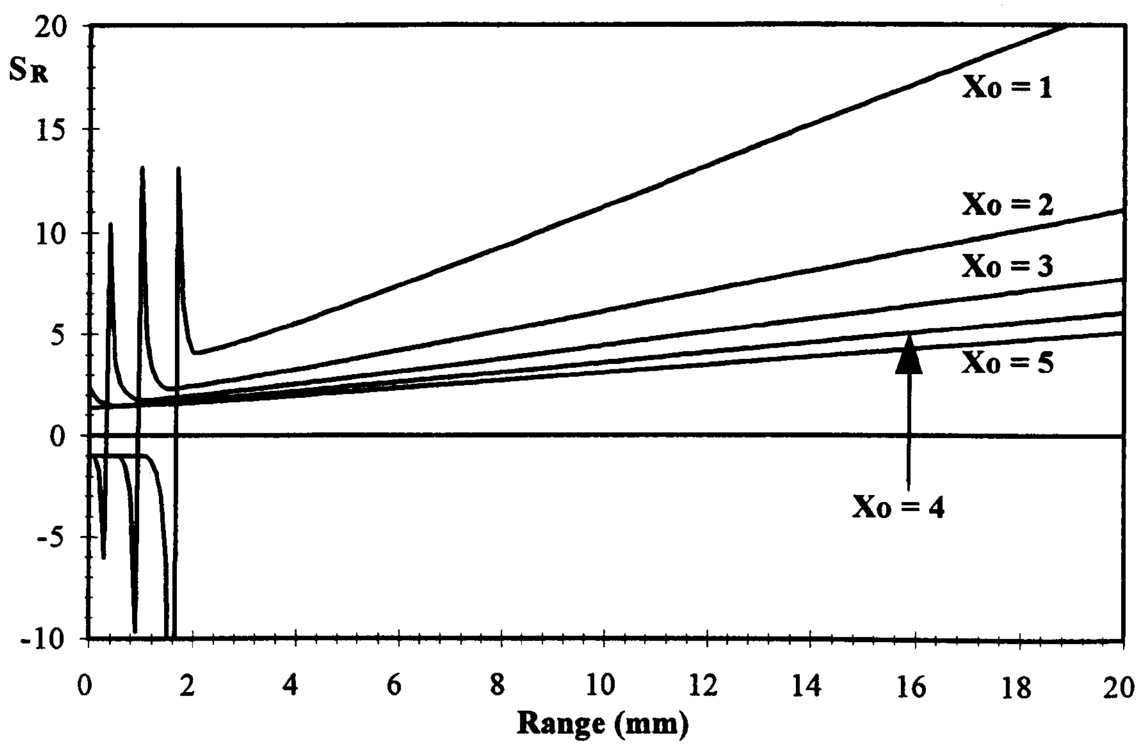

Fig. 5.11: Linearity of response (computed) breaks down at short ranges for $\rho = 1$

As shown in Figure 5.11 extreme non-linear response (to be called spike) exists at the very short ranges (R < 2 mm) depending on the X_0 separation. This is readily understood in terms of the finite numerical aperture of the emitting POF which has an acceptance angle of $\pm 28^0$ (NA = 0.47). The level of illumination that the detecting POFs receive due to this limitation is affected.

Figure 5.12 explains the cause of the spike by showing the images of the two detecting POFs in the reflecting surface (target) of Figure 5.1. The mirror is, at each instance, positioned in the middle of the distances shown in the Figure 5.12 denoted as dA, dB and dC.

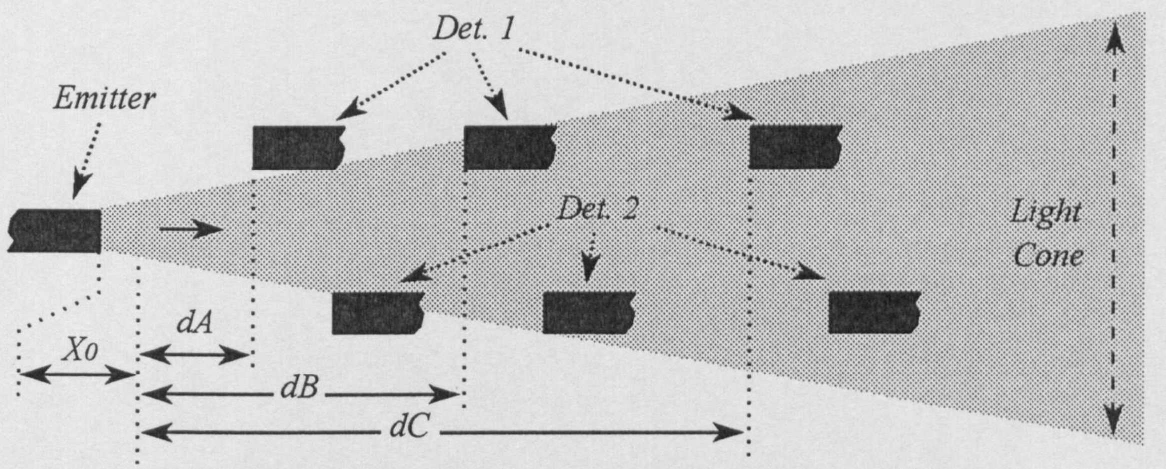

Fig. 5.12: The finite numerical aperture of the emitting POF affects detection

For a small emitter-detector separation such as dA no light would be collected by either of the detectors and so $S1_R = S2_R = 0$. When the distance is increased to dB, detector 2 collects light over the whole of its surface whilst detector 1 is only partially illuminated, so $S1_R < S2_R$ and so $S_R < 0$. Ultimately, at large distances such as dC where both the detectors are fully illuminated and as a result of the inverse square law, $S1_R > S2_R$ and thus $S_R > 0$, the sensor follows a linear response.

Figure 5.13 can also explain this effect in terms of a single X_0 separation (X_0 = 1 mm) showing the two detected (computed) signals ($S1_R$ and $S2_R$) and the S_R response. Here it is even clearer what really happens. Detector 2 is fully illuminated ($S2_R$ = max) at R = 0.9 mm whilst detector 1 still receives no illumination at all ($S1_R = 0$). S_R is negative at a fixed value ($S_R = -1$). At R = 1.1 mm $S1_R$ begins to increase and so S_R begins to decrease even more due to the value of the denominator (-ve) of the transfer function (eq. 5.6). Following $S1_R$ increases and $S2_R$ decreases and at the point where $S1_R$ is marginally smaller than $S2_R$, S_R tends towards negative infinity. When they are illuminated equally ($S1_R = S2_R$) S_R tends to infinity. From this point up to R = 2 mm $S1_R$ continues to increase and S_R

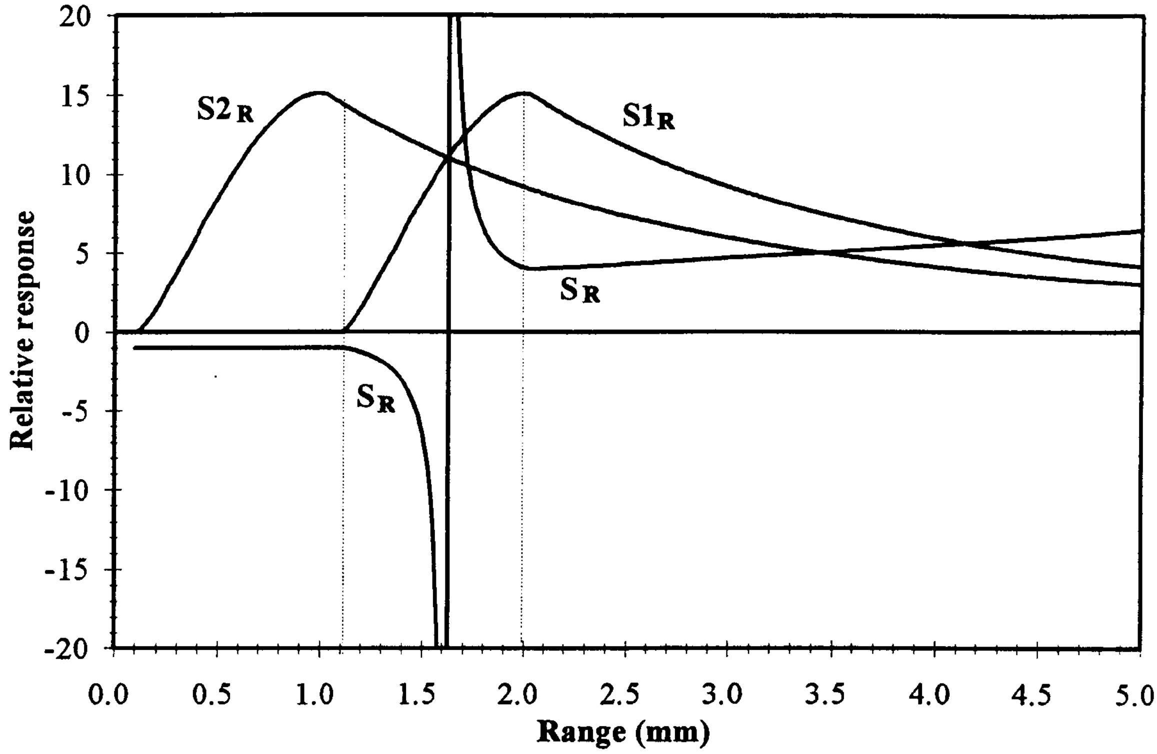

Fig. 5.13: The two computed signals ($S1_R$ and $S2_R$) and the S_R response for $X_0 = 1$ mm

decreases due to the increasing value of the denominator of the transfer function. At R = 2 mm $S1_R$ is at its maximum value and starts to decrease. From this point onwards the inverse square law holds for both detected signals thus the response of the sensor becomes more linear.

An important factor causing the spike observed at the short ranges is the X_0 separation. Since zero range (R = 0 mm) is measured from the front detecting fibre (Det.1) a larger X_0 separation will allow for the two detectors to be positioned further away from the emitting fibre thus being illuminated relatively earlier than if the X_0 separation was smaller. A sensor having $X_0 \geq 5$ mm will not show a spike (Figure 5.11).

An even more important factor concerning the range where the spikes occur is the y separation. Linearity of response is again affected at the short ranges due to the fact that the relative position of the detecting fibres with respect to the finite numerical aperture of the emitting fibre varies. By using only one value of X_0 separation (X_0 = 2 mm) and by varying the y separation equally for both detecting fibres the response was computed and the results are shown in Figure 5.14.

From here it can be seen that a small y separation will not produce a spike at short ranges whereas a large y separation will do so. The position where the spike is taking place

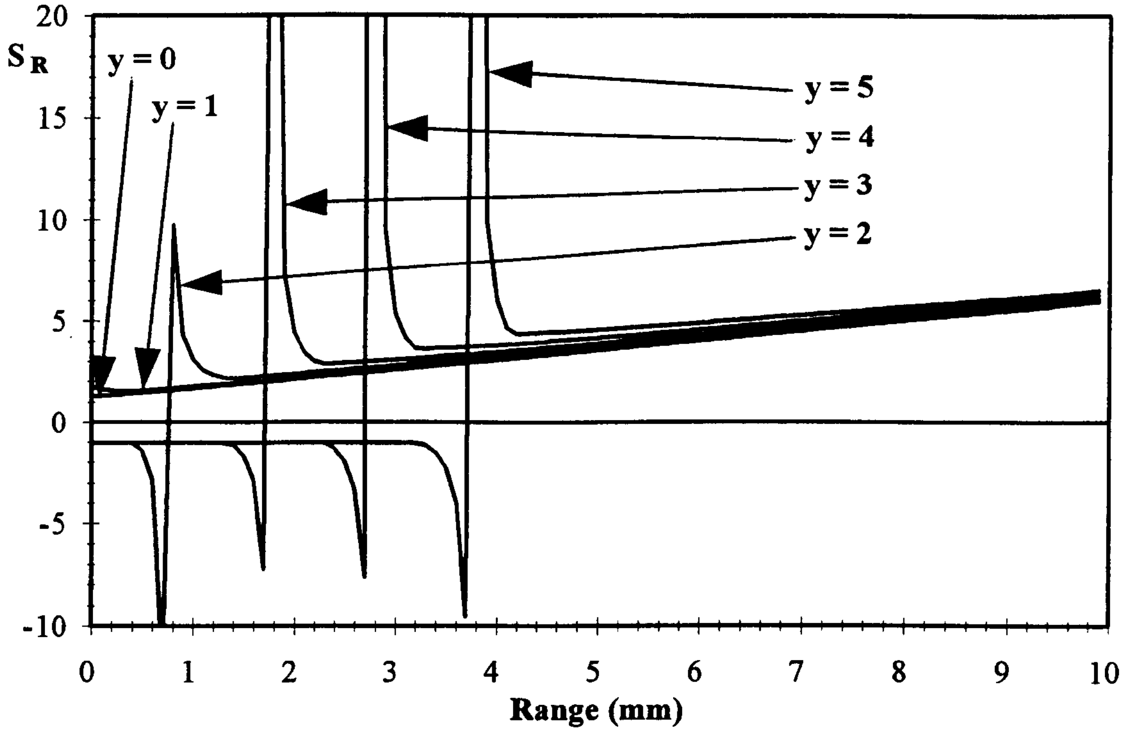

Fig. 5.14: Varying the y separation causes the spike to occur at different range (ρ = 1)

will be determined by the y separation with the largest separations producing one further in the range thus delaying the linearization of the response. This can also be understood by considering Figure 5.12 with the relative distance between the two detecting fibres increased causing them to enter the light cone at a longer range.

Thus linearity of response holds from a certain minimum range, depending on the X_0 and y separations, up to the maximum computed range (R = 100 mm). The minimum range from where the LSF can be applied relates to the point when both signals can be assumed to follow an inverse square law distribution (i.e. R = 2 mm in Figure 5.13 for X_0 = 1 mm).

Following the above analysis the target was changed to a 100 % diffusive, i.e. $\rho = 0$, and although linearity of response was obtained for the longer ranges, similar effects to those observed at the short ranges for $\rho = 1$, i.e. in the form of spikes, were observed here as well. The X_0 and y values used were the combinations shown in Table 5.3. Figure 5.15 concentrates only on the region where these spikes occur.

It can be clearly seen from this figure that the spikes occur at a longer range. This is due to the fact that when a 100 % diffusive target is used the source is considered to be only the area on the target illuminated by the emission from the emitting POF. Also, the y separation which has been increased to avoid blockage of the emission from the front detecting fibre has caused the spike to occur at an even longer range.

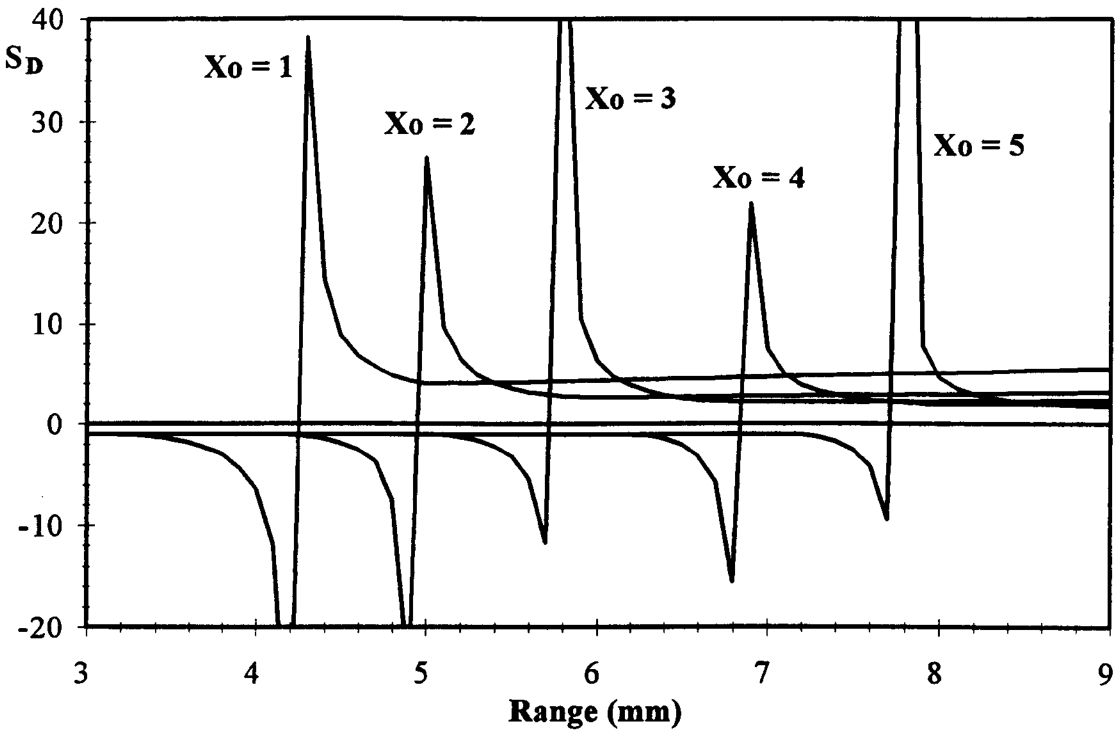

Fig. 5.15: Spikes occurring when ρ = 0 (X_0 and y values from Table 5.3)

Assuming a maximum desirable percentage difference between true and computed range (R_{Comp}) of 1 % for ρ = 1 and ρ = 0 the LSF routines were applied for each individual case of X_0 and y separation and the cases listed in Tables 5.4 and 5.5 resulted with the responses shown in Figures 5.16 and 5.17 respectively.

Table 5.4: Computed response with 1 % difference between true and computed range for ρ = 1

POF Separation (mm)	$X_0 = 1$	$X_0 = 2$	$X_0 = 3$	$X_0 = 4$	$X_0 = 5$
LSF Range, (mm)	2.0 - 100	1.5 - 100	1.0 - 100	0.5 - 100	0.0 - 100
R_{min}, (mm)	11.1	11.5	12.1	12.8	13.4
X_0^{-1}	1.0000	0.5000	0.3333	0.2500	0.2000
(dS / dR), LSF	0.9969	0.4982	0.3318	0.2486	0.1986
C, LSF	1.2577	1.1512	1.1276	1.1229	1.1250
$\alpha_{(L)}$, (%)	0.6014	0.6455	0.8065	1.0341	1.2713

Table 5.5: Computed response with 1% difference between true and computed range for ρ = 0 assuming the y separation values from Table 5.3.

POF Separation (mm)	$X_0 = 1$	$X_0 = 2$	$X_0 = 3$	$X_0 = 4$	$X_0 = 5$
LSF Range, (mm)	12 - 100	13 - 100	13 - 100	14 - 100	14 - 100
R_{min}, (mm)	16	18	20	21	22
$(2X_0)^{-1}$	0.5000	0.2500	0.1666	0.1250	0.1000
(dS / dR), LSF	0.4971	0.2477	0.1644	0.1226	0.0974
C, LSF	0.7902	0.7325	0.7359	0.7528	0.7702
$\alpha_{(L)}$, (%)	2.3345	3.6565	5.3083	7.4948	9.6094

For $\rho = 1$ the LSF routines were applied from a different starting range for each X_0 separation, decreasing as X_0 was increasing, with $X_0 = 1$ mm starting at R = 2 mm and $X_0 = 5$ mm starting from R = 0 mm since it is the one which is less affected by spikes. The opposite held for $\rho = 0$ since an increasing X_0 separation was linked with an also increasing y separation (see Table 5.3). The earliest starting point in the range, however, is given by $X_0 = 1$ mm for both $\rho = 1$ (R = 11.1 mm) and $\rho = 0$ (R = 16 mm) whereas $X_0 = 5$ mm started from R = 13.4 mm and R = 22 mm respectively. The slope of the graphs is again closely equal to the simplified mathematical prediction having a slope very close to $(X_0)^{-1}$ and $(2X_0)^{-1}$. The highest percentage deviation from linearity was found at $X_0 = 5$ mm for both targets. For $\rho = 1$ it was 1.29 % but for $\rho = 0$ it was 9.61 % which was caused by the occurrence of the spike at R = 8 mm.

The distribution of the points for the percentage difference between true and computed range for $\rho = 1$ and $\rho = 0$ are shown in Figures 5.16 and 5.17 respectively. From here the effect of the spikes can clearly be seen from the distribution of the curves which show their non-linearity. When $\rho = 1$ the points are more linear resulting in a maximum 0.15 % (for $X_0 = 5$ mm) difference between true and computed range from R > 20 mm. For $\rho = 0$ due to the occurrence of the spikes at longer ranges, the non-linearities are much larger resulting in a maximum 0.75 % (for $X_0 = 5$ mm) difference between true and computed range from R > 23 mm. In both cases the arrangement with $X_0 = 1$ mm results in the best linearity of response.

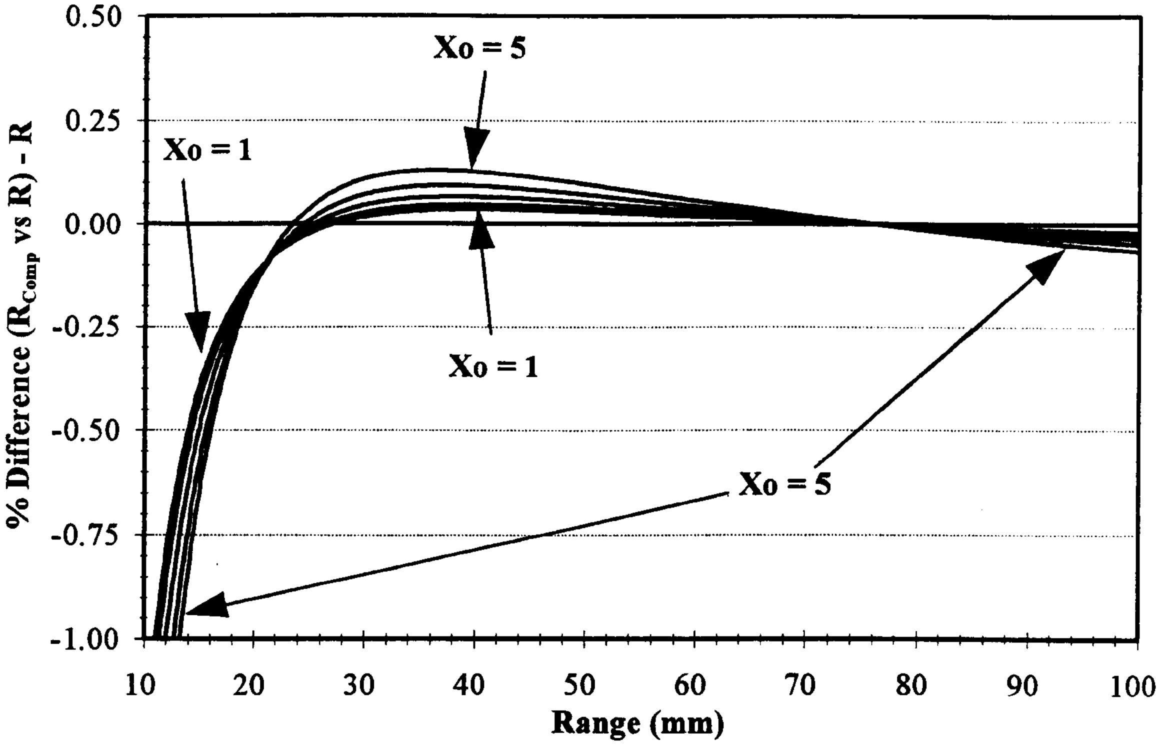

Fig. 5.16: Percentage difference between true and computed range for ρ = 1

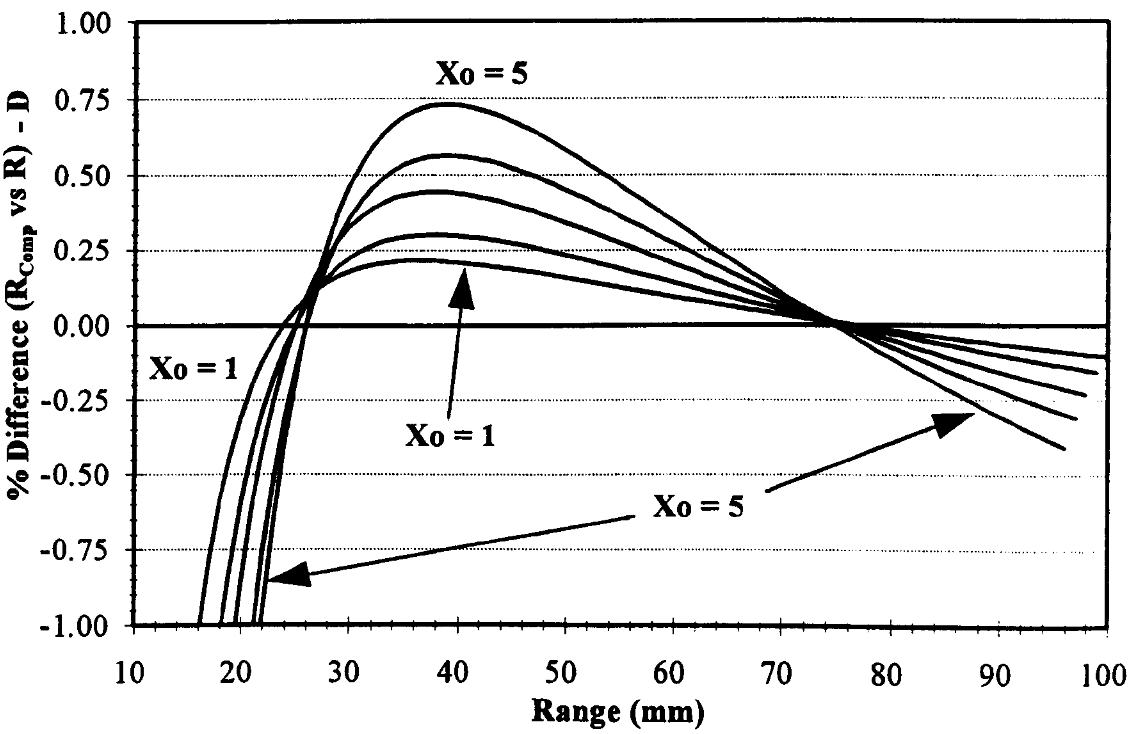

Fig. 5.17: Percentage difference between true and computed range for ρ = 0

A question arises as to why when having $\rho = 1$ and $X_0 = 5$ mm the beginning of the operational range (R_{min}) is at a later point than the other smaller X_0 separations since it is affected least by the argument of finite numerical aperture of the fibres. Consider Figure 5.18 which shows the arrangement of the sensor for two X_0 separations, i.e. $X_0 = 1$ mm and $X_0 = 5$ mm, with the images of the detectors behind the mirror. The upper part of the figure indicates the settings for $X_0 = 5$ mm and the lower part the settings for $X_0 = 1$ mm.

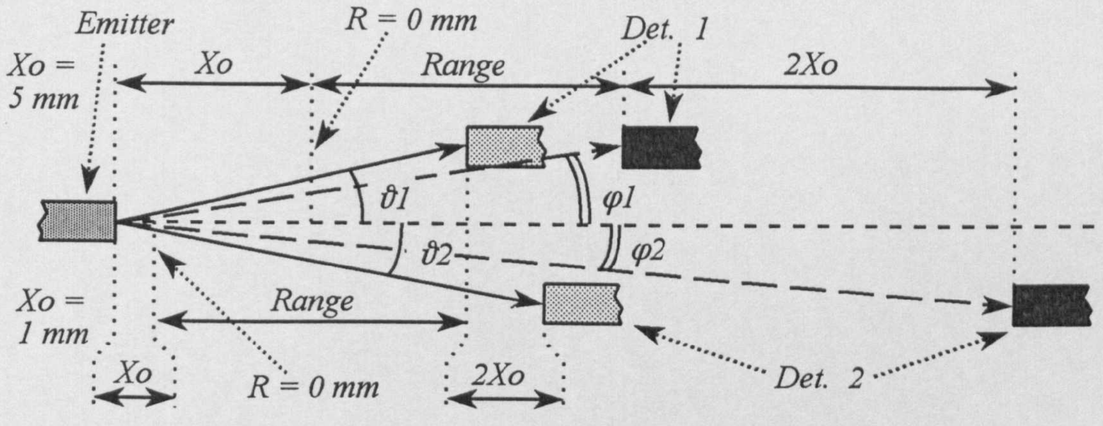

Fig. 5.18: Geometric considerations affect the starting point of the operational range for $\rho = 1$

In the figure above $\vartheta 1$ and $\vartheta 2$, and $\varphi 1$ and $\varphi 2$ are the angles between the optical axis of emission and the lines joining the centre of the emitting fibre with the centre of Det. 1 and Det. 2 for $X_0 = 1$ mm and $X_0 = 5$ mm respectively. The lighter shaded detecting fibres indicate the arrangement for $X_0 = 1$ mm whereas the darker shaded ones the arrangement for $X_0 = 5$ mm. The beginning of the range is different for each arrangement and the relative distance between the two detecting fibres for each X_0 separation, with $X_0 = 5$ mm having the larger distance between the two detecting fibres. The range indicated is assumed to be the same for both arrangements.

Clearly, the two angles for each arrangement are not the same. The angles involved in the $X_0 = 1$ mm are larger than those involved in the $X_0 = 5$ mm, i.e. $\vartheta > \varphi$. For $X_0 = 1$ mm the angles between the optical axis and the detecting fibres ($\vartheta 1$ and $\vartheta 2$) are closer to each other since the separation between the two detecting fibres is small. For both cases, the difference becomes smaller as the range increases which is understood considering the geometrical arrangement of the fibres.

At the same time, the angles involved for the front detecting POFs for any of the X_0 separations are bigger than those involved for the rear detecting POFs, i.e. $\vartheta 1 > \vartheta 2$ and $\varphi 1 > \varphi 2$. This inequality between the two angles for each X_0 separation will introduce a geometric error in the response. This error will result in the two detecting fibres receiving a different level of illumination for each range. The illumination is related to the part of the emission directed towards each detecting fibre. Ideally, the two detecting POFs should be having the same amount of light radiated towards them ($\vartheta 1 = \vartheta 2$ and $\varphi 1 = \varphi 2$ for equal illumination towards the detecting POFs) with only the distance between each detecting fibre and the emitting fibre causing variations in the intensity of light.

By taking into consideration the angular emission of the emitting fibre towards each detector and the solid angles involved for the detecting fibres for these two X_0 separations the values shown in Table 5.6 have been obtained. The intensity values shown for each detector are normalised. The differences between them are also shown. The range involved was not taken into consideration in the calculations for comparison purposes.

Table 5.6: Normalised intensities with solid angles for X_0 = 1 mm and X_0 = 5 mm (X_0 values in mm) for ρ = 1

Range (mm)	A_R $X_0 = 1$	B_R $X_0 = 1$	$(A_R - B_R)/A_R$ (%)	C_R $X_0 = 5$	D_R $X_0 = 5$	$(C_R - D_R)/C_R$ (%)
10	0.9891	0.9909	-0.1809	0.9923	0.9961	-0.3778
15	0.9950	0.9956	-0.0589	0.9961	0.9976	-0.1557
20	0.9971	0.9974	-0.0261	0.9976	0.9984	-0.0789
30	0.9987	0.9988	-0.0081	0.9989	0.9991	-0.0285
50	0.9995	0.9995	-0.0018	0.9996	0.9996	-0.0073
80	0.9998	0.9998	-0.0005	0.9998	0.9998	-0.0020

A_R and B_R, and C_R and D_R in Table 5.6 are the light intensities received by Det. 1 and Det. 2 for X_0 = 1 mm and X_0 = 5 mm respectively. Effects of angular emission and solid angle determine the level of intensity received by the detectors. The differences are very small with the smaller X_0 separation having the smaller error. An error of - 0.38 % at R = 10 mm for X_0 = 5 mm may seem very small but explains why larger X_0 separations take longer to become linear. This may suggest that different y separations may be necessary in order to obtain better response from the sensor for the larger X_0 separations (Section 5.6).

Similar geometrical effects are expected to affect the linearity of response when targets with $\rho < 1$ are considered in the sensor. In this case all the light emitted onto the target will be rearranged into a near lambertian distribution and will be directed towards the sensor head. These effects will be emphasized by the fact that larger X_0 separations are linked to larger y separations (see Table 5.3). And again, as the range increases, these effects will decrease causing an improvement in the linearity of response of the sensor.

As shown so far the slope of the sensor response is expected to be a function of the nature of the surface of the target. A 100 % reflective target ($\rho = 1$) will result in a sensor response with a slope close to $(X_0)^{-1}$ whereas a 100 % diffusive target ($\rho = 0$) will result in a sensor response with a slope close to $(2X_0)^{-1}$. A partly reflective and partly diffusive target ($0 < \rho < 1$) is therefore expected to result in a sensor response with a slope lying in between $(X_0)^{-1}$ and $(2X_0)^{-1}$. The resultant slope should depend on the reflectivity coefficient of the surface of the target. The computer program investigated the behaviour of the sensor under these conditions with $X_0 = 3$ mm and y = 3.4 mm. The reflectivity coefficient (ρ) was arranged to be 1, 0.75, 0.5, 0.25 and 0.

The spike was present here as well in the very short ranges, i.e. R < 6 mm. It tended to take place at a shorter range if a more reflective target was used and further away for a more diffusive target. The spikes will not be dealt with any further since no more information than what is already obtained is gained.

The sensor responses obtained are shown in Figure 5.19 and in Table 5.7 quantitatively. It is clear that the slope of the sensor response varies depending on the target reflectivity coefficient although it does not change linearly with reflectivity coefficient changes, but is more affected (increases) as the value of the reflectivity coefficient increases.

Table 5.7: Computed response with $0 \leq \rho \leq 1$ for $X_0 = 3$ mm and y = 3.4 mm

Reflectivity Coefficient, (ρ)	1.00	0.75	0.50	0.25	0.00
(dS / dR), LSF	0.3320	0.2224	0.1892	0.1732	0.1638
C, LSF	1.1381	0.9558	0.8656	0.8158	0.7844
R_{min}, mm	14	17	18	18	18

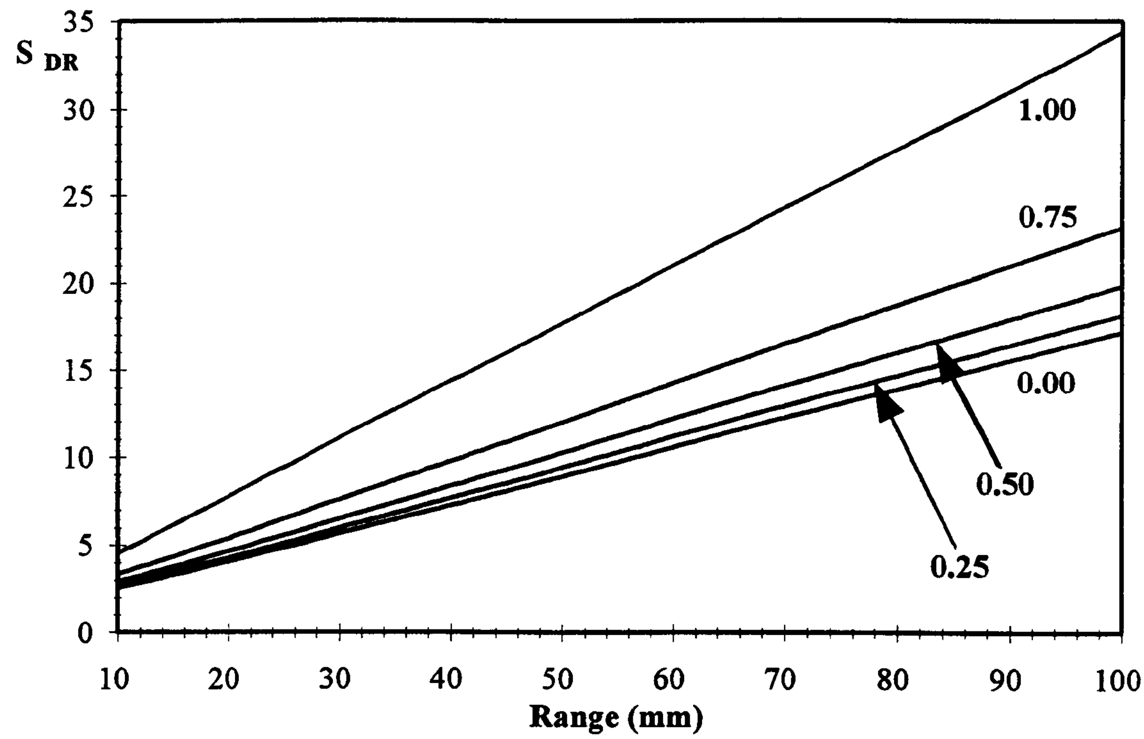

Fig. 5.19: The sensor response for various reflectivity coefficients

As seen in Table 5.7 when $\rho = 1$ the slope of the response is close to $(X_0)^{-1}$, i.e. 0.333, whereas when $\rho = 0$ the slope of the response is close to $(2X_0)^{-1}$, i.e. 0.167. A reflective coefficient other than these two results in a slope which lies between $(X_0)^{-1}$ and $(2X_0)^{-1}$, but being closer to $(2X_0)^{-1}$ rather than $(X_0)^{-1}$. The influence that the diffusive part of the surface of the target has on the sensor response affects the starting point (R_{min}) of the operational range with $\rho = 0.5$ giving the same minimum range as $\rho = 0$ does. The LSFs for all attempts were taken between 10 mm and 100 mm.

In order to understand why the slope of the response does not change linearly with linear changes in the reflectivity coefficient the computed signals shown in Figure 5.20 were considered. Here the $S1_R$ and $S2_R$ signals are the ones computed for the attempt with $\rho = 1$ and the $S1_D$ and $S2_D$ signals are the ones computed for the attempt with $\rho = 0$ with the sensor arranged with $X_0 = 3$ mm and $y = 3.4$ mm. As seen, the separation between the two signals is different, with the $S1_D$ and $S2_D$ having the larger separation between them thus making them more tolerable to any changes in the signals due to changes in ρ which will influence the effects of specular and diffuse reflection. It is obvious that any change taking place between the two pairs of signals will be noticed immediately if the surface of the target is more reflective than emissive. The opposite will be the case if the surface of the target is

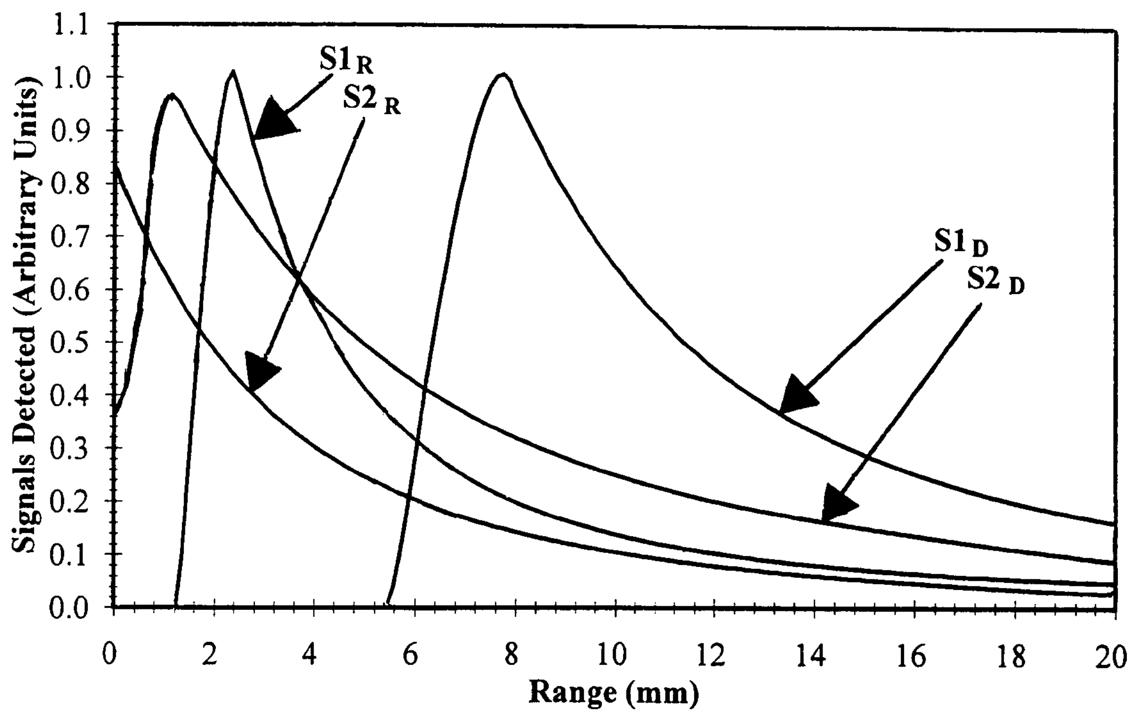

Fig. 5.20: The computed signals for a 100 % reflective and a 100 % diffusive target

more diffusive than reflective. The denominator of the transfer function of the sensor (eq. 5.6) and the difference between the two signals are the reasons for this effect.

Also shown in Figure 5.20 is the crossing of the two computed signals for each arrangement (X_0 = 3 mm) which shows the position in the range where the spike will occur. For the 100 % reflective target the two signals, $S1_R$ and $S2_R$, cross each other at R = 1.7 mm whereas for the 100 % diffusive target the two signals, $S1_D$ and $S2_D$, cross each other at R = 5.8 mm.

More important than the crossing of the signals is the difference between the two signals for each arrangement. For the reflective target the two signals tend closer to each other at a very early stage whereas the signals for the diffuse target tend to stay apart for a much longer range. These features are in fact the ones that determine the slope of the linear response for the same X_0 and y separations (see denominator of transfer function). Any errors in these signals will result in an erroneous sensor response with possibly increased non-linear effects over the useful linear range of the sensor (Section 5.5).

The partly reflective and partly diffusive target which was to be used in the experimental work of the sensor was matt white (typing) paper (MWP). At ~ 650 nm the reflectivity coefficient of MWP is ρ = 0.82.

The sensor head separations for the simulation were arranged to be X_0 = 1 mm and X_0 = 2 mm having a y separation of 2.2 mm and X_0 = 3 mm, X_0 = 4 mm and X_0 = 5 mm having a y separation of 3.34 mm. The y separations were checked experimentally so that they would not block the emitted light.

The computed results are shown in Figure 5.21 and numerical data are presented in Table 5.8. The LSF was applied over the range between 10 mm and 100 mm for all X_0 separations.

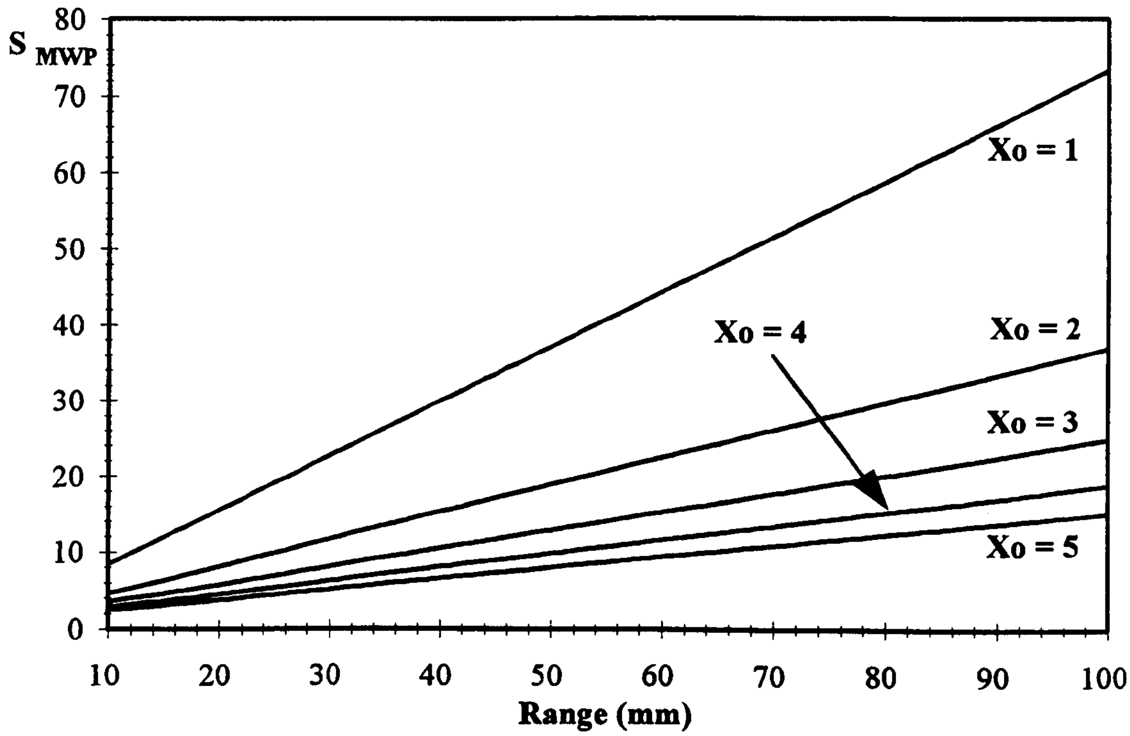

Fig. 5.21: The computed sensor response using matt white paper (MWP) as target

Table 5.8: Computed sensor response results using matt white paper as target

X_0 Separation (mm)	$X_0 = 1$	$X_0 = 2$	$X_0 = 3$	$X_0 = 4$	$X_0 = 5$
y separation	2.2	2.2	3.4	3.4	3.4
R_{min}, mm	15	15	16	17	17
(dS / dR), LSF	0.7222	0.3609	0.2391	0.1792	0.1432
C, LSF	1.0633	0.9058	0.9950	0.9389	0.9110

As seen in Figure 5.21 linearity of response is maintained when MWP is used as target. The slope of the responses for each X_0 separation is close to $(1.385X_0)^{-1}$. The minimum range for each sensor arrangement varies from 15 mm up to 17 mm. A 100 % reflective target would result in a minimum range between 11.1 mm and 13.4 mm (Table 5.4) whereas a 100 % diffusive target would result in a minimum range between 16 mm and 22 mm (Table 5.5). The minimum ranges here are closer to the ones for a 100 % diffusive target.

Using computer simulation the performance of the sensor was investigated in more depth and more accurately. The program calculated through numerical integration the light incident on the detecting POFs taking into account factors such as the nature of the surface of the target, the physical orientation of the fibres with respect to each other, the shape and size of the cores of the fibres and their numerical aperture and the distance that the light will have to travel towards each detecting fibre for each case. The targets investigated using computer simulation were of different reflectivities, i.e. $1 \geq \rho \geq 0$.

In all cases a linear response was achieved. When a target with $\rho = 1$ was used, the slope of the response was closely equal to the inverse of the X_0 distance separating the three POFs, i.e. $(X_0)^{-1}$. When a target with $\rho = 0$ was used, the slope of the response was closely equal to $(2X_0)^{-1}$. When targets of intermediate ρ were used the resultant slope of the response was in between $(X_0)^{-1}$ and $(2X_0)^{-1}$. The separation (difference) between the two detected signals, which is greater when $\rho = 0$ at any given range, will affect a bigger change in the slope of the response if the reflectivity of the target is very high. If $\rho < 0.5$ the slope of the response is only marginally affected from that of $\rho = 0$.

Linearity of response extends to the longer ranges and is only breaking down, causing a spike to appear, at the very short ranges for $0 \leq \rho \leq 1$ targets due to the finite numerical aperture of the fibres. The lateral, y separation between the fibres also affects the range at which the spike would occur, with the larger y separations resulting in the spike taking place at a longer range. Linearity was obtained for the arrangement with $\rho = 1$, for a range starting around 12 mm up to the maximum range investigated, i.e. that of 100 mm. For the arrangement with $\rho = 0$, linearity was obtained from around 18 mm up to 100 mm.

Inequalities in the light signal directed towards each detecting fibre arise from the geometric arrangement of the fibres in the sensor head. The normalised relative intensity radiated towards the front detecting fibre is always smaller than that radiated towards the rear detecting fibre. The linearity of response of the sensor is affected at short ranges for all X_0 separations with the larger X_0 causing a larger non-linearity. As the range increases, however, non-linearity decreases.

Matt white paper was also used as target in the computer simulation and the slope of the responses was predicted to be close to $(1.385X_0)^{-1}$. Although this type of target has a fairly high reflectivity coefficient ($\rho = 0.82$) the beginning of the operational range (around 16 mm) was found to be closer to a very diffusive surfaced target rather than a very reflective one.

5.5. ERRORS ON THE SIGNALS

The previous section analysed the behaviour of the sensor under conditions affected only by the physical arrangement and shortcomings of the sensor head arrangement. In order to determine how the sensor response would be affected if errors existed on the signals the following analysis was performed. Consider the following errors on the signals:

The error in S1 is $\Delta S1$ and the error in S2 is $\Delta S2$.

The error in (S1 + S2) is:

$$\Delta(S1 + S2) = \sqrt{(\Delta S1^2 + \Delta S2^2)} \qquad \textbf{Eq. (5.23)}$$

The error in (S1 - S2) is:

$$\Delta(S1 - S2) = \sqrt{(\Delta S1^2 + \Delta S2^2)} \qquad \textbf{Eq. (5.24)}$$

Hence:

$$\Delta(S1 + S2) = \Delta(S1 - S2) \qquad \textbf{Eq. (5.25)}$$

The error in S is:

$$\Delta S = S\sqrt{\left(\frac{\Delta(S1+S2)}{S1+S2}\right)^2 + \left(\frac{\Delta(S1-S2)}{S1-S2}\right)^2} \qquad \textbf{Eq. (5.26)}$$

Equation 5.26 is used to calculate the percentage error in S_R, shown in Table 5.9, and S_D, shown in Table 5.10, when the two signals have errors of 0.1 %.

Table 5.9: Application of equation 5.26 for 100 % reflective targets

Range (mm)	$S1_R$ (10^{-2})	$S2_R$ (10^{-2})	S_R	ΔS_R	Error in S_R (%)
20	1.9502	1.5037	7.7353	0.0430	0.5561
30	0.9111	0.7599	11.0479	0.0870	0.7876
40	0.5255	0.4571	14.3700	0.1467	1.0210
50	0.3414	0.3049	17.6964	0.2221	1.2553
60	0.2395	0.2177	21.0249	0.3133	1.4901
70	0.1772	0.1632	24.3548	0.4201	1.7250
80	0.1364	0.1269	27.6853	0.5427	1.9602
90	0.1082	0.1015	31.0167	0.6810	2.1955
100	0.0880	0.0830	34.3485	0.8350	2.4309

Table 5.10: Application of equation 5.26 for 100 % diffusive targets

Range (mm)	$S1_D$ (10^{-2})	$S2_D$ (10^{-2})	S_D	ΔS_D	Error in S_D (%)
20	8.8425	5.2849	3.9711	0.0119	0.2986
30	3.9840	2.7760	5.5958	0.0228	0.4083
40	2.2518	1.7052	7.2401	0.0378	0.5217
50	1.4444	1.1524	8.8929	0.0566	0.6368
60	1.0042	0.8303	10.5501	0.0794	0.7527
70	0.7383	0.6266	12.2099	0.1061	0.8692
80	0.5656	0.4895	13.8713	0.1368	0.9859
90	0.4470	0.3929	15.5339	0.1713	1.1030
100	0.3622	0.3224	17.1973	0.2098	1.2201

As shown in Table 5.9, a 0.1 % error on the two computed signals ($S1_R$ and $S2_R$) will result in errors in the response of the sensor which will increase as range increases. ΔS_R is increasing as range increases and so does S_R. But ΔS_R is increasing relatively faster than

S_R resulting in errors larger than 1 % from as early as R = 40 mm. At R = 100 mm the error in S_R is 2.4 %.

Table 5.10 shows that ΔS_D increases as range increases and so does S_D. But although ΔS_D is increasing relatively faster than S_D it is increasing at a slower pace than ΔS_R (Table 5.9) causing a smaller error in S_D resulting in errors smaller than 1 % up to R = 80 mm.

Further analysis is required in order to determine what is causing these errors. Equation 5.26 is thus broken down and each term under the square root is considered individually. Consider the following equations:

$$A = \left(\frac{\Delta(S1 + S2)}{S1 + S2}\right)^2 \quad \textbf{Eq. (5.27)}$$

and:

$$B = \left(\frac{\Delta(S1 - S2)}{S1 - S2}\right)^2 \quad \textbf{Eq. (5.28)}$$

Equation 5.27 describes the error involved with the sum in the numerator of the transfer function of the sensor of equation 5.6. Equation 5.28 describes the error involved with the difference in the denominator of equation 5.6. Both these equations are applied in Table 5.11 for both target arrangements of the sensor.

Table 5.11: Equations 5.27 and 5.28 and their differences

Range (mm)	A_R **(10^{-6})**	B_R **(10^{-6})**	$(B_R - A_R)/B_R$ **(%)**	A_D **(10^{-6})**	B_D **(10^{-6})**	$(B_D - A_D)/B_D$ **(%)**
20	0.5084	30.4177	98.3287	0.5317	8.3848	93.6587
30	0.5041	61.5276	99.1807	0.5160	16.1564	96.8064
40	0.5024	103.7485	99.5157	0.5095	26.7097	98.0923
50	0.5016	157.0804	99.6807	0.5063	40.0418	98.7355
60	0.5011	221.5239	99.7738	0.5045	56.1523	99.1016
70	0.5008	297.0779	99.8314	0.5034	75.0408	99.3292
80	0.5007	383.7387	99.8695	0.5026	96.7071	99.4803
90	0.5005	481.5192	99.8961	0.5021	121.1518	99.5856
100	0.5004	590.4101	99.9152	0.5017	148.3738	99.6619

Looking at the A_R and A_D results shown in Table 5.11 it is obvious their values change from R = 20 mm to R = 100 mm by 1.6 % and 5.6 % respectively showing a very small decreasing trend as range increases. Exactly the opposite is taking place when B_R and B_D are considered. As range increases both are increasing fast making them the dominant error involved. The values of B_R and B_D change from R = 20 mm to R = 100 mm by 1841 % and 1670 % respectively. It is noticeable that B_R is increasing much faster than B_D. The percentage difference between the corresponding sets for each arrangement, i.e. A_R to B_R and A_D to B_D, is large enough to make the error involved in the numerator of the transfer function, i.e. A_R and A_D, unnecessary to consider in the error analysis.

In a similar treatment the effect of errors (0.1 % of each signal's amplitude) on the response of the sensor for various X_0 separations for $\rho = 1$ and $\rho = 0$ was investigated to determine the maximum operational range that could be obtained with 1 % accuracy. The results are shown in Table 5.12.

Table 5.12: The maximum range for $\rho = 1$ and $\rho = 0$ is a function of the X_0 separation for a given error on each signal (error = 0.1 %)

X_0 Separation (mm)	$\rho = 1$ R_{max}, (mm)	Operational Range (mm)	$\rho = 0$ R_{max}, (mm)	Operational Range (mm)
1	14	2.9	27	11
2	27	15.5	55	37
3	40	27.9	82	62
4	53	40.2	109	88
5	66	52.6	136	114

As seen from the table above the X_0 separation plays a very important role on the maximum range, and thus the operational range, that the sensor can operate with an accuracy of 1 %. The bigger the X_0 separation the longer the maximum range obtained. The type of target used played an equally important role since the maximum range achieved when $\rho = 0$ is more than twice as long as the one achieved for $\rho = 1$. The target with $\rho = 0$ seems to be a very attractive target to use for applications where a long operational range is necessary. The resulting maximum ranges suggest that a relationship between the X_0 separation and the maximum range for an error on the signal of 0.1 % is approximately

$13.5X_0$ for $\rho = 1$ and $27X_0$ for $\rho = 0$. For signal error higher than 0.1 % then one would have shorter operational ranges. This result is important to the scalability of the sensor.

The fact that the arrangement with $\rho = 0$ offers the lower error in S stems from the fact that the two signals $S1_D$ and $S2_D$, shown in Figure 5.20, are keeping a level of difference between them which is much greater than the one between $S1_R$ and $S2_R$. This fact makes the denominator in the transfer function (equation 5.6) to have a much larger value than when a reflective target is used. All these indicate that for a better error rejection the difference between the signals has to be as large as possible. Extension of the range into longer ranges will only be possible if the errors on the signals are kept to the minimum possible level.

A very important factor concerning the maximum operational range, as well as the resolution of the sensor, is the length of the POFs used in the sensor head. Three POFs of 5 m length each will be employed in the sensor head. Such a length will result in attenuation of the signal at the end of each 5 m length of approximately 1 dB. In other words, the signal received by each of the two detectors will be attenuated by 2 dB. This will mean that the denominator of the transfer function will result in a much smaller signal with which the numerator is divided, thus resulting in lower maximum operational range.

Other sources of error which may affect the linearity and accuracy of the sensor are mis-calibration between and offset voltages on the two detectors. The analysis of these effect follows.

Calibration of the two detectors refers to the degree of similarity in their operation over the useful operational range of the sensor. Ideally, the degree of similarity of the two detectors should be very high and the aim is always to make their operation as identical as possible.

To determine the possible effects that mis-calibration of the two detecting circuits would have on the sensor response, the transfer function was redefined as shown in equation 5.29, with Q_1 and Q_2 being the calibration factors for S1 and S2 respectively:

$$S = \frac{Q_1 S1 + Q_2 S2}{Q_1 S1 - Q_2 S2} \qquad \textbf{Eq. (5.29)}$$

For ideal calibration $Q_1 = Q_2 = 1$. Analytical sensor responses (Figure 5.22) were obtained for a range of combinations of Q_1 and Q_2 values, the maximum difference being 2 %. Numerical data are presented in Table 5.13 for $\rho = 1$.

Table 5.13: Mis-calibration of the detectors for ρ = 1

Q_1 (Mis-Calibr.)	Q_2 (Mis-Calibr.)	(dS / dR) (20 - 21 mm)	(dS / dR) (99 - 100 mm)	$\alpha_{(L)}$ (%)
0.98 (2%)	1.00 (0%)	0.3902	0.7771	49.7877
0.99 (1%)	1.00 (0%)	0.3584	0.4857	26.2096
1.00 (0%)	1.00 (0%)	0.3305	0.3332	0.8103
1.00 (0%)	0.99 (1%)	0.3057	0.2426	-26.0099
1.00 (0%)	0.98 (2%)	0.2834	0.1841	-53.9381

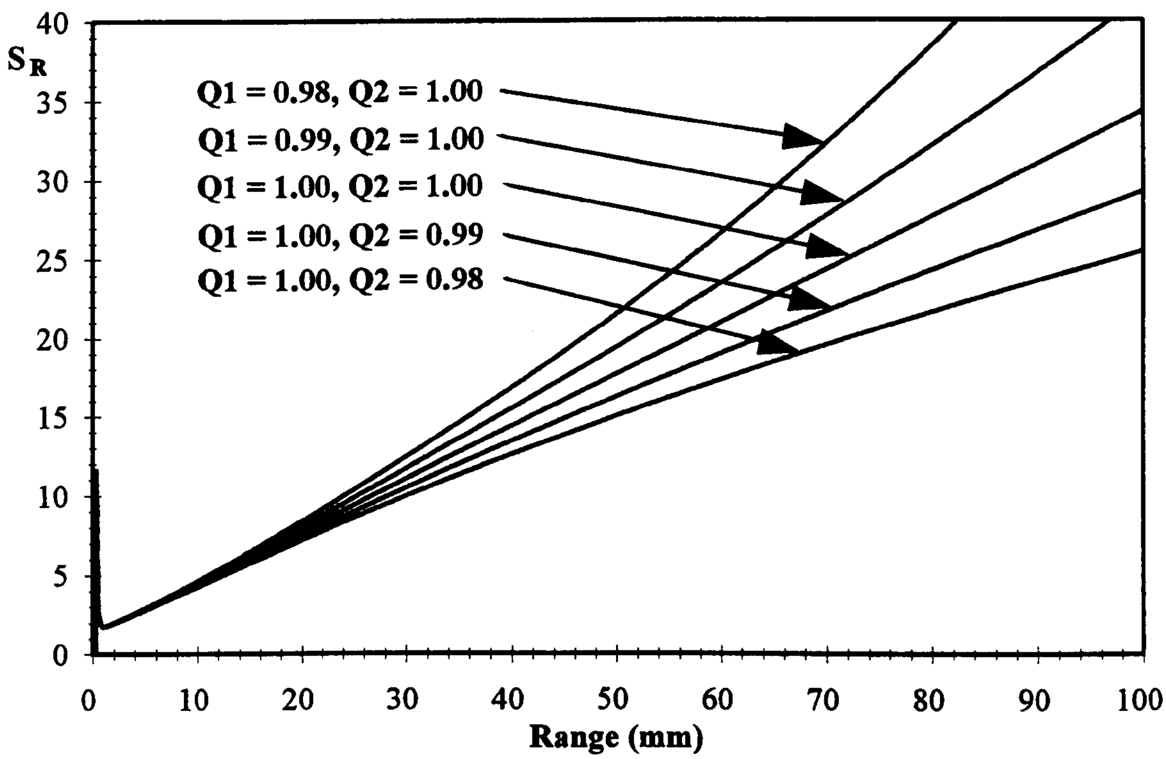

Fig. 5.22: Effects of mis-calibration between the two detectors for ρ = 1

From what is shown in Figure 5.22 it is obvious that a small mis-calibration could lead to major errors in the linearity of response. It is noticeable that the errors start at short ranges and increase considerably as range increases. Table 5.13 shows the level of miscalibration, the slope of the response taken at two regions and the non-linearity induced (as defined by equation 5.15). The short range was chosen in order to give a non-linearity figure of < 1 % for the case where $Q_1 = Q_2 = 1$. For $\rho = 1$ this was taken between 20 mm and 21 mm. The long range remained the same, taken between 99 mm and 100 mm.

Mis-calibration also affects the arrangement with $\rho = 0$ in a similar way as shown in Figure 5.22 (for $\rho = 1$). The results are presented numerically in Table 5.14. For this arrangement, the short range was chosen to be taken between 40 mm and 41 mm in order to give a non-linearity figure better than 1 % for the case where $Q_1 = Q_2 = 1$.

Table 5.14: Mis-calibration of the detectors for $\rho = 0$

Q_1 (Mis-Calibr.)	Q_2 (Mis-Calibr.)	(dS / dR) (40 - 41 mm)	(dS / dR) (99 - 100 mm)	$\alpha_{(L)}$ (%)
0.98 (2%)	1.00 (0%)	0.1924	0.2431	20.8586
0.99 (1%)	1.00 (0%)	0.1778	0.1991	10.6981
1.00 (0%)	1.00 (0%)	0.1650	0.1664	0.8413
1.00 (0%)	0.99 (1%)	0.1535	0.1410	-8.8652
1.00 (0%)	0.98 (2%)	0.1430	0.1209	-18.2796

As shown in Table 5.14 a small mis-calibration leads to errors here as well, but they do not have the magnitude that the errors of the arrangement with reflective targets have. The errors start at short ranges and increase as range increases but at a slower rate.

Mis-calibration of the two detecting circuits affects the two cases of sensor arrangement differently. For $\rho = 1$ the effects induced on linearity are more than double those induced when $\rho = 0$. This can be understood in terms of the differences of the signals computed as shown in Figure 5.20 where $S1_D$ and $S2_D$ have the bigger difference between them and so would be affected the least by external effects.

When offset voltages exist on one of the two, or even both detectors the linearity of response will again be affected. The effect that this may have on the transfer function of the sensor has been investigated by adding or subtracting an offset voltage on the computed signal(s) in various combinations. To do this the transfer function was redefined as shown in equation 5.30, with V_{OFST1} and V_{OFST2} being the offset voltages added (or subtracted) to S1 and S2 respectively:

$$S = \frac{(V_{OFST1} + S1) + (V_{OFST2} + S2)}{(V_{OFST1} + S1) - (V_{OFST2} + S2)} \qquad \text{Eq. (5.30)}$$

The offset voltage was taken to be either 1 % or 2 % of the signal computed for any of the two detectors at maximum range (R = 100 mm). Non-linearity was obtained in a similar way as with the investigation on mis-calibration effects, i.e. to give a non-linearity figure better than 1 % for the case where $V_{OFST1} = V_{OFST2} = 0$ % of S1 and S2 respectively.

Table 5.15 shows on which detector (or both) the offset voltage was added or subtracted and at what percentage value for $\rho = 1$. The effects that offset voltage has on the response if only added or subtracted to detector 1 is shown in Figure 5.23. Similar effects are expected to occur if offset voltage is added or subtracted to detector 2.

Table 5.15: Effects of offset voltage on the detectors for $\rho = 1$

Offset $S1_R$ (%)	Offset $S2_R$ (%)	(dS / dR) (20 - 21 mm)	(dS / dR) (99 - 100 mm)	$\alpha_{(L)}$ (%)
-	-	0.3305	0.3332	0.8103
1	-	0.3279	0.1610	-103.6646
2	-	0.3254	0.0610	-433.4426
-1	-	0.3330	0.6515	48.8872
-2	-	0.3356	1.3081	74.3445
-	1	0.3334	0.6410	47.9875
-	2	0.3363	1.2472	73.0356
-	-1	0.3276	0.1613	-103.0998
-	-2	0.3247	0.0591	-449.4078
1	1	0.3310	0.3434	3.6109
2	2	0.3315	0.3535	6.2235
-1	-1	0.3299	0.3230	-2.1362
-2	-2	0.3294	0.3128	-5.3069
1	-1	0.3249	0.0554	-486.4621
-1	1	0.3361	1.3321	74.7692

Table 5.15 shows that even a 1 % offset voltage of the signals detected at R = 100 mm added to any of the detectors will render the sensor unreliable especially at medium to long ranges. The shorter ranges do not seem to be affected to as high a degree as the longer ranges. The worst case for a given level of offset voltage appears to be if both detectors have offset voltage with opposite polarity. The more favourable case is when both the detectors have offset voltage of the same polarity. The operational range of the sensor and the magnitude of non-linearity will depend on the actual level of offset voltage on the detector(s).

Figure 5.23 also shows how the response of the sensor would be if a 10 % offset voltage is added to detector 1. Clearly, it renders the sensor unusable for most of the range.

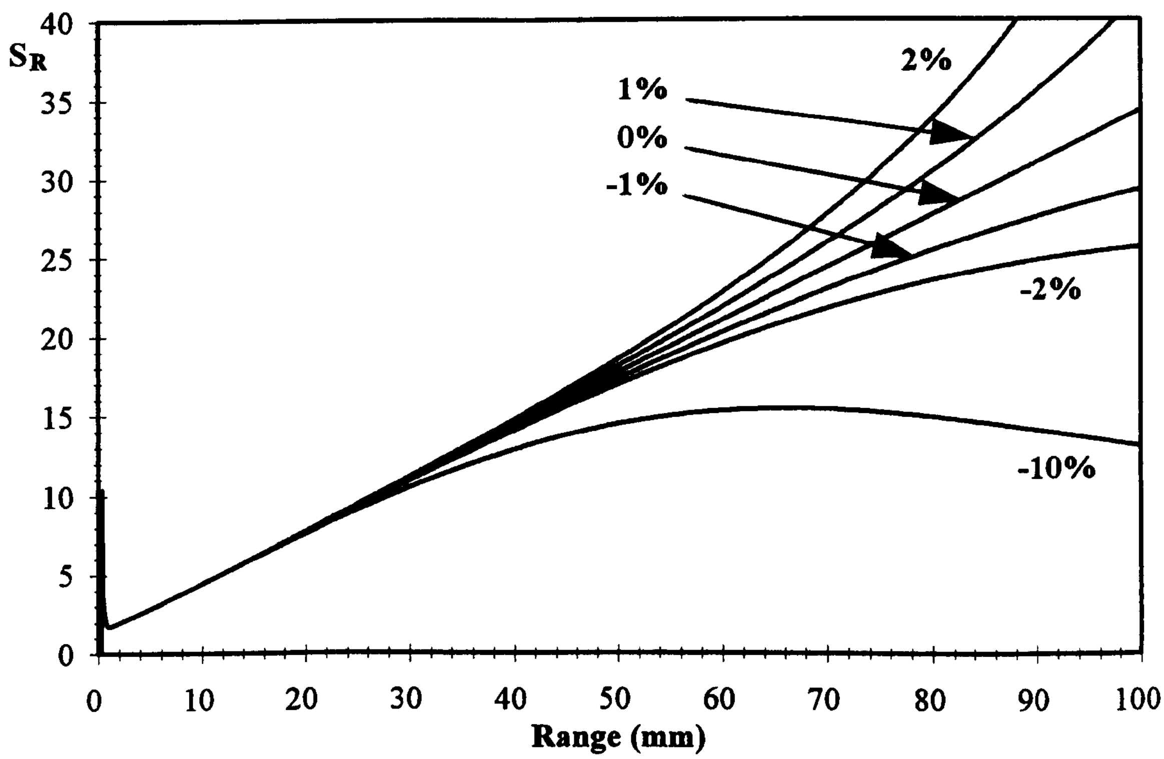

Fig. 5.23: The effect that offset voltage has on the response of the sensor if it affects detector 1 only for $\rho = 1$

A similar approach is followed for the case with $\rho = 0$. Table 5.16 shows offset voltage effects and results on the response of the sensor from this arrangement. Similar effects are taking place with $\rho = 0$ as they did with $\rho = 1$ although the magnitude that these effects have on this response are much smaller.

Table 5.16: Effects of offset voltage on the detectors for $\rho = 0$

Offset $S1_D$ (%)	Offset $S2_D$ (%)	(dS / dR) (40 - 41 mm)	(dS / dR) (99 - 100 mm)	$\alpha_{(L)}$ (%)
-	-	0.1650	0.1664	0.8233
1	-	0.1609	0.1171	-37.4678
2	-	0.1569	0.0803	-95.5424
-1	-	0.1692	0.2338	27.6385
-2	-	0.1734	0.3283	47.1707
-	1	0.1696	0.2308	26.5243
-	2	0.1742	0.3178	45.1790
-	-1	0.1605	0.1178	-36.2976
-	-2	0.1562	0.0805	-93.9034
1	1	0.1654	0.1648	-0.3752
2	2	0.1658	0.1632	-1.5778
-1	-1	0.1646	0.1680	2.0180
-2	-2	0.1642	0.1697	3.2093
1	-1	0.1566	0.0804	-94.7151
-1	1	0.1738	0.3230	46.1776

The magnitude of the effect of offset voltages on the two detecting circuits is different for the two cases of sensor arrangement. As with the investigation on mis-calibration effects, when $\rho = 1$ the effects induced on linearity are more noticeable than those induced when $\rho = 0$. The reason for this is again the difference between the two detecting signals where $S1_D$ and $S2_D$ have the bigger difference between them and so are affected the least by external effects.

When targets of $1 > \rho > 0$ are considered for cases of errors on the signals, mis-calibration and offset voltages, the resulting effects will depend on the actual value of ρ. If these errors do not exist, the linearity of the sensor response will be around 0.8 % from a minimum range up to 100 mm. If mis-calibration exists the errors on the response will start showing from a fairly early range, increasing considerably as range increases. If offset voltages exist the medium and long ranges will be the ones affected most. The worst case for a given level of offset voltage will be if both detectors have offset voltages of opposite polarity, whereas the most favourable case will be if they both have offset voltage of the same polarity. It is thus very important to make sure that these effects are kept to a minimum level since an immediate effect will be observed in the medium and longer ranges affecting the accuracy and linearity of the sensor response.

5.6. SEPARATION VARIATIONS ON THE SENSOR HEAD

Variations in X_0 and y separations could be introduced during production and could affect the behaviour and performance of the sensor. Investigation on the effects of such variations are presented in this Section.

The physical dimensions of the separations of the POFs on the sensor head were varied in the simulation to investigate in what way the sensor response would be affected. To do this, the computer program was arranged to accept different values of X_0 and y separations. In order to be able to differentiate between these separations the following terms have been used, considering Figure 5.1, which illustrates the sensor head arrangement:

$X_0$1 the X_0 separation between emitter and Det. 1,

$X_0$2 the X_0 separation between emitter and Det. 2,

y1 the y separation between emitter and Det. 1, and

y2 the y separation between emitter and Det. 2.

The total separation between the two X_0 separations was kept constant since a different distance will introduce a different slope, i.e. $X_01 + X_02 = 2X_0 = 6$ mm. The position of the emitting fibre with respect to the two detecting fibres was varied.

Table 5.17 shows the arranged X_01 and X_02 separations for $\rho = 1$ and the consequent effects. The attempt where $X_01 = X_02 = 3$ mm (i.e. the normal $X_0 = 3$ mm separation) is also shown for comparison purposes. The y separation was kept constant at 2.2 mm, i.e. $y1 = y2 = y$. Figure 5.24 shows the effect that this variation has on the response at the short ranges. For $\rho = 1$ the LSF was applied over the range 10 mm < R < 100 mm.

The variation in the X_0 separations shifts upwards or downwards the response which remains linear, as is shown in Figure 5.24. This is due to the changing difference between the two detecting signals at each position on the range. Table 5.17 shows how the signals percentage difference with respect to each other change at R = 10 mm. The slope of the response does not change remaining essentially the same as before since it depends on the separation between the two detecting POFs, i.e. $X_0 1 + X_0 2 = 2X_0$.

Table 5.17: Effects of inequality between the X_0 separations for $\rho = 1$

$X_0 1$ (mm)	$X_0 2$ (mm)	Spike (R, mm)	(dS / dR) (LSF)	Intersection with S_R-axis (C, LSF)	$(S1_R - S2_R) / S1_R$ (%) (R = 10 mm)
0	6	1.9	0.3325	0.5869	40.2324
1	5	1.4	0.3325	0.7512	38.9713
2	4	0.9	0.3325	0.9158	37.7830
3	3	0.4	0.3325	1.0804	36.6633
4	2	0.0	0.3326	1.2451	35.6055
5	1	0.0	0.3326	1.4100	34.6042
6	0	0.0	0.3326	1.5749	33.6565

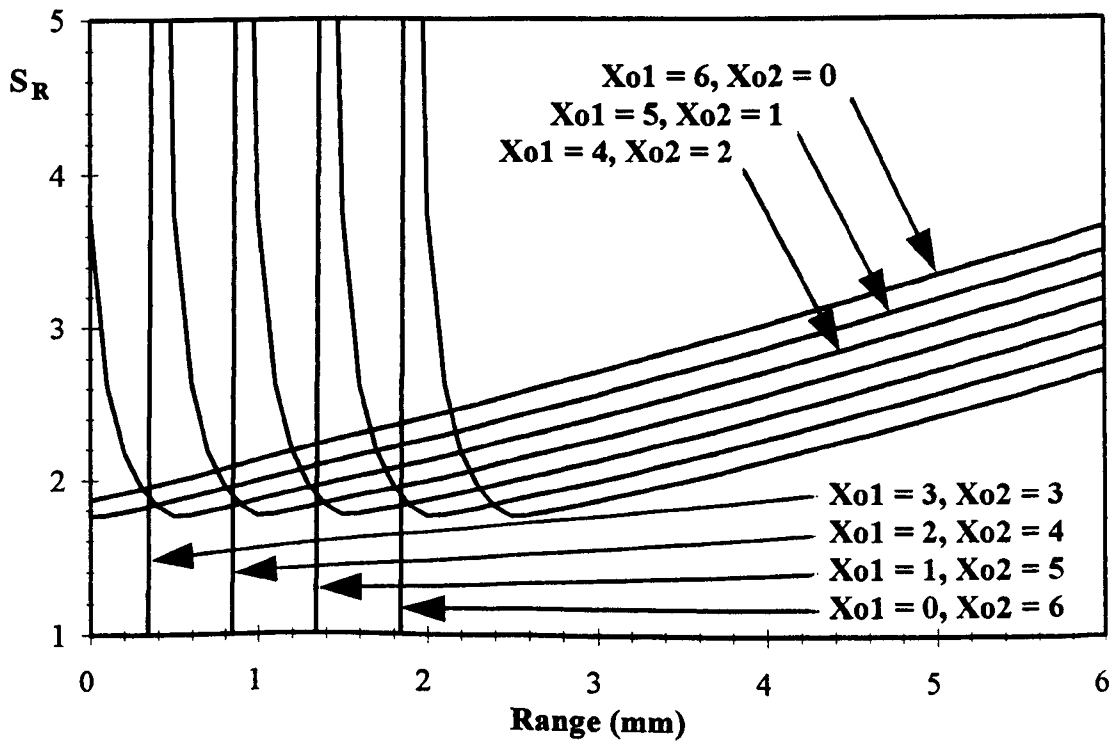

Fig. 5.24: Effects due to unequal X_0 separations for $\rho = 1$

The spike changes position in the range depending on where the emitting fibre with respect to the two detecting ones is positioned. This, as expected, is due to the finite emission cone from the emitting fibre. If $X_0 1$ = 0 mm then the end of the emitting fibre is positioned right next to the end of Det. 1 thus the two detecting POFs will have to be at a longer range in order to be fully illuminated by the emitted light. When $X_0 2$ = 0 mm the emitting fibre is positioned right next to Det. 2 and due to its distant position from the target, i.e. $X_0 1 + X_0 2$, the emission cone is already open enough to illuminate both detecting fibres even at R = 0 mm and as seen in Figure 5.24 the spike does not exist.

The straight line response shown in Figure 5.24 suggests that for best possible linearity the emitting POF should be positioned right next to Det. 2, i.e. $X_0 1$ = 6 mm and $X_0 2$ = 0 mm. But this response is not realisable. In the computer simulation the sensor was arranged in an unfolded situation (see Figure 5.8). In reality the sensor arrangement would be the one shown in Figure 5.1. Thus, in order to be able to illuminate both detecting POFs fully the sensor head will have to be positioned at a longer range (see Figure 3.6). The front detecting POF is the one which is more difficult to fully illuminate since its side blocks the emission towards the target. In order to do so the minimum ranges shown in Table 5.18 should hold for each $X_0 1$ and $X_0 2$ arrangement.

Table 5.18: Minimum range for complete illumination of Detector 1 for $\rho = 1$

$X_0 1$ (mm)	$X_0 2$ (mm)	Spike (R, mm)	Total Illumination of Det. 1 (R_{min}, mm)
0	6	1.9	1.5
1	5	1.4	1.5
2	4	0.9	2.7
3	3	0.4	4.0
4	2	0.0	5.3
5	1	0.0	6.7
6	0	0.0	8.0

Looking at Table 5.18 it can be seen that the advantage gained by positioning the emitting POF with $X_0 1$ = 6 mm and $X_0 2$ = 0 mm becomes a disadvantage once the true positioning of the POFs in the sensor head is considered since in such an arrangement the emission from the emitting POF is blocked by the front detecting fibre. The positioning of the emitting fibre in a $X_0 1 < X_0 2$ arrangement may thus be the most attractive solution. But considering the occurrence of the spikes in such arrangement then the most suitable solution should be the initial $X_0 1 = X_0 2 = X_0$.

When the $X_0 1$ and $X_0 2$ separations were varied in the arrangement with $\rho = 0$ for $X_0 = 3$ mm and y = 3.2 mm the signals computed and the response of the sensor were not affected. The reason is the fact that since the target acts as an emitter and the variations in the $X_0 1$ and $X_0 2$ separations will not result in much difference in the response with the spike occurring at around R = 5.8 mm which is the same as when $X_0 = 3$ mm. The Lambertian emission will be a problem in this arrangement since the front detecting fibre will block some of the light emitted from the emitting POF towards the target in the direction of Det. 1. This will cause an imbalance in the light which will be diffusively reflected towards the two detecting POFs causing an erroneous response.

The y separations in the sensor head were altered as well in order to investigate what effects this will have on the response for $\rho = 1$. The X_0 separation was kept constant at 3 mm for all attempts. The minimum y separation was kept at 2.2 mm since this will be the closest the three fibres will be positioned due to the size of the POFs. The y1 and y2 separations were varied to 3.0 mm, 3.5 mm and 4.0 mm for one of the y separations while keeping the other fixed at 2.2 mm. The results are shown in Table 5.19 and in Figure 5.25 only for the short ranges where the effects are more noticeable.

Table 5.19: Effects of inequality between the y separations for ρ = 1

y1 (mm)	y2 (mm)	Spike (R, mm)	(dS / dR)	Intersection with S_R-axis (C, LSF)	$(S1_R - S2_R) / S1_R$ (%) (R = 10 mm)
4.0	2.2	2.3	0.3318	1.4622	33.9902
3.5	2.2	1.8	0.3321	1.3294	34.8943
3.0	2.2	1.3	0.3323	1.2181	35.6731
2.2	2.2	0.4	0.3325	1.0804	36.6633
2.2	3.0	0.4	0.3324	0.9825	37.2814
2.2	3.5	0.4	0.3322	0.9083	37.7579
2.2	4.0	0.4	0.3320	0.8249	38.3011

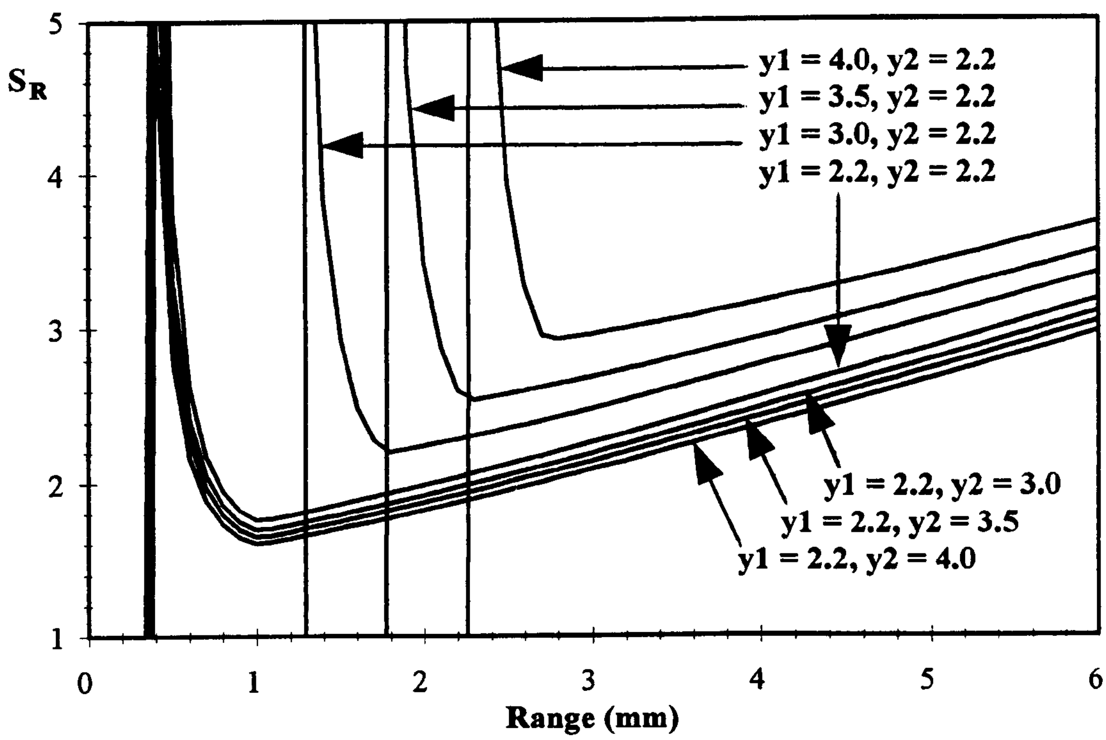

Fig. 5.25: Effects of unequal y separation for ρ = 1

It can be seen in Figure 5.25 that when the y1 separation is increasing from the set y = 2.2 mm value (set by external diameter of POF) effects take place immediately since an increase in y1 will take the fibre closer to the boundaries of the emission cone of the emitting fibre affecting the levels of illumination.

If y2 is increased and y1 is kept constant, as is also shown in Figure 5.26, the effects are not so obvious since the boundaries of the emission cone of the emitting fibre are further away from Det. 2 than for Det. 1 (see Figure 5.12). The variation in y separations shifts the linear response of the sensor but again does not affect its slope which remains the same for the same reasons outlined for the X_0 separation variations above.

In section 5.4 it was suggested that if the y2 separation was increased to compensate for some geometrical effects then an extension of the linear part of the response towards the shorter ranges could be obtained. From what Figure 5.26 shows the increase in y2 will not offer extension of the operational range towards the shorter ranges.

Although X_0 separation variations do not affect the behaviour of the sensor with $\rho = 0$, y separations are expected to affect it. This is due to the finite acceptance angle of the detecting fibres. An increase in the y separation of the fibres will result in delaying the overlap of the light acceptance cones of the detecting fibres with the emitting area on the target, i.e. the point on the target which receives the emission from the emitting POF. Table 5.19 shows numerical results of such an attempt and Figure 5.26 shows the short ranges where the effects are taking place. For this case the LSF was applied over the range 20 mm $< R <$ 100 mm.

As seen in Figure 5.26 the y separation affects the response of the sensor at the short ranges. An increase in the y1 separation moves the spike further in the range. An increase in the y2 separation again does not offer extension of the operational range towards shorter ranges.

Table 5.20: Effects of inequality between the y separations for $\rho = 0$

y1 (mm)	y2 (mm)	Spike (R, mm)	(dS / dR) (LSF)	Intersection with S_D-axis (C, LSF)	$(S1_R - S2_R) / S1_R$ (%) (R = 20 mm)
4.5	3.2	8.5	0.1645	1.0524	36.8961
4.0	3.2	7.5	0.1649	0.9006	38.0275
3.2	3.2	5.8	0.1653	0.7758	38.9997
3.2	4.0	5.8	0.1656	0.6245	40.2324
3.2	4.5	5.8	0.1654	0.5351	40.9557

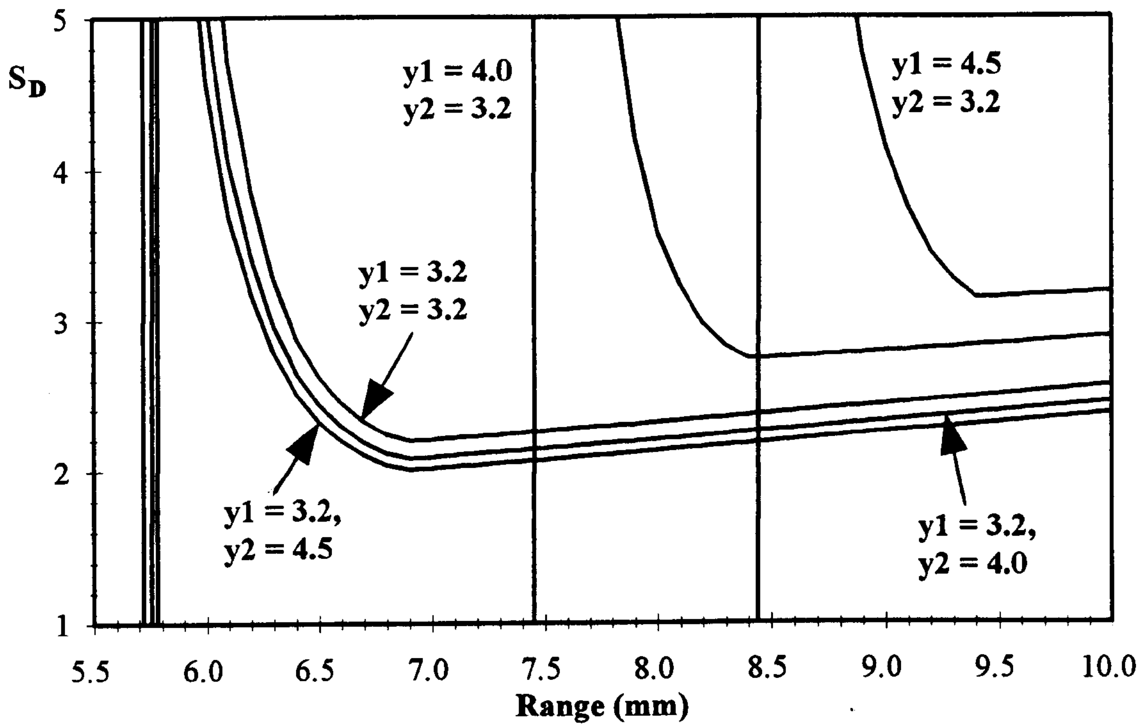

Fig. 5.26: Effects of unequal y separation for ρ = 0

Thus, from the above analysis, variations in the sensor head separations which could be present during production would affect the sensor response in various ways. Variation in the $X_0 1$ and $X_0 2$ or y1 and y2 separations will shift the linear part of the response up or down without changing its slope. They will also move the spike further in or further out in the range. When ρ = 1, a large $X_0 1$ separation could seem to be increasing the linear response of the sensor by eliminating the occurrence of the spike suggesting that this may be a better arrangement of the sensor head. But, considering the blockage of the emission by the front detecting POF in a realistic arrangement this advantage becomes a disadvantage which results in a full illumination of Det. 1 at a longer than necessary range.

An increased y2 separation proposed in Section 5.4 suggesting that an arrangement such as this would assist in increasing the linearity of response of the sensor towards the very short ranges. But, by doing so, an increase in the linearity is not observed.

Variations in the X_0 and y separations will not affect the sensor response in a dramatic way but it does suggest that for best results calibration of the sensor prior to any arrangement or application will be necessary.

5.7. SUMMARY AND CONCLUSIONS

Two forms of investigation were performed on this novel displacement sensor, one using a simple mathematical analysis and another using a more exact computer simulation. In the simple mathematical approach the sensor response was based only on the distance that the light travels before detection, i.e. the inverse square law. In the case of a 100 % reflective target ($\rho = 1$) that would be the distance that the light will have to travel from the emitting fibre to the target and then back to each detecting POF. In the case of a 100 % diffusive target ($\rho = 0$) that would be the distance between the part of the target which diffusely reflects the light incident on it and each detecting POF.

In the computer simulation approach the performance of the sensor was investigated in more depth and more accurately. The program calculated through numerical integration the light incident on the detecting POFs taking into account the nature of the surface of the target, the physical orientation of the fibres with respect to each other, the shape and size of the cores of the fibres and their numerical aperture and the distance that the light will have to travel towards each detecting fibre for each case. The targets investigated using computer simulation were of different reflectivities, i.e. $1 \geq \rho \geq 0$.

In all cases a linear response was achieved. When a target with $\rho = 1$ was used, the slope of the response was closely equal to the inverse of the X_0 distance separating the three POFs, i.e. $(X_0)^{-1}$. When a target with $\rho = 0$ was used, the slope of the response was closely equal to $(2X_0)^{-1}$. When targets of intermediate ρ were used the resultant slope of the response was in between $(X_0)^{-1}$ and $(2X_0)^{-1}$. The separation (difference) between the two detected signals, which is greater when $\rho = 0$ at any given range, will affect a bigger change in the slope of the response if the reflectivity of the target is very high. If $\rho < 0.5$ the slope of the response is only marginally affected from that of $\rho = 0$.

Linearity of response extends to the longer ranges and is only breaking down, causing a spike to appear, at the very short ranges for $0 \leq \rho \leq 1$ targets due to the finite numerical aperture of the fibres. The lateral, y separation between the fibres also affects the range at which the spike would occur, with the larger y separations resulting in the spike taking place at a longer range. Linearity was obtained for the arrangement with $\rho = 1$, for a range starting around 12 mm up to the maximum range investigated, i.e. that of 100 mm. For the arrangement with $\rho = 0$, linearity was obtained from around 18 mm up to 100 mm.

Inequalities in the light signal directed towards each detecting fibre arise from the geometric arrangement of the fibres in the sensor head. The normalised relative intensity radiated towards the front detecting fibre is always smaller than that radiated towards the rear detecting fibre. The linearity of response of the sensor is affected at short ranges for all X_0 separations with the larger X_0 causing a larger non-linearity. As the range increases, however, non-linearity decreases.

Matt white paper was also used as target in the computer simulation and the slope of the responses was predicted to be close to $(1.385X_0)^{-1}$. Although this type of target has a fairly high reflectivity coefficient ($\rho = 0.82$) the beginning of the operational range (around 16 mm) was found to be closer to a very diffusive surfaced target rather than a very reflective one.

The behaviour of the sensor has been investigated in this chapter for operation under non ideal conditions. In order for the sensor to operate reliably care must be taken so that the signals have the lowest possible error on them. If a 0.1 % error exists on the signals then the choice of X_0 separation will affect the maximum operational range of the sensor, through scalability. Therefore, the larger X_0 separations will offer the longer operational ranges whose extend will also be a function of the type of target used with the 100 % diffusive targets offering twice as long a maximum range than the 100 % reflective targets do (for $X_0 = 1$ mm the operational range will be limited to 2.9 mm for $\rho = 1$ and 11 mm for $\rho = 0$, whereas for $X_0 = 5$ mm the operational range will be limited to 52.6 mm for $\rho = 1$, and 114 mm for $\rho = 0$). The scalability offered will only hold true if the various sources of noise are kept to the minimum level and there is adequate illumination from the source to keep high levels of signal to noise ratios over these long ranges. The separation (differentiation) between the detected signals also plays a very important role.

Offset voltage on, and mis-calibration of the detectors will again affect the sensor response. If these errors do not exist, the linearity of the sensor response will be around 0.8 % from a minimum range up to 100 mm. But in the case where offset voltages exist the medium and long ranges will be the ones affected most. The worst case for a given level of offset voltage will be if both detectors have offset voltages of opposite polarity, whereas the most favourable case will be if they both have offset voltage of the same polarity. In the case of mis-calibration the errors on the response will start showing from a fairly early range, increasing considerably as range increases.

X_0 separation variations shift up or down the linear part of the response without affecting its slope or its linearity only when a reflective target is used. They also shift the spike closer or further away at the low end of the range. Y separation variations affect the sensor response by shifting the spike closer or further away. An unequal y separation does not offer any improvements on the sensor performance.

The preceding analysis supports the view that the sensor can be made into a useful device if care is taken to minimise the effects that arise from the various imperfections mentioned above and this is further supported by the experimental work accomplished on the sensor during the course of this study and which is discussed in Chapter 7 (Sections 7.4 to 7.6). At worst and in the case where unknown unquantifiable factors may be present the sensor may still be useful, but its performance must be calibrated for the specific condition or application it is to be used in.

Chapter 6

Development of Sensor Head and Control Electronics

The development of the sensor head and control electronics are presented in this Chapter. Various sensor head jigs were developed for use with the sensor and the way by which they were developed will be explained along with the various changes which led to their final forms. A polishing jig was also developed to allow for properly polishing the end surfaces of the POFs which were to be used in the sensor head.

The control electronics involved in the development of the sensor are also presented. Various effects and shortcomings are described and reasons are given for the way they were tackled in order to develop the appropriate control circuitry for the sensor.

6.1. DEVELOPMENT OF THE SENSOR HEAD JIGS

The purpose of the sensor head jigs was to hold the three POFs in the required arrangement in front of the target. When designing the sensor head jigs various requirements had to be considered. The sensor head jigs had to be able to hold the three POFs parallel to each other and also be able to allow for the chosen X_0 separation to be arranged. The ends of the three POFs were allowed to protrude from the front end of each jig.

The first sensor head jig developed was cylindrical, as shown in Figure 6.1, and was made of black acrylic material. The three POFs would be positioned in the three holes of the jig and be kept in position, after setting the chosen X_0 separation, by three plastic screws.

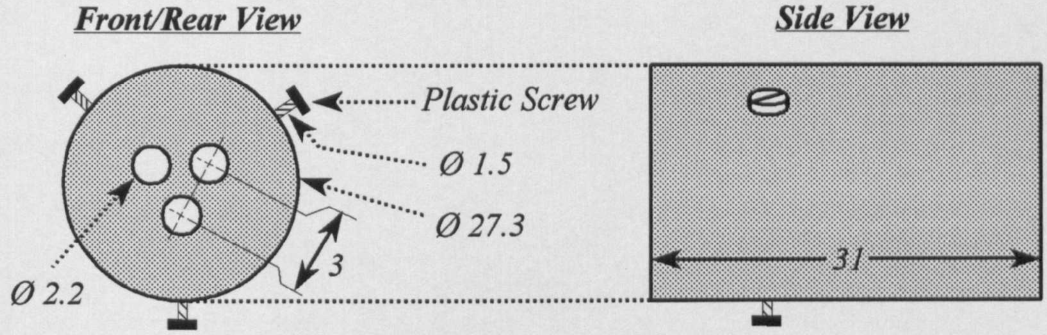

Fig. 6.1: The cylindrical fibre optic sensor head

Note: The dimensions shown in the above and in every following diagram are in millimetres unless stated differently.

This arrangement was preferred to the one where the three POFs would be positioned in the same plane since an arrangement with the two detecting fibres positioned close together would decrease the effect of any emission misalignments from the emitting fibre. But tightening the screws on the side of the POFs to secure them in place in the jig, although only finger tight, pressurized the fibres introducing microbends thus affecting their mode distribution. Consequently, the smoothness of the far field emission distribution of the emitting POF was also affected. This could clearly be observed with a naked eye when the emission was directed on a matt white paper. This problem was minimised (but not eliminated) by positioning small cylindrical rubber material of length 2 mm in between the screws and the fibres.

In order to overcome the problems caused by the structure of the cylindrical jig a new flat jig was developed where all three fibres were arranged to be positioned side by side, as shown in Figure 6.2. This change was done for two reasons. The first one was to bring the three POFs closer together since in this case a central body to push against it each fibre for individual positioning would not be necessary. By doing so the spike would also occur earlier in the range thus improving the linearity of the sensor at the shorter ranges. The other reason was to avoid the need for side screws to tighten the fibres in place. In this arrangement a flat surface would be used to keep the fibres in place applying pressure over a much larger area thus minimising the disturbance of the modal distribution in the fibres.

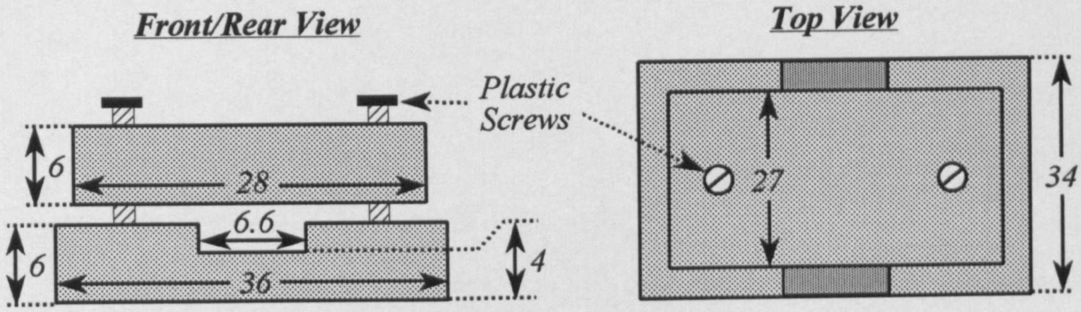

Fig. 6.2: The new sensor head

The flat jig, although better than the cylindrical one, had its own shortcomings. Each of the three POFs, all of which were positioned in a fixed area of 6.6 mm, would have to be supported by the neighbouring POF. In cases where the outer diameter of the POF varied by a few microns then the three POFs might be squeezed or in the worst case be loose in that area thus increasing the possibility of misalignments.

To overcome these uncertainties a new sensor head jig was developed which is shown in Figure 6.3. This new jig had three V-shaped grooves in which the three POFs would be positioned. The walls of the V-grooves would support the POFs independently, instead of relying on the neighbouring POF as done before. In this way better positioning of the fibres in the jig without increasing their separation was achieved thus avoiding possibilities of loose fibres in the jig which may result in angular misalignments. The front end of the jig was also shaped in a way that it would not directly reflect light back into the mirror thus avoiding another source of error.

In order to accommodate the needs for an increased y separation, when the sensor was to be used with diffuse reflective targets, a sensor head jig similar to that shown in Figure 6.3 was constructed but with 7 V-grooves instead of three, the outer V-groove pairs being at a distance of 3.34 mm and 4.6 mm from the middle V-groove.

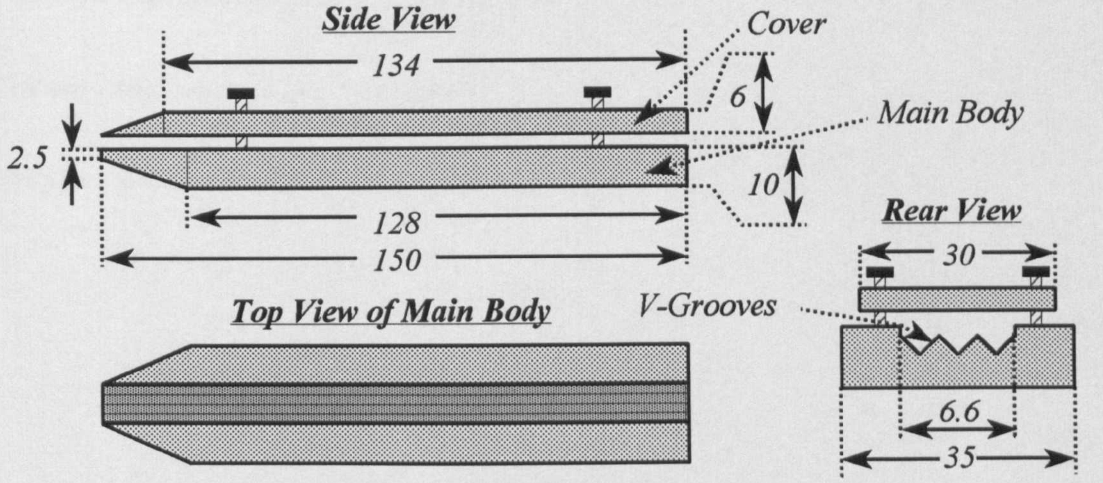

Fig. 6.3: The sensor head with the V-grooves

6.2. POLISHING JIG FOR THE PLASTIC OPTICAL FIBRES

When polishing the POFs to be used in the displacement sensor care was taken to make sure that the polished surface was perpendicular to the physical axis of the fibre, since this axis was the one that was used to align the fibres in the sensor head jigs. In doing so the optical axis of emission of the POF would be the same as its physical axis and so misalignments would be avoided. A perfect, perpendicularly polished POF would emit symmetrically around its optical and physical axes, as shown in Figure 6.4.a. A POF angularly polished would emit as shown in Figure 6.4.b.

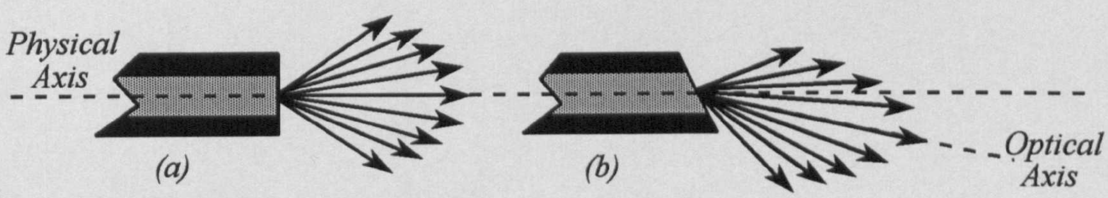

Fig. 6.4: The emission is affected by angular polishing of the POF

In order to achieve this desired state of polishing, the jig shown in Figure 6.5 was designed. It was made of PMMA (Polymethyl Methacrylate) material which is the same material as that of which the POFs used are made.

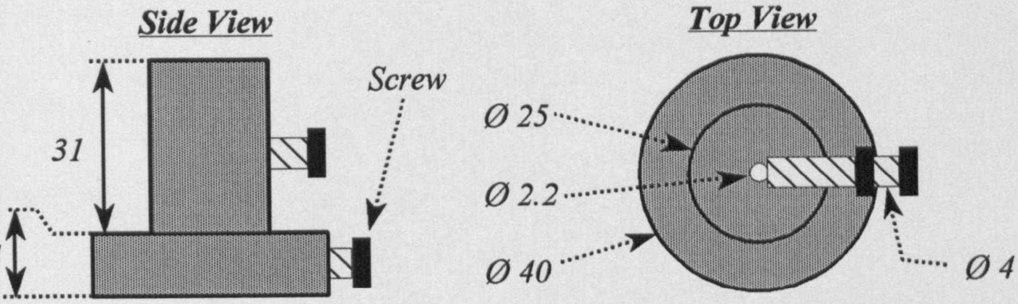

Fig. 6.5: The jig used to polish the POF

What influenced the choice of material was the fact that when a metal polishing jig was used metal material was removed from the jig whilst polishing and caused damage to the fibres by scratching them. By using a material which had the same characteristics as those of a POF, particles removed from the jig whilst polishing are of the same hardness as POF thus minimising the chances for scratching the POF surface .

The upper body of the polishing jig was made as long as possible so that it would keep the fibres perpendicular to the lapping film, thus assisting in achieving a high angular alignment finish. The screws were also made thicker than the POFs (they had a diameter of 4 mm) with a flat end surface so as when screwed on the fibres they would push against a larger area thus avoiding point pressure which could fracture the fibres.

Ideally, the hole through which the POF would have to be inserted and kept secure in the polishing jig should have the same inner diameter as the outer diameter of the POF which is 2.2 mm. In reality, however, the jig hole should have a slightly larger diameter for the POF to be able to slide in. The measured inner diameter of the jig hole was found to be ~ 2.22 mm, i.e. ~ 0.02 mm larger than the diameter of the POF. Considering the positioning of the screw nearer the polishing end of the jig then an angular misalignment of 0.23^0 is estimated. This figure may vary by the fact that the outer diameter of the POF itself may vary by a few microns. The softness of the jacket of the POF may also add to this figure. The angular misalignment quoted in Chapter 7.4 for the reflective target is very similar to the figure calculated here.

Polishing of the end surfaces of the POFs was performed manually with various grades of lapping film which varied from 600 μm down to 1 μm. The rough grade film was used first, and progressed towards the finer grades. A little water was put on each lapping film prior to polishing. A figure of 8 stroke was used whilst polishing, which lead to a smooth and uniform material removal operation, under light pressure. Rinsing with water and wiping off the polishing jig in between the different polishing stages, so as not to carry contamination from coarse to fine polishing steps, was essential. Moderate downward pressure was applied on the finest lapping films to overcome hydroplaning (jig sliding). Very good quality polishing was achieved in this way.

6.3. DEVELOPMENT OF CONTROL ELECTRONICS

The development of control electronics was a very important issue in the successful realization of the development of the displacement sensor. Electronic circuits had to be build which would drive the LED and amplify the signal detected by the photodiodes so that it can be adequately measured. The similarity in operation of the two detecting circuits was a very important parameter in the operation of the sensor. Identical performance of the two detecting circuits will ensure that the only difference in the two detected signals will be the distance between each detecting fibre and the target. Means to achieve such a behaviour were pursued to a great extend.

Initially, the simple circuits shown in Figure 6.6 were prepared on a printed circuit board (PCB). An LED with a broad emission pattern operating at 660 nm was used as the source (Appendix B2). The two detectors operated by measuring the voltage generated across the resistive loads connected in series with the reverse biased PIN photodiodes (Appendix B2). By applying a reverse biased voltage, i.e. operating in the photoconductive mode, the linearity of the photodiodes would be improved and a much larger load voltage ($V_{load} = I_{photo}\ R_{load}$) would be permissible before the junction potential was significantly reduced (Melles Griot, 1990). In a photoconductive mode linearity and dynamic range of the resistive load circuit could be extended for an output close to 30 % of the applied bias voltage. With no reverse bias and for the same circuit arrangement, the output signal is typically restricted to about 0.3 % of the output level achieved when bias voltage is applied.

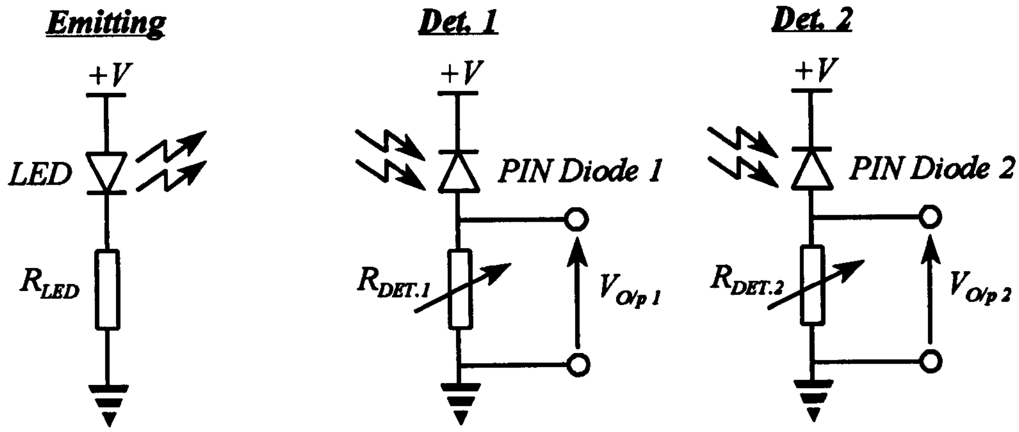

Fig. 6.6: The simple emitting and detecting circuits constructed for the sensor

The sensor was arranged to operate under dc conditions, i.e. with the LED always on. Necessary precautions had to be taken so that background illumination would not affect the measurements. These were achieved by positioning the sensor head and target in a dark area. This was an enclosed area of dimensions 1.75 m * 1.25 m * 1.5 m (l*w*h) where the sensor head and target were positioned prior to any measurements being taken. The output voltages across the load resistors of the PIN photodiodes were measured using two digital multimeters (DMMs) with a 3.5 digit display simultaneously so as to avoid possible errors to the measurements caused by the intensity variation of the LED if the output voltages were read one after the other from a single DMM.

In the attempts where a single meter was employed to measure the detected signals, the results were concluded unreliable. That is when an optical power meter, calibrated at 650 nm, was used to measure the two outputs one after the other, the sensor response was not very linear. It was observed that by simply disconnecting and reconnecting the same fibre on the power meter with no other changes taking place, the measured signal varied by up to 1 %. The FSMA type POF connectors used were of the screwing type and could not offer the exact repositioning of the fibre on the power meter photodiode every time this operation was performed. A keying connector could offer a better repeatability of connection but these were not available for use with POF when this work began.

The use of a lock-in amplifier to measure the intensity of ac detected signals one after the other from the detecting circuits and extract noise by using a narrow band pass filter did not prove a better arrangement. The long integration times that the lock-in amplifier needed to perform each measurement meant that over this long period (~1 minute) the source intensity could vary considerably.

Some precautions were taken before the start of the experimental work. These were:

- The two DMMs were tested for similarity in operation given the same voltage input;
- Stable power supplies were used to bias the detecting circuits (0.1 % stability);
- The circuits were positioned in an EMI shielded box to avoid interference;
- The resistors used in the circuit were chosen to have a good temperature coefficient ($\pm$ 100 ppm/^{0}C).

The present simple detecting circuits were built to test whether linearity of response over a minimum operational range could be obtained before more sophisticated detecting circuits employing precision opamps were to be constructed. These achieved to do so (see Chapter 7.2).

But changes in the detecting circuits were necessary in order to improve the performance of the sensor (see Chapter 7.2). The present detecting circuits did not offer offset adjust facilities and when large value load resistors were used to amplify the detected signal non-linearity effects occurred when the voltage drop across the load resistors exceeded 30 % of the bias voltage. Also, due to the way the detecting circuits were configured (photoconductive mode) the shot noise was more pronounced due to the increased dark current with a consequent reduction in detectivity (Melles Griot, 1990).

Examination of the I - V characteristics of a PIN photodiode (Figure 6.7) shows that true linear response can be obtained by holding the photodiode at zero bias. If an effective short circuit to the load of the photodiode is provided, a load voltage will not develop and the junction of the photodiode will not become forward biased. An operational amplifier circuit, in a transimpedance configuration (Melles Griot, 1990) can hold the photodiode at zero bias and thus generate a load voltage equivalent to a high resistive load voltage. Its output voltage is also proportional to the photocurrent flowing from the photodiode. Linearity is also increased since the circuit maintains a constant voltage across the photodiode junction.

True linear response can also be obtained by operating the photodiode reverse biased. If a reverse bias is applied on the PIN photodiode the transimpedance amplifier will hold the photodiode at a constant reverse bias instead of zero bias. The reverse bias will enhance the speed of response of the photodiode and will further increase its linearity of response but will also increase its dark current.

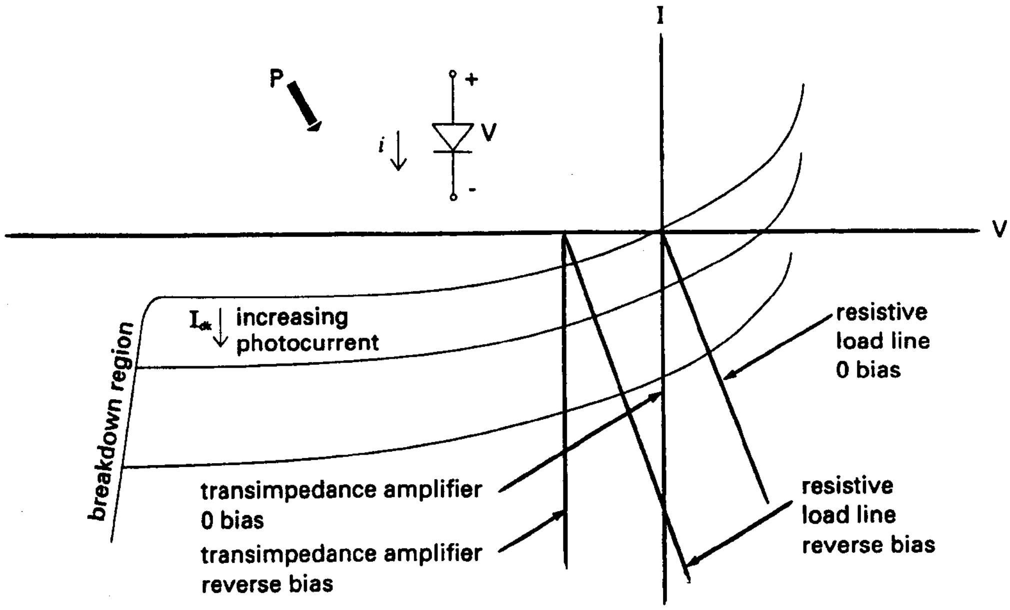

Fig. 6.7: Photodiode I - V characteristics with load line (Melles Griot, 1990)

In a detecting circuit with a transimpedance configuration (whether reverse or no bias) the linearity (and hence dynamic range) of the circuit could extend with an output up to 60 % of the supply voltage of the opamps.

For the reasons above it was decided to use a new circuit employing opamps in a transimpedance configuration (Figure 6.8) and the PIN diodes operating with no bias. Operating with reverse bias would increase the dark current of the photodiodes which is not desirable. The enhancement in speed response of the detector is not essential since the detecting circuits operate under dc conditions.

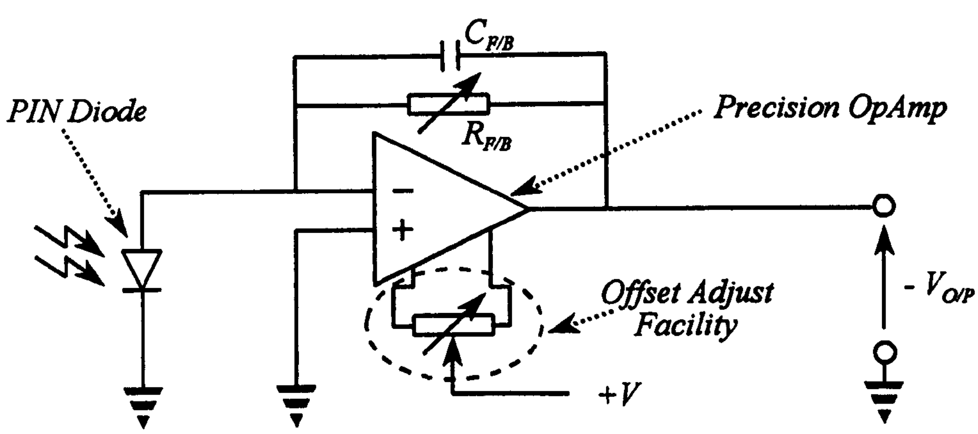

Fig. 6.8: The new detecting circuits in a transimpedance configuration with no bias

The opamp chosen for the circuit was the OP97FP (Precision Monolithics Inc.). This is a precision opamp featuring very low input offset voltage of 30 μV at 25 ^{0}C and very good average temperature coefficient of offset voltage of 0.3 μV/^{0}C.

The feedback capacitors ($C_{F/B}$) chosen were polystyrene for high stability to avoid leakage which could cause drifting effects. Decoupling capacitors (1 μF solid tantalum) were also used at the supplies.

Apart from building a new circuit the components that were to be used in this circuit were tested for similarity in operation under identical conditions. The opamps operated similarly (0.8 %), the POFs transmitted similarly (0.5 %), but the PIN photodiodes did not operate similarly (15 % difference in responsivity). Thus new ones with similar responsivity were obtained (0.8 %) and they were used in the circuit, although tests performed with PIN photodiodes with different responsivities suggested that this is not an important requirement in the successful operation of the sensor.

The offset voltage due to the dark current of the circuit was tested by monitoring the output of the two circuits simultaneously without any illumination on the photodiodes. Over a period of 40 hours the two circuits drifted slowly by a maximum of 0.5 mV, both in the same direction simultaneously, showing the temperature dependance of the photodiodes dark current and of the opamps offset voltage.

New 4.5 digit DMMs were also employed which offered higher accuracy than the previously used 3.5 digit ones. They were also checked for similarity in operation given the same voltage input and were found to be very close (< 0.05 %) over an input voltage range which varied between 10 V and 0.1 mV, a dynamic range of 100 dB (electrical).

The emitting circuit which remained the same as before (Figure 6.7) was positioned in an EMI shielded box on its own. The new detecting circuits were positioned in another EMI shielded box in order to avoid any unwanted effects from the operation of the LED which might cause temperature increase and probably drift effects. This step was taken as a preventative measure.

From tests performed, this opamp/PIN photodiode combination was concluded not to be a good choice for this sensor. The detected signals seemed to drift when the temperature rose, or even when it did not. Better electronic components therefore, especially opamps, had to be used if the sensor were to become a useful device.

A search for a better opamp to be used in the sensor detection circuit under dc conditions led to the decision to use chopper stabilized opamps. These opamps operate by separating the ac and dc components of the input signal, amplifying each component separately and then combining the two amplified components thus achieving the best possible stability of operation. The chopper stabilized opamp chosen was the MAX430CPA (MAXIM). It features an input offset voltage of 1 μV at 25 °C and average temperature coefficient of input offset voltage of 0.02 μV/°C.

The PIN photodiodes used so far had an effective active area of 1 mm^2. The POFs have a core diameter of nearly 1 mm and a numerical aperture of 0.46. A certain amount of light is expected to be lost due to the small separation between the POFs and the active element of the photodiodes (~ 0.5 mm). So PIN photodiodes with larger effective active area (13 mm^2) were used to enable a more efficient collection of the received light from the receiving POFs. These were the Hamamatsu S1336-44BQ (Appendix B3).

Another effect that was cured by using these larger effective active area photodiodes was that when the POFs were moving/swinging the intensity level of the light detected seemed to vary slightly. This effect was caused by the variation of the modal distribution on exit from the POF towards the active element of the photodiode when not all the light exiting the fibre was collected from the photodiode.

The two detectors were checked for linearity and similarity in their operation by comparing them with a linear reference. This was provided by an optical power meter (Photom 225) whose specifications quote linearity over a dynamic range of 60 dB (optical). The two detecting circuits were found to operate very similarly with a percentage deviation from the reference of less than 0.125 % over an operational range of 25 dB (optical).

Also, the detecting circuits were tested for possibilities of drift by connecting them to the outputs of a 1 X 2 coupler which was used to connect them to an LED. The intensity of the LED was arranged so as the two detecting circuits were reading a voltage value around 150 mV and was kept operating under these conditions for a period of five hours during which readings were taken approximately every five minutes. The two signals and their ratio were plotted against time, as shown in Figure 6.9.

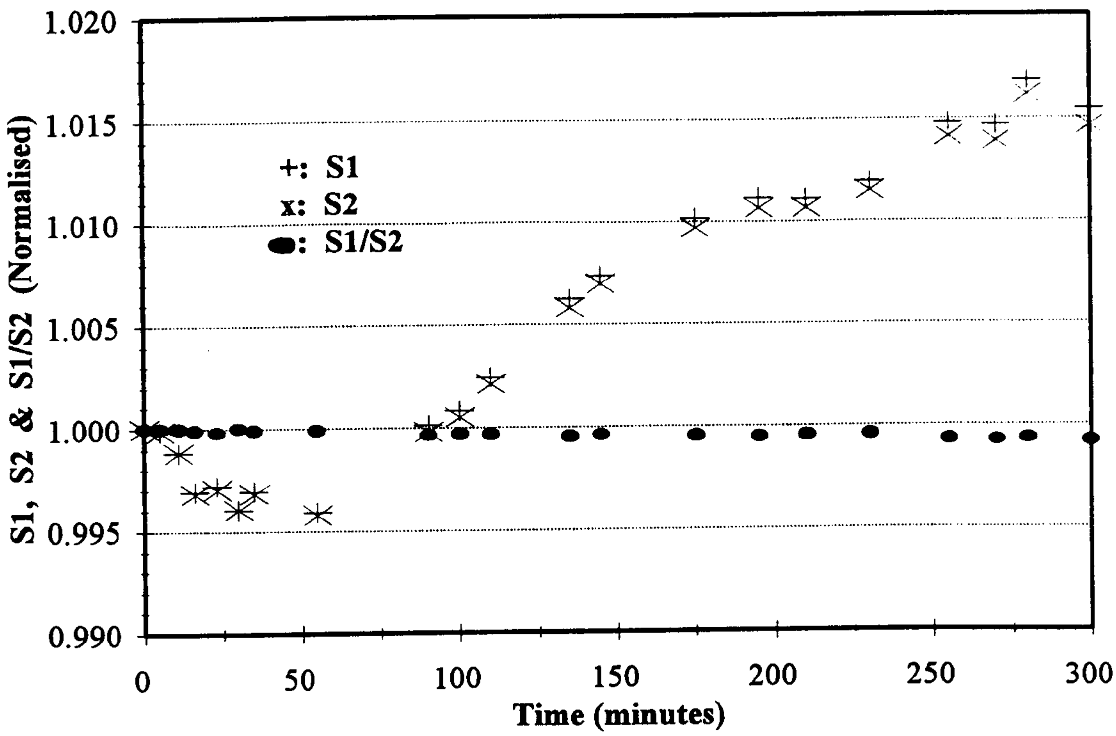

Fig. 6.9: Continuous measurement at a fixed range for the MAX430CPA

During this period, the readings of the two detectors varied by 2.5 %. But the variation occurred at both detectors, simultaneously and in the same direction. Therefore, this variation is attributed to the intensity variation of the LED. By looking at the ratio of the two signals where a true indication of any detector circuit drift would show, the relative drift was less than 0.08 % over these 5 hours suggesting very stable circuitry. In cases where the relative drift between the two detecting circuits is large then the performance of the sensor will be affected.

In search for improvements to the detecting circuit it was concluded that for the best possible similarity between opamps these should be on the same IC, i.e. "dual" opamps. The possibility of two single opamps behaving similarly is greatly enhanced if they are produced in the same production line and under the same conditions. In addition, better temperature behaviour would be expected due to uniformity of the immediate environment.

Dual chopper stabilized opamps are the LTC1051CN8 (Linear Technology) which also offer even better performance than the MAX430CPA type. These opamps have input offset voltage of 0.5 μV and input offset voltage drift coefficient of 0.01 μV/^{0}C but do not offer offset adjust facilities. These were provided in the new circuit by adding the AD586JN opamps (Analog Devices), which are precision voltage references, with external resistors arranged in a voltage divider configuration for a variable output. Connection of this voltage reference signal to the positive input of the dual chopper stabilized opamp would offer offset voltage cancellation. The LTC1051CN8 was also tested for the usual linearity and drift and showed similar results to those of the MAX430CPA.

The development of the electronic circuitry was an important area in the proper operation of the sensor. Simple detecting circuits in a photoconductive mode gave an indication (see Chapter 7.2) of the potential of the sensor (operational range of 18 mm). Improvements in the detecting circuits resulted in better performance (operational range of 75 mm). But overall the performance of the sensor is expected to be limited not only by the level of attainable similarity in the operation of the two detecting circuits but on tolerances in the arrangement of the optics involved in the sensing area as well.

6.4. EFFECT OF ACCURACY OF THE MEASURING INSTRUMENTS

The maximum operational range and resolution of the sensor will be determined by the ability of the processing electronics to discern changes in the signals detected by the two detecting circuits. This will also be dependent on the amplitude of the individual signals and on the difference between them.

Initial experimental work was to be performed with two digital multimeters (DMMs) measuring the output voltage from each detector. Three possible cases have been considered. A 3.5 digit DMM offering a maximum resolution for each scale of 0.05 %, a 4.5 digit DMM offering a resolution of 0.005 % and a 5.5 digit DMM offering a 0.0005 % resolution. The transfer function (eq. 5.6) is plotted in Figure 6.10 for a target with $\rho = 1$ after the computed signals have been treated to the resolution limits of each DMM by rounding the appropriate decimal points on the computed signals for each case. For clarification reasons the response of the 4.5 and 5.5 digit DMMs were plotted with a constant offset (different for each case) so as not to overlap on each other.

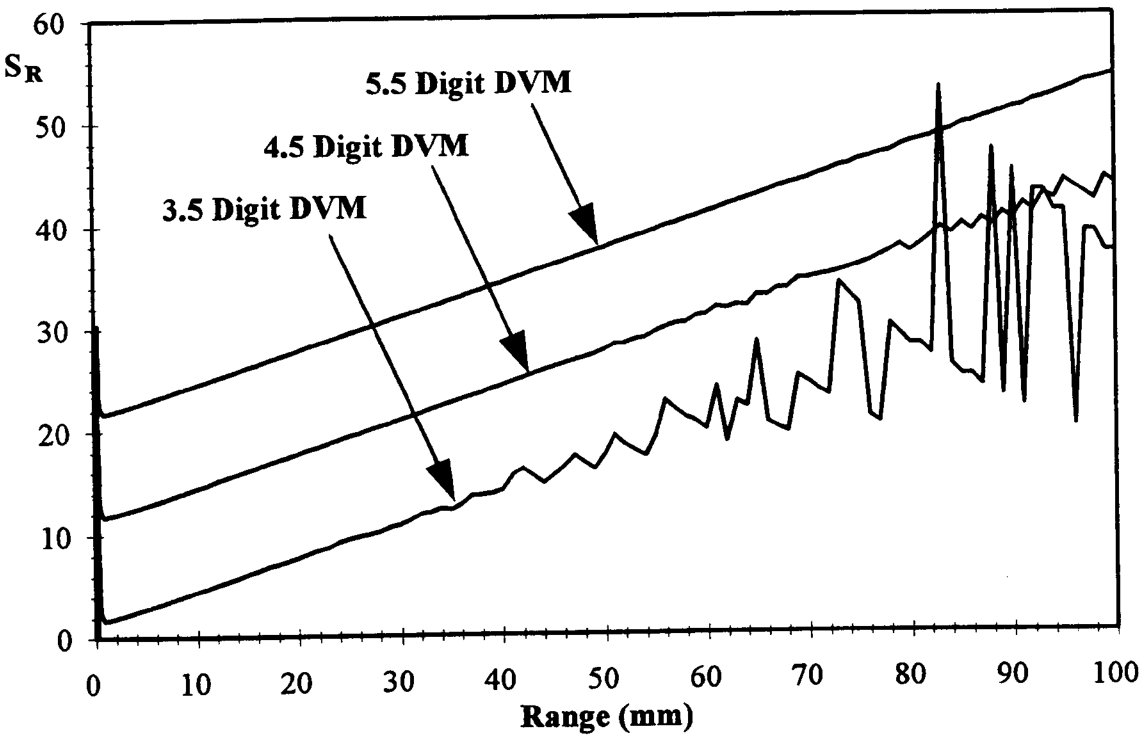

Fig. 6.10: The resolution of a DMM affects the response of the sensor (ρ = 1)

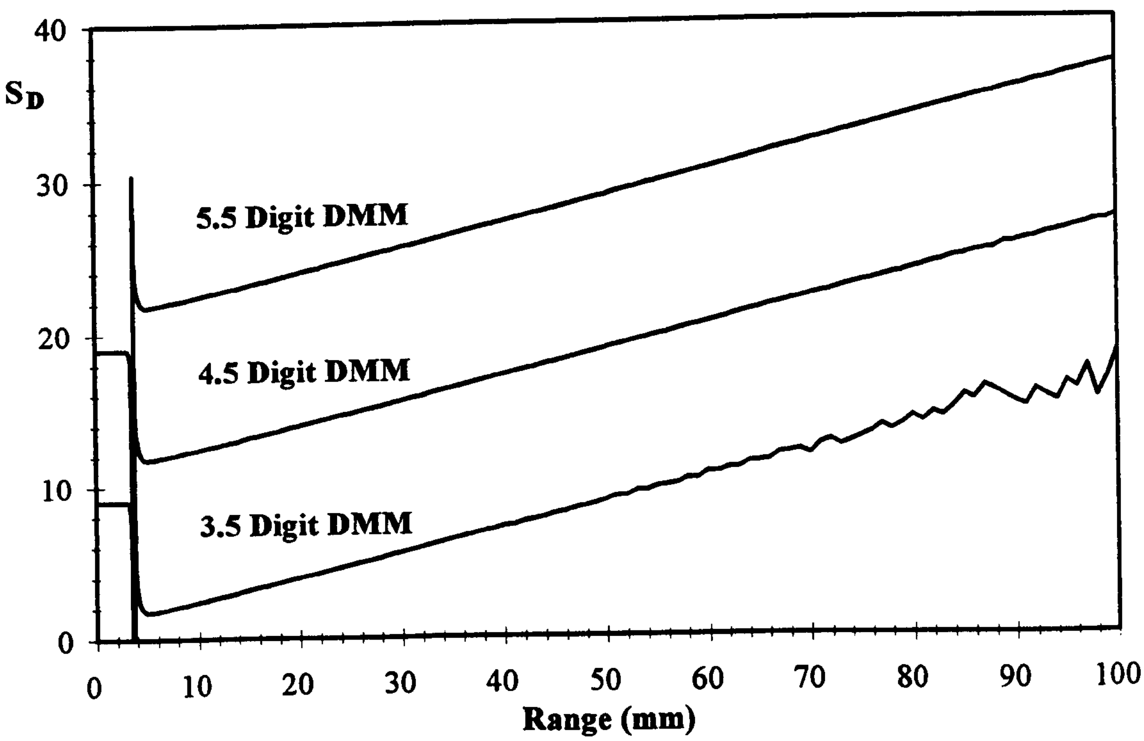

Fig. 6.11: The resolution of a DMM affects the sensor response (ρ = 0)

From Figure 6.10 it can be seen that the 3.5 digit DMM offers the lowest resolution and also limits the range since at long ranges it cannot discern small changes in the detected signals. The 5.5 digit DMM offers the best resolution leaving the S_R response unaffected even at R = 100 mm. The 5.5 digit DMMs seem to be the right measuring instrument to use although its usefulness will depend on the noise level of the detected signals.

When a target with $\rho = 0$ is to be used (Figure 6.11), the DMMs are expected to result in a longer linear operational range due to the fact that the two signals have a larger difference between them than the ones from the arrangement with a target with $\rho = 1$. Here, the lower resolution DMMs are still useful with a $\rho = 0$ target. For the maximum range of 100 mm there seems to be no difference between the 4.5 and the 5.5 digit DMMs. The 3.5 digit DMM seems to perform as well as the 4.5 digit DMM does for the $\rho = 1$ target.

Table 6.1 summarises the maximum range achievable by each DMM with regards to the two targets considered. It is clear that when a target with $\rho = 0$ is used due to the largest separation between the two detected signals it achieves longer operational ranges when compared with the arrangement with a target with $\rho = 1$ for the same DMM.

Table 6.1: The maximum range achievable by each DMM for two targets

DMM Digits	Accuracy (%)	$\rho = 1$ (mm)	$\rho = 0$ (mm)
3.5	0.05	35	50
4.5	0.005	50	100
5.5	0.0005	100	100

6.5. OPERATION OF THE CONTROL ELECTRONICS UNDER ac CONDITIONS

Operation of the control electronics under ac conditions would enable the sensor to operate under ambient illumination. This is an important requirement for the success of the sensor. In its present form where the sensor operates under dc conditions the sensor could perform displacement measurements accurately over long ranges (see Chapter 7.2) but maintaining its linearity of response is dependent on operation under dark room conditions (see Figure 7.41).

In an attempt to desensitize the sensor from the effects of ambient illumination the emitting and detecting circuits were modified to operate under ac conditions. The modifications consisted of modulating the LED using square pulses of 7.5 kHz and including a passive RC High Pass Filter (HPF) in the detecting circuits to remove the dc component due to ambient illumination. The outputs from the two detecting circuits would still be connected to the two 4.5 digit DMMs. The new circuit is shown in Figure 6.12.

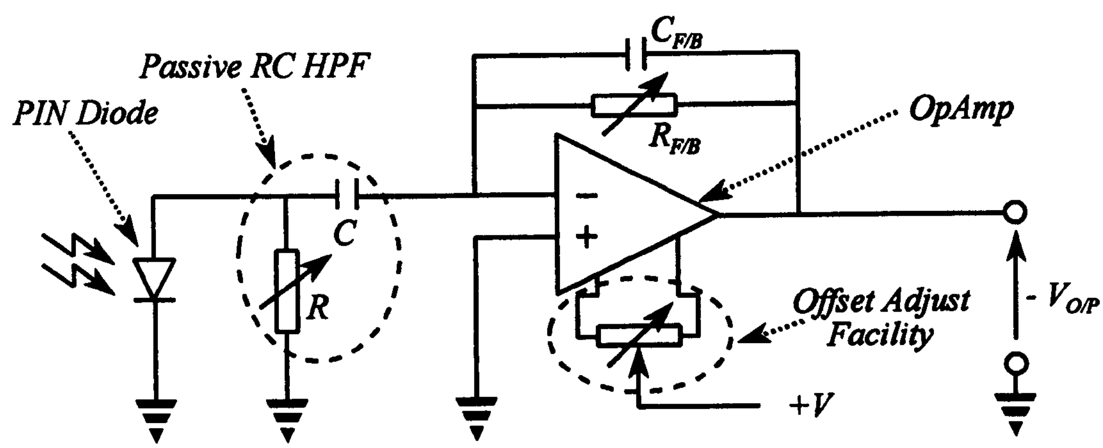

Fig. 6.12: The new detecting circuit operating under ac conditions

The values chosen for the components of the filter were a 1 μF polyester capacitor and a 2 kΩ variable resistor to allow for variation of the filtering which would affect the shape of the detected pulse. The cut-off frequency of the filter was ~ 100 Hz.

Once the detecting circuits were modified they were tested for rejection of the ambient illumination by pointing the ends of the detecting POFs towards various sources of illumination such as desk lamps, fluorescent tubes and sunlight and also under dark room conditions. No change in the level of the detected signals was observed although sudden changes (above 100 Hz) did affect the detected signals.

A look at the component specifications used so far revealed that the chopper stabilized opamps were not meant to operate under ac conditions due to their internal structure. Their low internal clock frequency (2.6 kHz) in conjunction with the level of closed loop gain would result in alias signals occurring on the output signal once the frequency of the input signal exceeded 750 Hz. Another effect observed with the chopper stabilized opamps was that when the closed loop gain was higher than - 10, spikes would appear at the output signal as shown in Figure 6.13. These spikes are caused by charge injection occurring during the sampling and holding of the opamps input offset voltage. These spikes are centred at 0 V level and although they do not add to the output offset voltage would affect the sampling of the output signal once ADCs are used.

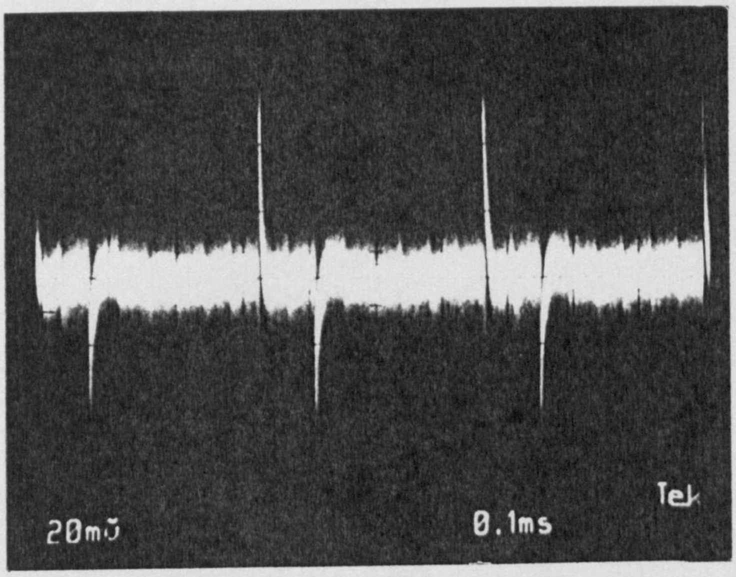

Fig. 6.13: Spikes caused on the output signal when the closed loop gain exceeds - 10

A search for a new opamp to use in the sensor detection circuit under ac conditions led to the decision to use the TLE 2037 opamps (Texas Instruments). These are low-noise, high-speed, precision, decompensated opamps which offer very good ac performance and dc precision although not as good as the ones offered by the chopper stabilized opamps. They feature an input offset voltage of 25 μV at 25 ^{0}C and average temperature coefficient of input offset voltage of 1 μV/^{0}C. They have a Gain-Bandwidth-Product of 50 MHz which will result in adequate amplification of the signals detected by using only one amplification stage thus minimising the built up of noise due to the otherwise necessary subsequent amplification stages.

Operating the control electronics under ac conditions will enable the operation of the sensor under ambient illumination. The use of a HPF will block the low frequency variation of background illumination but will allow for the detection of the higher frequency pulses of light modulated by the LED. The TLE2037 opamps will enable high amplification levels of the detected signals from only one amplification stage keeping noise levels low.

6.6. AUTOMATION OF THE CONTROL ELECTRONICS

An important area which needed to be addressed was the recording and analysis of the obtained data which at the present stage was performed manually. This was adequate for the purposes of investigation of the validity of the sensor for static displacement measurements under laboratory conditions. In view of the fact that at a later stage in the sensor development the measurement of dynamic variables such as vibration (see Chapter 8) would be necessary, automation of the sensor was an important requirement. This was achieved by connecting the detecting circuits via Analogue to Digital Converters (ADCs) and the emitting circuit via an Input/Output (I/O) card to a Personal Computer (PC), as shown in Figure 6.14, and controlling these using software. Experimental results for static displacement measurements using the ADC's are presented in Chapter 7.7.

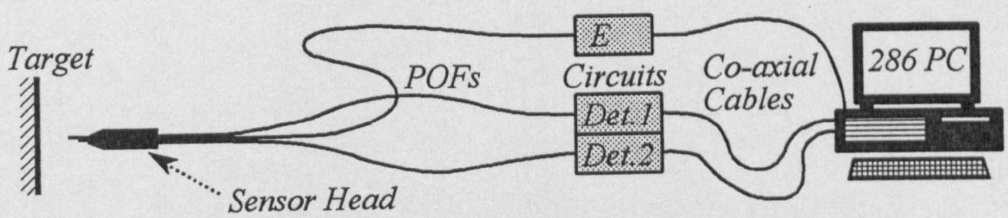

Fig. 6.14: The automated sensor

In doing so the first task was to determine what number of bits on the ADCs would be necessary for the operation of the sensor. ADC's with 8-, 10- and 12-bits were considered and analysis was performed on how they would affect the sensor response using experimental data obtained with the 4.5 digit DMMs. As an example, the calibration curve of an experimental run with X_0 = 5 mm, y = 2.2 mm and a mirror target is:

$$S_R = (0.193\pm0.001)R + (1.426\pm0.08) \qquad \textbf{Eq. (6.1)}$$

Figure 6.15 shows the above calibration curve and how it would be affected if the two detected signals were read by a pair of ADCs of 8-, 10- or 12-bits. Each resulting S_R response is shifted upwards by a constant for clarity.

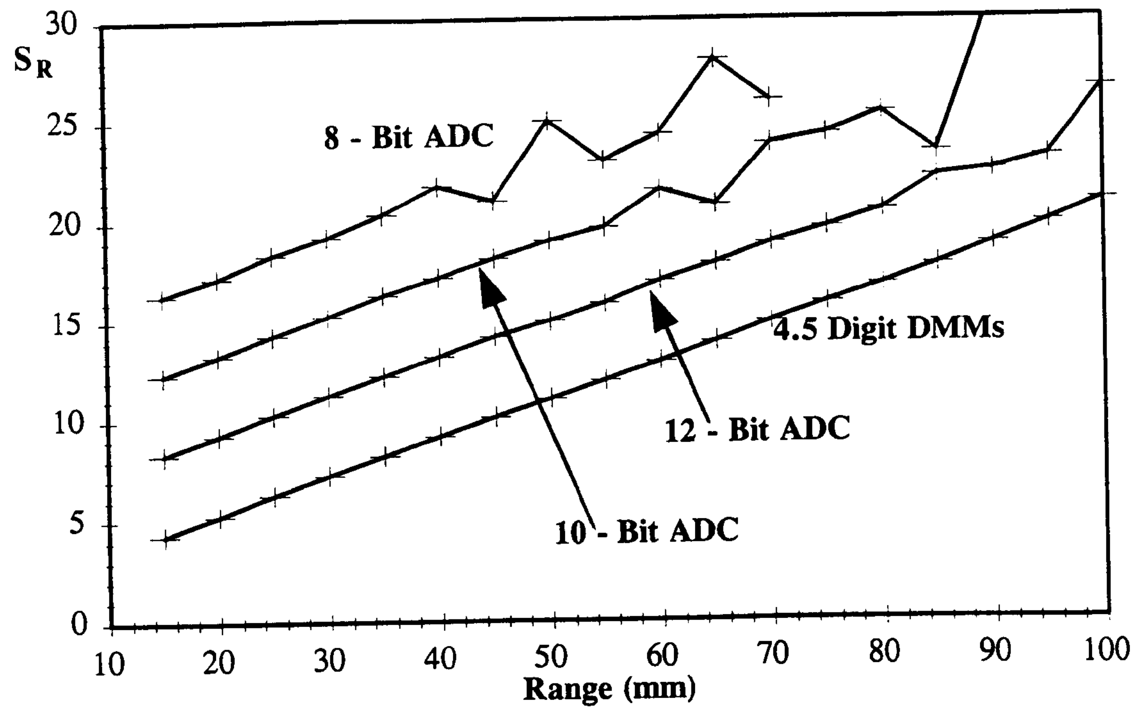

Fig. 6.15: The effect of the ADC bits on the experimental run obtained using DMMs (S_R values with 8-, 10- and 12-bit ADCs are shifted for clarity)

It is obvious from what is shown in Figure 6.15 that a pair of 12-bit ADCs would be the best option. Although these will not be able to identically reproduce the response obtained using the 4.5 digit DMMs at longer ranges due to quantisation noise effects, they seem to offer adequate resolution to reproduce a result which is very close to the one obtained by the DMMs. The operational range and accuracy achieved by the application of each pair of ADCs compared to those obtained with the DMMs is shown in Table 6.2.

Table 6.2: Effects of the measuring instrument on the response of the sensor

Measuring Instrument	Operational Range (mm)	Accuracy (%)
4.5 digit DMMs	15 - 100	1.0
12-bit ADCs	15 - 80	1.7
10-bit ADCs	15 - 50	1.7
8-bit ADCs	15 - 35	2.0

An existing design layout of a 12-bit ADC card was reproduced twice for the two detectors. The ADCs used were the 12-bit AD 7572 (Analog Devices) with 10 μs conversion time interfaced with the AD 585 (Analog Devices) sample and hold opamp as shown in Figure 6.16. The reason for reproducing an existing design and not create a new one tailor-made for this sensor was to avoid the time consuming procedure of designing, building and troubleshooting that a new design would necessitate.

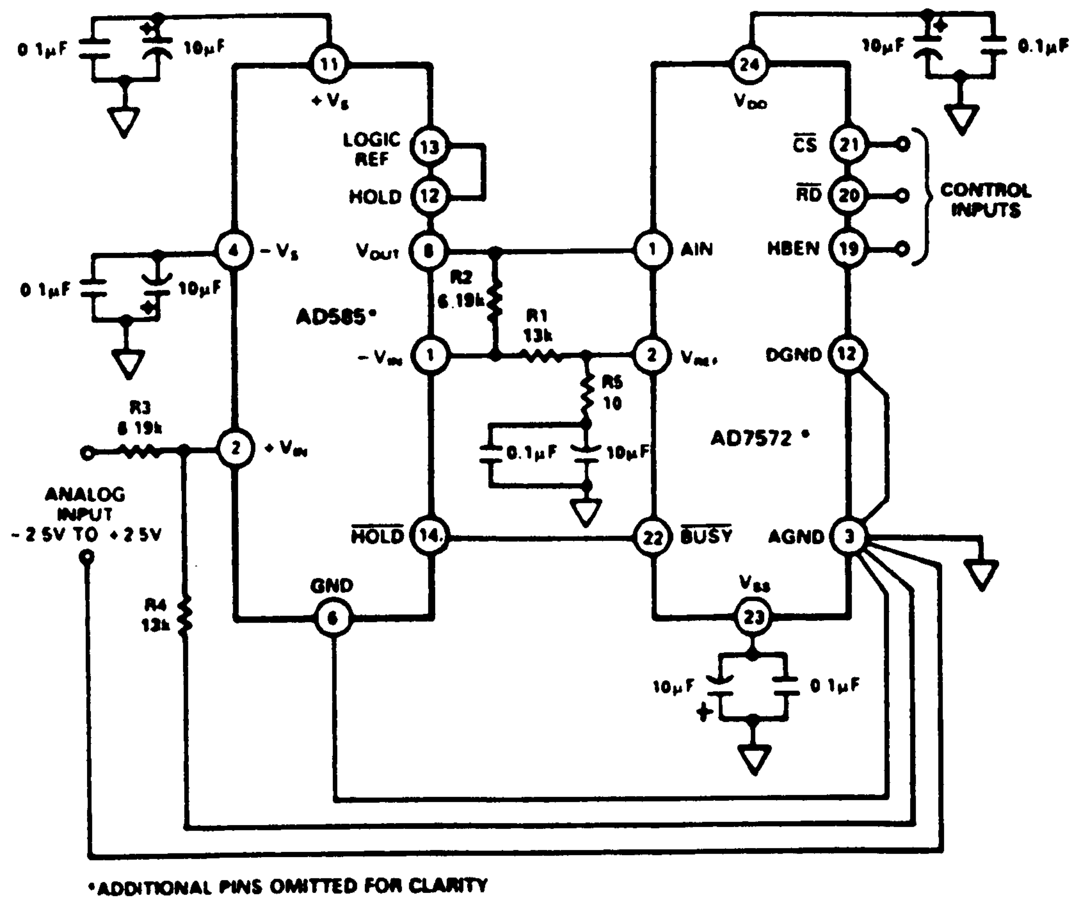

Fig. 6.16: The AD 7572 - AD 585 interface

Once the two ADC cards had been built they were positioned in a 10 MHz 286 PC which was considered adequate for this purpose. They were tested with a very simple program written in Turbo C by connecting them to a power supply whose output was varied between - 2.5 V and + 2.5 V in order to ascertain the similarity between the two ADC cards. They indeed read their input over that range very closely with a maximum difference of only one or two levels between them. The ADC cards had facilities to allow for the shifting of their Full Scale Reading (FSR) between ground and +5 V, -5 V and ground or -2.5 V and +2.5V or indeed any intermediate value which would comply to an FSR of 5 V.

Following, the emitting circuit was arranged to operate at a frequency of 8 kHz (pulses) driven from the I/O card in the PC which was controlled by the program of

Appendix A2. The unipolar pulses that were detected were passed through the HPF (see Figure 6.12) and at the outputs of the detecting circuits appeared as bipolar with any effects from ambient illumination rejected.

The program was arranged so as to switch the LED on, read the ADC connected to detector 1 (ADCS1), then read the ADC connected to detector 2 (ADCS2), switch off the LED, read the ADCS1, read the ADCS2 and then repeat this sequence as many times as required (adjustable), as shown in the timing diagram of Figure 6.17.

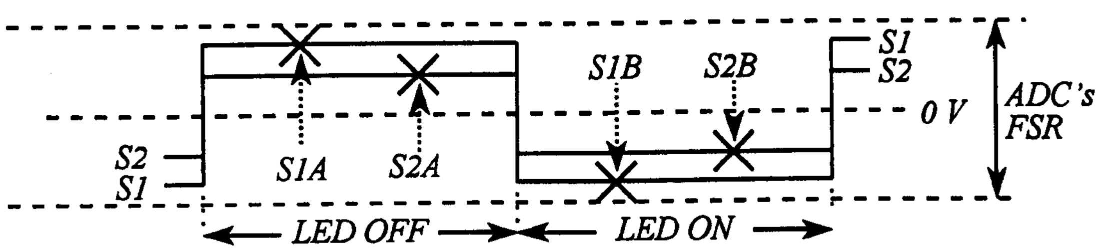

Fig. 6.17: The timing diagram for the ADC sampling

The reason for reading the signals when the LED is off (S1A and S2A) as well as when it is on (S1B and S2B) was to reduce any effects of offset voltage and obtain the peak-to-peak values of each detected signal and the difference between them, i.e.:

$$S1 = S1A - S1B \qquad S2 = S2A - S2B \qquad \textbf{Eq. (6.2)}$$

The above approach, however, resulted in excessive errors primarily due to the fact that in order to obtain S1 and S2, two measurements were required which resulted in the error involved increasing considerably. Experimental runs with this attempt for static displacement measurements resulted in errors in the range of 50 %. Another reason for the high levels of errors involved was the noise of the ADC and sample and hold opamp.

In an attempt to correct this problem, the FSR of the ADCs was arranged to start from - 2.5 V and finish at 2.5 V and each signal was read only once, i.e. at S1A and S2A, which resulted in the errors shown in Figure 7.44.

When vibration measurements were performed, the FSR of the ADCs was arranged to start at - 6 V and finish at - 1 V. In this case the signals were read at S1B and S2B. This arrangement enabled the signals to be read very close to the FSR of the ADCs which would result in the largest difference between the two detected signals.

6.7. CALIBRATION OF THE TWO DETECTING CIRCUITS

Calibration of the two detecting circuits will result in the same signal output from them if the same level of light is incident on the two photodiodes. Calibration was to be performed by varying the variable resistor of one of the two detecting circuits in order to equalise the voltage read by the other detector when the same light radiant intensity was incident on both photodiodes.

Various calibration methods were tried in order to establish the repeatability of the sensor performance. Initially a plane surface with a V-groove was used. The two detecting POFs (one at a time) were positioned in the V-groove facing and coming in contact with the emitting POF (coupled to an LED) and were secured in place. But after calibration was performed repositioning of the first POF in the V-groove did not reproduce the initial reading. Reasons for this were attributed to possible variations in the thickness of the jacket of the POF and the level of pressure applied on the POF tips in order to secure them in place. There could also be axial, longitudinal or even angular misalignments. The mode distribution of the fibres could also have been affected by the pressure applied on the fibre causing more uncertainties. In addition, the source intensity variations could also give rise to additional uncertainties.

In another arrangement a tungsten filament lamp emitting white light was used for the calibration of the two detectors. In this case the two detecting fibres were positioned equidistantly (various ranges) from the lamp and calibration was performed. But again linearity of response for the sensor was not obtained. A probable reason is the fact that calibration was performed over a very broad wavelength band. The photodetectors' responsivity curves over this wavelength band is very likely not to be identical thus resulting in significant differences over the much narrower LED spectral width used for the sensor. The LED used has typically a spectral width of ~ 40 nm around 660 nm. Equalisation of the detectors over this narrower wavelength band is therefore unlikely to have been achieved with this method.

Various other methods were also employed such as the use of narrow band interference filters (633 nm) or neutral density filters with the tungsten filament lamp, diffusers and/or lenses with 650 nm laser collimated beams, bundles of red LEDs with broad emission pattern, even the use of sunlight. They all proved unreliable for the calibration of the two detectors.

Of all the methods attempted the most satisfactory proved to be the one using the LED of the sensor. In this case it is believed that since one uses the actual sensor LED differences in the responsivity of the two detectors are restricted to a much narrower spectral band when balancing the detector outputs.

Also, another method resulted in satisfactory sensor calibration. Here, the theoretical S response was used as a guideline. In order to calibrate, the three POFs were arranged with a particular X_0 separation and the sensor head was positioned in front of the mirror at a certain range. By using the reading from one of the two detectors and from the expected theoretical value of S for this X_0 separation, at that particular range, the value of the other detector could be extrapolated. Consider the transfer function of the sensor:

$$S = \frac{(S1 + S2)}{(S1 - S2)} \qquad \text{Eq. (6.3)}$$

which can be rearranged to be:

$$S1 = S2\,\frac{(S + 1)}{(S - 1)} \qquad \text{Eq. (6.4)}$$

Thus, for any particular range the value of the feedback resistor ($R_{F/B}$) of detector 1 could be varied so that S1 becomes the value given by equation 6.4. Similarly, S2 could be varied if necessary to a particular value.

With this calibration method it was thought important to calibrate at a range where the DMMs are most sensitive (the DMMs used could show tens of microvolts). The reason for this is the fact that the sensor is very sensitive to the presence of small offset voltages and mis-calibration effects should show immediately at long ranges. Ideally, calibration should be performed very close to the end of the proposed operational range. Calibration with this method could also be performed at close ranges where a stronger signal is present if only the DMMs could show their last digit which would be critical at long ranges.

Various assumptions were made with this calibration method. It was assumed that the mirror was 100 % reflective, that there were no emission misalignments originating either from the emitting POF or from the target (see Chapter 7.1 and Figure 7.5) and that the X_0 and y separations were the ideal for this particular sensor head arrangement.

Always, before calibration was performed the offset adjust facilities of the opamps were used to minimise the offset readings of the detecting circuits under dark conditions. The offset voltage could be lowered down to approximately 20 μV for the detecting circuits using chopper stabilized opamps (Section 6.3).

Calibration of the two detectors was a very important area in the operation of the sensor. If the two detectors were calibrated identically then the only difference that would exist between the two detected signals would be the one resulting from the distance between the target and each of the two detecting fibres. The best calibration method was the one employing the LED of the sensor since the differences in the responsivity of the two detectors are restricted to a much narrower spectral band when balancing the two detector outputs.

6.8. SUMMARY AND CONCLUSIONS

The development of the sensor head and polishing jigs and control electronics were presented in this Chapter.

The sensor head jigs developed were a cylindrical, a flat one and one which incorporated V-grooves. The last one was preferred since the three fibres would be positioned in the V-grooves and would be supported individually by their walls. They would also be held in place with a large flat cover which would spread the pressure exerted on the fibres over a large area thus minimising effects of modal disturbance.

The control electronics were initially built to operate under dc conditions. This resulted in them operating properly only under dark room conditions. Various improvements in the detecting circuits were achieved by using opamps in a transimpedance configuration. These opamps were chosen to have very low noise figure.

In order to enable the operation of the sensor under ambient illumination conditions the emitting and detecting circuits were modified to operate under ac conditions by modulating the LED using pulses and including a HPF with a cut off frequency ~ 100 Hz in the detecting circuit in order to remove the dc component due to ambient illumination.

The DMMs were tested for accuracy and the 5.5 digit DMM was the best choice for a target with $\rho = 1$ whereas for a target with $\rho = 0$ a 4.5 digit DMM would be adequate.

Automation of the sensor was achieved by connecting the emitting circuit, via an Input/Output card, and detecting circuits, via 12-bit Analogue to Digital Converters, to a PC. Software written in TurboC would control the operation of the sensor.

Calibration was also considered and the best method for calibrating the two detecting circuits was the one which employed the LED of the sensor. Here, the differences in responsivity of the two detectors are restricted to a much narrower spectral band when balancing the detector outputs.

Chapter 7

Experimental Work on the Proposed Displacement Sensor

The experimental work in this chapter, aims to show/prove that the theoretical predictions presented in Chapter 5 hold and to further investigate possible effects that are suggested by the experimental results. Various problems and undesired effects which have risen from the experimental work, and methods employed to tackle them and improve the sensor performance are also being presented. These problems relate to calibration accuracy, symmetry in the emission distribution around the fibre axis and target alignment tolerances. A sensor head arrangement employing seven POFs is also considered aiming for improvement in linearity of response.

Initial experimental work was performed under dark room conditions. Following, the sensor was converted to operate under ambient illumination conditions. Finally, operation under automated conditions was attempted by connecting the emitting and detecting circuits to a PC. The targets used were a mirror and then matt white paper.

An important parameter to be considered before experimental work on the sensor was started would be to prove that the basic assumptions taken in the theoretical considerations were also true experimentally. These were whether the detected signals S1 and S2 followed an inverse square law distribution and whether the emission from the POF was, if not Lambertian as expected, at least close to being one for the few degrees of interest around the axis of emission of the emitting POF.

7.1. VERIFICATION OF SOME BASIC ASSUMPTIONS

The two basic assumptions followed in the analytical considerations on the behaviour of the displacement sensor are investigated here. These are whether the detected signals S1 and S2 follow an inverse square law distribution and how close to a Lambertian emission the far field emission distribution of the emitting POF is for the few degrees of interest around the axis of emission of the emitting POF. Further analytical investigation on the behaviour of the sensor followed based on the results.

7.1.1. Distribution of the Detected Signals

The first basic assumption investigated was the distribution of the experimentally detected signals. Ideally they should follow an inverse square law distribution. In order to prove that, an experimental set up was arranged with two POFs positioned facing each other, one emitting and the other receiving. The axial distance between them was then varied taking measurements of the signal detected by the detecting POF for 1 mm $\leq$ R $\leq$ 50 mm at 1 mm intervals. The detected signals were then compared with the theoretical distribution of the inverse square law (eq. 5.1).

Normalisation of the two responses (theoretical - eq. 5.1 - and experimental) was performed for comparison purposes and was applied with respect to the signals detected and calculated at the longest range (R = 50 mm). The reason behind this choice was the fact that the errors between the two cases were expected to be large at short ranges since the emitting POF cannot be a point source. The normalised responses are shown in Figure 7.1 with their percentage difference shown in the inset graph of the same Figure.

Clearly, as shown in Figure 7.1, the experimental response from the POF is very similar to the theoretical one following an inverse square law distribution (eq. 5.1) and becomes more so as the range increases. As expected, the percentage difference between the two responses is very small at longer ranges giving a difference of less than 1 % at R > 25 mm. At R < 25 mm their difference is increasing at a steep rate, as shown in the inset of Figure 7.1, becoming very large at R = 1 mm (510 %).

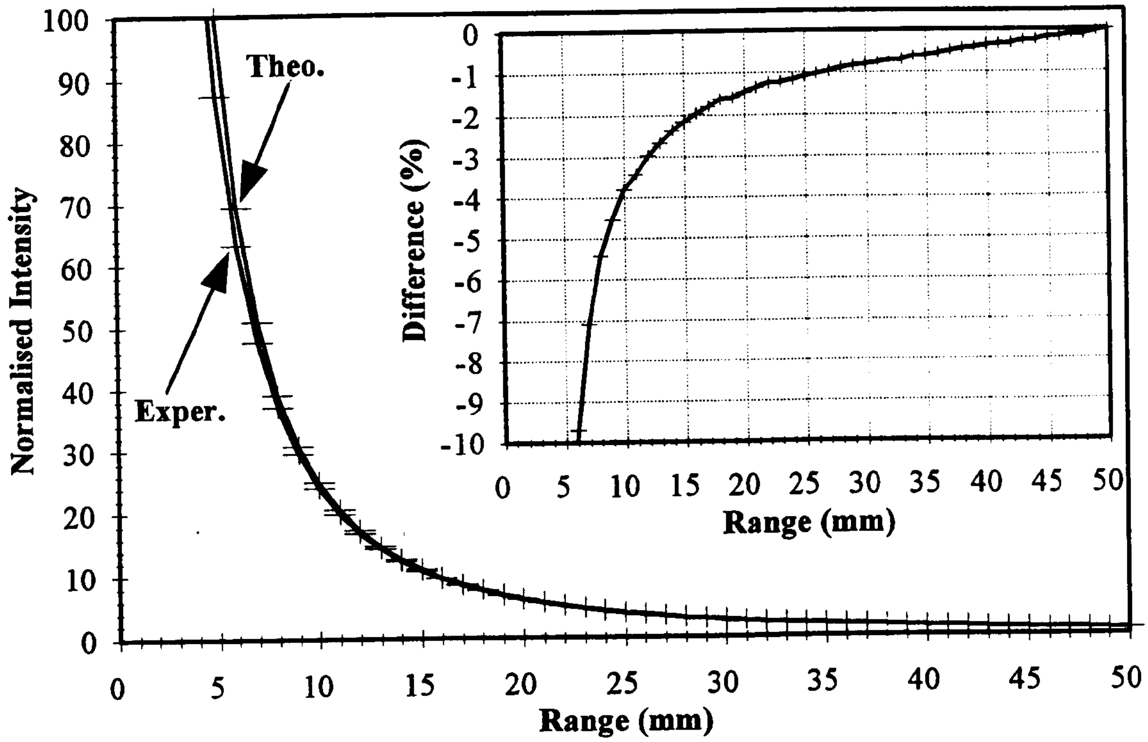

Fig. 7.1: Normalised responses for inverse square law (theoretical) and experimental signal detection from POF

The above shows that the signals S1 and S2 were correctly assumed to follow an inverse square law distribution in the theoretical investigation presented in Chapter 5. The fact that the similarity between the two responses holds to a lesser degree at short ranges will not affect the performance of the sensor since at these ranges linearity of response is expected to break down. But in the case where measurements had to be performed at these ranges, the difference between the inverse square law and the experimental distribution would have to be taken into consideration.

7.1.2. The Far Field Emission Distribution of the Emitting POF

Another assumption that had to be investigated experimentally was the far field emission distribution of an emitting POF in order to see how close to a Lambertian distribution it was. A POF and a detector (PIN photodiode) were arranged in an angular configuration (see Figure 3.5). The detector was positioned 10 cm in front of the stationary emitting POF and the angle between the detector and the axis of the emitting POF was varied by a total of 60^0 ($\pm 30^0$). The distance between the emitting POF and the detector was always constant and the detecting surface of the moving detector was always positioned perpendicular to the line joining its centre with the emitting POF. This result, along with a Lambertian distribution and the distribution of $\cos^4\vartheta$, are shown in Figure 7.2.

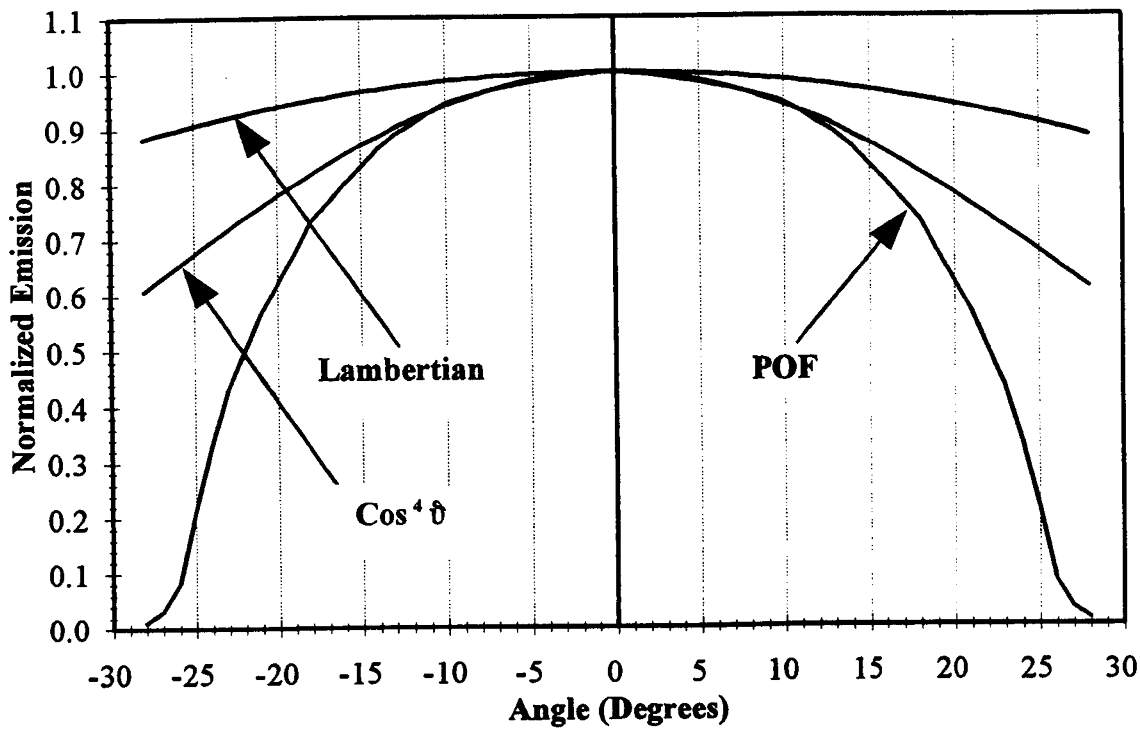

Fig. 7.2: Lambertian (cos ϑ), $\cos^4\vartheta$ and POF emissions

As seen in Figure 7.2 the emission from a POF is much narrower than a lambertian emission. The two emissions are very similar around the axis of emission with a percentage difference between them of less than 1 % for an angle of $\pm$ 4^0 of the optical axis of emission. $\mathrm{Cos}^4\vartheta$ is a much narrower profile and is very close to the experimental emission up to $\pm$ 12^0 where they differ by < 1 %.

7.1.3. Analytical Investigation of the Sensor Response using the POF Emission Distribution

In order to investigate the effect that the POF emission distribution would have on the sensor response the computer program (Appendix A1) was modified for this purpose, thus introducing the experimentally obtained POF far field emission distribution. The target chosen was the one where $\rho = 1$, the X_0 separation was varied between 1 mm and 5 mm but the y separation used was 2.2 mm. Differences took place only at the short ranges at the points where the spikes were occurring which were taking place at a slightly longer range for all X_0 separations. Table 7.1 is showing where these spikes occur.

Table 7.1: Spike effects at short ranges take place later on if POF emission instead of a lambertian one is used (values shown in mm)

X_0	Spikes (Lambertian)	Spikes (POF)	Difference in position
1	1.6	2.2	0.8
2	1.0	1.6	0.6
3	0.4	0.9	0.5
4	0.0	0.3	0.3
5	0.0	0.0	0.0

Traces of a spike occurring started showing up for $X_0 = 4$ mm although $X_0 = 5$ mm remained almost the same. The slope of the linear part of the response for these five X_0 separations remained the same as before for the ranges of interest.

Considering the difference in the two distributions (POF and Lambertian) and the effects observed on the response of the sensor, it can be seen that a narrower emission tends to shift the spike to a longer range and consequently the operational range must start once the response becomes linear. It is clear that the broader the emission distribution of the emitting fibre the shorter the range the spikes occur, thus extending the operational range at the close ranges end. This also suggests that if an LED with a narrow emission is used or that if the emitting fibre is considerably bent, thus narrowing its energy distribution through mode scrambling, the response of the sensor should also be affected. A broad emission distribution for the emitting fibre is clearly preferred.

Another effect is also noticed from the inclusion of the POF emission in the program. This stems from the stepwise changes used in the profile distribution values, over constant intervals (angles), and which are seen by the program as an array of numbers which it rounds up to the nearest value. It is interesting that this effect should also, in principle, account for differences between a very smooth emission and one that is slightly rugged. Figure 7.3 shows the percentage difference between true and computed range for $X_0 = 1$ mm and $X_0 = 5$ mm. It is noticeable where the stepwise changes in the POF emission take place.

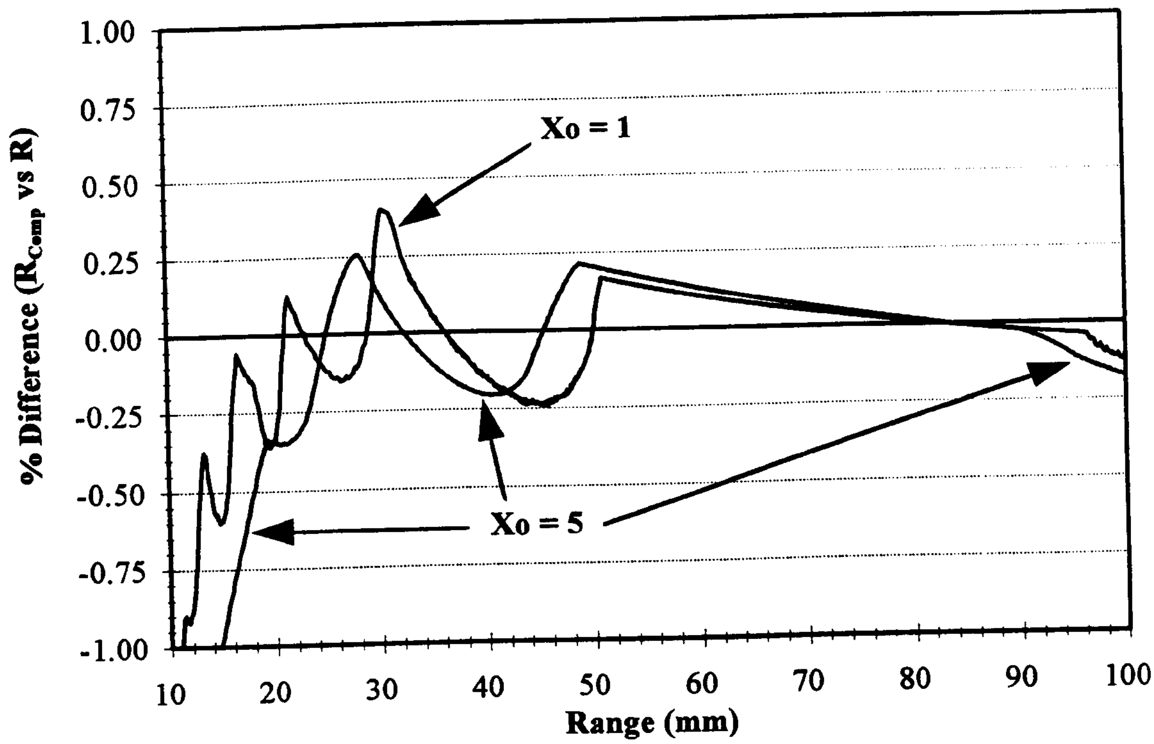

Fig. 7.3: Percentage difference between true and computed range (experimental POF emission and $\rho = 1$)

7.1.4. Misalignment of the Emission Distribution

Misalignment of the emission distribution can be a cause of error for the sensor response. The result of such an effect would be an uneven level of illumination falling on the detecting POFs. It can be caused by factors such as an angular misalignment of the target with the axis of the emitting POF, a small angle on the end of the emitting POF caused during polishing or even both. To investigate such a possibility a much narrower emission distribution was chosen which resembles more closely that of a POF than the Lambertian one used so far. Equation 7.1 (see Figure 7.2) represents the emission distribution used in these calculations since it provides a satisfactory match to the experimental profile up to $\pm$ 12^0:

$$I_A = Cos^4(\vartheta) \qquad \textbf{Eq. (7.1)}$$

Equations 7.2 and 7.3 represent the emission distribution used for an angular misalignment towards detector 1 and towards detector 2 respectively. Here, ϑ is the angle corresponding to a point on the profile (in radians), and Misalignment is the angular misalignment involved (in degrees).

$$I_B = Cos^4[\vartheta - (\pi \frac{Misalignment}{180})] \qquad \textbf{Eq. (7.2)}$$

$$I_C = Cos^4[\vartheta + (\pi \frac{Misalignment}{180})] \qquad \textbf{Eq. (7.3)}$$

Equations 7.1, 7.2 and 7.3 are plotted in Figure 7.4. The misalignment shown is for 10^0. The equations were then used in the computer program as the emission distribution towards the detecting POFs with angular misalignments for 5^0 and 10^0 in each direction. The detecting POFs were assumed to have no misalignment at all. The same held for the target used. The only misalignment introduced into the calculations was the one from the emitting fibre.

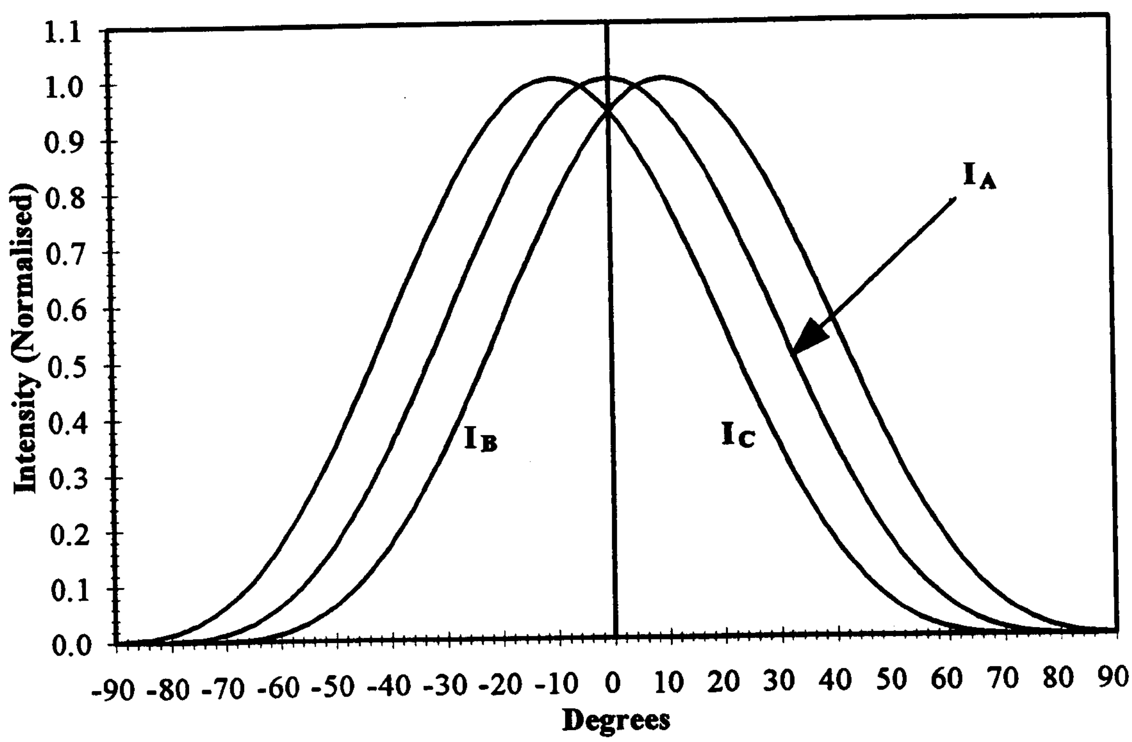

Fig. 7.4: The distributions used to simulate emission misalignment

The results obtained are shown in Table 7.2. The LSF was applied over the same range for all attempts of each sensor arrangement limiting the maximum percentage difference between true and computed range to 1 %. The minimum range is also shown for each attempt along with the spike at the beginning of the range. The slope of each attempt is shown along with the interception point, C, with the S_R-axis. The sensor responses are shown in Figure 7.5.

Table 7.2: Emission misalignment for $\rho = 1$ ($X_0 = 2$ mm)

Misalignment	10° (Det.1)	5° (Det.1)	None	5° (Det.2)	10° (Det.2)
LSF Range, (mm)	5 - 100	5 - 100	5 - 100	5 - 100	5 - 100
R_{min}, (mm)	12	11	11	11	11
Spike, (R, mm)	1.3	1.2	1.1	1.0	0.9
X_0^{-1} (Theoretical)	0.5000	0.5000	0.5000	0.5000	0.5000
(dS / dR), LSF	0.8152	0.6172	0.4980	0.4173	0.3582
C, LSF	2.0927	1.5021	1.1831	0.9836	0.8468
$\alpha_{(L)}$, (%)	2.0794	1.4042	1.0555	0.8745	0.7969

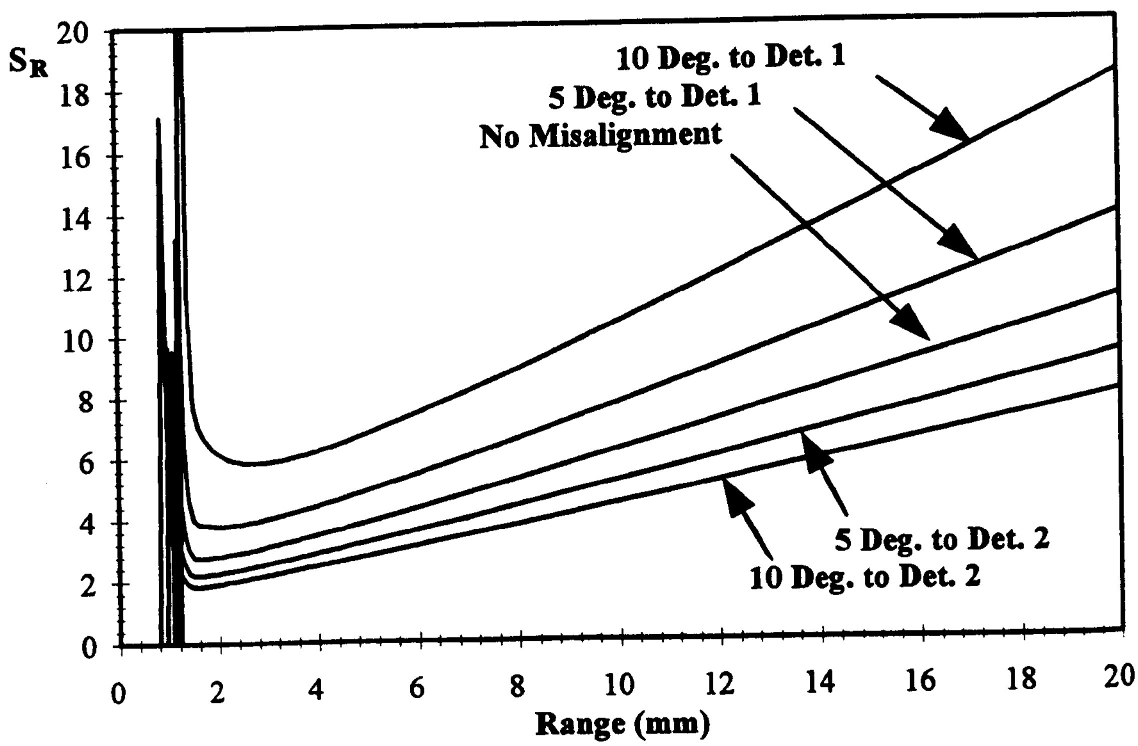

Fig. 7.5: The sensor response with emission misalignment for $\rho = 1$

The immediately evident effect is that depending on the level of misalignment the slope of the response changes drastically. If the emission misalignment is towards detector 1 the slope of the response increases whereas if it is towards detector 2 it decreases.

The minimum range (R_{min}) is almost constant but the point on the beginning of the range where the spike occurs varies depending on the misalignment of the emission. If the misalignment tends towards detector 2 the spike occurs at a shorter range but only marginally. A misalignment such as this, i.e. towards detector 2, slightly improves the linearity of response of the sensor (~ 0.8 % for 10^0) although a decreased slope occurs. The difference between true and computed range increased but remained well within the 1 % requirement.

The arrangement with $\rho = 0$ was also considered resulting in the responses being affected in a very similar way as with $\rho = 1$, i.e. the slope of the response changing drastically, depending on the level of misalignment, and if the emission misalignment is towards detector 1 the slope of the response increases whereas if it is towards detector 2 the slope decreases.

Emission misalignment can be caused easily due to polishing, target misalignment with the optical axis of emission of the emitting POF or even by a combination of both. If the emission misalignment is located only on the emitting fibre then the major effect caused by such a case is the drastic change in the slope of the sensor response. What is important is that linearity of response is maintained.

It must be stressed here, however, that since the misalignment investigated was the one affecting the emitting fibre only, in the case where all three fibres suffer from such misalignments the result obtained here may not hold. In this case the response may not be linear depending on the misalignment involved in any of the fibres and the one present on the target.

The basic assumptions taken in the analytical considerations (Chapter 5) were investigated experimentally for their validity. The detected signals S1 and S2 were found to follow an inverse square law distribution having a percentage difference between the experimentally obtained distribution and the theoretical one (eq. 5.1) of < 1 % for R > 25 mm.

The far field emission distribution from the emitting POF was also investigated for similarity to a Lambertian one. The experimental distribution was found to be narrower resembling a $\cos^4\vartheta$ distribution which was similar to the experimentally obtained emission distribution by < 1 % for ± 12^0 around the axis of emission.

Based on the results obtained further analytical investigation on the behaviour of the sensor was performed. The introduction of the experimentally obtained emission distribution of the emitting POF to the computer program resulted in the spike moving towards the longer ranges due to the narrower emission distribution. Linearity of response remained for the longer ranges.

Emission misalignments were also investigated using the $\cos^4\vartheta$ distribution. When the emission from the emitting fibre was misaligned the slope of the response was changing although the linearity of response remained. If misalignment is present on all fibres then a non-linear response is expected.

7.2. EXPERIMENTAL MEASUREMENTS OF STATIC DISPLACEMENT WITH THE PROPOSED SENSOR USING A MIRROR TARGET

Experimental measurements with the proposed sensor were performed for static displacements in order to investigate whether the theoretical predictions of Chapter 5 would be verified.

Initial experimental work was performed under dark room conditions, with the circuits shown in Figure 6.6. Once calibration was performed ($R_{DET.1}$ = 0.95 MΩ and $R_{DET.2}$ = 0.75 MΩ) the three POFs were positioned in the circular jig shown in Figure 6.1 facing a mirror with X_0 = 3 mm. The POF coupled to the LED was emitting around 400 μW towards the mirror. The signals detected, shown in Figure 7.6, varied from a maximum of 800 mV at R = 0 mm to 7 mV at R = 60 mm. The resulting response (S_R) is shown in Figure 7.7 for six repeated measurements.

Notes: (1) In the graphs that follow the lines connect points that belong to the same group of measurements. For subsequent figures to Figure 7.6, the points where measurements were taken also show the estimated error.

(2) The signal to noise ratios (SNR) quoted onwards refer to optical measurements.

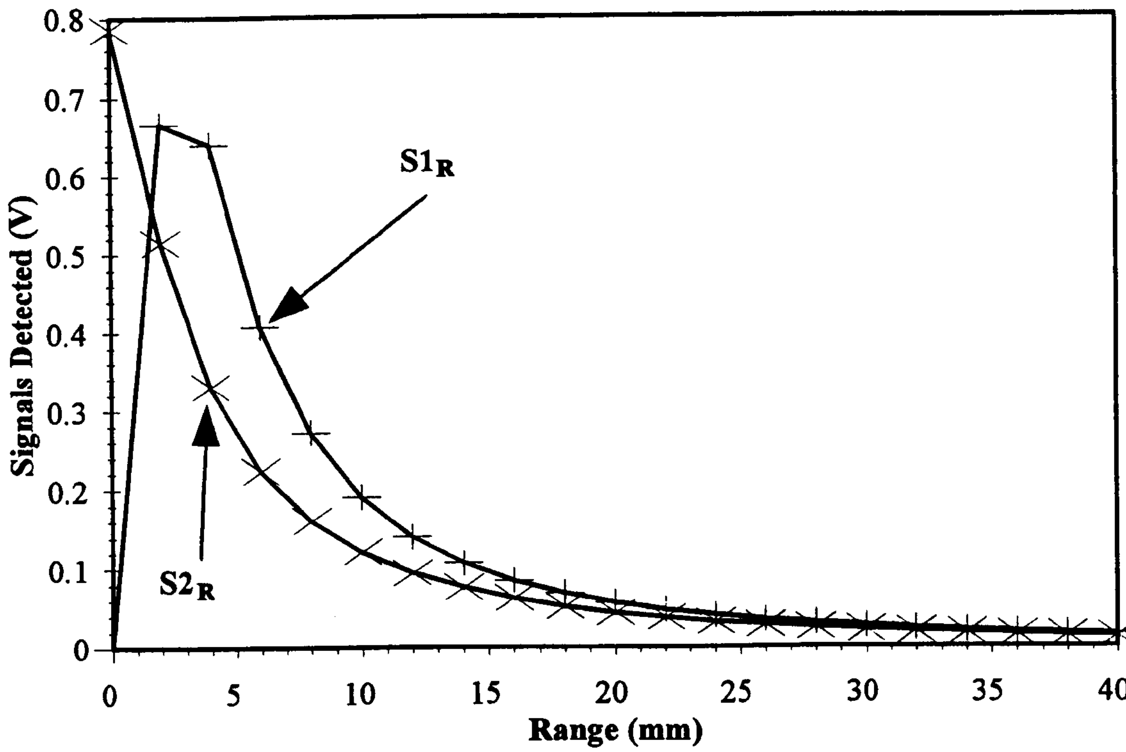

Fig. 7.6: The detected signals

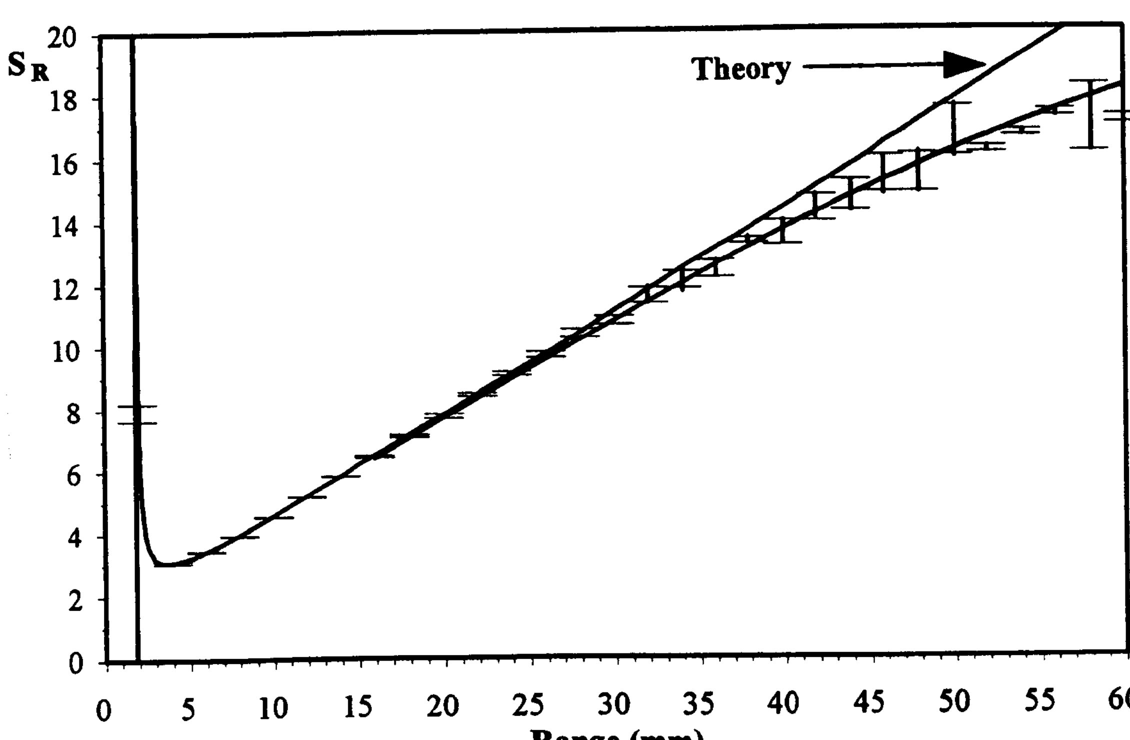

Fig. 7.7: The response of the sensor with $X_0 = 3$ mm

The detected signals shown in Figure 7.6 follow a response similar to the one predicted in the theoretical simulation (see Figure 5.20) for $\rho = 1$, crossing at a short range due to the finite NA of the POFs and decrease according to the inverse square law.

Excellent agreement between experiment and theory for ranges up to 28 mm, including the spike at 2 mm, is shown in Figure 7.7. Over the range 10 mm < R < 28 mm the experimental points lie on a straight line. This shows that for a distance over which the two signals are equal as result of the calibration then a linear response can be achieved.

By applying a least squares fit (LSF) routine over the range 10 mm < R < 28 mm it is found that this line is represented by:

$$S_R = (0.323 \pm 0.001)R + (1.254 \pm 0.013) \qquad \textbf{Eq. (7.4)}$$

Taking the inverse of this to define the relationship for measured range, R_M:

$$R_M = \frac{S_R - (1.254 \pm 0.013)}{(0.323 \pm 0.001)} \qquad \textbf{Eq. (7.5)}$$

Figure 7.8 shows the errors for the experimental points represented by the standard deviation from the six repeated measurements. From this it can be seen that the sensor gives an error between true (measured using the micrometre scale of the translation unit where the target was positioned on - accurate to ± 1 μm) and experimentally determined range (10 mm < R < 28 mm) of less than 1 %. Allowing for the observed fluctuations in S_R, typical errors in the measured range are shown in Table 7.3:

Table 7.3: Typical errors in measured range for the simple circuit arrangement

Range (mm)	Errors in Measured Range (%)	Corresponding Range (μm)
10	-0.14 ± 0.55	-14 ± 55
20	0.04 ± 0.36	8 ± 72
28	0.30 ± 0.50	83 ±139

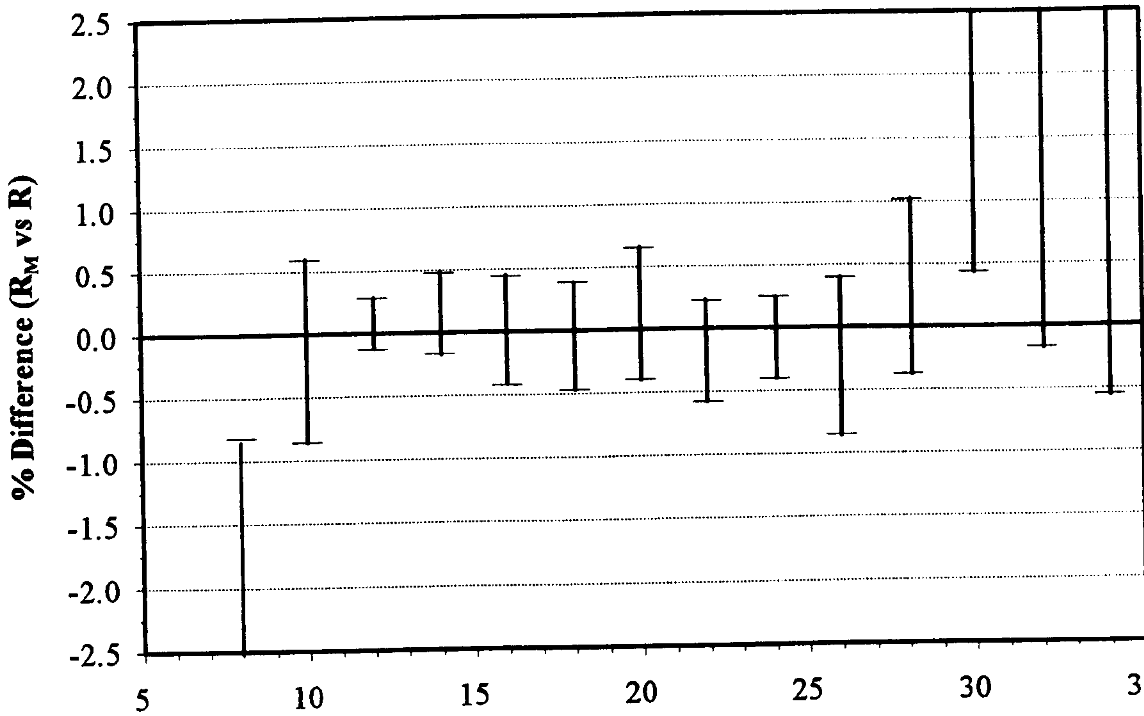

Fig. 7.8: Difference (%) between true and experimental range

Beyond R = 28 mm the experimental S_R values deviate from the analytical curve, the deviation increasing as the range increases. The reason for this deviation was attributed to the way the detecting circuits were built (Figure 6.6). These were arranged in a photoconductive mode where the shot noise is more pronounced due to the increased dark current with a consequent reduction in detectivity. This resembled an offset voltage existing on the two detecting circuits. When the signal current was very large compared to the dark current, as was the case at R < 28 mm, the S_R value is least affected. But once R > 28 mm, the magnitude of the dark current with respect to the smaller detected signals was considerable and so affected the measurements. This was also verified by modifying the computer program and adding an offset voltage to $S2_R$ (1.5 % of $S2_R$ at R = 60 mm becoming 0.4 %, i.e. 0.1 mV for 25.5 mV signal, at R = 28 mm). In Figure 7.7 the upper curve is the ideal with no offset voltage while the lower one is affected by the assumed presence of an offset voltage (dark current). The fluctuations observed at R > 28 mm in Figure 7.7 are caused by the limited accuracy (3.5 digits) of the DMMs.

It can be concluded that with this simple system used, linearity of response was obtained over an operational range of 18 mm with an accuracy of 1 % when a mirror was used as target. In order to achieve linearity over a longer range it is necessary to calibrate both detectors over the whole of the proposed operational range and to eliminate offset voltages. The spikes predicted in the theoretical analysis were also observed experimentally.

The detecting circuits were changed to use the improved ones shown in Figure 6.8 which were connected in a transimpedance configuration and their outputs were connected to 4.5 digit DMMs for higher accuracy. Calibration was performed at R = 60 mm and the values of the feedback resistors were $R_{F/B.1}$ = 16 MΩ and $R_{F/B.2}$ = 15.5 MΩ. The signals detected varied from a maximum of 5 V at R = 10 mm down to 80 mV at R = 90 mm. Assuming that the readings of the DMMs under dark conditions is the noise of the detectors then the signal to noise ratio (SNR) at R = 10 mm of Det. 1 was 54 dB and of Det. 2 was 52.2 dB. At R = 90 mm the SNR for detector 1 was 36.2 dB and of detector 2 was 35.9 dB. The difference between the detected signals at R = 10 mm was 35 % and at R = 90 mm was 6 %. The results obtained are shown in Figure 7.9 for six repeated measurements taken over a period of one hour.

From what is shown in Figure 7.9 excellent agreement between experiment and theory for the whole of the range was obtained. Over the range 10 mm < R < 90 mm the experimental points lie on a straight line. Using a LSF routine over the range 10 mm < R < 90 mm it is found that this line is represented by:

$$S_R = (0.325 \pm 0.001)R + (1.491 \pm 0.077) \qquad \textbf{Eq. (7.6)}$$

Taking the inverse of this to define the relationship for measured range, then:

$$R_M = \frac{S_R - (1.491 \pm 0.077)}{(0.325 \pm 0.001)} \qquad \textbf{Eq. (7.7)}$$

The errors for the experimental points represented by the standard deviation from the six repeated measurements are shown in Figure 7.10. From this it can be seen that the sensor gives an error in the operational range 10 mm < R < 90 mm of less than 1 %. Allowing for the observed fluctuations in S_R, typical errors in the measured range are shown in Table 7.4.

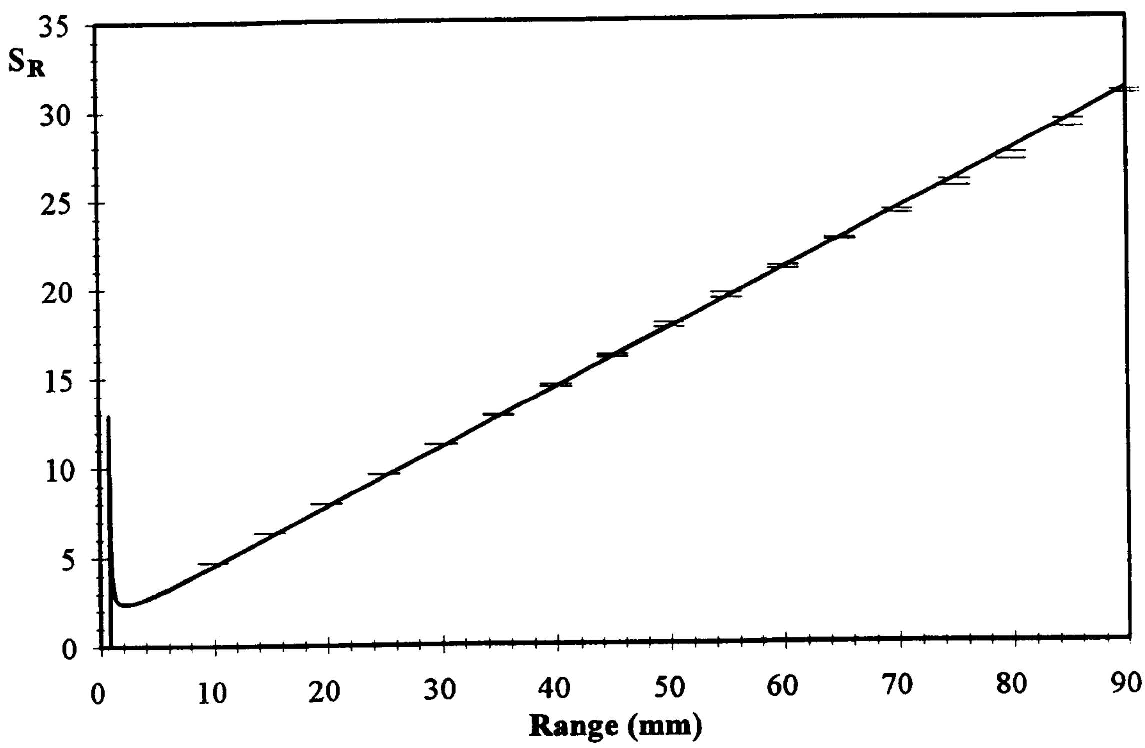

Fig. 7.9: The response of the sensor with X_0 = 3 mm using the transimpedance amplifiers

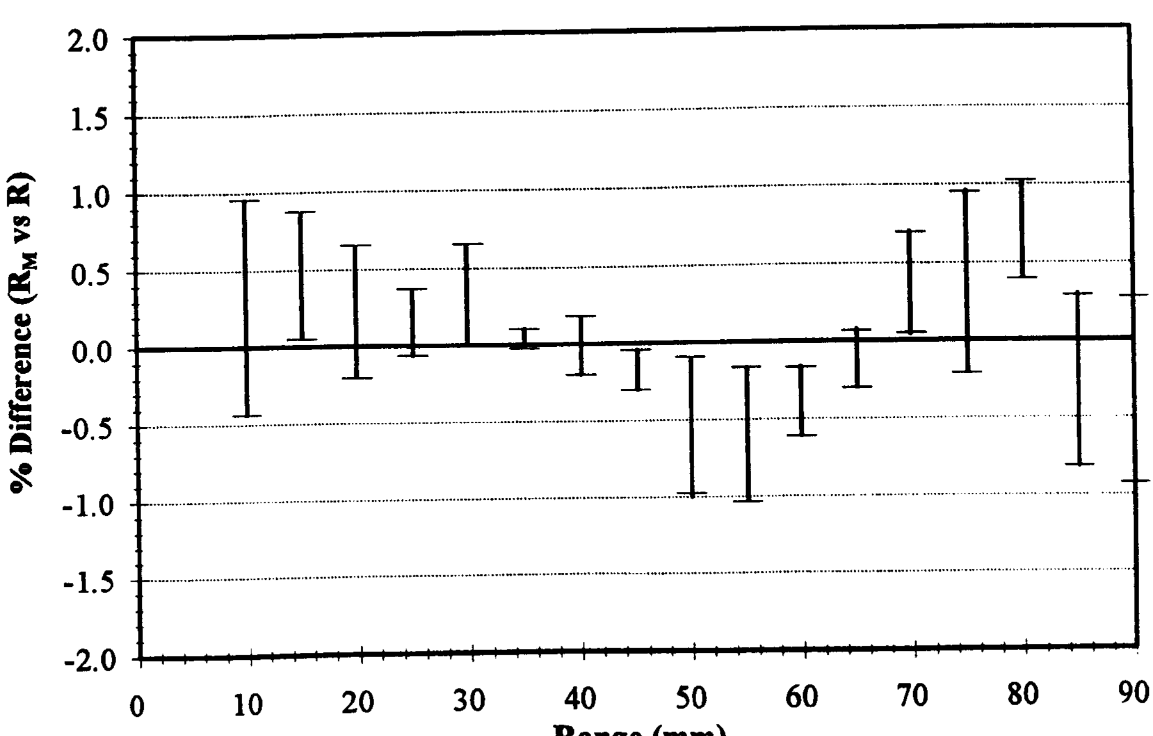

Fig. 7.10: Difference (%) between true and experimental range

Table 7.4: Typical errors in measured range for the improved system

Range (mm)	Deviation in Measured Range (%)	Corresponding Range (μm)
20	0.21 ± 0.29	43 ± 57
40	0.02 ± 0.12	7 ± 49
60	-0.39 ± 0.15	-235 ± 88
80	0.74 ± 0.22	594 ± 176

From what is shown in Figure 7.10 and Table 7.4 the sensor can clearly become a usable device having an operational range of 80 mm and an accuracy of 1 %. These figures were achieved over six repeatable runs.

What is important to note here, however, is that the above was obtained under room temperature conditions. Elevation of temperature is expected to upset the operation of the sensor. In order to investigate this possibility the emitting and detecting circuits were positioned in an electric oven. The sensor head and target remained in room temperature conditions. The temperature (T) of the electronic circuitry was raised to T = 35 ^{0}C, T = 45 ^{0}C and T = 55 ^{0}C. Three runs of measurements were taken at each of these temperatures. Calibration was performed at T = 22 ^{0}C at R = 65 mm using equation 6.4. The response of the sensor at T = 22 ^{0}C is a linear one. At higher temperatures the responses are deviating fast. Applying a LSF routine at the average of the three responses taken at T = 22 ^{0}C over the range 10 mm < R < 90 mm it is found that this average line is represented by:

$$S_R = (0.321 \pm 0.002)R + (1.315 \pm 0.197) \qquad \textbf{Eq. (7.8)}$$

Taking the inverse of this to define the relationship for measured range, then:

$$R_M = \frac{S_R - (1.315 \pm 0.197)}{(0.321 \pm 0.002)} \qquad \textbf{Eq. (7.9)}$$

The responses obtained are shown in Figure 7.11. Equation 7.9 was used to determine the percentage difference between true and measured range for all the attempts. Error bars of the results are shown in Figure 7.12 with the average of the three runs taken at each temperature shown with a solid line.

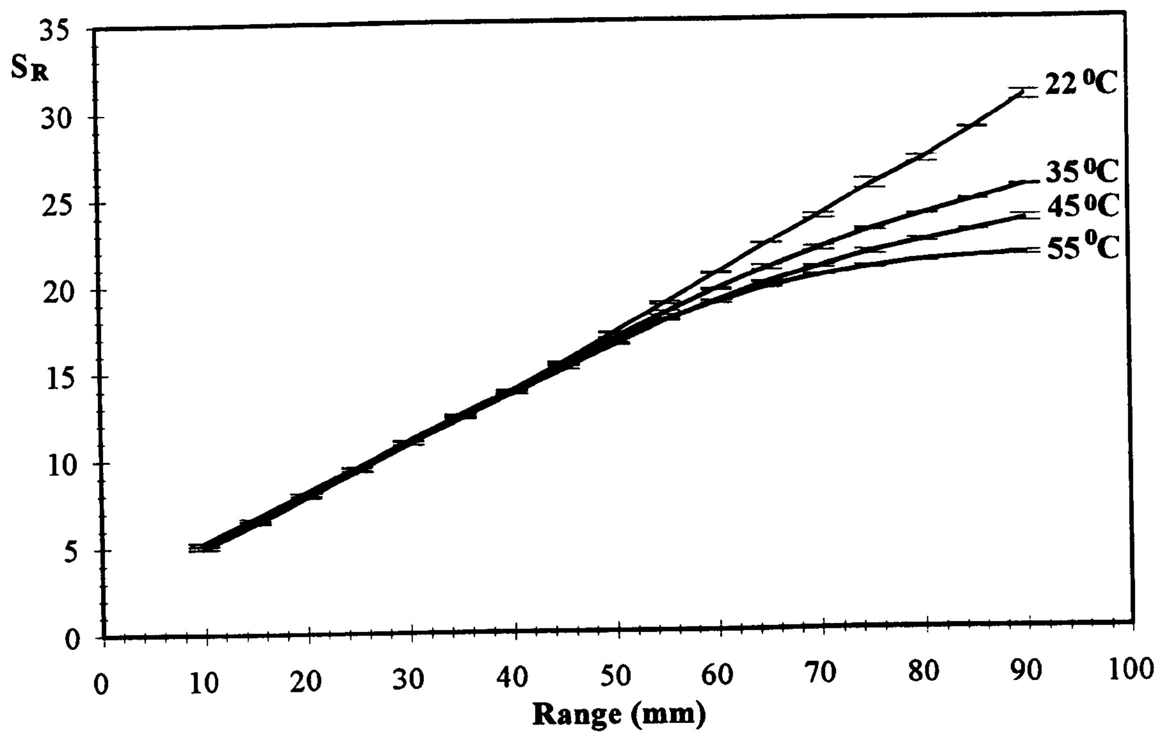

Fig. 7.11: The response of the sensor at various temperatures

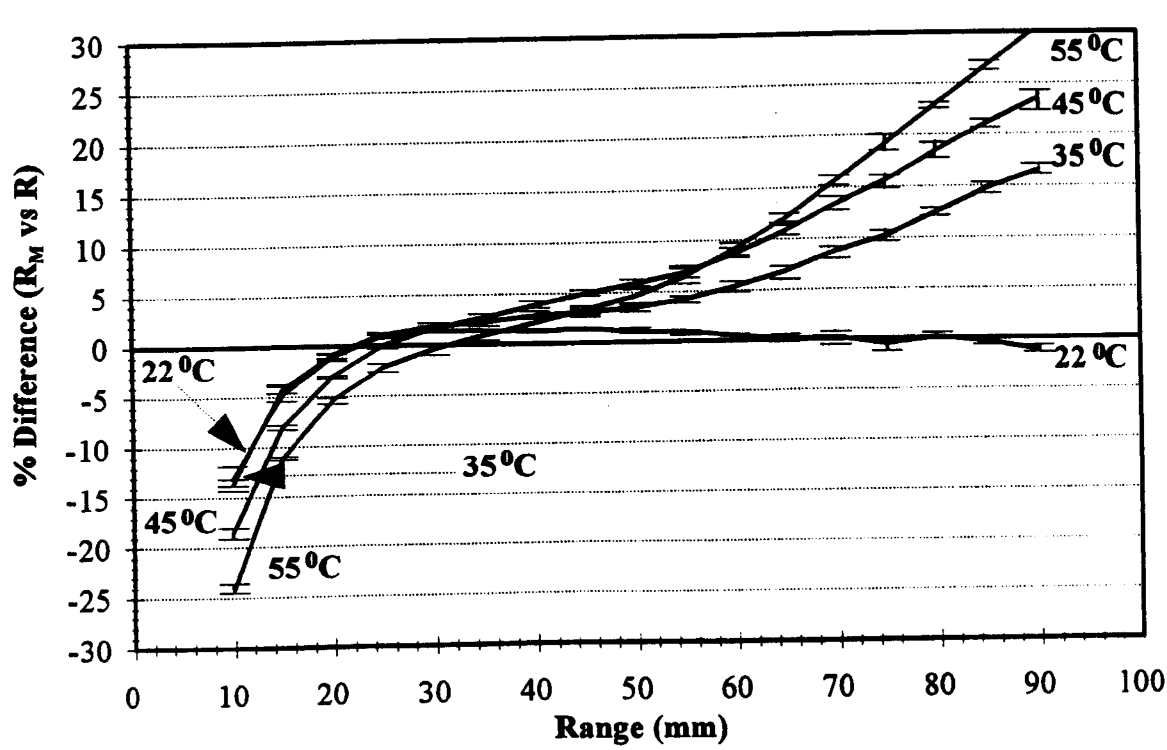

Fig. 7.12: Difference (%) between true and measured range at various temperatures

At T = 22 °C the sensor gives an error in the operational range 20 mm < R < 90 mm of 1.5 %. It is noticeable that the minimum range starts at R = 20 mm. This is due to the fact that linearity at short ranges depend on the numerical aperture of the POFs and is very sensitive to any changes of it.

At higher temperatures the operational range of the sensor is drastically affected and decreased. At T = 35 °C the operational range of the sensor is 20 mm < R < 30 mm, at T = 45 °C is 25 mm < R < 30 mm and at T = 55 °C is 30 mm < R < 35 mm (1.5 % error).

In order to understand what happens the ratio of the signals detected from each detectors at T = 35 °C, T = 45 °C and T = 55 °C over the signals detected from the same detector at T = 22 °C were taken. The result is shown in Figure 7.13.

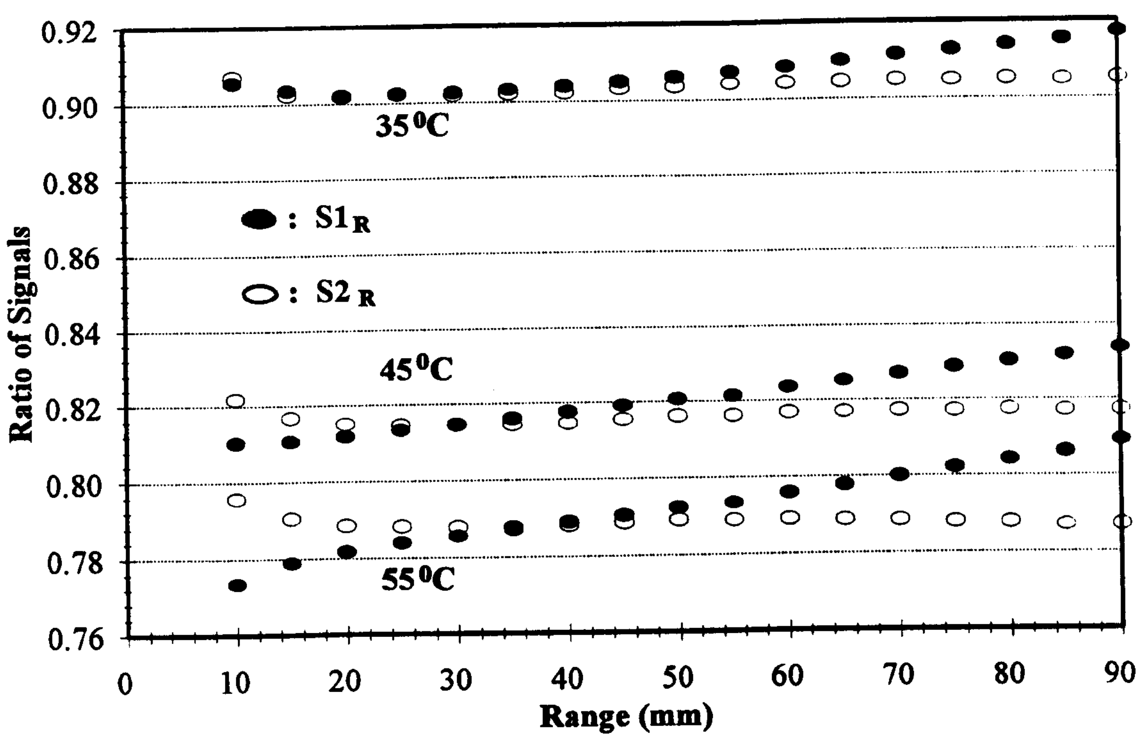

Fig. 7.13: The ratio of the detected signals

Ideally, the groups of ellipses shown should have been horizontal, i.e. slope of 0, and superimposed on each other at 1 on the y-axis. As expected the increase in temperature caused ageing effects on the LED (and spectral shift) thus lowering its intensity. The PIN diodes also aged suffering a decrease in their responsivity. This explains the positioning of the groups of circles with respect to the ideal 1 on the y-axis. This decrease on the signal level, however, does not explain the drastic change in the sensor response.

What is important in Figure 7.13 is the difference in slope that the circles have from the ideal slope of 0. It can be seen that the ellipses representing the signals detected from detector 1 have a more noticeable slope compared to the ones from detector 2. This effect is a result of the combination of dark current from the PIN photodiodes and offset voltage from the opamps. Typically, the dark current of a PIN photodiode approximately doubles or halves for every 10 ^{0}C increase or decrease in temperature.

By applying a LSF between R = 10 mm and R = 90 mm on all these groups of ellipses individually the above can be more clearly shown by the resulting equations 7.10 up to 7.15:

$$\frac{S1_{(T=35^0C)}}{S1_{(T=22^0C)}} = (0.180 \pm 0.019)\ 10^{-3}\ R + (0.899 \pm 0.002) \qquad \textbf{Eq. (7.10)}$$

$$\frac{S1_{(T=45^0C)}}{S1_{(T=22^0C)}} = (0.302 \pm 0.006)\ 10^{-3}\ R + (0.806 \pm 0.001) \qquad \textbf{Eq. (7.11)}$$

$$\frac{S1_{(T=55^0C)}}{S1_{(T=22^0C)}} = (0.398 \pm 0.012)\ 10^{-3}\ R + (0.773 \pm 0.001) \qquad \textbf{Eq. (7.12)}$$

$$\frac{S2_{(T=35^0C)}}{S2_{(T=22^0C)}} = (0.029 \pm 0.013)\ 10^{-3}\ R + (0.902 \pm 0.001) \qquad \textbf{Eq. (7.13)}$$

$$\frac{S2_{(T=45^0C)}}{S2_{(T=22^0C)}} = (0.008 \pm 0.018)\ 10^{-3}\ R + (0.816 \pm 0.002) \qquad \textbf{Eq. (7.14)}$$

$$\frac{S2_{(T=55^0C)}}{S2_{(T=22^0C)}} = (-0.044 \pm 0.016)\ 10^{-3}\ R + (0.791 \pm 0.002) \qquad \textbf{Eq. (7.15)}$$

Equations 7.10, 7.11 and 7.12 show the characteristics of the ratios of the signals detected from detector 1 and equations 7.13, 7.14 and 7.15 show the characteristics of ratios of the signals detected from detector 2. The slope that the ratios of the signals detected from detector 1 have are indeed noticeably different than the slope of the ratios of the signals detected from detector 2. Their position with respect to the y-axis is also shown.

The above equations show that detector 1 has been affected differently by temperature elevation rather than detector 2 since the slopes of the ellipses from detector 1 adopt a positive change in their slope whereas the ones from detector 2 adopt a negative slope change.

The above performed test suggests that at higher temperatures the sensor would be virtually unusable. The electronic circuits are thought to be responsible for the deterioration in performance of the sensor. Better electronic components therefore, especially opamps (chopper stabilized) were used to improve the sensor behaviour.

In another test the intensity of the LED was varied (by varying the drive current) in order to determine whether the response of the sensor can remain linear and unaffected, and measurements were repeated. Calibration was performed by having the three fibres next to each other with $X_0 = 0$ mm facing the mirror. The feedback resistors were varied and the signals were arranged to be the same, i.e. $S1_R = S2_R = 167.02$ mV at $R = 55$ mm ($R_{F/B} \approx 11$ MΩ). The POFs in the sensor head were then set at $X_0 = 3$ mm. The LED driving current (I_{LED}) was set at various values (27 mA < I_{LED} < 80 mA) and two runs of measurements were performed at each current setting. The error bars shown include all the measurements taken during this test for all the I_{LED} values superimposed.

Figure 7.14 clearly shows that the responses (all superimposed) of all the runs performed are very linear, and that the variation of the LED intensity has no effect on the behaviour of the sensor. The solid line in the figure represents the average response when $I_{LED} = 67$ mA with a drive voltage of 5 V. Typical signal values detected, their percentage difference and SNR for each detected signal are shown in Table 7.5. Here, it can be seen that the magnitude of the signals detected by the two detectors at one particular range depend on the intensity of the LED which is proportional to the current driving it. The S_R value remains constant as the LED intensity varies. As expected, the SNR values of the detected signals vary depending on the signal level.

When a LSF is applied on the response with $I_{LED} = 67$ mA the result is:

$$S_R = (0.334 \pm 0.001)R + (1.202 \pm 0.041) \qquad \textbf{Eq. (7.16)}$$

Taking the inverse of this to define the relationship for measured range, then:

$$R_M = \frac{S_R - (1.202 \pm 0.041)}{(0.334 \pm 0.001)} \qquad \textbf{Eq. (7.17)}$$

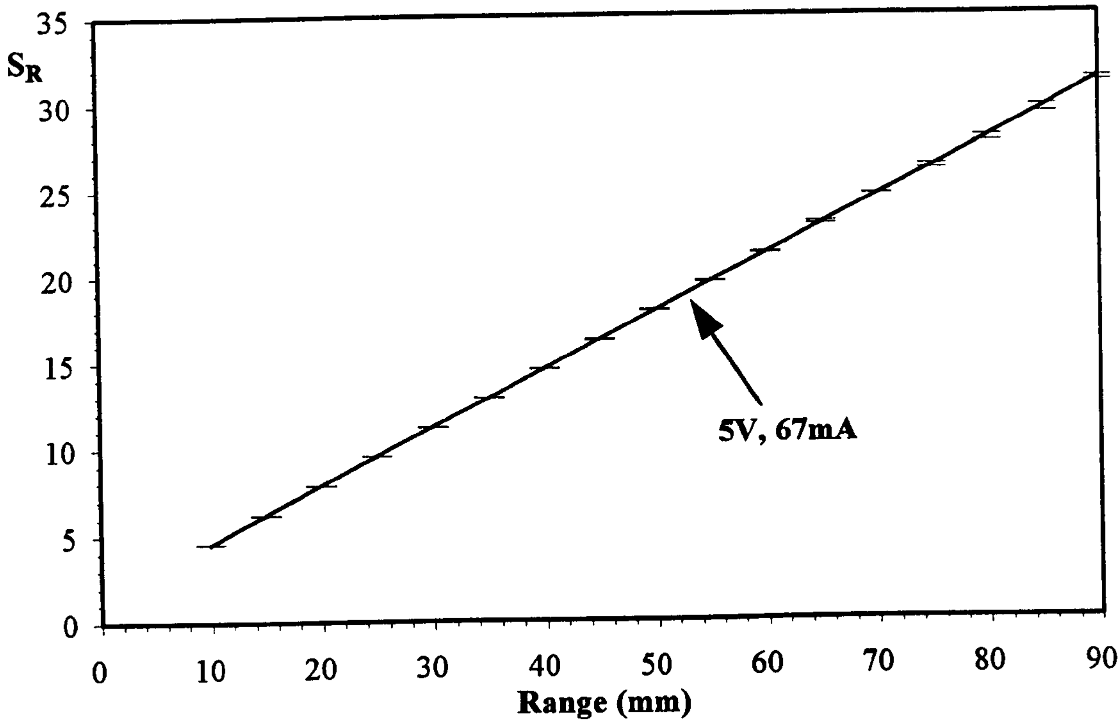

Fig. 7.14: The sensor response when the LED drive current is varied

Table 7.5: Detected signals at two ranges for various LED drive currents

I_{LED} (mA)	80	67	53	40	27
$S1_R$ (mV) @ R = 10 mm	3920	3778	3048	1951.1	516.8
$S2_R$ (mV) @ R = 10 mm	2507	2417	1950	1248.2	330.5
S_R @ R = 10 mm	4.549	4.551	4.552	4.552	4.548
$(S1_R)$NR (dB) @ R = 10 mm	52.9	52.8	51.8	49.9	44.1
$(S2_R)$NR (dB) @ R = 10 mm	51.0	50.8	49.9	48.0	42.2
$S1_R$ (mV) @ R = 90 mm	63.71	62.25	50.69	32.22	8.53
$S2_R$ (mV) @ R = 90 mm	59.75	58.38	47.55	30.22	8.00
S_R @ R = 90 mm	31.177	31.171	31.287	31.220	31.189
$(S1_R)$NR (dB) @ R = 90 mm	35.0	34.9	34.0	32.1	26.3
$(S2_R)$NR (dB) @ R = 90 mm	34.8	34.7	33.8	31.8	26.0

where: $(S1_R)$NR and $(S2_R)$NR are the SNR values for detectors 1 and 2 respectively.

Equation 7.17 was used to determine the percentage difference between true and measured range for all the attempts with the result shown in Figure 7.15. Error bars are used and the solid line represents the average error for I_{LED} = 67 mA.

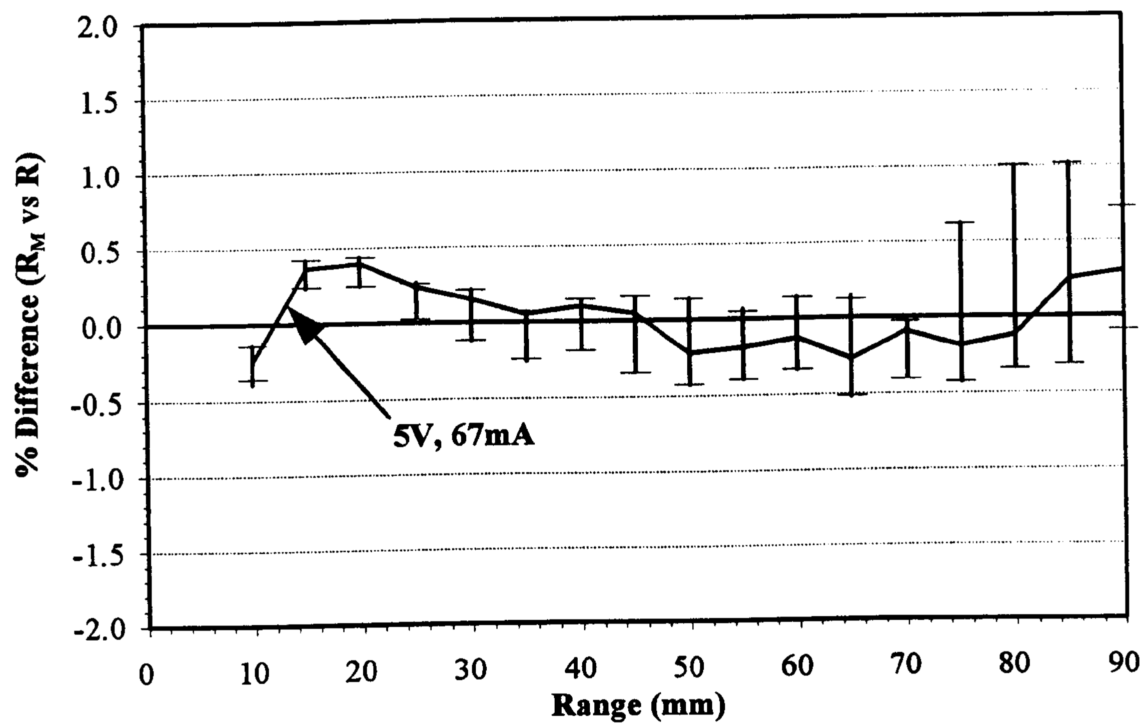

Fig. 7.15: Difference (%) between true and measured range for various I_{LED}

As seen from Figure 7.15, the percentage difference between true and measured range is less than 1 % approaching 1 % at R > 80 mm. Clearly, the variation in I_{LED} does not affect the sensor response or its accuracy verifying that this referencing technique is not affected by any reasonable variations in the intensity of the source.

In a similar way the supply voltage of the detecting circuit was varied from a maximum value of ± 18 V down to ± 13 V and no change was observed. It must be stressed, however, that in circuits like the one used here, where the offset adjust facilities offered by the opamps are entirely dependent on the supply voltage, offset problems are bound to be caused if only the positive or negative side of the supply voltage varies. Similarly, the behaviour of the opamps themselves will also be affected by uneven supply voltage variations. To overcome this either stable power supplies must be used or even better voltage reference opamps which can supply a constant voltage output for varying supply conditions should be employed to feed the differential input of each opamp.

The behaviour of the sensor under increased temperature levels needed to be investigated again under the present circuit arrangement. In order to do this the electronic circuitry was placed in the electric oven. Calibration took place at T = 20 °C and R = 45 mm where the gain of the two detecting circuits was varied and their outputs became equal ($S1_R$ = $S2_R$ = 182.55 mV for$_0$ X = 0 mm). The values of the feedback resistors were approximately 11 MΩ. The signals detected varied from a maximum of 2.8 V at R = 10 mm down to 45 mV at R = 90 mm.

Measurements of the sensor response were taken at four temperatures, i.e. T = 20 °C, T = 25 °C, T = 35 °C and T = 45 °C. Three runs at each temperature were performed and the responses are shown in Figure 7.16 with error bars and the average of the response at each temperature shown with a solid line.

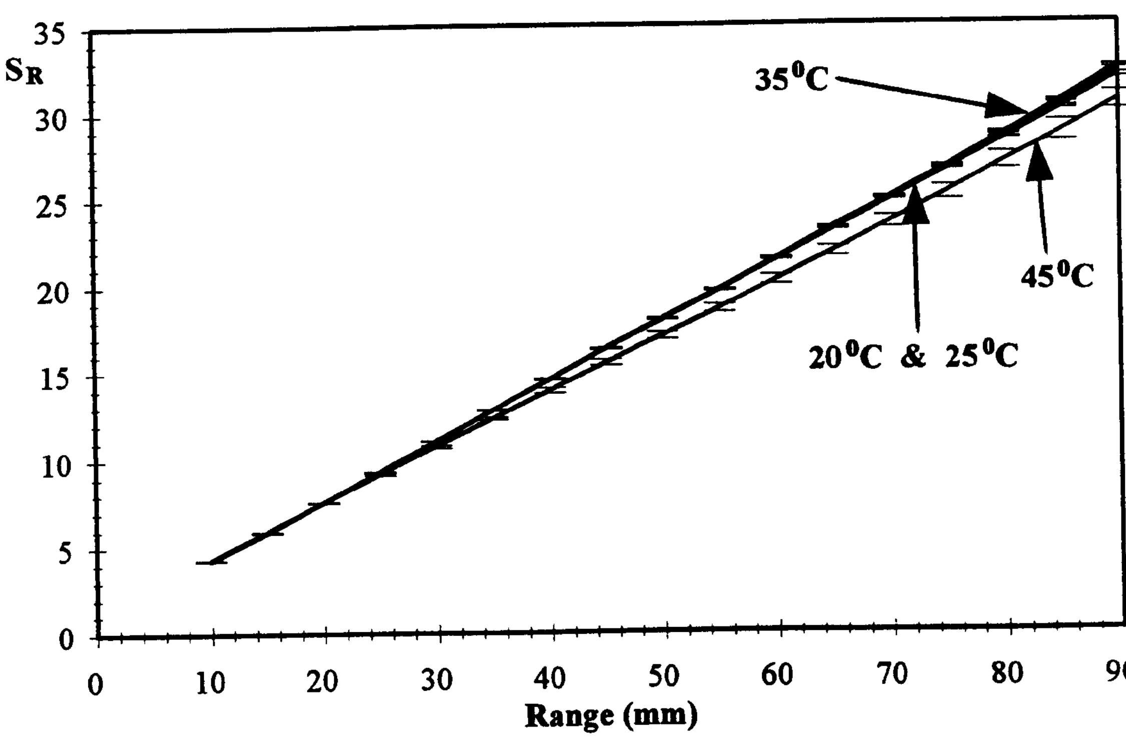

Fig. 7.16: The response of the sensor at various temperatures with the chopper stabilized opamps

The response of the sensor at T = 20 °C is used when applying the LSF and is:

$$S_R = (0.349 \pm 0.001)R + (0.607 \pm 0.121) \quad \textbf{Eq. (7.18)}$$

Taking the inverse of this to define the relationship for measured range, then:

$$R_M = \frac{S_R - (0.607 \pm 0.121)}{(0.349 \pm 0.001)} \quad \textbf{Eq. (7.19)}$$

Equation 7.19 was used to determine the percentage difference between true and measured range for all the attempts. Error bars and a solid line showing the average of each result are shown in Figure 7.17.

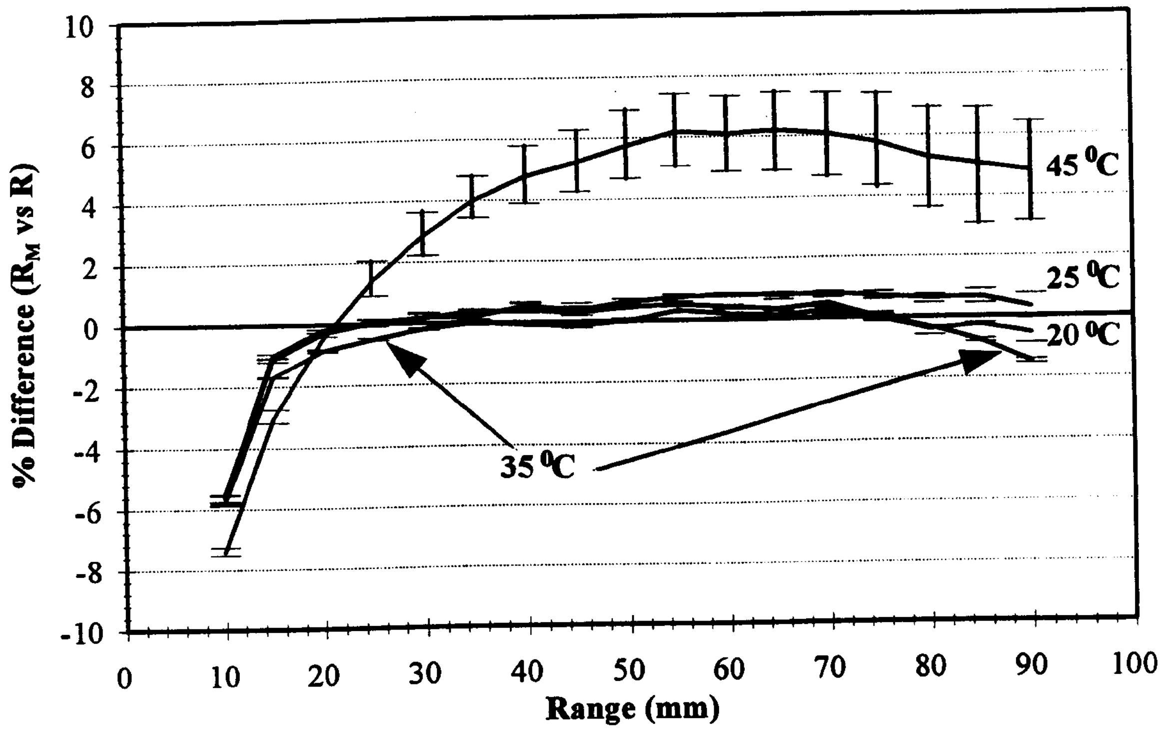

Fig. 7.17: Difference (%) between true and measured range at various temperatures with chopper stabilized opamps

From Figure 7.17 it can be seen that the sensor gives an error in the operational range 10 mm < R < 90 mm of less than 1 % at T = 20 ºC and T = 25 ºC. At T = 35 ºC the error remains below 1 % for R < 85 mm. At T = 45 ºC the error increases to 8 %.

The ratio of the signals detected at T = 25 ºC, T = 35 ºC and T = 45 º C over the signals detected from the same detector at T = 20 ºC are shown in Figure 7.18.

Looking at Figure 7.18 it can be seen that the ellipses overlap at T = 25 ºC and at T = 35 ºC showing an equal effect as a result of the increase in temperature of the detecting circuits. At T = 45 ºC the ellipses are separated showing an unequal temperature effect on each detecting circuit. It can be seen that when R < 20 mm the open ellipses are below the closed ones relating to the negative increase in percentage error seen in Figure 7.17, and at R > 20 mm move above to a positive percentage error.

The above clearly suggest that when the temperature effects in the two detecting circuits are similar, then the satisfactory performance of the sensor can be maintained, i.e. for T < 35 ºC. When the two detecting circuits are not affected similarly, then effects such as those appearing at T = 45 °C could be taking place affecting the accuracy of the sensor.

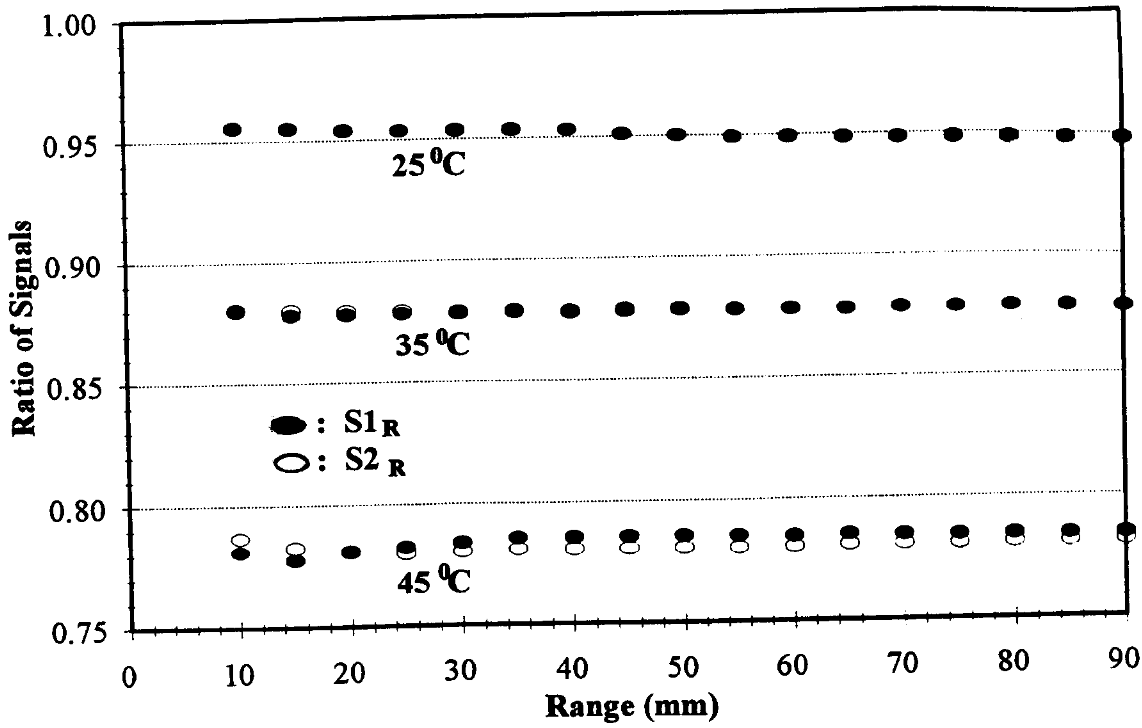

Fig. 7.18: The ratio of the detected signals (chopper stabilized opamps)

In another set of measurements the experimental variation of S_R for 500 randomly selected points with range was taken from 10 mm < R < 90 mm measured at T = 25 °C for X_0 = 2 mm. Calibration was performed with X_0 = 0 mm prior to arranging the sensor head with X_0 = 2 mm separation. The application of LSF to the experimental points 14 mm < R < 83 mm resulted in equation 7.20. The sensor response is shown in Figure 7.19 and the percentage difference between true and measured range deduced from the inverse of equation 7.20 is shown in Figure 7.20.

$$S_R = (0.493 \pm 0.001)R + (0.466 \pm 0.095) \qquad \textbf{Eq. (7.20)}$$

Figure 7.20 shows that less than 1 % difference between true and measured range is possible over 14 mm < R < 83 mm.

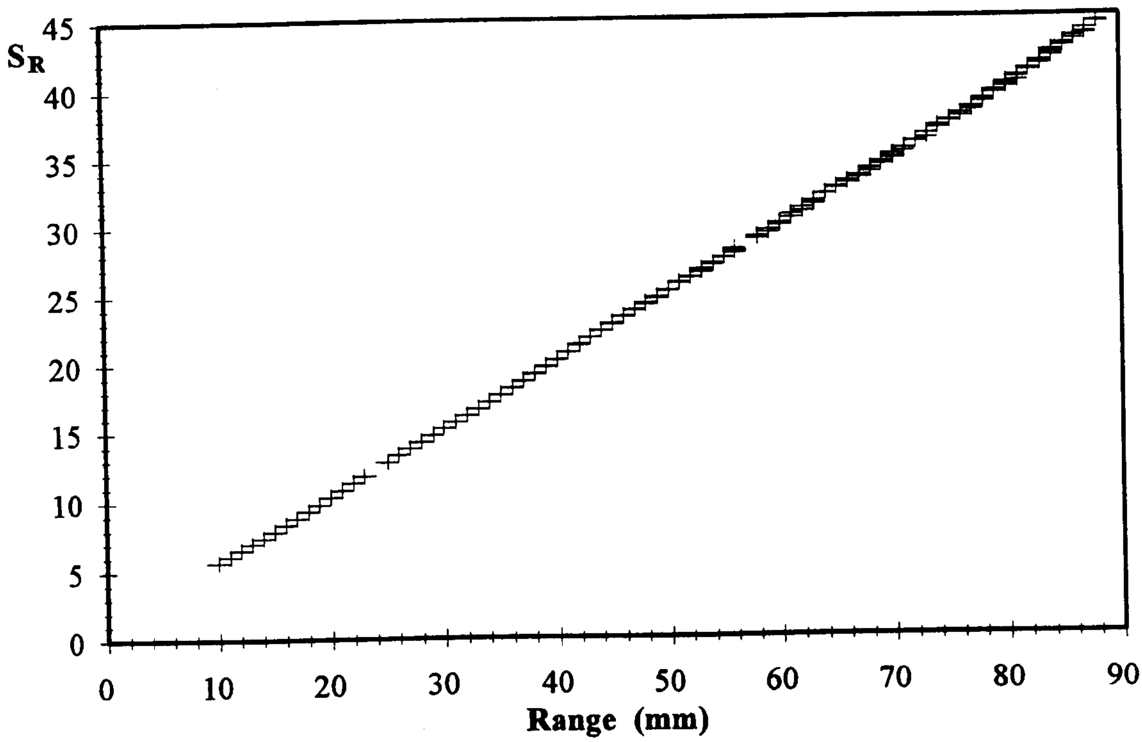

Fig. 7.19: The sensor response for 500 randomly repeated measurements

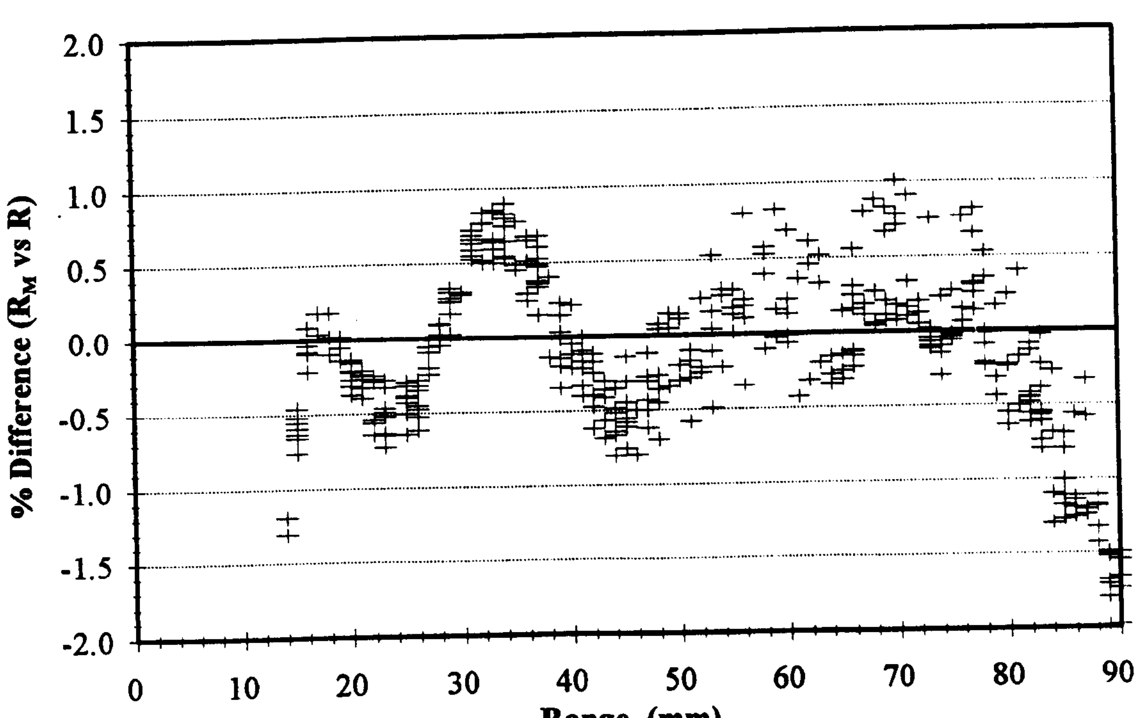

Fig. 7.20: Difference (%) between true and measured range for the 500 randomly repeated measurements

In Figure 7.20 it is interesting to note that there is an oscillatory behaviour in the distribution of the points. These points have a very similar distribution to the one shown in Figure 7.3 where the experimental points from the emission of the POF have been used in the program as an array of numbers in order to simulate the sensor response. The array used introduced stepwise changes on the calculations. This suggest that the emission from the emitting POF may be coarse having a non-uniform structure.

In order to test if the sensor is indeed "scalable", measurements with various X_0 separations starting from 1 mm up to 5 mm were taken. Calibration was performed with $X_0 = 0$ mm at R = 90 mm resulting in $S1_R = S2_R = 114.57$ mV. A single run for each X_0 separation was performed and the results are shown in Figure 7.21.

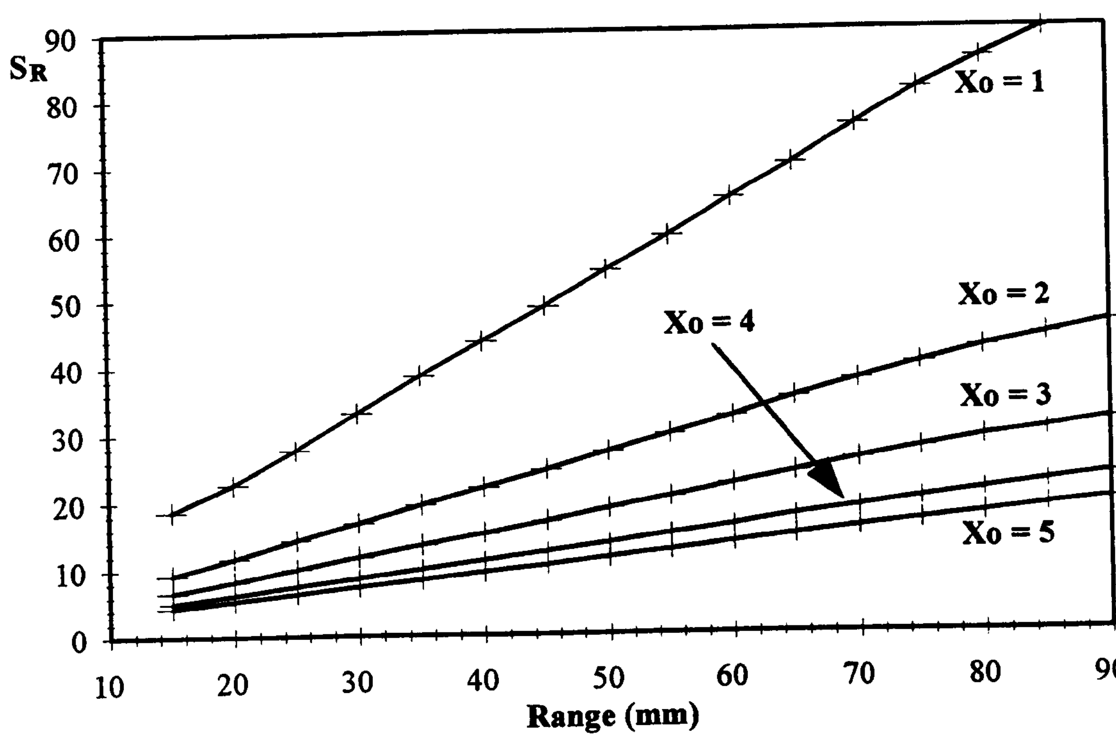

Fig. 7.21: The sensor response for various X_0 separations

The responses shown above resulted in the following equations when the LSF was applied to each of them individually:

$$S_{R_{X_0=1mm}} = (1.060\pm0.003)R + (1.273\pm0.230)$$ **Eq. (7.21)**

$$S_{R_{X_0=2mm}} = (0.513\pm0.002)R + (1.445\pm0.117)$$ **Eq. (7.22)**

$$S_{R_{X_0=3mm}} = (0.345\pm0.001)R + (1.374\pm0.057)$$ **Eq. (7.23)**

$$S_{R_{X_0=4mm}} = (0.244\pm0.001)R + (1.387\pm0.073)$$ **Eq. (7.24)**

$$S_{R_{X_0=5mm}} = (0.203\pm0.001)R + (1.275\pm0.043)$$ **Eq. (7.25)**

The above equations show that this sensing technique is indeed a scalable one with the slope of each attempt being very close to the one predicted by the simplified mathematical analysis in Chapter 5, i.e. $(X_0)^{-1}$.

The inverse of the above equations was taken and was used to define the relationship for the measured range. All the attempts produced a linear response with accuracy better than 1 %. The LSF was applied for X_0 = 1 mm and X_0 = 2 mm over the range 20 mm < R < 80 mm, for X_0 = 3 mm over the range 15 mm < R < 80 mm and for X_0 = 4 mm and X_0 = 5 mm over the range 15 mm < R < 90 mm. The operational range of each X_0 separation was the same as the range where the LSF was applied. To achieve extended scalability, however, we need to have considerably more emitted power for monitoring a satisfactory SNR at the longer ranges.

The smaller X_0 separations have a smaller operational range than the larger ones. This is due to the fact that for the smaller X_0 separations effects arising from offset voltages or errors in the signals, since their difference is smaller than those with the larger X_0 separations, can be more pertinent.

From the experimental measurements of static displacement with the proposed sensor performed under dark room conditions using a mirror target it was concluded that this sensor can measure static displacements over long ranges with a linear response. The referencing technique has been proven a success and the sensor behaviour remained unaffected when the intensity of the light source varied. The scalability of the sensor has also been proved with the smaller X_0 separations resulting in shorter operational ranges than the larger X_0 separations and with a steeper response. The operation of the sensor was shown to remain unaffected up to 40 °C with the main limiting factor being the dark current from the photodiodes. The theoretical predictions concerning the spike at the short ranges and the linear response at longer ranges were proved correct.

7.3. EXPERIMENTAL MEASUREMENTS OF STATIC DISPLACEMENT WITH THE PROPOSED SENSOR USING A MATT WHITE PAPER AS TARGET

Experimental measurements on static displacement were also performed using matt white paper (MWP) as target. The sensor was arranged as explained in Chapter 5.4 (see Figure 5.21). For this purpose a new sensor head jig similar to that shown in Figure 6.3 was constructed but with 5 V-grooves, the outer ones being at a distance of 3.34 mm from the middle V-groove. This was necessary so that the front detecting POF would not block part of the emission distribution from the emitting POF when $X_0 > 2$ mm.

For the smaller X_0 separations, i.e. $X_0 = 1$ mm and $X_0 = 2$ mm, calibration was performed with $X_0 = 0$ mm at R = 100 mm resulting in $S1_{MWP} = S2_{MWP} = 31.87$ mV ($S1_{MWP}$ and $S2_{MWP}$ stand for the signals detected and S_{MWP} the transfer function of the sensor when the target used is matt white paper). For the other, larger, X_0 separations calibration was performed again since the three POFs had to be removed and positioned in the outer V-grooves of the new sensor head jig. Thus, calibration was performed with $X_0 = 0$ mm at R = 100 mm resulting in $S1_{MWP} = S2_{MWP} = 31.3$ mV. A single run for each X_0 separation was performed and the results are shown in Figure 7.22. The responses shown resulted in the following equations when the LSF was applied to each of them individually:

$$S_{MWP_{X_0=1mm}} = (0.746 \pm 0.003)R + (1.354 \pm 0.380) \qquad \textbf{Eq. (7.26)}$$

$$S_{MWP_{X_0=2mm}} = (0.370 \pm 0.001)R + (1.700 \pm 0.078) \qquad \textbf{Eq. (7.27)}$$

$$S_{MWP_{X_0=3mm}} = (0.239 \pm 0.001)R + (1.545 \pm 0.077) \qquad \textbf{Eq. (7.28)}$$

$$S_{MWP_{X_0=4mm}} = (0.180 \pm 0.001)R + (1.487 \pm 0.047) \qquad \textbf{Eq. (7.29)}$$

$$S_{MWP_{X_0=5mm}} = (0.150 \pm 0.001)R + (1.345 \pm 0.035) \qquad \textbf{Eq. (7.30)}$$

As before the inverse of the above equations was taken and was used to define the relationship for measured range. Numerical data are shown in Table 7.6.

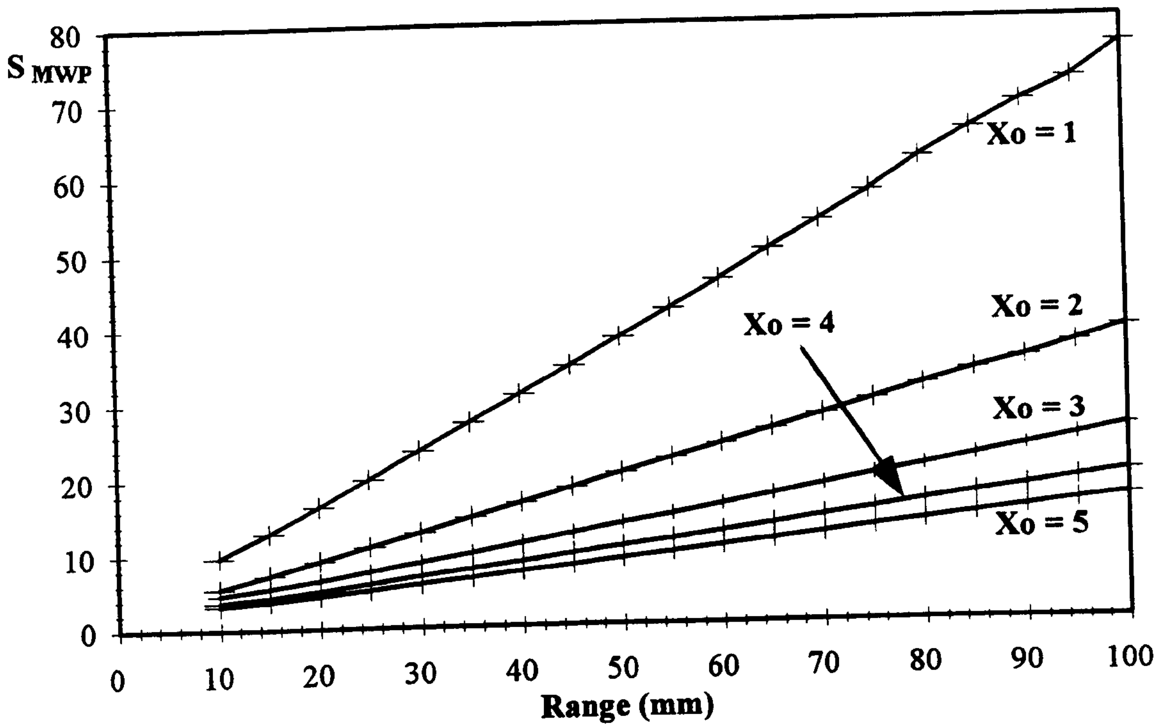

Fig. 7.22: The sensor response for various X_0 separations when matt white paper is used as target

Table 7.6: Experimental sensor response when matt white paper is used as target

X_0 separation, mm	$X_0 = 1$	$X_0 = 2$	$X_0 = 3$	$X_0 = 4$	$X_0 = 5$
y separation, mm	2.2	2.2	3.4	3.4	3.4
LSF, mm	10 - 100	10 - 100	20 - 100	20 - 100	25 - 100
(dS / dR), Theoretical	0.722	0.361	0.239	0.179	0.143
(dS / dR), Experimental	0.746	0.370	0.239	0.180	0.150
C, LSF	1.354	1.700	1.545	1.487	1.345
Operational Range, mm	20 - 100	15 - 100	25 - 100	20 - 100	25 - 100
Accuracy, (%)	1.0	0.7	1.0	0.6	0.7

As seen in Figure 7.22 and Table 7.6 this version of the sensor is indeed a scalable one experimentally as well with the smaller X_0 separations having a higher slope than the larger ones. There is also very good agreement between the theoretically and experimentally obtained slopes (Chapter 5.4). All the attempts produced a linear response with an accuracy better than 1 %. The minimum range of all X_0 separations is controlled by the diffusive nature of the target, even though the reflectivity coefficient of matt white paper is quite high, and would tend to make the operational range start at a longer range. This is also aided by the increased y separation of the larger X_0 separations.

It is important to note here that the maximum operational range of all X_0 separations is at R = 100 mm which is the maximum point in the range where experimental data could have been obtained due to hardware limitations. When a mirror was used as target the maximum point in the range where accuracy better than 1 % was obtained was R = 90 mm for X_0 = 4 mm and X_0 = 5 mm. This may suggest that since X_0 = 1 mm achieved accuracy better than 1 % up to R = 100 mm when matt white paper was used, then a much longer operational range would be expected for the larger X_0 separations since the separation (difference) between the two detected signals could be larger.

When matt white paper is used as target it was concluded that the proposed displacement sensor performs even better than what it did when a mirror was used as target offering longer linear operational ranges with higher accuracy. The scalability of the sensor has also been proved to hold with this arrangement as well.

7.4. RESOLUTION

The resolution of any sensor is an important parameter and has to be determined. It invariably depends upon the accuracy with which the individual signal values can be measured, any inherent fluctuations in these, and hence the resultant S values. With the existing arrangement, $S1_R$ and $S2_R$ are measured using DMMs with an accuracy of ± 0.01 mV at 80 mV and so lack of accuracy is not expected to be a limiting factor.

Resolution measurements were performed at two ranges for 1 mm ≤ X_0 ≤ 5 mm. The ranges were 20.00 mm ≤ R ≤ 20.25 mm and 70.00 mm ≤ R ≤ 70.25 mm. The measurements were performed in steps of 10 μm change in range. The intensity of the LED was arranged so that full advantage of the DMMs accuracy could be taken. For $X_0 = 1$ mm, $S1_R \approx 1995.1$ mV and $S2_R \approx 1817.7$ mV at the short range and at the long range $S1_R \approx 171.42$ mV and $S2_R \approx 166.61$ mV. Resolution measurements at short ranges are shown in Figure 7.23 and at long ranges in Figure 7.24. The S_R values shown for both ranges and all X_0 separations have been normalised with respect to their first reading and an arbitrary different constant was added to each case so that they would not overlap but would be close enough for comparison purposes.

As seen in Figure 7.23 a resolution of 10 μm (0.05 %) for all X_0 separations at the short ranges is possible. It is also noticeable that the distribution of the experimental points becomes more linear (smoother) at larger X_0 separations. This must be due to the larger difference between the two signals as seen in Table 7.7.

From Figure 7.24 where the resolution measurements performed at longer ranges are shown, it is obvious that the attainable resolution is not as good as at the short ranges. Resolution of 70 μm (0.1%) for all X_0 separations has been obtained. Here again the distribution of the experimental points becomes more linear at larger X_0 separations. Table 7.7 shows the percentage difference between the signals $S1_R$ and $S2_R$ for this attempt as well.

Table 7.7: Difference (%) between the detected signals at the two ranges

X_0 Separation (mm)	$X_0 = 1$	$X_0 = 2$	$X_0 = 3$	$X_0 = 4$	$X_0 = 5$
Difference (%), R = 20 mm	8.8872	16.3767	23.0400	28.1950	32.4532
Difference (%), R = 70 mm	2.8060	5.2432	7.5998	9.7732	11.5385

The distribution of the points in Figure 7.24 is not smooth, especially for $X_0 = 1$ mm at long ranges. This effect, i.e. fall of S_R as range increases, is due to the limited accuracy of the DMMs in conjunction with the denominator of the transfer function (eq. 5.6). This effect was confirmed using the computer program by limiting the number of digits available for the calculations and proved that this is the reason.

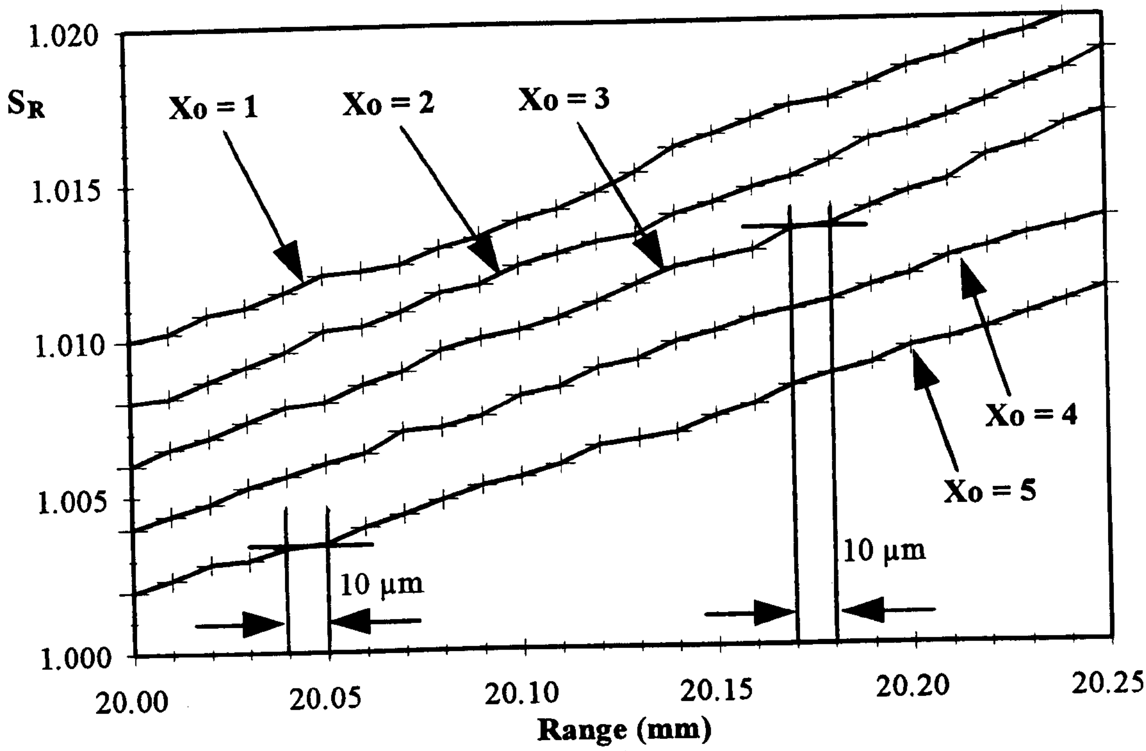

Fig. 7.23: Resolution measurements at close ranges
(S_R values normalised plus constant)

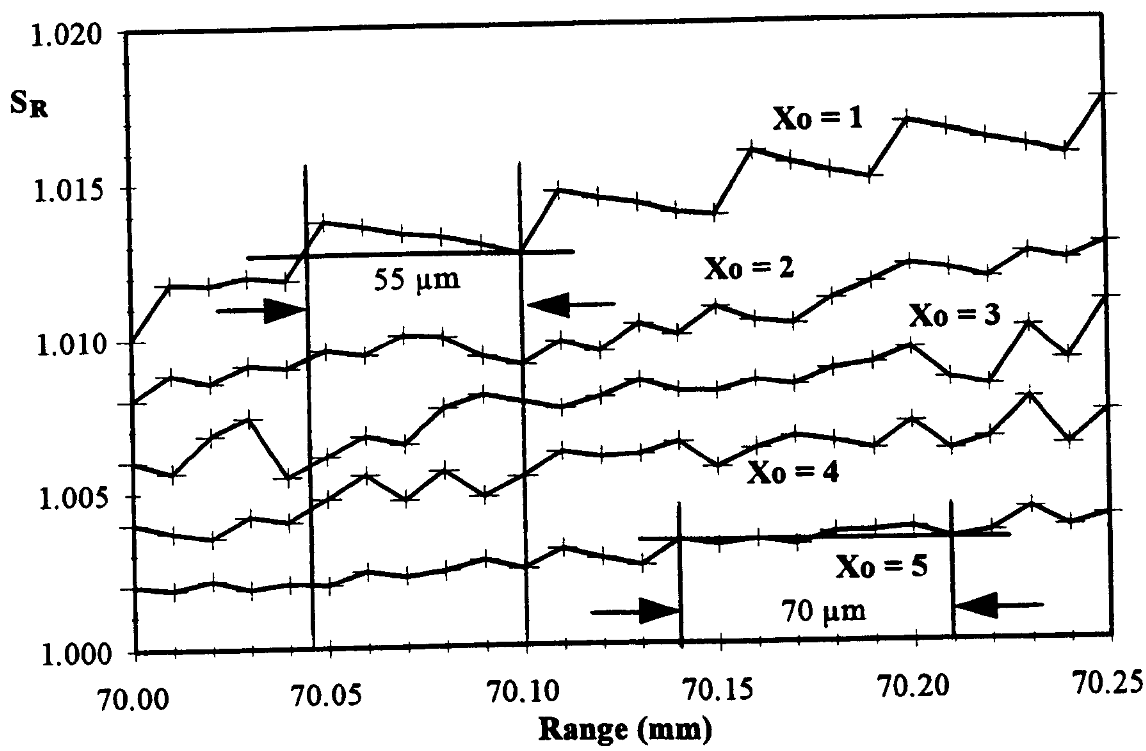

Fig. 7.24: Resolution measurements at long ranges
(S_R values normalised plus constant)

Also, any fluctuations in the measured signals will affect the attainable resolution by lowering it. Here again the denominator of the transfer function has a major effect. In order to check this the signals detected and their resultant S_R value at R = 70.00 mm for X_0 = 1 mm were considered:

$S1_R$ = 171.42 mV $S2_R$ = 166.61 mV S_R = 70.2765

If the $S2_R$ value fluctuates by its last digit, then:

$S1_R$ = 171.42 mV $S2_R$ = 166.62 mV S_R = 70.4250

which is a change in S_R of 0.21 %.

If in addition of this the $S1_R$ value fluctuates by its last digit in the opposite direction, then:

$S1_R$ = 171.41 mV $S2_R$ = 166.62 mV S_R = 70.5699

which is a change in S_R from the initial value of 0.42 %.

In this case, the 0.1 % resolution claimed earlier for this long range becomes 0.42 %. The accuracy of the DMMs used may be assisting in this shortcoming of the sensor but DMMs of higher accuracy can only be used under laboratory conditions and will offer no advantages towards commercialisation of the sensor. In a later section of this Chapter analogue to digital converters (ADC) are used. If these are offering the accuracy of the DMMs used here, will only cause the price of the sensor to increase considerably.

Resolution measurements were also performed for matt white paper (MWP) targets at two ranges for three X_0 separations using steps of 5 μm for the short ranges (shown in Figure 7.25) and 10 μm for the long ranges (shown in Figure 7.26). The S_{MWP} values shown for both ranges and all three X_0 separations have been normalised with respect to their first reading and a different constant was added to each response.

At short ranges, a resolution of 45 μm (0.18 %) for X_0 = 1 mm, 30 μm (0.12 %) for X_0 = 3 mm and 5 μm (0.02 %) for X_0 = 5 mm is possible. The stepwise increase of S_{MWP} for X_0 = 1 mm is caused by the inadequate accuracy of the DMMs in conjunction with the low level signals detected, since only one third of the full scale of the DMMs was used. The X_0 = 5 mm separation has similar amplitude signals detected but the larger separation between them makes it an arrangement with a smoother scatter of the experimental points offering higher levels of resolution.

At long ranges resolution of 60 μm (0.6 %) for the three X_0 separations has been obtained. The scatter of the experimental points becomes less at large X_0 separations.

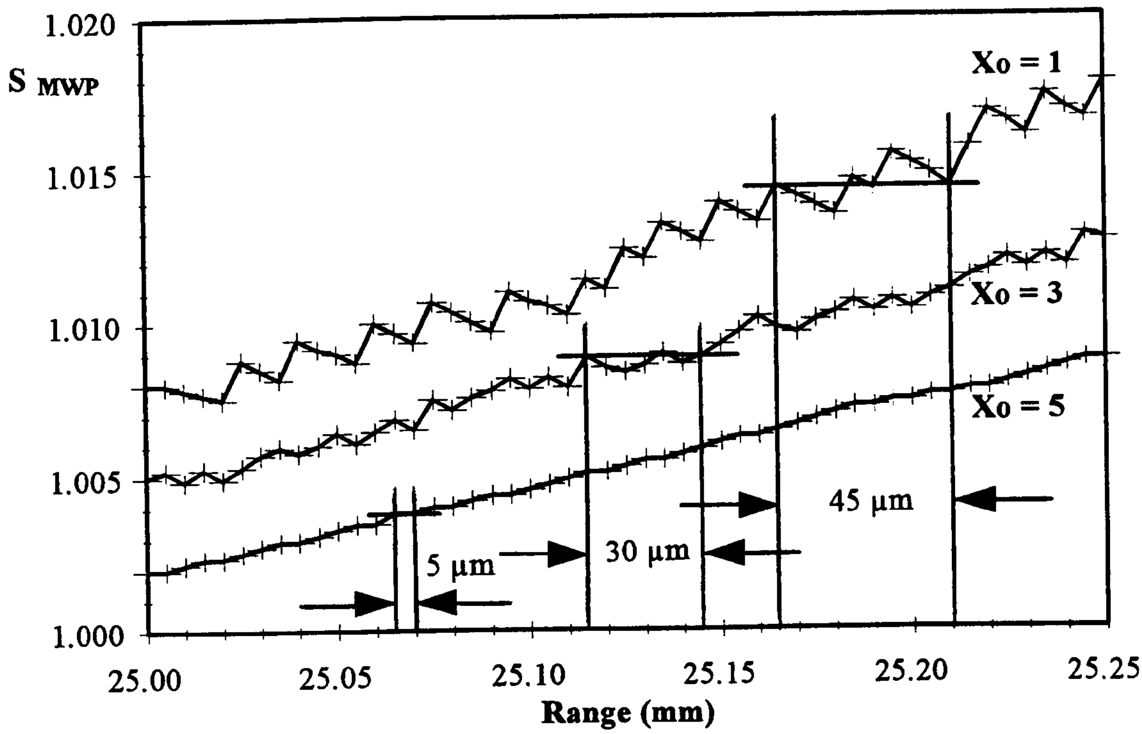

Fig. 7.25: Resolution measurements at close ranges (S_{MWP} values normalised plus constant)

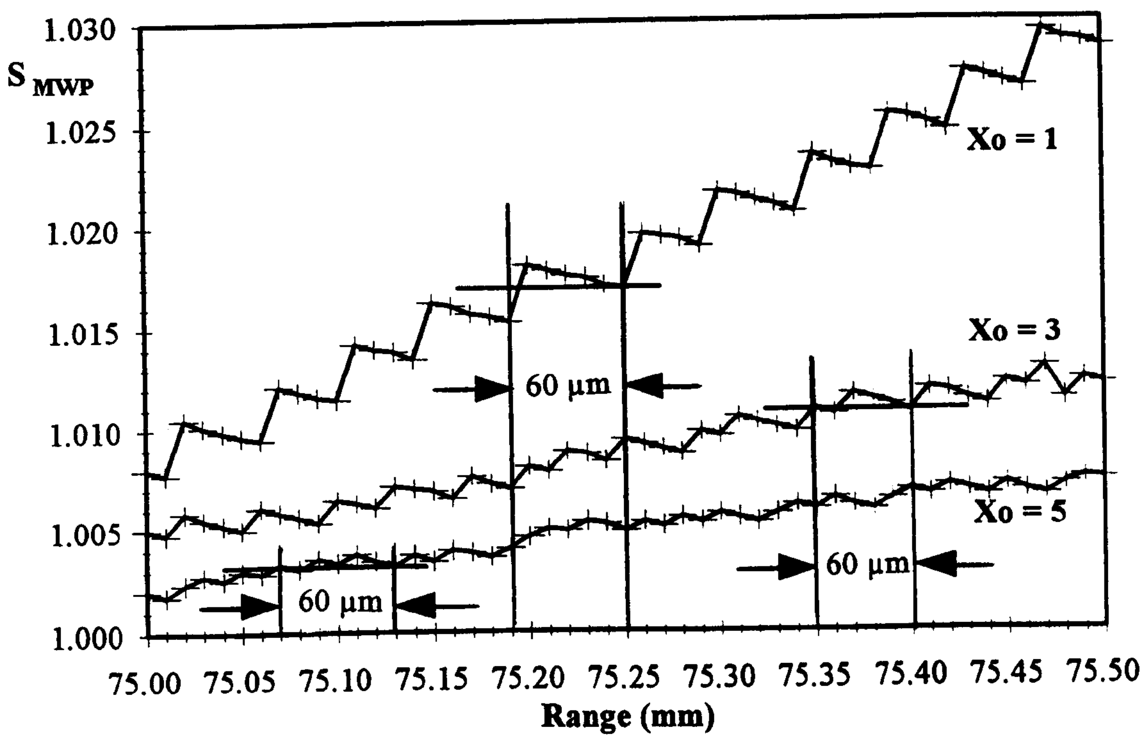

Fig. 7.26: Resolution measurements at long ranges (S_{MWP} values normalised plus constant)

The signals detected for $X_0 = 1$ mm at the short range were $S1_{MWP} \approx 676.9$ mV and $S2_{MWP} \approx 611.3$ mV, and at the long range $S1_{MWP} \approx 81.26$ mV and $S2_{MWP} \approx 77.83$ mV. If the maximum accuracy that the DMMs offer (4.5 digits) was taken into consideration (as done for the mirror target) then a higher resolution would have been obtained.

The influence of fluctuations in the measured signals was also checked in a similar way as it was done for the mirror, using their resultant S_{MWP} value at R = 75 mm for X_0 = 1 mm and resulted in the resolution increasing from 0.06 % to 0.58 %.

Another factor which would affect the resolution of the sensor is the length of the three POFs used, as explained in Chapter 5.5 since each 5 m length will itself introduce a 1 dB attenuation to the signal (emitted and detected).

Overall, the resolution of the method will not only depend on the digits of the measuring instruments, whether these are DMMs or ADCs, and any fluctuations induced by them, but will also depend on factors such as temperature variation, ageing of the detectors and the LED, similarity in the operation and stability of the detecting circuits and changes in the reflectivity of the target used. Temperature elevation will cause ageing effects on the LED and detectors with a decrease in the output of the LED as well as a spectral shift, and a decrease in the responsivity of the detectors. These effects will not only affect the resolution of the sensor but will affect every aspect of its operation which will include its accuracy and operational range and should be taken into consideration when designing any sensor system.

7.5. VERIFICATION OF SUCCESS OF CALIBRATION

Since the calibration of the two detecting circuits is considered to be of paramount importance, its validity and success should be investigated and verified. Calibration of the two detectors, as explained in Chapter 6.7, refers to the degree of similarity in their operation over the useful operational range with the aim being to make them operate as identically as possible. Consider Figure 7.27 which shows the result of calibrating the two detectors by arranging them with $X_0 = 0$ mm prior to obtaining the experimental responses shown in Figure 7.21 where a mirror was used as target.

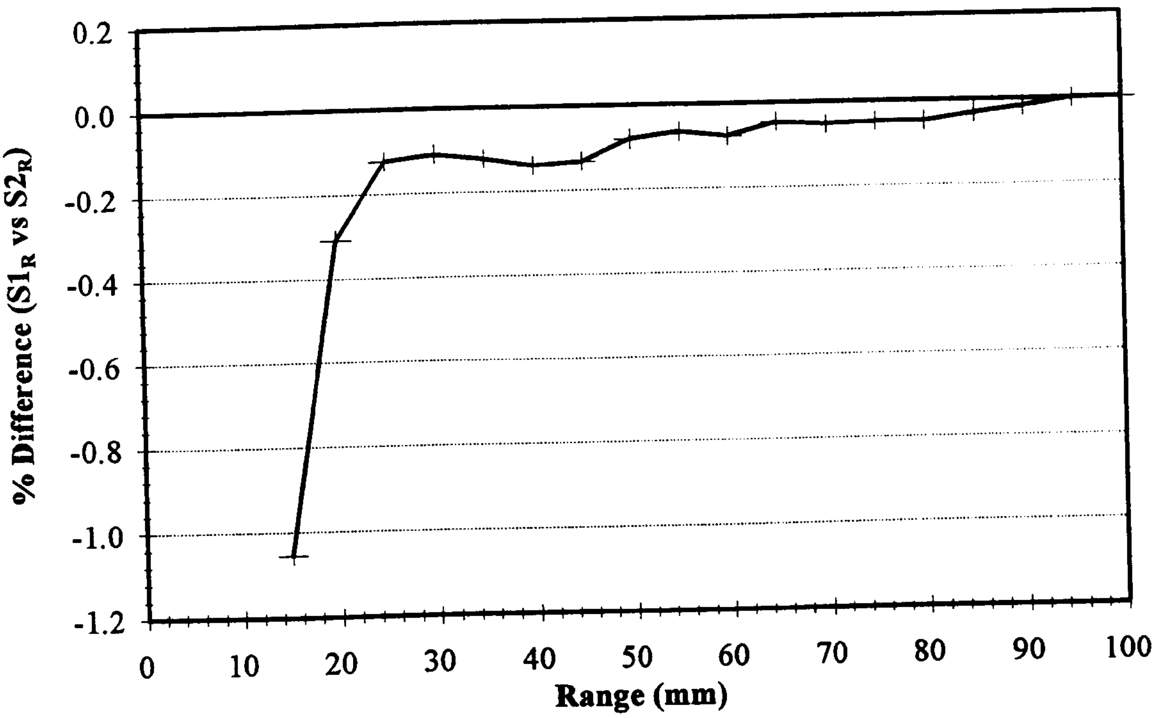

Fig. 7.27: Difference (%) between the two detectors (mirror target)

It is obvious from Figure 7.27 that detector 2 receives more light than detector 1, hence the negative percentage difference values of the experimental points shown. This suggests that there is a slight angular misalignment involved in the arrangement which may be caused by the mirror, the support or polishing of the three POFs or even a combination of all resulting in the two detecting fibres not receiving the same amount of light. The distribution of the points may also suggest that the fibre emission is slightly non-uniform.

Calibration, for the attempt shown in the figure above, was performed at R = 90 mm. Here the difference between the two detectors is very small (~ 0.02 %) and remains so for the ranges 25 mm < R < 100 mm (< 0.13 %). At the shorter ranges the difference starts to increase rapidly becoming 0.31 % at R = 20 mm and 1.05 % at R = 15 mm.

The effect of angular misalignment suggested above is of course more noticeable at the shorter ranges where the angles involved between the emitting fibre, the mirror and the detecting fibre are larger than if at the longer ranges. Consider Figure 7.28 which shows the angles involved when considering the emission and reception for one detecting fibre. The same holds for the other detector since they are arranged symmetrically around the emitting fibre with X_0 = 0 mm.

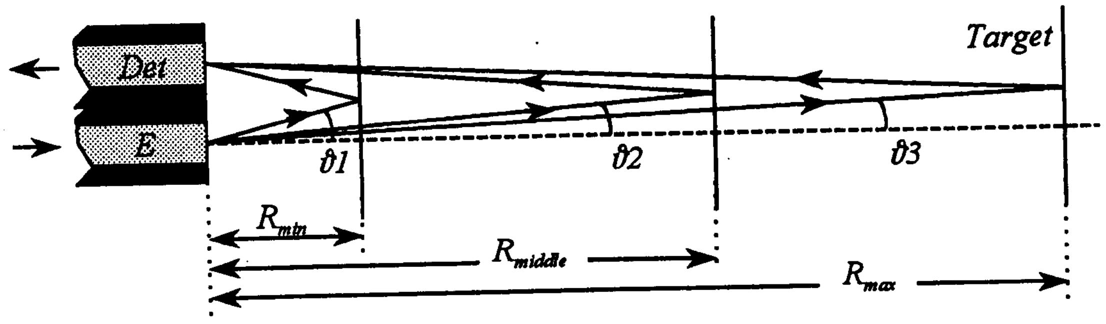

Fig. 7.28: The angle of emission depends on the range

The angle involved in the emission towards the detector at R_{min} is larger than the other two and the angle involved at R_{max} is the smallest one, i.e. $\vartheta 1 > \vartheta 2 > \vartheta 3$. Under ideal conditions, i.e. the fibres being polished perpendicularly to their axis and the mirror being perfectly aligned, the light received from each detecting fibre would come from the opposite side of the emission distribution of the emitting fibre (Figure 7.29) and should be the same for both detecting fibres for each range. This would not be the case if there is a misalignment in the angle involved. Consider Figure 7.29 which shows two emission distributions, one without a misalignment (eq. 7.1) and the other with a misalignment of 3^0 (eq. 7.2) for a mirror target.

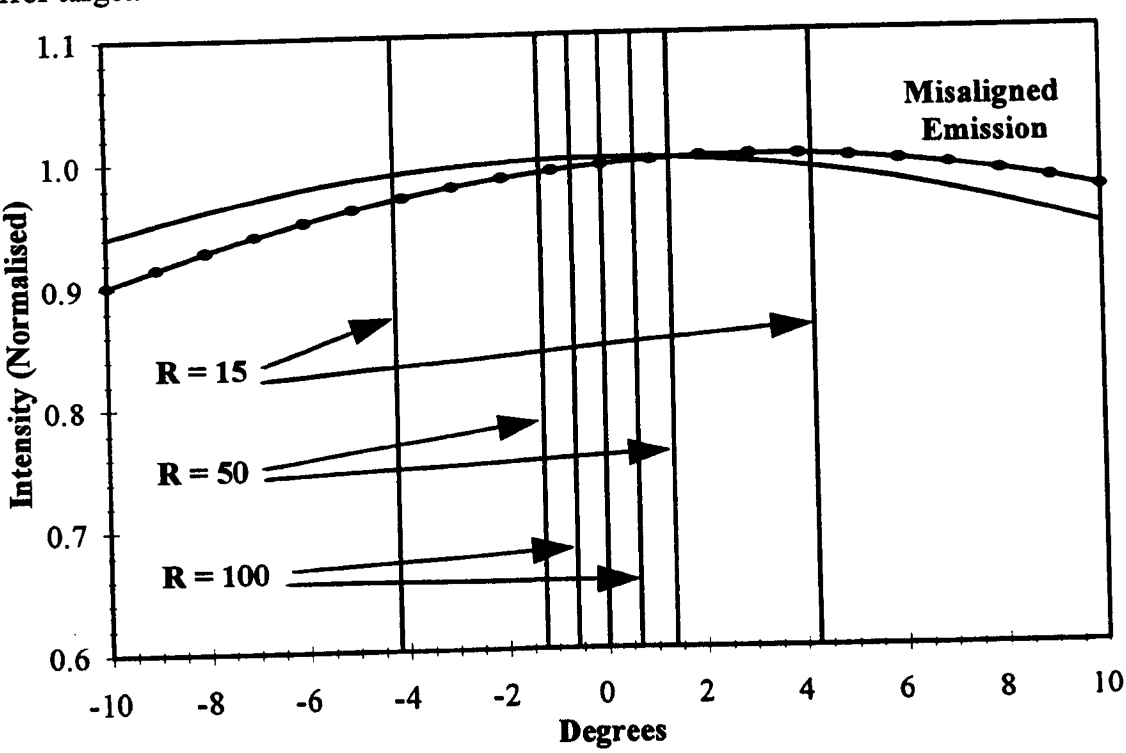

Fig. 7.29: The emission detected by the detecting fibres at various ranges with and without misalignment (mirror target)

The perpendicular lines shown in Figure 7.29 indicate which part of the emission will be detected by the two detecting fibres at three points in the range, R = 15 mm, R = 50 mm and R = 100 mm if a mirror is used as target. The angle involved at R = 15 mm is 4.2^0, at R = 50 mm is 1.3^0 and at R = 100 mm is 0.6^0. At longer ranges, the two points on the emission distribution which direct light towards the two detecting fibres are closer, thus any error from possible misalignments that may be present becomes smaller. Also, as the range increases the part of the emission which is reflected back to the two detecting fibres becomes flatter. At short ranges, where the angle involved is large and the emission distribution changes more significantly, any misalignment present is immediately affecting the balance between the two detectors.

Assuming that the only signal difference that may exist between the two detectors (as shown in Figure 7.27) is caused by a misalignment of the emission distribution, the two signals were modified and their difference was calculated using equation 7.2. The result for a misalignment of 0.3^0 is shown in Figure 7.30 for the experimental points shown in Figure 7.27.

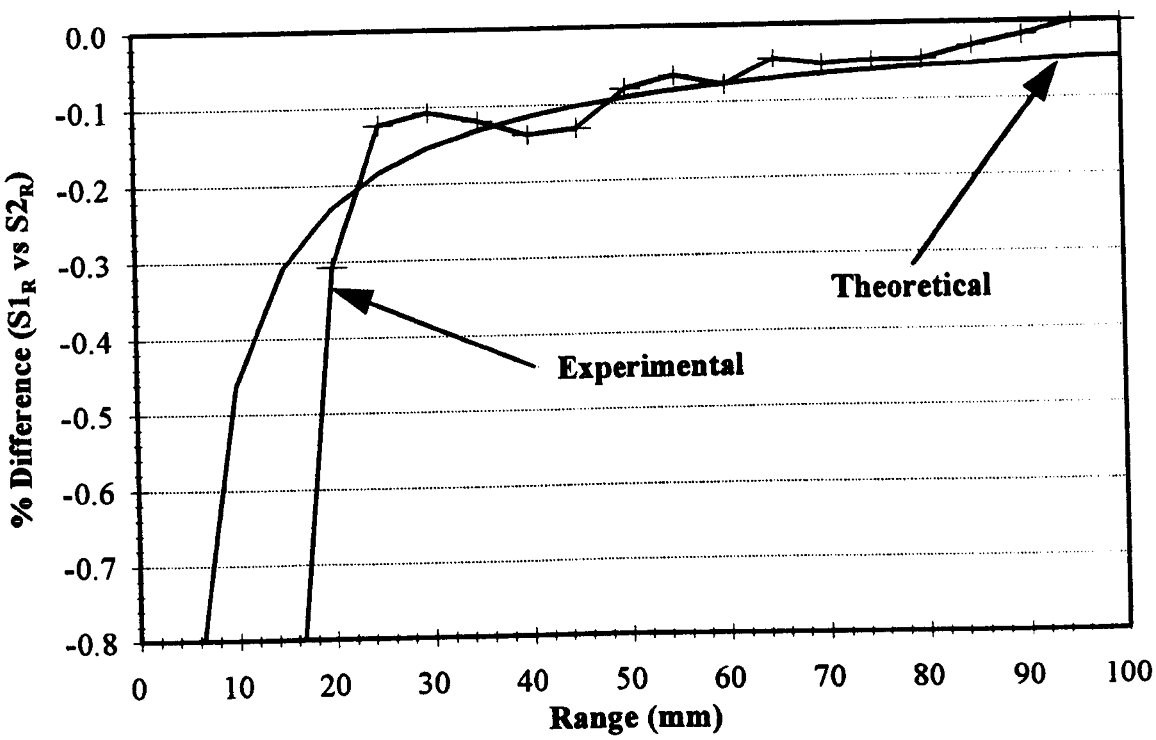

Fig. 7.30: Theoretical misalignment compared to the experimental points of Figure 7.27 (mirror target)

The similarity between the distribution of the experimental points and the theoretical one is very good over the range 20 mm < R < 100 mm. At R < 20 mm the experimental points deviate at a faster rate than the theoretical ones. This is accounted by the fact that the distribution used (eq. 7.1) for the theoretical analysis is broader than that determined experimentally (see Figure 7.2).

The angular arrangement achieved during the calibration stage is bound to alter once the three fibres are arranged in their displacement sensing configuration, shown in Figure 5.1, with the emission directed towards the detecting fibre positioned closer to the mirror having the larger angle (see Chapter 5.4 and Figure 5.18).

When considering an assumed 0.3^0 misalignment and the very small difference between the two detected signals (0.13 % for 25 mm < R < 100 mm) this has to be considered a very successful calibration attempt since linear responses resulted from this calibration with 1 % difference between true and measured range for operational ranges up to 75 mm for $X_0 = 5$ mm. This now suggests that if a maximum difference between true and measured range of 1 % is desirable with a mirror as target, then a difference of around 0.1 % between the two detected signals should be obtained for the range of interest.

In a similar attempt using matt white paper as target, the percentage difference of the two signals varied as shown in Figure 7.31 (calibration with $X_0 = 0$ mm at R = 100 mm). The sensor responses are shown in Figure 7.22.

As seen in Figure 7.31 the difference between the two detected signals is very small (< 0.04 %) over the range 30 mm < R < 100 mm increasing to 0.31 % at R = 10 mm with detector 2 receiving slightly more light than detector 1. The distribution of the points is smoother than the one shown in Figure 7.27 and this is due to the diffusing effect of light by the matt white paper, resulting in smoothing the beam profile.

When matt white paper is used as target the total amount of light emitted from the emitting POF hitting the target will be re-emitted in a Lambertian way. The detecting fibres will receive the re-emitted light directed towards them from the target with various levels of intensity as long as this is within their acceptance angle. The angles of Figure 7.28 show the path that the beam of light with the highest intensity will follow towards each of the detecting fibres.

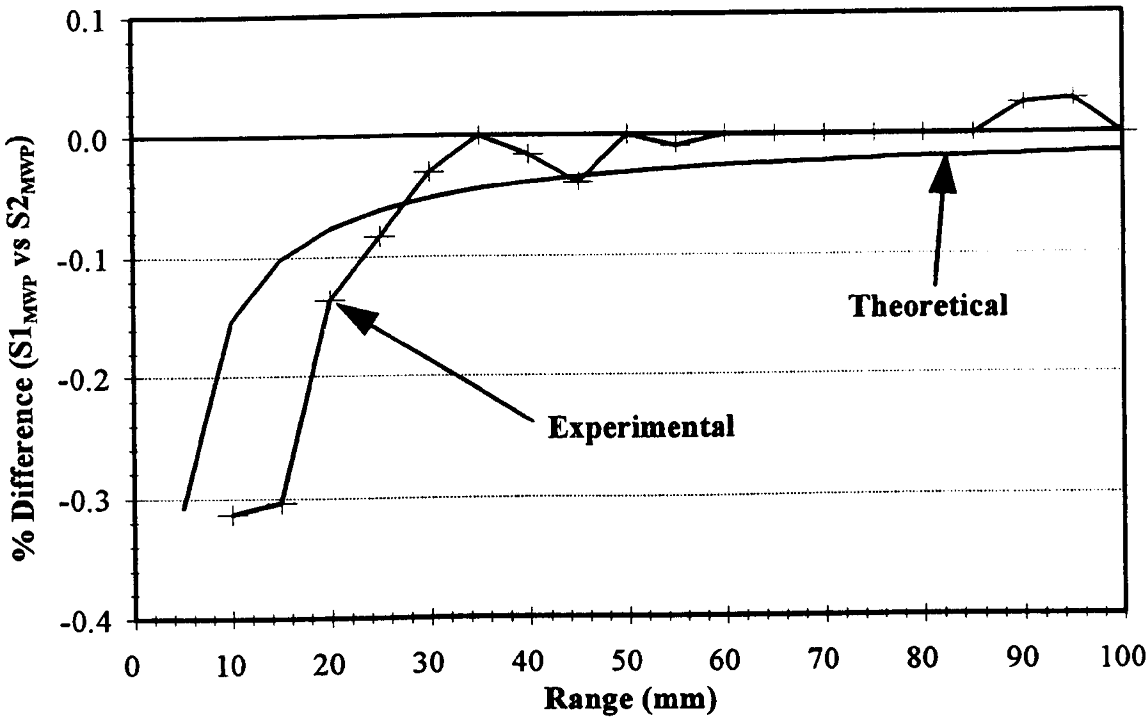

Fig. 7.31: Difference (%) between the two detectors after calibration has been performed (matt white paper as target)

The imbalance shown in Figure 7.31 at the very short ranges (R < 15 mm) is again thought to be caused by emission misalignment. In this case the imbalance is mainly caused by angular misalignments on the detecting fibres. The emission misalignment calculated for this attempt is 0.05^0 and the theoretical distribution is shown in Figure 7.31 alongside the experimental points for comparison purposes.

This calibration attempt is also considered a very successful one since only a 0.05^0 misalignment was involved and it resulted in operational ranges of 85 mm with an accuracy of < 1 % being limited only by the maximum range (R = 100 mm) where measurements of displacement were performed, due to hardware limitations. This result shows that the difference of 0.05 % obtained between the two detecting signals for the range of interest, with matt white paper as target, can result in a difference between true and measured range of 0.7 % (X_0 = 5 mm in Table 7.6).

The above experiment and investigation showed that calibrations with very small angular misalignments involved in the measurements can be achieved. The attempt where matt white paper was used obtained the best calibration due to the nature of the target itself. Although such accurate alignments as the ones shown above may not be necessary for the successful operation of the sensor, if they are achieved they will assure larger operational ranges with a relatively early starting point and with high accuracy.

In order to achieve calibrations such as the ones presented in this section, care has to be taken in the way the POFs are polished. Polishing of the POFs is outlined in Chapter 6.2.

7.6. SYMMETRY IN THE EMISSION OF A POF

An accurately polished fibre should have a symmetrical emission around the optical and physical axes of the POF, which should coincide. To determine whether the polishing of the POFs resulted in the desired degree of symmetry of emission the following test was performed.

The three POFs were positioned in the sensor head jig facing the mirror target with $X_0 = 0$ mm and calibration was performed at R = 100 mm. Measurements were then performed over the range 15 mm < R < 100 mm in steps of 5 mm and the percentage difference between the two detected signals was calculated. Then, the emitting POF was rotated by 90^0 clockwise and calibration was again performed at R = 100 mm and the measurements were repeated (every time the fibres in the sensor head jig had to be adjusted in any way, calibration had to be performed again). The same procedure was repeated two more times with the emitting POF rotated to 180^0 and 270^0 clockwise from the original 0^0 reference position. The results are shown in Figure 7.32.

As seen in Figure 7.32 the percentage difference between the two detected signals is changing slightly when the emitting POF is rotated. The biggest changes take place at the shorter ranges. The level of difference change is small (< 1 %) suggesting that the polishing procedure was successful in providing a POF whose physical and optical axes were, if not totally coincident, very close. The structure of some of the responses shown above suggests that the emission distribution may not be very uniform. It also suggests that if the detecting fibres themselves were now to be rotated by an unknown amount then the percentage differences shown might be affected, aiming for an improvement.

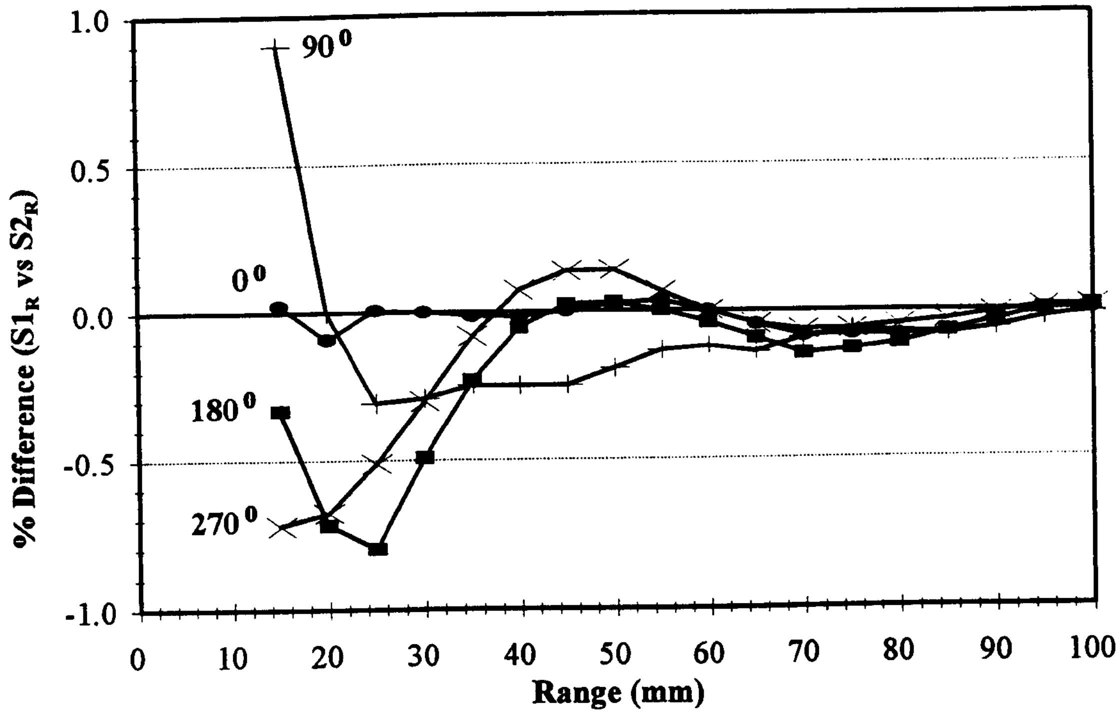

Fig. 7.32: Rotation of the emitting POF resulted in various percentage differences between the two detected signals when a mirror was used as target

In another attempt, a similar test was performed using matt white paper as target. Calibration was performed at R = 100 mm and the emitting POF was rotated by 90^0 clockwise each time with the percentage difference between the detected signals taken and shown in Figure 7.33.

From Figure 7.33 it can be seen that a similar effect is present when matt white paper is used as target. The distribution of the points is smoother than the ones where a mirror was used as target, which is due to the diffuse (Lambertian nature) reflection of paper. The increase in the difference between the signals detected at the shorter ranges suggests that the polishing jig itself, although helping in producing a very good polish quality, may suffer uneven material removal due to the non-uniform pressure applied on it during polishing. This may also lead to angular misalignments. A much harder non-metal material therefore should be used in order to avoid this effect and also avoid the presence of metal particles during polishing which scratch the fibres.

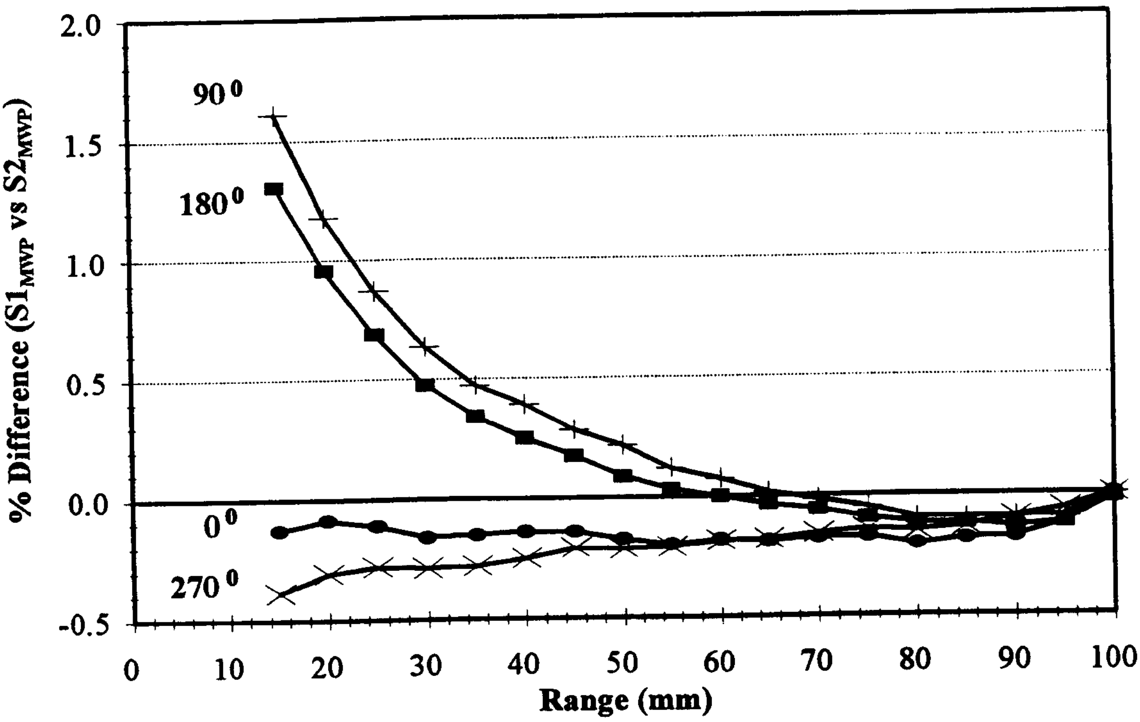

Fig. 7.33: Rotation of the emitting POF resulted in various percentage differences between the detected signals when matt white paper was used as target

Further tests showed that polishing the POFs to the finest grade, i.e. 1 μm, is not necessary. When polishing the emitting POF was stopped at 30 μm and the fibre was repositioned in the sensor head jig in exactly the same way as it was before, a very similar percentage difference response between the detecting fibres was obtained. This test emphasises the fact that the symmetry of emission around the optical/physical axes of the emitting fibre (rather than the POF polish state) is the important factor in obtaining a good calibration and thus a linear displacement sensor response.

A good balance between the two detecting fibres was shown to be obtainable by using the method of rotating the emitting fibre with any type of target used. In some attempts where the rotation of the emitting fibre did not give the desired result improvement was achieved by rotating one (or two) of the detecting fibres.

The method of rotating the POFs assisted in achieving a long, linear and accurate operational range. This, however, may not be a realistic method for mass producing a sensor for displacement measurements. In such a case, ways of limiting angular misalignments will have to be devised.

7.7. TARGET ALIGNMENT

The alignment of the target is also a very important factor in achieving the desired similarity in operation between the two detectors. In order to determine the importance of alignment of the target the following tests were performed.

The three POFs were positioned horizontally in front of the mirror target with X_0 = 0 mm and calibration was performed at R = 90 mm only once before any measurements were taken since the fibres were not to be disturbed again. Measurements were then performed over the range 15 mm < R < 100 mm in steps of 5 mm and the results are plotted in Figure 7.34. The mirror was rotated horizontally by 0.25°, 0.5°, 0.75° and 1° clockwise (CW) and 1° counterclockwise (CCW), -1° in Figure 7.34. Accurate angular rotation was achieved by using the reflection of a laser beam by the mirror onto a graduated surface.

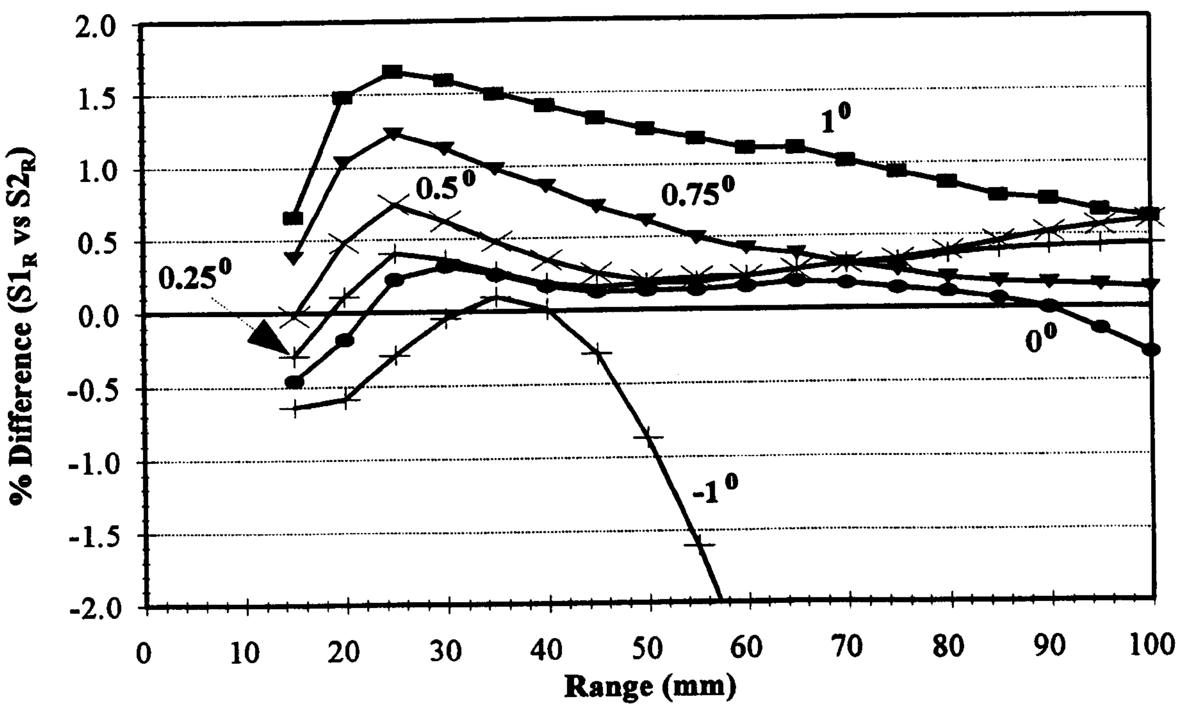

Fig. 7.34: Rotation of the mirror in the direction of the fibres (about a vertical axis)

It is immediately evident from this test that the alignment of the mirror target is a very important factor in the operation of this sensor. As seen in the above figure a rotation of the mirror of 1° CW will cause a significant imbalance between the detectors. A -1° rotation (CCW) breaks the balance from the middle towards longer ranges. The 1% difference between the two detectors remains for 0°, 0.25° and 0.5° CW rotation. The level of imbalance obtained was 0.3 %/0.25^0 (1.3 %/^{0}) for a horizontal rotation of the target.

The same test was performed with the mirror rotated vertically with respect to the three POFs. The horizontal position of the mirror was returned to the 0^0 position and then similar measurements were performed for 0.5^0 and 1^0 upwards and 1^0 downwards (-1^0). The results are shown in Figure 7.35.

The result shown in Figure 7.35 is again important suggesting that a slight misalignment of the mirror can again seriously limit the operational range of the sensor. It must be pointed here that the misalignment in this direction will not harm the sensor as much since, as is shown, a rotation of 1^0 downwards did not cause a big imbalance over the range 15 mm < R < 80 mm.

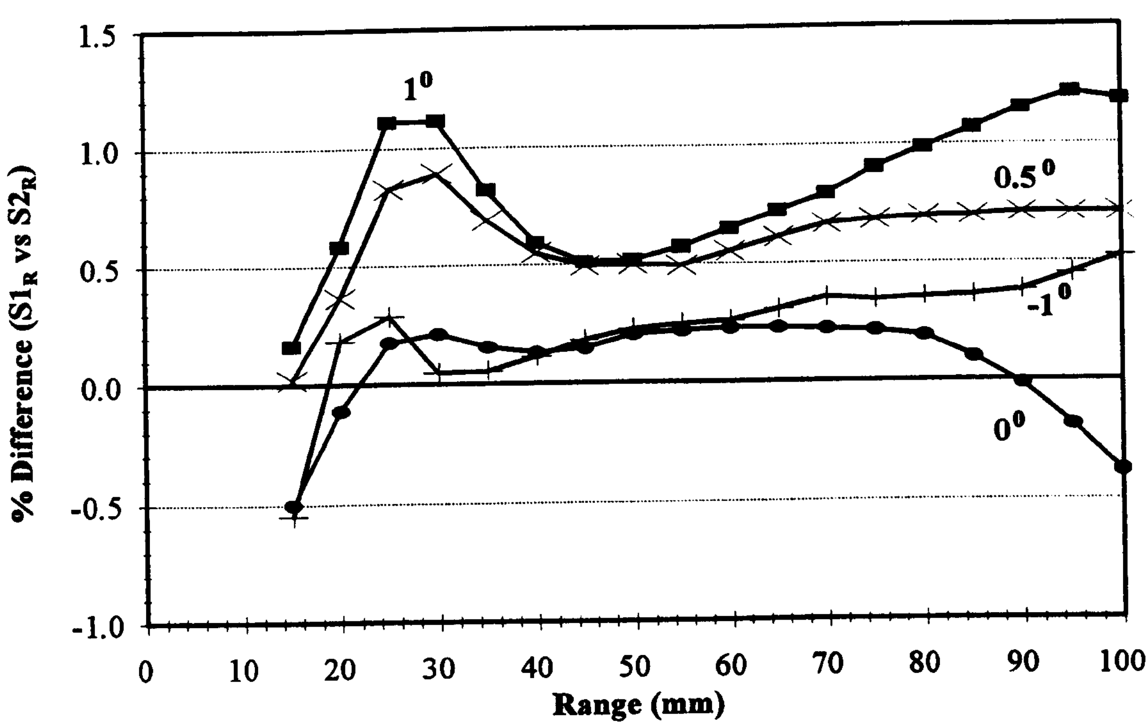

Fig. 7.35: Rotation of the mirror target about a horizontal axis

The same tests were performed with a matt white paper as target. Calibration was performed at R = 100 mm and the target was rotated between 0^0 and 5^0 CW in steps of 1^0 and the results are shown in Figure 7.36.

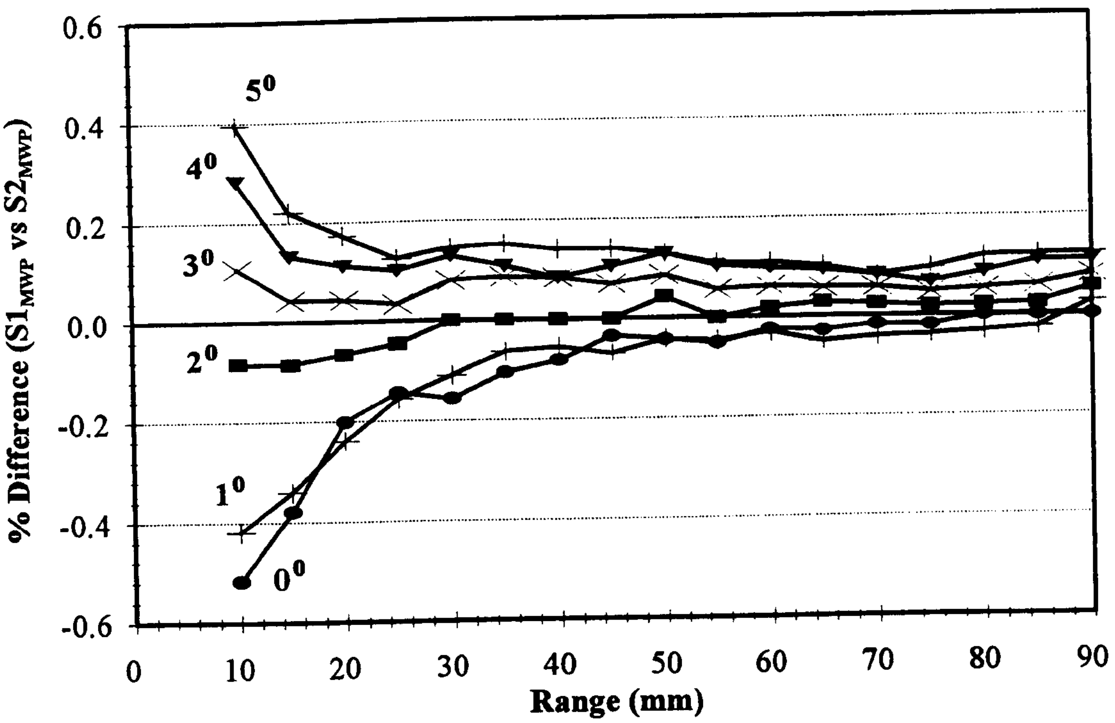

Fig. 7.36: Rotation of the target (matt white paper) about a vertical axis

It is immediately evident from figure 7.36 that target rotation when matt white paper is used will not affect the balance between the two detectors as much as it did when a mirror was used as target. The rotation of the target seems to affect the balance between the two detectors only at the short ranges (R < 20 mm) and even so it does that by a very small amount. The imbalance caused is 0.06 %/^{0} for R > 20 mm and 0.15 %/^{0} for R = 15 mm. The best position of the target seems to be at the 2^0 position.

The vertical rotation of the target was performed once the target was returned back to the 0^0 point without recalibrating. Rotation was performed only once to 5^0 upwards and the result is shown in Figure 7.37.

The 5^0 rotation of the mirror upwards caused only a 0.1 % difference in the imbalance of the two detectors for the whole range (10 mm < R < 100 mm). This suggests a level of imbalance of 0.02 %/^{0} of target rotation.

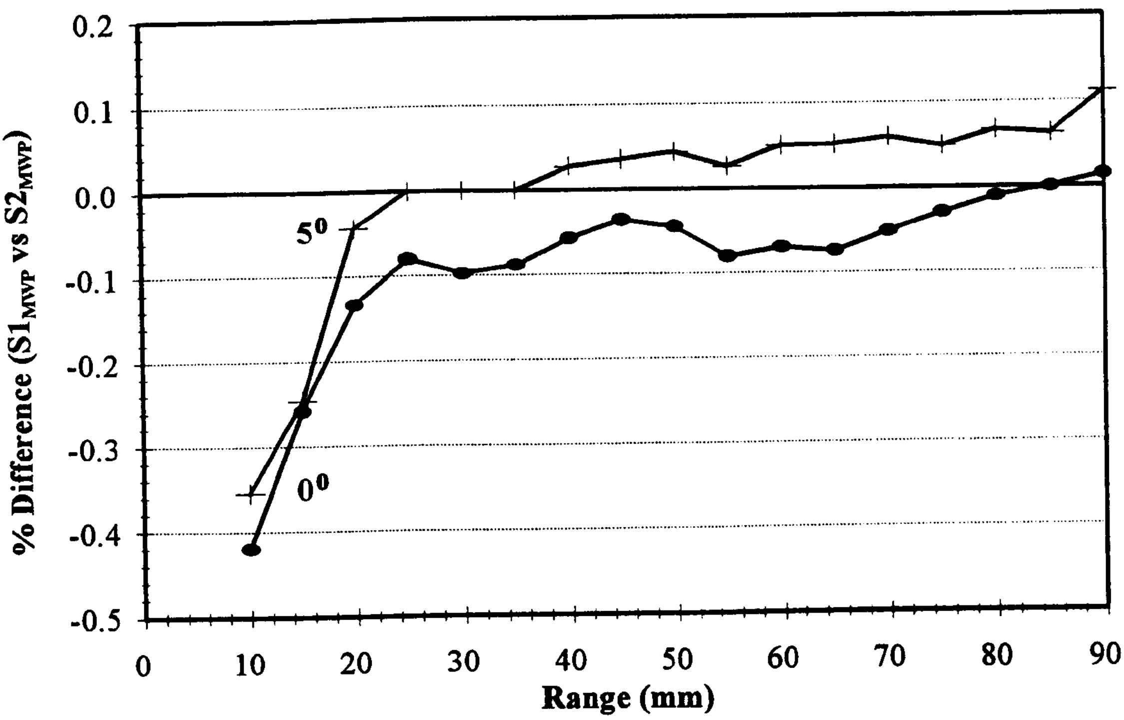

Fig. 7.37: Rotation of the target (matt white paper) by 5^0 about a horizontal axis

The rotation of the two targets used resulted in the sensor arrangement which uses matt white paper as target being very stable in its response and being affected the least by target misalignments (0.06 %/^{0}). The opposite can be said for the sensor arrangement which uses a mirror as target. A rotation of the mirror by 0.25^0 resulted in an obvious imbalance between the two detectors (0.3 %/0.25^0). Therefore, from the above, the sensor using matt white paper as target could be a very attractive option against the equivalent using a mirror as target due to the diffuse reflective nature of its surface.

7.8. USING SEVEN (7) PLASTIC OPTICAL FIBRES

An alternative version of the sensor was constructed using 7 POFs instead of 3 in a coaxial arrangement, as shown in Figure 7.38, in order to overcome possible misalignment problems encountered and obtain more efficient light detection.

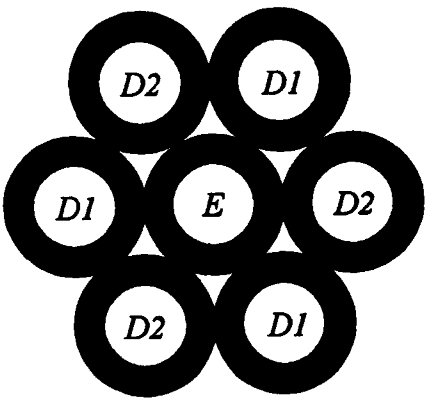

Fig. 7.38: Sensor arrangement using 7 POFs

As seen in the figure above, the emitting fibre was positioned in the middle of the six detecting fibres, which were surrounding it and were positioned in an alternating configuration. In the sensing arrangement, the group of POFs denoted as "D1" would be positioned ahead of the emitting POF by an X_0 separation whereas the group of those denoted as "D2" would be positioned behind having the same X_0 separation. The X_0 for each fibre could be set with ~ 0.05 % accuracy.

In this arrangement each group of three POFs would be looking at three different parts of the emission and so be able to compensate for any unevenness/misalignment in the distribution of the emitted light.

The other end of the detecting fibres of each group was positioned in one SMA connector which has been machined so as to be able to accommodate the cores of all three POFs. Polishing was performed once the cores of the three POFs of each group were glued inside the SMA connectors. The emitting and detecting electronic circuitry remained the same.

The first thing noticed was the saturation of the detector outputs due to the increased level of illumination detected by the fibres. Thus the driving current of the LED was decreased from 60 mA to 35 mA in order to decrease the light output from it.

Calibration was performed at R = 100 mm (mirror target) having all the fibres arranged at $X_0 = 0$ mm. Calibration testing followed and the resulting difference between the two detectors was taken and is shown in Figure 7.39. The distribution of the points was not a linear one suggesting that misalignment may be present. The emitting fibre was then rotated in a similar way as it was rotated at section 7.6. These results are also shown in

Figure 7.39.

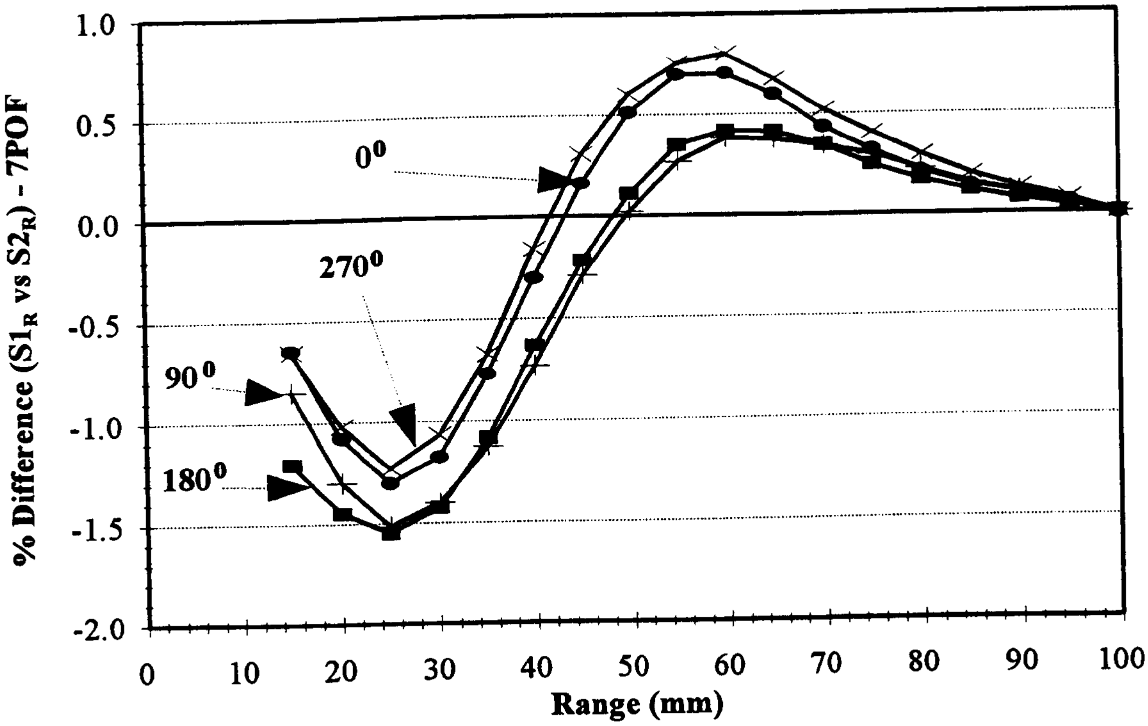

Fig. 7.39: Rotating the emitting fibre when in a 7 fibre arrangement

As seen in the figure above, the reproducibility of the non-linear distribution points of the percentage difference between the two detectors is maintained although the emitting fibre has been rotated. This is an effect caused by the alternating arrangement of the detecting fibres in the sensor head jig. This arrangement seems to be able to smoothen the distribution of the points but does not seem to be able to compensate for the inherent misalignments that are present due to polishing. This calibration was not expected to result in a linear response once the fibres were arranged in their displacement sensing configuration. This was also proved and is shown in Figure 7.40.

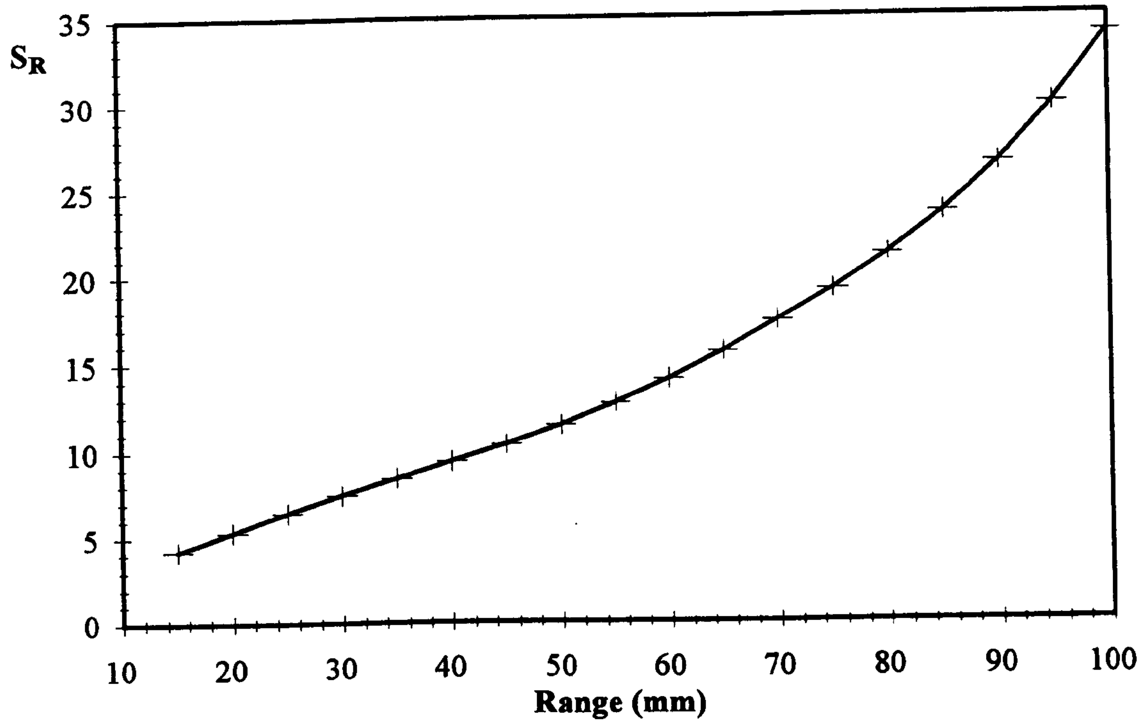

Fig. 7.40: The sensor response resulting when 7 POFs are used

The arrangement where 7 POFs are used in the sensor head has resulted in increased levels of illumination being detected. This was the only advantage gained whereas the overall performance of the sensor deteriorated resulting in a non-linear response. The alternating arrangement of the detecting fibres left no room for balancing of the emission misalignment through rotation of the emitting fibre. An arrangement such as this cannot improve the performance of the sensor apart from offering a smoothing effect on the distribution of the points detected.

The detecting fibres could also be arranged in various other configurations such as those shown in Figure 3.7. The intensity of the light detected will definitely increase, but as far as linearity of response is concerned the result would be uncertain. The arrangement where three POFs are used seems to offer the best linearity of response.

7.9. OPERATION OF THE SENSOR UNDER AMBIENT ILLUMINATION CONDITIONS

Due to the way that the electronic circuitry operated, i.e. under dc conditions, the successful operation of the sensor was dependent on the sensor operating under dark room conditions. At this stage it was important to find out how much the sensor would be affected if it were to operate under ambient illumination conditions, i.e. daylight or room illumination.

In order to investigate this possibility the sensor was calibrated and arranged to operate with X_0 = 5 mm and matt white paper as target under dark room conditions. Although it resulted in a linear response with 1 % accuracy between 25 mm < R < 100 mm, when the dark conditions where switched to ambient illumination conditions, the response shown in Figure 7.41 resulted.

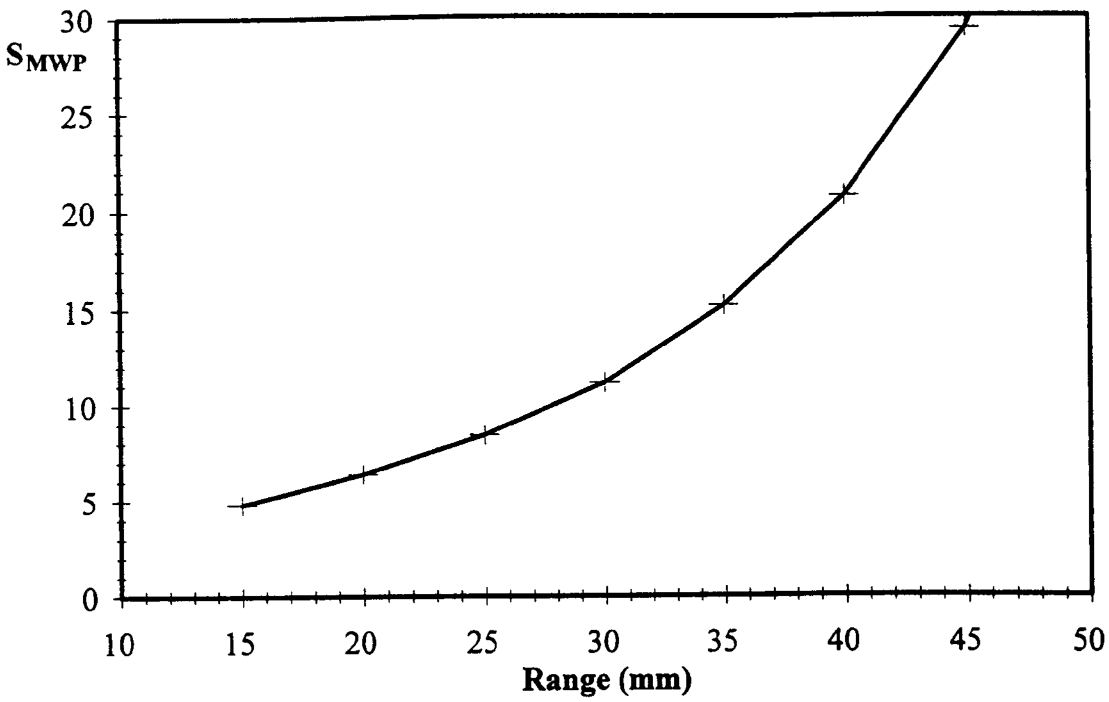

Fig. 7.41: Operation of the sensor under ambient illumination conditions (MWP)

As shown in the figure above when the sensor is operating under ambient illumination conditions the linearity of response breaks down completely making the sensor unusable. The response shown in the figure may vary depending on the level of ambient illumination with the highest levels having most detrimental effect. Similar effects were observed with a mirror target. It is therefore most important that some means to desensitise the ambient illumination effects is found.

In an attempt to solve this problem the emitting and detecting circuits were modified to operate under ac conditions. The modifications consisted of modulating the LED using pulses (~ 7.5 kHz) and including a high pass filter in the detecting circuits to remove the dc component due to ambient illumination (Chapter 6.5).

Following the successful operation for removal of the ambient illumination effects from the detected signals, the sensor was arranged to measure static displacements under ambient illumination conditions with a matt white paper as target. Calibration was performed at R = 90 mm ($S1_{MWP} = S2_{MWP} = 65$ mV) and then the X_0 separation was arranged at 5 mm. The detected signals, which were measured using the two 4.5-digit DMMs, varied from 1.4 V at R = 15 mm down to 50 mV at R = 100 mm. The resulting sensor response is shown in Figure 7.42.

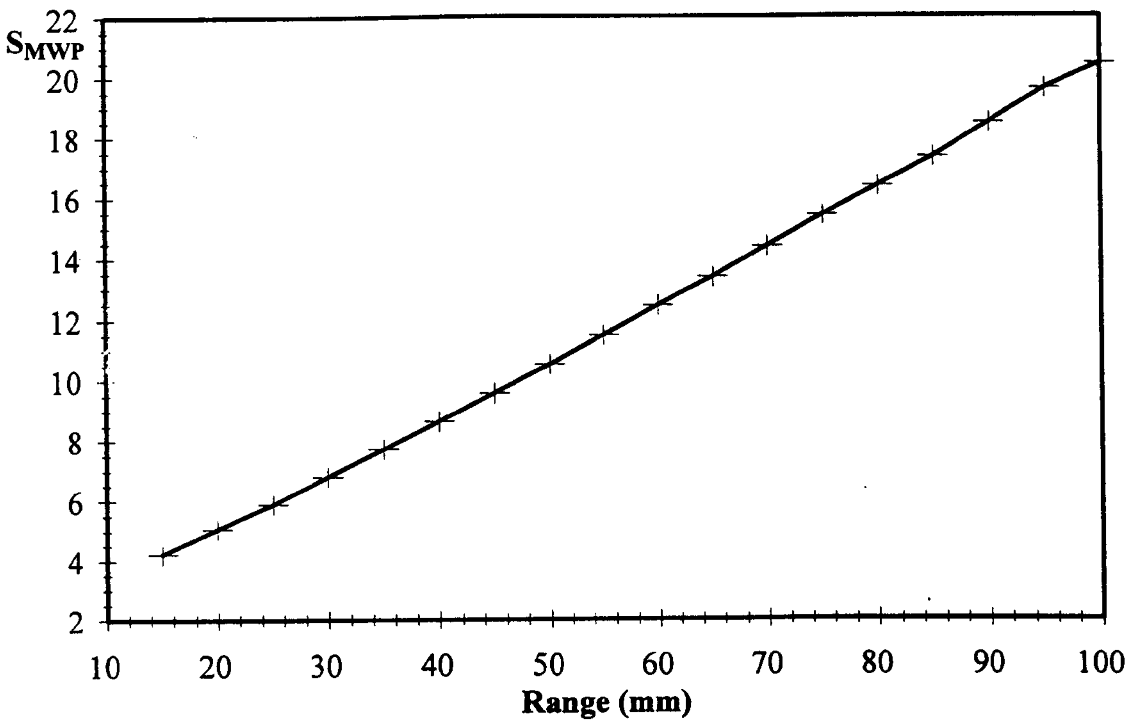

Fig. 7.42: The sensor response with matt white paper as target and $X_0 = 5$ mm under ambient illumination conditions

From what is shown in Figure 7.42 a linear response has been obtained with the present arrangement. The calibration curve of this response is shown in equation 7.31:

$$S_{MWP} = (0.189\pm0.001)R + (1.130\pm0.087) \qquad \textbf{Eq. (7.31)}$$

The inverse of equation 7.31 was used to define the relationship for measured range. A linear operational range between 25 mm and 85 mm with a 1 % accuracy was achieved.

Compared with the attempt with $X_0 = 5$ mm shown in Figure 7.22 (Table 7.6) there is a definite change in the slope of the two responses with the one taken under dark room conditions (0.150) being closer to the theoretical (0.143) than the one obtained under ambient illumination conditions (0.189). The reason for that may be the fact that the X_0 separation was not arranged to be exactly 5 mm but it was smaller. Also, the detecting electronics which operated under very different conditions than before, will have an effect in the detection of the signals. What is important here, however, is the fact that this new arrangement which enabled the sensor to operate under ambient illumination conditions has resulted in a linear response over an operational range of 60 mm. The smaller operational range achieved here is due to the higher noise levels of the opamps used, the lower levels of illumination from the LED due to its modulation and also by the optical filters introduced between the end of the two detecting POFs and the active element of the PIN photodiodes. These would limit the detecting wavelength range of the photodiodes to a few tens of nanometres around 660 nm, but would also lower the level of the detected signals thus affecting the extend of the operational range towards the longer ranges.

7.10. AUTOMATED OPERATION OF THE SENSOR

In view of the fact that the next stage in the sensor development was the measurement of dynamic variables such as vibration (see Chapter 8) automation of the sensor was an important requirement. This was achieved by connecting the detecting circuits via 12-bit Analogue to Digital Converters (ADCs) and the emitting circuit via an Input/Output (I/O) card to a Personal Computer (PC) and control them using software. Experimental results with this automated version of the sensor performed under ambient illumination conditions for static displacement measurements are presented in this section.

Once the automated version of the sensor has been built and tested, calibration of the two 12-bit ADCs was performed by connecting them to a power supply which would supply a voltage input to both ADCs over the whole of their operational range. Calibration of the two detecting circuits was performed using the two DMMs with $X_0 = 0$ mm at R =

80 mm. Following, the outputs of the two detecting circuits were connected to the inputs of the two ADCs. Calibration was then confirmed using the complete system.

The X_0 separation between the POFs was then arranged to 5 mm and the target used was matt white paper. The program shown in Appendix A2 was used to control the operation of the sensor and the collection of data. A set of 50 measurements was taken for each range and the resultant response, using ADCs (S_{MWP}), is shown in Figure 7.43.

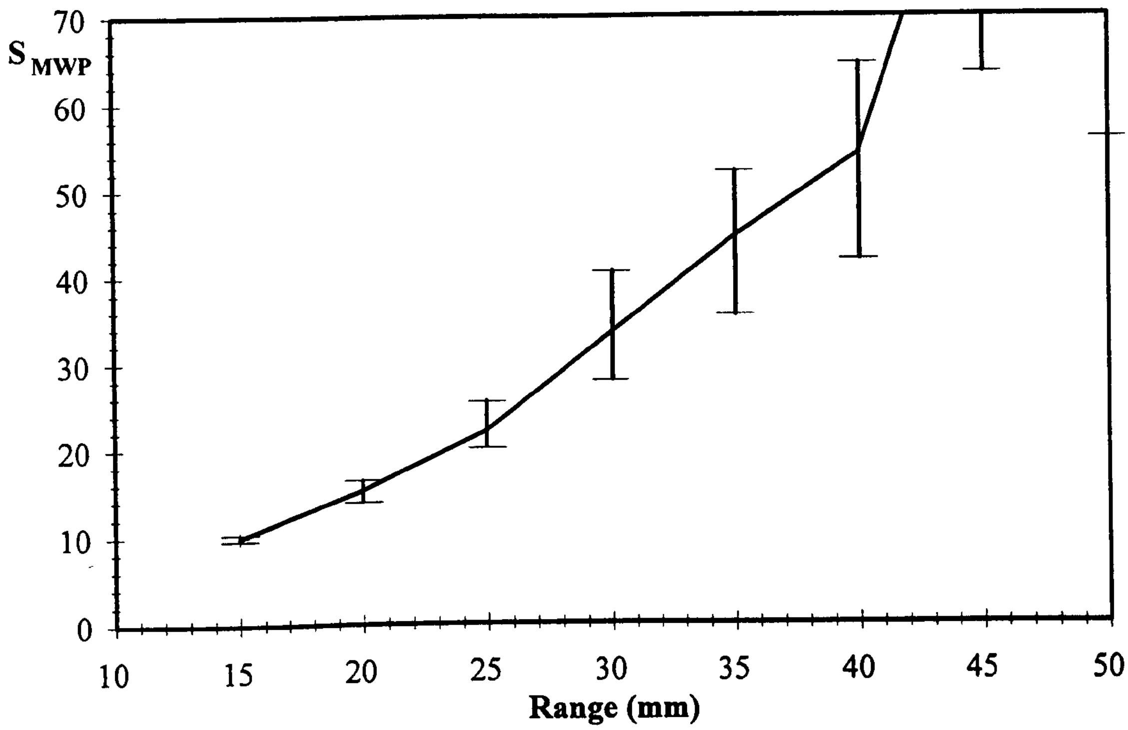

Fig. 7.43: The automated sensor response with matt white paper as target and X_0 = 5 mm under ambient illumination conditions

From what is shown in the figure above, linearity of response is obtained only for small parts of the range but the overall response is not very linear. The deterioration in sensor performance is an effect caused by the use of ADCs. The spread of points at each range is large increasing at longer ranges. The solid line shown connects the average points from the spread of each range. The LSF was applied between 25 mm and 40 mm.

The response resulted in the following calibration curve (eq. 7.32) whose inverse was used to define the relationship for measured range. The percentage differences between true and measured range for this attempt are shown in Figure 7.44.

$$S_{MWP} = (2.151 \pm 0.066)R + (-31.268 \pm 0.739) \qquad \textbf{Eq. (7.32)}$$

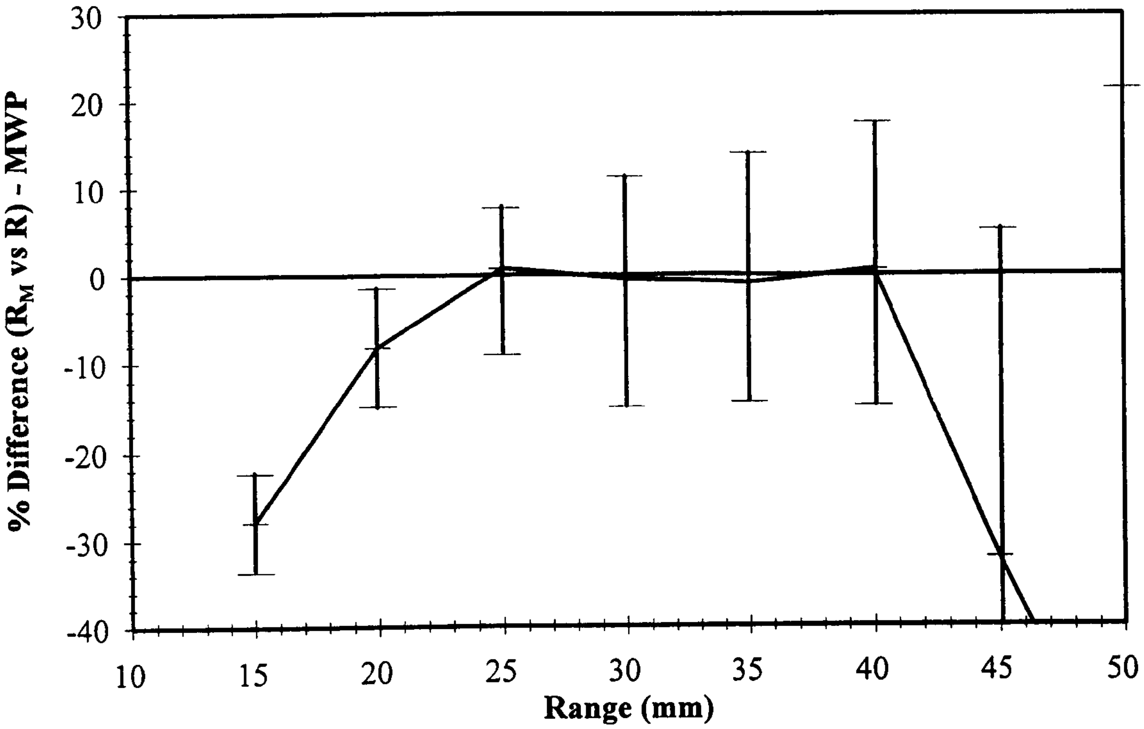

Fig. 7.44: Percentage difference between true and measured range for the automated version of the sensor (X_0 = 5 mm, MWP)

It is immediately evident from Figure 7.44 that the sensor response obtained with the automated version of the sensor has lower accuracy than the one with the DMMs. Although the average accuracy with the ADCs is 1 %, for the range between 25 mm and 40 mm, a maximum error of 17 % is possible towards the longer ranges. With the DMMs better accuracy (1 %) is obtained over the whole operational range.

From the above experiment it can be seen that the automated version of the sensor will result in a lower operational range with lower accuracy than if DMMs are used. However, linearity of response over the range 25 mm < R < 40 mm has been obtained from the average of 50 repeated measurements, and the average accuracy in the range is 1 %. With the use of DMMs one can obtain a much longer range 25 mm < R < 100 mm with a 1 % accuracy. Linearity of response was also achieved when a mirror was used as target with similar effects.

There are clearly some advantages that the DMMs have which help achieve this performance. Firstly, their reading range can be arranged to vary depending on the level of signal input returning a much higher reading accuracy. Secondly, their frequency of response is extremely slow (hundreds of ms) resulting in integration of the detected signal thus rejecting high frequency noise which on the other hand is detected by the high-speed ADCs

(10 μs). Nevertheless, the use of ADCs for automating the sensor measurements has been demonstrated as successful.

7.11. SUMMARY AND CONCLUSIONS

In this chapter experimental work done on the sensor has been presented. Two types of target were used these being a mirror and a matt white paper. The two signals detected were measured using two digital multimeters and the analysis of the data has been performed manually apart from Section 7.9 where the sensor has been automated.

At first, the basic assumptions taken in the theoretical considerations were shown to hold experimentally as well. Experimental investigation showed that the behaviour of the detected signal from a POF is very similar to the theoretical one based on the inverse square law having a difference of < 1 % for R > 25 mm. The POF far field emission distribution was also measured experimentally and was found to be narrower than the lambertian distribution used in the theoretical analysis. It was found to be similar to $\cos^4\vartheta$ having a difference < 1 % for ± 12^0 around the axis of emission. This only affects the sensor response by slightly shifting the beginning of the operational range towards longer ranges. A broad Lambertian emission, therefore, extends the beginning of the operational range towards closer ranges. The $\cos^4\vartheta$ distribution was then used to simulate the sensor behaviour in case where misalignments existed in the emitting fibre only. It was found that such a case would change the slope of the linear response but wouldn't affect its linearity.

Experimental measurements on static displacements were then performed on the sensor with simple circuits using the PIN photodiodes in the photoconductive mode, and showed that linearity of operation with 1 % accuracy over an operational range of 18 mm was possible with a mirror as target. Effects of resembling offset voltage did not allow this method to achieve a longer operational range. Also, for the range that calibration held true a linear operational range has been achieved. The spike predicted theoretically at the very short range, was also observed experimentally.

Experimental results when using detecting circuits with opamps in a transimpedance configuration, showed that the operational range could extend up to 80 mm at room temperature. At higher temperatures the linear response of the sensor was breaking down to a level which depended on the ability of the opamps to maintain their characteristics under such influences. The chopper stabilized opamps used managed to withstand changes in their operation due to increase of temperature better than the other types of opamp used. The operation of the sensor was shown to remain unaffected up to 40 ^{0}C. The main limiting factor of the detecting circuits was the dark current from the photodiodes.

The referencing technique used has been shown to be successful when the driving current of the LED was varied from 27 mA up to 80 mA, thus varying the light output of the LED, for individual runs of the same sensor arrangement and resulted in an accuracy better than 1 % and an operational range of 80 mm for any current setting. The intensity of the detected signals and thus their corresponding signal to noise ratio at any given range varied but the percentage difference between the two detected signals remained the same for any of those LED current settings.

The range was also varied randomly and 500 repeated measurements were taken. From this test an operational range of almost 70 mm with an accuracy of 1 % was concluded. The distribution of the points on the percentage error graph suggested that the emission from the emitting POF is not the smooth near lambertian far field emission distribution assumed to be but most likely had a distribution which was somewhat non-uniform (ragged).

The scalability of the sensing technique was also proved by taking measurements with the same arrangement for various X_0 separations again using a mirror target. The larger X_0 separations offered the longer operational range. The slopes of the resultant responses were very close to the theoretical predictions of Chapter 5.

Experimental work performed with matt white paper as target was in agreement with the results obtained through computer simulation. The slopes of all the responses were indeed very close to the ones predicted. The operational range extended up to R = 100 mm for all X_0 separations which was the maximum point that measurements could be performed due to hardware limitations. This suggests that the operational range could extend beyond R = 100 mm for all X_0 separations, with the larger separations achieving better performance in the longer range due to the larger separation of the signals detected.

The best case resolution of the method was investigated at two ranges. For a mirror target the measured resolution was 10 μm (0.05 %) at R = 20 mm and 70 μm (0.1 %) at R = 70 mm for all X_0 separations. For matt white paper the measured resolution was 45 μm

(0.18 %) for $X_0 = 1$ mm, 30 μm (0.12 %) for $X_0 = 3$ mm and 5 μm (0.02 %) for $X_0 = 5$ mm at R = 25 mm. Resolution of 60 μm (0.6 %) for the three X_0 separations has been obtained at R = 75 mm.

The resolution of the sensor could, however, be affected by many other factors, these being the length of the three POFs used, the number of the digits of the measuring instruments, whether these are DMMs or ADCs, and any fluctuations induced by them, on temperature variation, ageing of the detectors and the LED, similarity in the operation and stability of the detecting circuits and changes in the reflectivity of the target used. These effects will not only affect the resolution of the sensor but will affect every aspect of its operation which will include its accuracy and operational range and should be taken into consideration when designing any sensor system.

Further investigation was also performed using the experimental results in order to obtain more information about the behaviour of the sensor.

The validity of calibration was investigated by comparing the closeness of the two detected signals when $X_0 = 0$ mm which should be very close. For the case of a mirror target the difference between the two signals was around 0.1 % for R > 20 mm which resulted in a maximum difference between true and measured range of 1 % over that range. When matt white paper was used the difference between the two detected signals was 0.04 % for R > 30 mm which resulted in a maximum difference between true and measured range of 0.7 % over that range. Below these ranges the percentage difference between the two detected signals was increasing due to the POF angular emission misalignments which affected the distribution of the emitted light. These misalignments were calculated and were found to be very close to 0.3^0 for a mirror target and 0.05^0 for matt white paper. Calibrations with such small misalignments are considered very successful and although such accuracies may not be necessary for the successful operation of the sensor, if they are achieved they will assure large operational ranges with a relatively shorter starting range and with high accuracy.

The symmetry in the emission distribution from the emitting fibre was tested by arranging the three fibres with $X_0 = 0$ mm and rotating the emitting fibre. The results showed that the balance between the two detecting fibres varied as the emitting fibre was rotated. Both kinds of target arrangements (mirror and matt white paper) were shown to be affected by the rotation of the emitting fibre. This rotation provided a means of balancing the two detected signals to the highest level.

Target alignment was another area which was investigated. Very stringent tolerances resulted for the arrangement where a mirror was used as a target (1.2 %/^{0}). The arrangement with matt white paper as target resulted in much less stringent tolerances (0.06 %/^{0}) making it a very attractive option.

The performance of the sensor is considered to be impressive when considering all possible errors with the sensor achieving long linear operational ranges with accuracy of 1 %. But it is true to say that for the sensor to achieve such impressive performance many factors have to be taken into consideration. These are calibration, symmetry and level of misalignments in the emission distribution of the emitting fibre, level of misalignments of the target, and other effects such as temperature variation which may affect the electronic circuitry of the sensor. Prior to arranging the sensor for measurements, if the calibration is performed with an error/difference between the two detected signals of < 0.2 % over the range of interest then the accuracy of the sensor will be expected to be around 1 % for the range where calibration holds with the above mentioned value. In fact the calibration procedure will highlight any problems which may exist in the sensor arrangement by delivering a large and sometimes uneven distribution of the points showing the difference between the two signals.

The use of 7 POFs in the sensor arrangement in order to overcome the misalignment problems that can be present and also obtain better light detection was also investigated. 6 detecting fibres were positioned in a coaxial arrangement with the emitting fibre in the middle and the detecting ones in an alternating configuration around it. The improvement obtained using this arrangement was more efficient detection of the reflected light from the target but the response was not linear. Rotation of the emitting fibre did not offer any improvements on the linearity of response. The best sensor head arrangement is therefore the one with the three POFs and this is justified by the results obtained.

Under dc conditions, the sensor can achieve displacement measurements accurately over long ranges but only if it is operated under dark room conditions. As expected, operation of the sensor under ambient illumination brings about detrimental effects. By changing the dc operating circuitry to an ac one, desensitisation of the sensor from ambient effects was demonstrated resulting in an operational range between 25 mm and 85 mm with a 1 % accuracy for matt white paper when the detected signals were measured using two 4.5 digit DMMs.

Automation of the sensor has been achieved by the use of an I/O card and two 12-bit ADC cards to connect the emitting and detecting circuits to a PC. They were controlled using software. Experimental results under ambient illumination conditions and a matt white paper as target resulted in a linear response between 25 mm and 40 mm with average accuracy of 1 %. The spread of the points (50 repeated measurements per point), however, resulted in an increasing error as range increased. Nevertheless, complete automation of the sensor has been achieved.

From the results presented in this chapter, it can be claimed that the displacement sensor is indeed a very usable device. The extend of the achievable operational range will depend on the control electronics. When the data was measured using two DMMs and processed manually, it resulted in very long and accurate operational ranges. When two ADCs were used, due to their higher noise contribution (quantization noise), it resulted in much shorter operational ranges.

Chapter 8
Application of the Sensor to Vibration Measurements

Having demonstrated successfully the operation of the sensor with static displacement measurements, then application of the sensor to single degree vibration was considered an obvious and very useful application.

The application of the sensor to vibration measurements was directed towards the monitoring of large amplitude single degree vibrations. The amplitude of vibration should be in the order of a few millimetres, an area where other vibration sensors could not perform measurements. The frequency of vibration was in the order of several tens or even a few hundreds of hertz. The limits in amplitude and frequency of vibration were expected to be set by the structure of the target used and by the speed with which the PC could perform the commands of the program and read the ADCs respectively.

In order to monitor vibrations the sensor head has been positioned in front of the dust cap of the cone of the bass driver of a loudspeaker. Initial measurements have been performed without exciting the bass driver of the loudspeaker to obtain the calibration curve of the arrangement. Following, the bass driver was excited and measurements were performed at various frequencies.

8.1. SENSOR HEAD AND TARGET ARRANGEMENT FOR VIBRATION MEASUREMENTS

The sensor head and target arrangement was changed in this Chapter in order to accommodate a target which would be able to vibrate. This was a loudspeaker whose bass driver was to be excited by a function generator supplying a sinusoidal output at a pre-determined frequency. The sensor head was positioned in front of the dust cap of the bass driver, as shown in Figure 8.1. This was a curved target with cross-sectional diameter of 70 mm and radius of curvature of 35 mm which was sprayed with white paint so as to increase the diffuse reflectivity coefficient of the target.

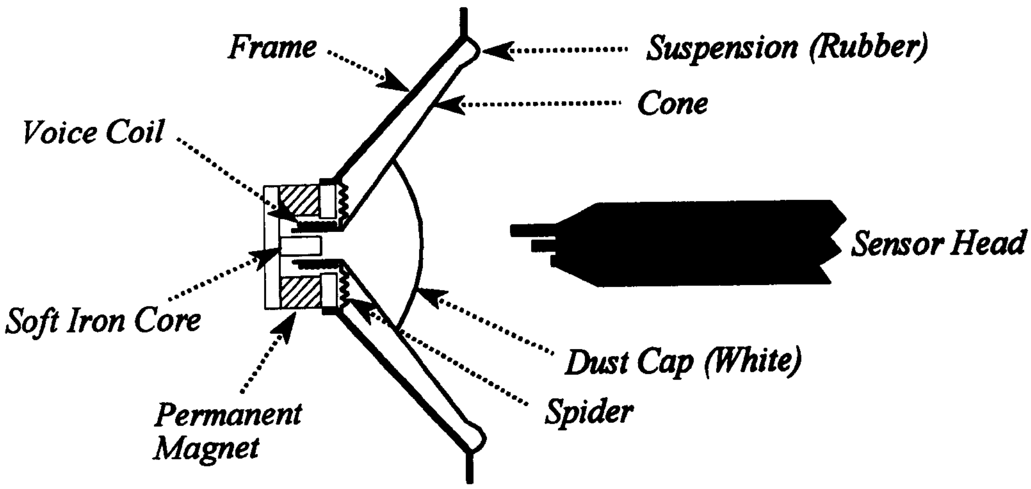

Fig. 8.1: The sensor arrangement for vibrational measurements and a cross-sectional view of a loudspeaker's bass driver (McComb *et al*, 1991)

The figure above also shows the cross-sectional view of a typical loudspeaker. This operates when electrical audio signals are applied to the voice coil which is wound around the neck of the cone thus producing a varying electromagnetic field around it. This interacts with the magnetic field produced by the permanent magnet resulting in the voice coil and cone vibrating back and forth with respect to the magnet, which is fixed on the frame. The suspension and spider control the level of flexible movement of the voice coil and cone so that they will not pop out or hit the soft iron core resulting in distortion of the sound produced (McComb *et al*, 1991).

8.2. SINGLE DEGREE VIBRATION MEASUREMENTS

Prior to performing single degree vibration measurements, static displacement measurements were performed, i.e. without exciting the loudspeaker, in order to obtain the calibration curve of the sensor arrangement. The range was to be varied manually using the translation stage which the loudspeaker was fixed on. The operational range needed for the measurements on the loudspeaker, which was not expected to exceed a few millimetres, was arranged to be as close to the start of the operational range as possible to achieve the biggest possible difference between the two detected signals so that accuracy and resolution are at their best. Calibration was performed at R = 25 mm with X_0 = 0 mm and y = 4.7 mm and then the sensor head was arranged with X_0 = 5 mm. The resultant response (S_{SPKR}) is shown in Figure 8.2 and the errors for the experimental points are shown in Figure 8.3.

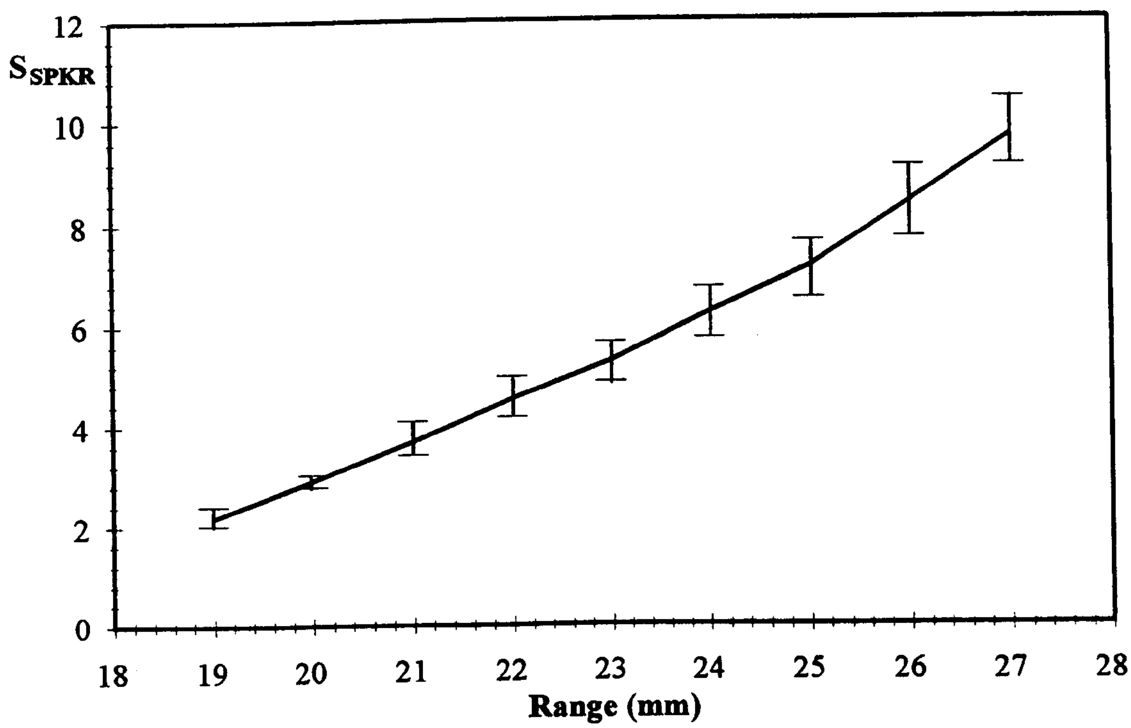

Fig. 8.2: Static displacement sensor response with the loudspeaker as target

The calibration curve obtained for the range between 19 mm and 25 mm was:

$$S_{SPKR_{X_0=5mm}} = (0.821 \pm 0.006)R - (13.5 \pm 0.209) \quad \textbf{Eq. (8.1)}$$

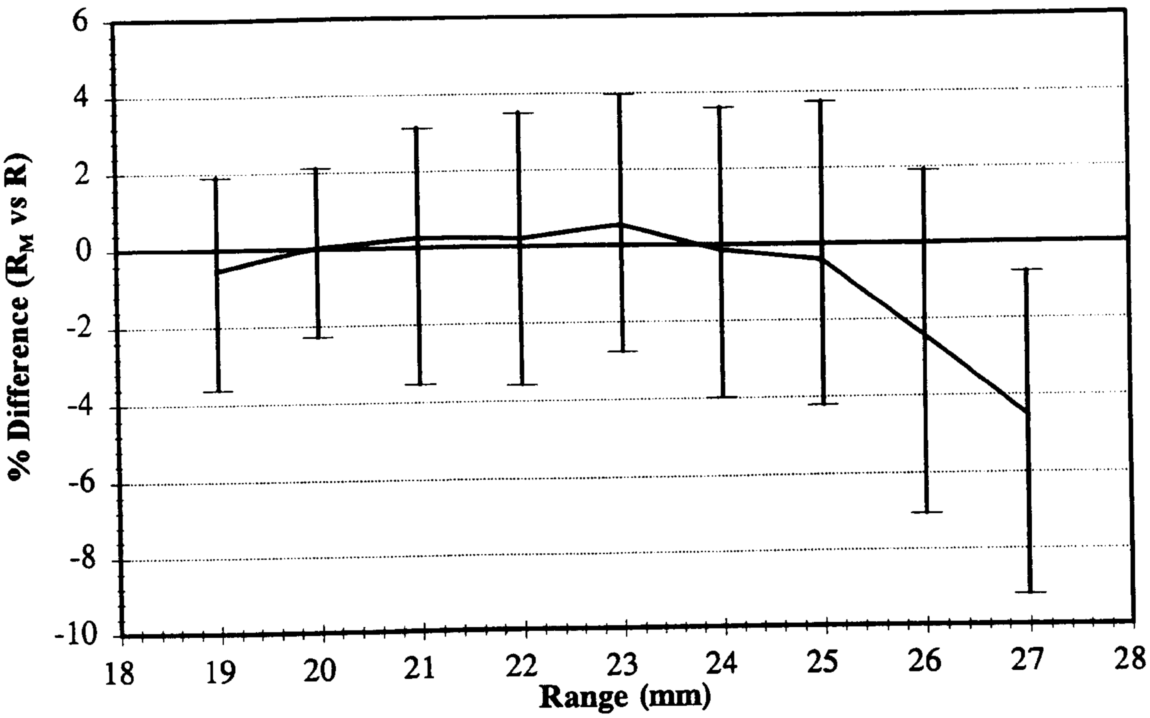

Fig. 8.3: Difference (%) between true and measured range for the static displacement response with the loudspeaker as target

Considering previous results with matt white paper, it is true that the range between 19 mm and 25 mm is not in the linear operational range of the sensor (Chapter 7.9 and Figure 7.43) which starts from 25 mm. For this arrangement it was decided that since the operational range needed for the vibration measurements was not larger than 6 mm, then it could be of advantage to the accuracy and resolution of the sensor to operate in a slightly less linear part of the sensor response just before the response becomes more linear, i.e. between 19 mm and 25 mm.

The slope of the experimental points was found to be 0.821. This is due to the fact that the unipolar signals detected are passed through a high pass filter which makes them bipolar spreading any changes in the level of the signals equally to both sides of ground. The ADCs sample only on the negative part of the signals detected, ignoring the positive side, thus recording only half the change in the level of the signals, as shown in Figure 8.4. The fact that the detected signals are only sampled once for each S_{SPKR} value lowers the error level considerably. Another factor affecting the slope may be the circular shape of the target.

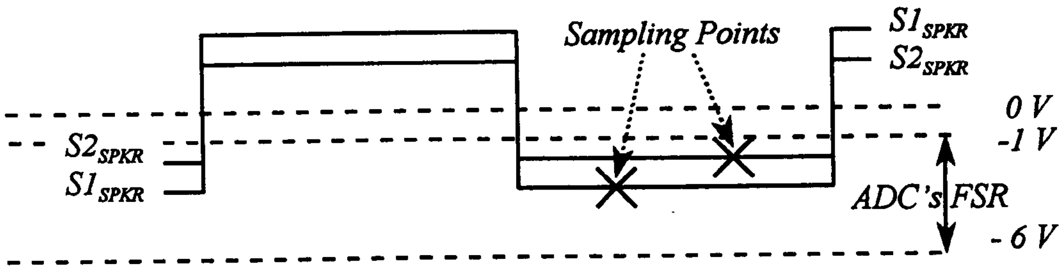

Fig. 8.4: Timing diagram for the ADCs for vibration measurements

Since at this stage the sensor was arranged to have a linear response over an operational range of 6 mm and a calibration curve was determined, vibration measurements could take place in this displacement range. Thus the sensor was positioned at a stand off distance from the dust cap of 22 mm. The function generator was then arranged to supply a sinusoidal wave to the input terminals of the bass driver bypassing the crossover network of the loudspeaker and the amplitude of the supplied signal was arranged at its maximum value and remained so for all the frequencies measured. The program shown in Appendix A2 was employed to control the operation taking approximately 750 sets of measurements. Initially the loudspeaker was arranged to vibrate at f = 25 Hz. The signals detected ($S1_{SPKR}$ and $S2_{SPKR}$) are shown in Figure 8.5 along with the resultant S_{SPKR} response.

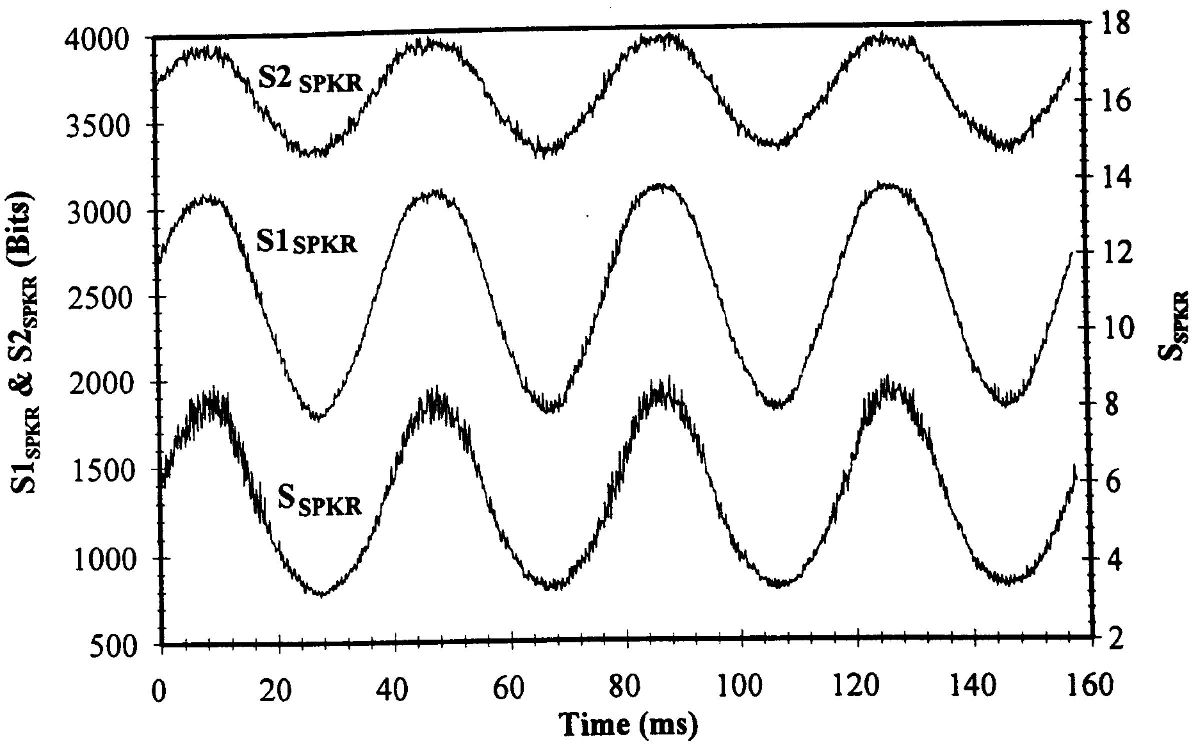

Fig. 8.5: $S1_{SPKR}$, $S2_{SPKR}$ and S_{SPKR} for a frequency of vibration of 25 Hz

As shown in Figure 8.5 the signal closer to the FSR, i.e. having the higher value, is $S2_{SPKR}$ and not $S1_{SPKR}$ which has the highest pre-ADC value since it is positioned closer to the loudspeaker. This is due to the way that the ADCs were arranged to sample the two signals (see Figure 8.4).

Looking now at the S_{SPKR} graph it can be seen that it follows a near sinusoidal wave itself as expected. The near and not pure sinusoidal nature of S_{SPKR} is thought to be caused by the frequency with which the bass driver is driven. A bass driver of this size (cone d = 18 cm) usually has a frequency range between 65 Hz and 3 kHz. The crossover network of the loudspeaker will ensure that the bass driver is not driven outside this frequency range since it is not intended to operate there. If the bass driver is driven above or below this range it will exhibit distorted operation. It is also evident that the noise observed on S_{SPKR} is larger when the difference between $S1_{SPKR}$ and $S2_{SPKR}$ is small. This is assisted by the fact that the two signals have a smaller difference at longer ranges where their SNR is also lower.

The calibration curve (equation 8.1) was used to derive the displacement of the cone with respect to time as shown in Figure 8.6. The positive values on the displacement graph show the motion of the cone moving away from the sensor. From here it can be observed that the maximum displacement (D) is 3 mm and again that the sine wave is not a pure one, i.e. is not having a 50/50 duty cycle. The positive side of the sine wave is narrower than the

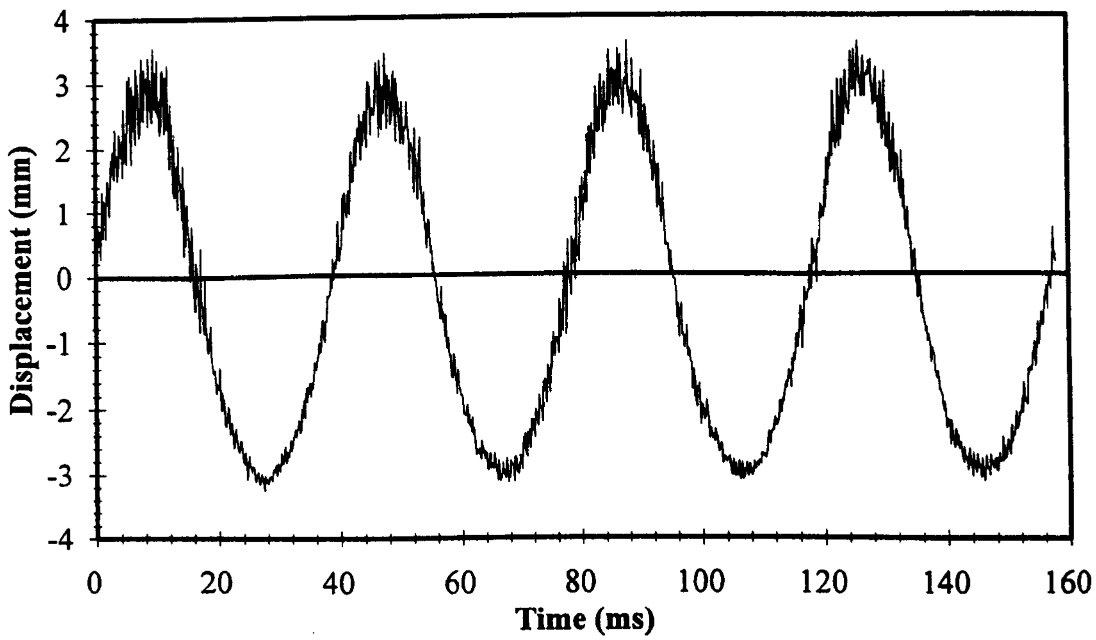

Fig. 8.6: Displacement graph for f = 25 Hz

negative one resulting in a 40/60 duty cycle. The narrower part of the cycle takes place when the voice coil attached to the cone is moving inside the gap between the magnet and the soft iron core.

The reproducibility deduced for displacement is the same as that for the accuracy of static displacement obtained from Figure 8.2, i.e. ± 4 %. The measured frequency is 25.52 Hz as opposed to 25 Hz. This is possibly due to the function generator frequency setting which could only be approximately set. The accuracy in deducing the frequency was in the range of ± 0.23 % estimated over 4 cycles.

Following the above tests, measurements were taken at nominal frequencies of 50 Hz, 75 Hz, 100 Hz, 125 Hz and 150 Hz and the displacement graphs for these attempts are shown in Figures 8.7 to 8.11 respectively. The results are summarised in Table 8.1.

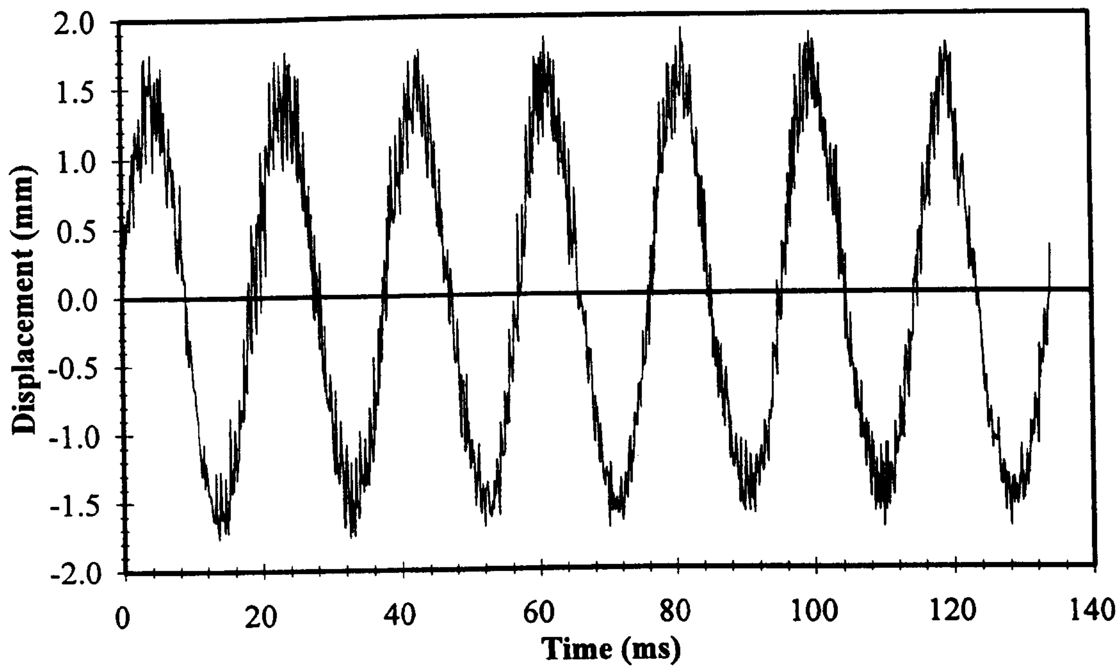

Fig. 8.7: The displacement graph for f = 50 Hz

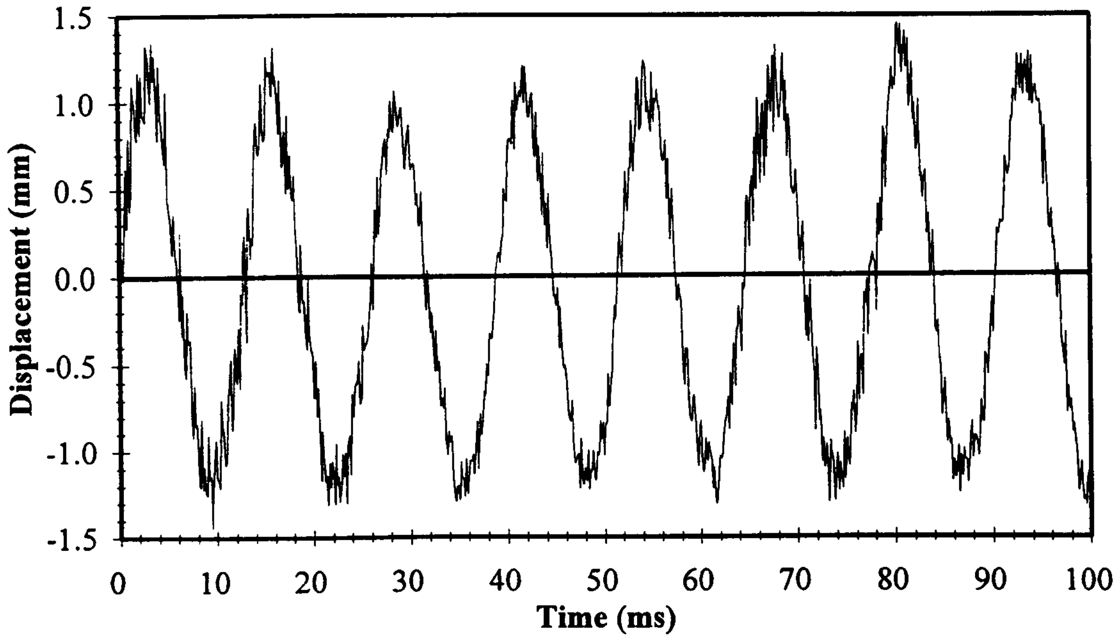

Fig. 8.8: The displacement graph for f = 75 Hz

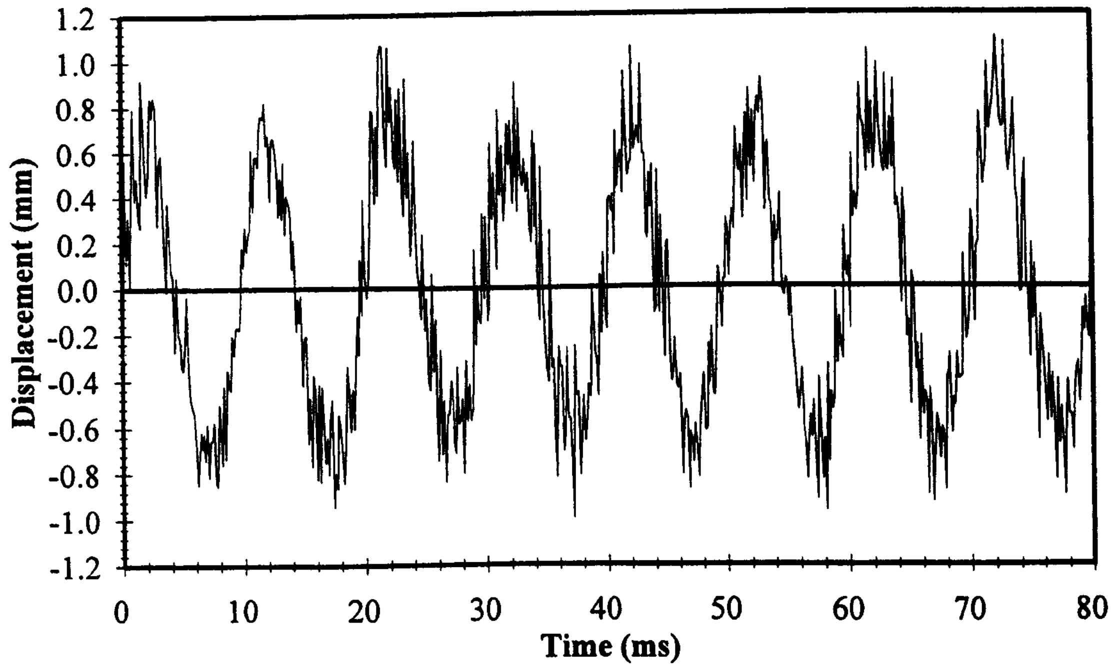

Fig. 8.9: The displacement graph for f = 100 Hz

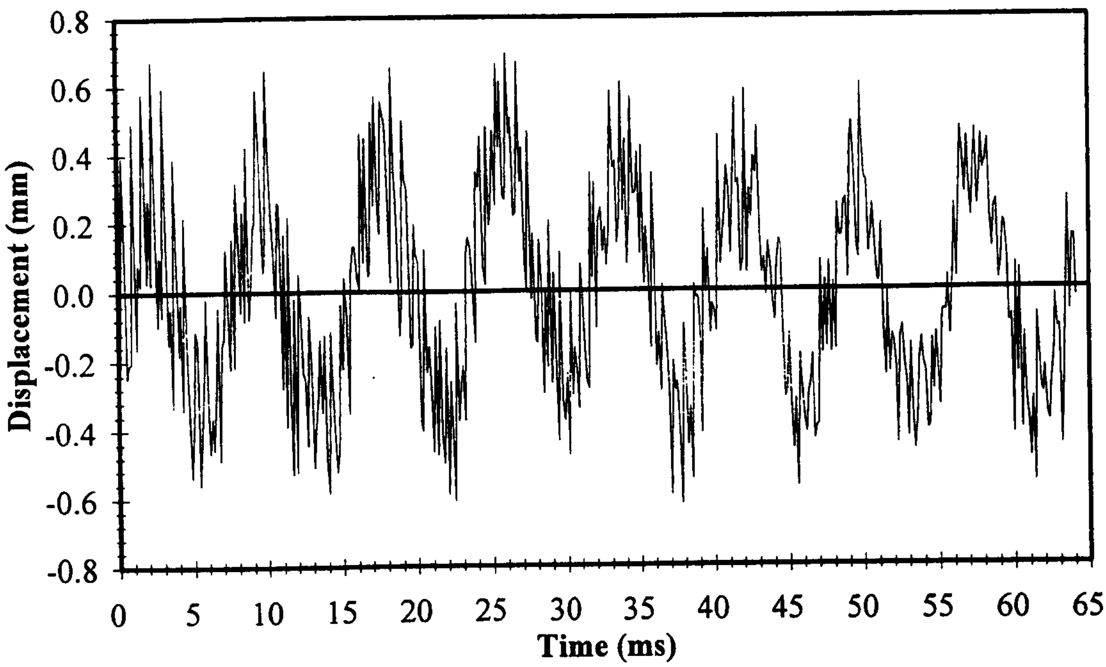

Fig. 8.10: The displacement graph for f = 125 Hz

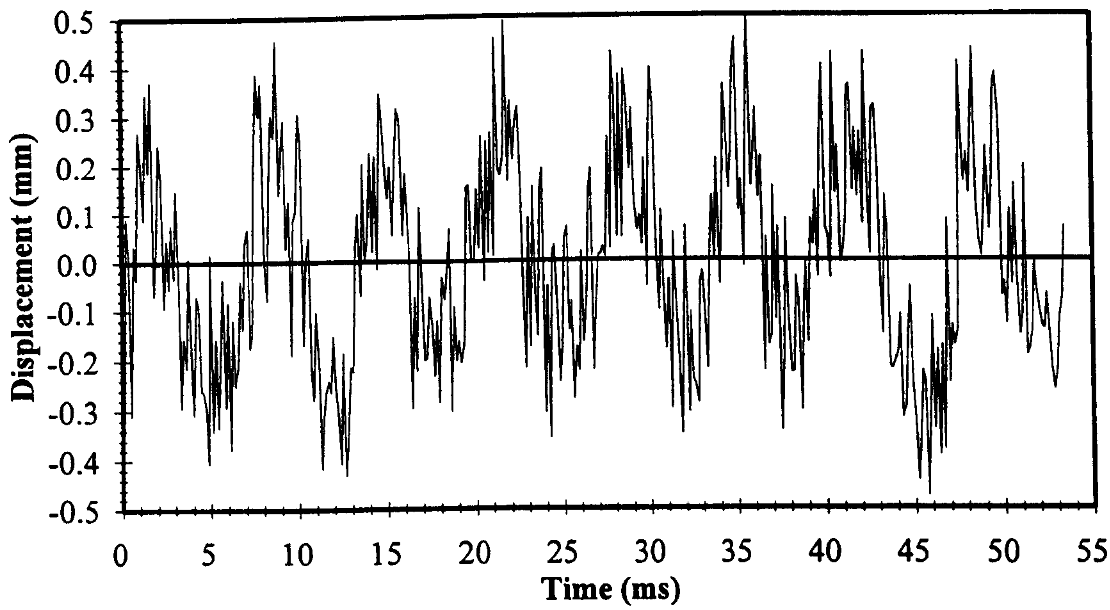

Fig. 8.11: The displacement graph for f = 150 Hz

Table 8.1: Results from single degree vibration measurements

Nominal Frequency Setting (Hz)	Maximum Displacement (mm)	Measured Frequency (Hz)	Accuracy of Frequency (%)	Cycles (w.r.t. Accuracy)
25	3.00	25.52	0.23	4
50	1.50	50.72	0.24	6
75	1.10	77.5	0.50	7
100	0.70	102.4	0.92	7
125	0.30	132.1	4.15	7
150	0.15	150	8.80	7

The first point to note from Table 8.1 of course, is that as the frequency input to the loudspeaker is increasing the displacement of the cone with respect to its rest position is decreasing. This is easily verified by observing the motion of the cone. The accuracy of displacement should be the same at a ± 4 % maximum for each particular range for all measurements since it is directly related to the static displacement measurements that were performed in order to obtain the calibration curve of the sensor. Also, the deduction of the frequency from the measurements is accurate to within ± 0.23 % at 25.52 Hz decreasing as the frequency increases due to the smaller displacement of the cone. At 150 Hz the frequency is estimated to be accurate to ± 8.8 % since the displacement of the cone is 0.15 mm. It is to be expected that since the displacement of the cone is accurate to ± 4 % then the frequency of the cone can only be determined with lower accuracy.

At lower frequencies where the displacement of the cone is large, the duty cycle of the sine wave is not equal, i.e. is not 50/50. At f = 25.52 Hz it is 42/58, at f = 50.72 Hz it is 53/47 and at 77.5 Hz it is 43/57. At higher frequencies, i.e. f = 102.4 Hz, f = 132.1 Hz and f = 150 Hz it becomes 50/50 since the displacement of the cone is smaller and therefore does not stretch the suspension and spider. At f = 77.5 Hz the duty cycle seems to be increasing rather than decreasing. But a check with the specifications of bass drivers of this size suggest that it is approximately at this frequency where their resonant frequency is. This is caused by the combination of the mass of the cone with the flexibility of the driver suspension and spider, and the air trapped inside the box. At the resonant frequency the impedance of a bass driver may rise from 8 Ω to 80 Ω or more thus modifying the behaviour of the bass driver. Hence, at this frequency the values obtained should not be expected to follow the decreasing trend of the duty cycles obtained at other frequencies. In cases where the driving frequency is similar to the resonant frequency of a bass driver then the cone may acquire a displacement value which is higher to the one which would have been achieved if this was not the case.

In order to investigate what is happening at an even higher frequency the function generator was arranged to excite the bass driver at f = 175 Hz. The resultant $S1_{SPKR}$, $S2_{SPKR}$ and S_{SPKR} are shown in Figure 8.12. Here, $S1_{SPKR}$ can just about change with displacement whereas with the $S2_{SPKR}$ signal there is hardly any variation as the target is further away. Clearly, the motion of the bass driver cannot be adequately resolved resulting in an S_{SPKR} response buried in noise although a vague form of vibration may seem to exist.

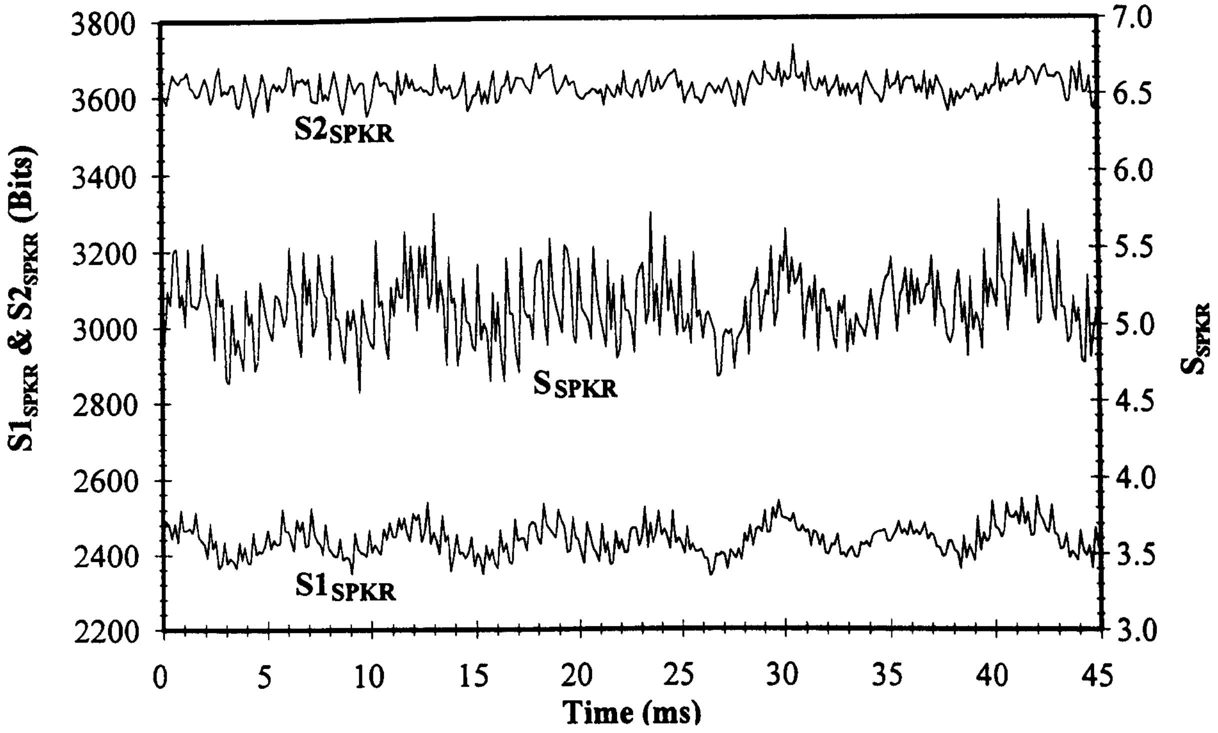

Fig. 8.12: $S1_{SPKR}$, $S2_{SPKR}$ and S_{SPKR} for a frequency of vibration of 175 Hz

Another set of measurements was also taken for a variable, increasing, frequency exciting the bass driver. The frequency was varied from around 15 Hz up to 150 Hz. The resulting $S1_{SPKR}$, $S2_{SPKR}$ and S_{SPKR} are shown in Figure 8.13. The resultant displacement graph is shown in Figure 8.14.

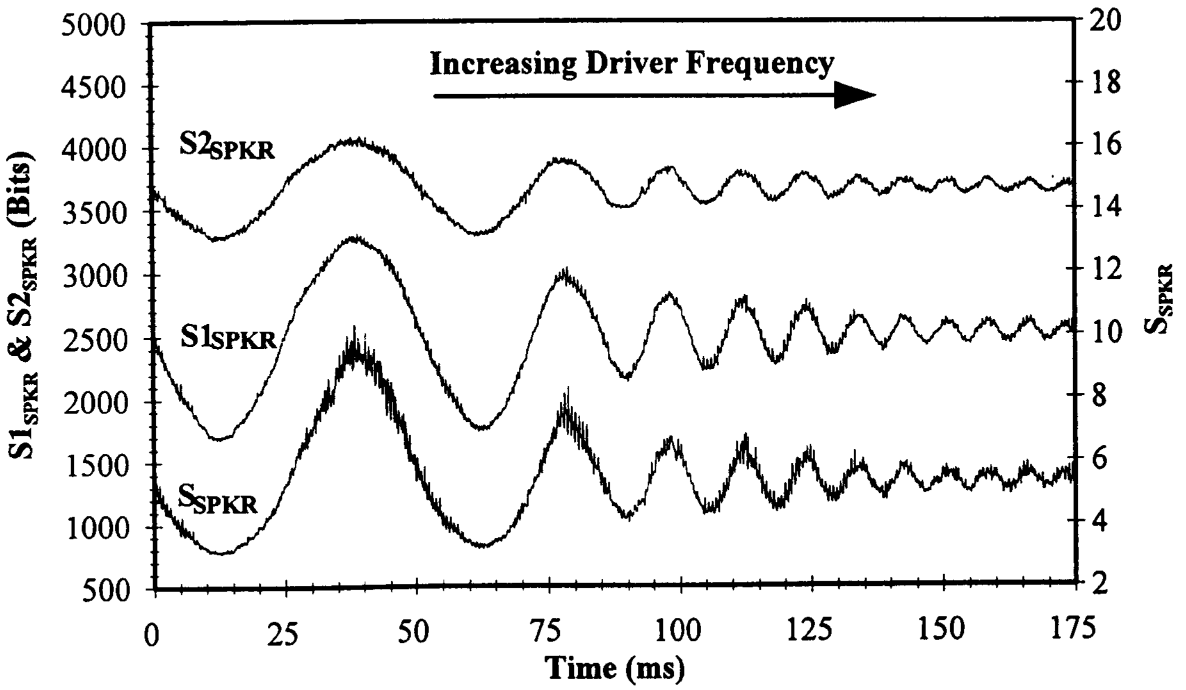

Fig. 8.13: $S1_{SPKR}$, $S2_{SPKR}$ and S_{SPKR} for 15 Hz < f < 150 Hz

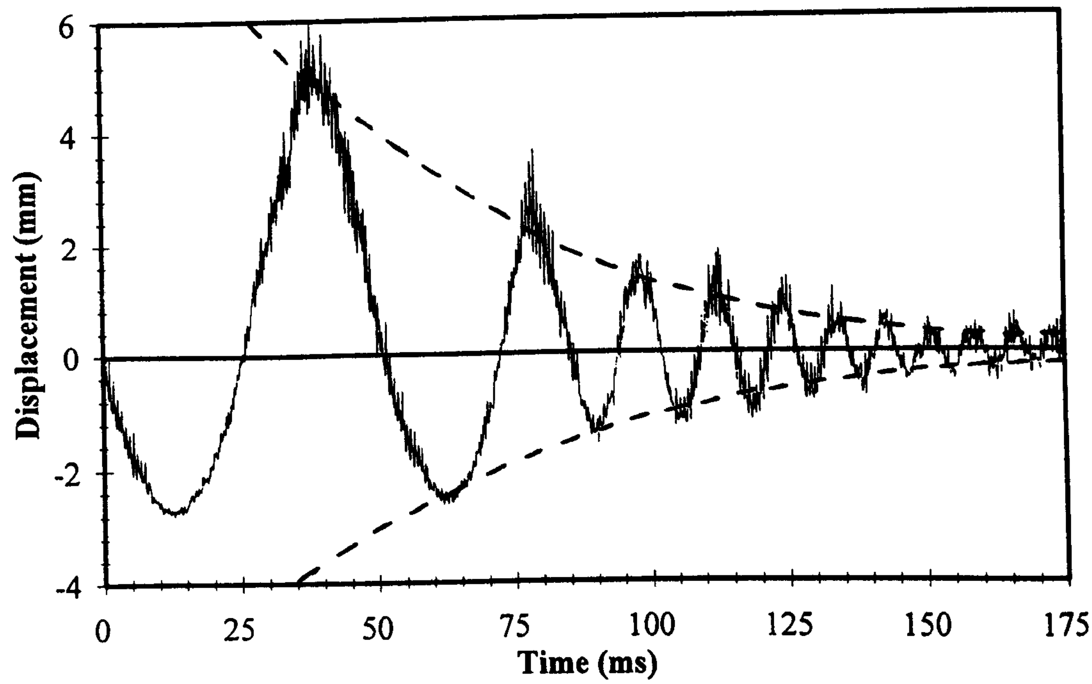

Fig. 8.14: Displacement graph for 15 Hz < f < 150 Hz

As expected, the signals detected ($S1_{SPKR}$ and $S2_{SPKR}$) followed the motion of the cone of the bass driver showing that as the frequency of vibration increased the displacement of the bass driver decreased. On the displacement graph (Figure 8.14) the rest position of the cone was arranged with respect to the higher frequencies, where the displacement is at its minimum and the spider and suspension of the bass driver are not stretched. It can clearly be seen that when the displacement, D < 2 mm the motion of the cone is fairly symmetrical. But when D > 2 mm the cone does not seem to be moving symmetrically. The displacement of the cone at t ≈ 10 ms seems to be at its maximum suggesting that at this point the suspension and spider of the bass driver cannot be stretched any more thus holding the cone back, also shown by the relationship between the displacement and the envelope drawn around it. This is not the case at t ≈ 40 ms where the cone is moving towards the magnet suggesting that the suspension and spider can be stretched more freely in this direction. Thus, if this bass driver were to be used to produce sounds with D > 2 mm then distortion of the sound would occur.

8.3. SUMMARY AND CONCLUSIONS

The automated version of the displacement sensor presented in this thesis has been arranged to measure single degree vibrations using the cap of the cone of the bass driver of a loudspeaker as target. A linear operational range of 6 mm has been defined with an average estimated accuracy of ± 0.5 %. The scatter of the individual experimental points was in the order of ± 4 %. Once the cone of the bass driver was excited with a single frequency of vibration, information about this vibration could be obtained. These were the displacement of the cone and its frequency.

The measurements performed with a loudspeaker as target in order to determine whether the sensor could perform dynamic displacement measurements are considered as successful. The sensor can determine the motion of the cone of the bass driver of a loudspeaker as long as the motion of the cone is kept above a minimum displacement corresponding to the resolution of the sensor (estimated to be better than 0.5 % of full scale range for this arrangement). The target used was able to vibrate above this minimum displacement up to the frequency of 150 Hz. The accuracy necessary in determining the parameters of vibration of the cone will also determine which is this minimum displacement value. Also, taking into consideration the bandwidth of the sensor electronics, which is 7.5 kHz, and the Nyquist sampling theorem (where the sampling frequency is double the vibration frequency), and given that the displacement of a vibrating surface can be resolved then in principle frequencies of vibration of up to 3.75 kHz could be measured. But for a more accurate frequency determination, oversampling (minimum 10 samples per cycle) should be performed thus expecting a lower measurable frequency of up to 750 Hz. A faster PC would allow for even higher frequencies of vibration to be measured, provided that the amplitude of vibration is satisfactorily larger than the resolution of the sensor.

The measurements performed on the bass driver revealed several points about the behaviour of its cone. The cone can be displaced to a higher value at very low frequencies whereas as the frequency is increasing the displacement of the cone becomes smaller. The suspension and spider holding the cone showed that they are more flexible allowing bigger displacements when the cone is moving towards the magnet of the bass driver, away from the sensor head. But this behaviour of the bass driver is understood in a sense since the cone must be stopped from popping out of its position, whereas when moving towards the magnet such problems do not exist. Although both effects result is a distorted operation of the bass driver, the frequencies where these effects are taking place are well below the frequency response of the bass driver. Amplifiers used to power such loudspeakers do not excite them at frequencies below a minimum of 20 Hz. The crossover networks employed in loudspeakers also ensure that the current driving the drivers never exceeds a certain predetermined maximum value in order to protect them from failure and also assure the quality of the sound produced.

From the vibration results obtained using the automated version of the displacement sensor presented in this thesis, it can be concluded that the experiment was a success and that this sensor with the present arrangement can be used to measure vibrations above a certain minimum displacement (0.15 mm) with a maximum frequency of 750 Hz.

Chapter 9

Summary and Conclusions, and Suggestions for Future Work

9.1. SUMMARY AND CONCLUSIONS

The characteristics and performance of a novel displacement sensor have been investigated both theoretically and experimentally in this thesis. This displacement sensor is an optical, extrinsic, differential one based on the inverse square law, has automatic intensity compensation and can employ optical fibres to allow for remote operation, but could also be configured, in principle, without optical fibres.

The version of displacement sensor investigated employs Plastic Optical Fibres (POFs) which have some important advantages over other types of optical fibre such as glass or glass bundles. POFs with 1 mm core diameter offer more efficient coupling from active devices, much easier alignment, interconnection and handling, are very flexible and do not require additional optics to assist in the collection of sufficient light signal, thus significantly lower the overall cost of the sensor. Active and passive opto-electronic devices and components are cheaply and readily available for use with POF.

Three POFs are employed in the sensor head positioned side by side and displaced from each other parallel to the axis of the sensor head by a scale factor X_0 and perpendicular to this axis by an amount y, both X_0 and y being in the order of millimetres. The middle POF is coupled to a red LED and directs light onto a target with the two outer ones receiving the reflected light from the target and guiding it to two silicon PIN photodiodes. Various sensor head jigs were developed to hold the three POFs together with the best one incorporating V-grooves. Here, the three fibres are positioned in the V-grooves and are supported individually by their walls. They are also held in place by a large flat cover which spreads the pressure exerted on the fibres over a large area thus minimising effects of modal disturbance.

Theoretical investigations on the expected behaviour of the sensor were performed for the ranges between 0 mm and 100 mm. The factors considered were the inverse square law, the light incident on each detecting POF calculated through numerical integration taking into account the physical orientation of the fibres with respect to each other, the shape and size of the cores of the fibres, their numerical aperture and solid angle effects. The targets assumed in the theoretical investigations were arranged to have a reflectivity coefficient, ρ, which could be varied from $\rho = 0$, for 100 % diffusive targets, to $\rho = 1$, for 100 % reflective targets.

For all cases of ρ a linear response was achieved. When a target with $\rho = 1$ (100 % reflective) was used, the slope of the response was closely equal to $(X_0)^{-1}$ whereas for $\rho = 0$ (100 % diffusive) it was closely equal to $(2X_0)^{-1}$. When targets of intermediate ρ were used the resultant slope of the response was in between $(X_0)^{-1}$ and $(2X_0)^{-1}$. The separation between the two detected signals, which is greater when $\rho = 0$ at any given range, makes a bigger change in the slope of the response if the diffuse reflectivity coefficient of the target is very high. If $\rho < 0.5$ the slope of the response is only marginally affected from that of $\rho = 0$. Linearity was obtained for the arrangement with $\rho = 1$, for a range starting around 12 mm up to 100 mm. For the arrangement with $\rho = 0$, linearity was obtained from around 18 mm up to 100 mm.

At very short ranges ($R < 10$ mm) linearity of response is breaking down for all types of target, causing a spike to appear. This spike is caused by the finite numerical aperture of the fibres and the lateral, y separation between the fibres, with the larger y separations resulting in the spike taking place at a longer range. X_0 separation variations also shift the spike closer or further away at the low end of the range as well as shifting up or down the linear part of the response, without affecting its slope or its linearity, only when a target with $\rho = 1$ is used. Y separation variations affect the sensor response by shifting the spike closer or further away. An unequal y separation does not offer any improvements on the sensor performance.

A target with $\rho = 0.82$ (matt white paper) was also used as target in the theoretical investigation and the slope of the responses was predicted to be close to $(1.385X_0)^{-1}$ being more similar to the approach with a very diffusive surfaced target rather than a very reflective one.

In order for the sensor to operate reliably under non ideal conditions care must be taken so that the two detected signals have the lowest possible error on them. If a 0.1 % error exists on the signals then the choice of X_0 separation will affect the maximum operational range of the sensor, through scalability, with the larger X_0 separations offering the longer operational ranges whose extend will also be a function of the type of target used. The scalability offered will only hold true if the various sources of noise are kept to the minimum level and there is adequate illumination from the source to keep high levels of signal to noise ratios (SNR > 25 dB) over these long ranges. The 100 % diffusive targets offer twice as long a maximum range than the 100 % reflective targets do (for $X_0 = 1$ mm the operational range will be limited to 2.9 mm for $\rho = 1$ and 11 mm for $\rho = 0$, whereas for $X_0 = 5$ mm the operational range will be limited to 52.6 mm for $\rho = 1$, and 114 mm for $\rho = 0$).

Offset voltage on and mis-calibration of the detectors affect the medium and long ranges of the sensor response. If these errors do not exist, the linearity of the sensor response will be around 0.8 % from the minimum range up to 100 mm. But if they do, and more so for mis-calibration rather than offset voltage, the errors on the response will start showing from a fairly early range, increasing considerably as range increases.

The geometrical arrangement of the detecting POFs with respect to the emitting POF in the sensor head, has also been shown to result in inequalities in the emission directed towards each detecting fibre affecting the linearity of response of the sensor at short ranges for all X_0 separations with the larger separations suffering the largest non-linearity.

Initial experimental investigation showed that the basic assumptions taken in the theoretical considerations held true experimentally as well. The behaviour of the detected signal from a POF was shown to be very similar to the theoretical one based on the inverse square law. The POF far field emission distribution, however, was found to be narrower than the lambertian distribution used in the theoretical analysis. This would only affect the sensor response by slightly shifting the spike, and hence the start of the operational range, towards longer ranges.

Experimental work on the sensor performed under dark room conditions and control electronics operating under dc conditions with two DMMs (4.5 digits) measuring the output from the detecting circuits showed that linearity of response is possible with a mirror as target for the range that calibration held true. The spike predicted theoretically at the very short range, was also observed experimentally. Linear operational ranges extending up to 80 mm at room temperature were achieved. The operation of the sensor was shown to remain essentially unaffected up to 40 ^{0}C. At higher temperatures the linear response of the sensor was breaking down to a level which depended on the ability of the opamps to maintain their characteristics under such influences. The main limiting factor of the detecting circuits was the dark current from the photodiodes.

The referencing technique used has been shown to be successful when the driving current of the LED was varied from 27 mA up to 80 mA for individual runs of the same sensor arrangement. The intensity of the detected signals and hence their corresponding signal to noise ratio at any given range varied but the percentage difference between the two detected signals remained the same for any of those LED current settings. This test resulted in an operational range of 80 mm with accuracy better than 1 % and for any current setting.

Random variation of the range with 500 repeated measurements resulted in an operational range of almost 70 mm with an accuracy of 1 %. The distribution of the points on the percentage error graph suggested that the emission from the emitting POF is not the smooth near lambertian far field emission distribution assumed to be but most likely had a distribution which was somewhat non-uniform (ragged).

The scalability of the sensing technique was also proved by taking measurements with the same arrangement for various X_0 separations again using a mirror target. The larger X_0 separations offered the longer operational range. The slopes of the resultant responses were very close to the theoretical predictions.

Experimental work performed with matt white paper as target proved the results obtained through computer simulation with the slopes of all the responses being very close to the ones predicted. The operational range extended up to R = 100 mm for all X_0 separations which was the maximum point that measurements could be performed due to hardware limitations. This suggests that the operational range could extend beyond R =

100 mm for all X_0 separations, with the larger X_0 separations achieving better performance in the longer range due to the larger separation of the signals detected.

The resolution of the method was investigated at two ranges. For a mirror target the measured resolution was 10 μm (0.05 %) at R = 20 mm and 70 μm (0.1 %) at R = 70 mm for all X_0 separations. For matt white paper the measured resolution was 45 μm (0.18 %) for X_0 = 1 mm, 30 μm (0.12 %) for X_0 = 3 mm and 5 μm (0.02 %) for X_0 = 5 mm at R = 25 mm. Resolution of 60 μm (0.6 %) for the three X_0 separations has been obtained at R = 75 mm.

More information on the validity of calibration was obtained by comparing the similarity of the two detected signals when X_0 = 0 mm which should be very close. For the case of a mirror target the difference between the two signals was around 0.1 % for R > 20 mm which resulted in a maximum difference between true and measured range of 1 % over that range. When matt white paper was used the difference between the two detected signals was 0.04 % for R > 30 mm which resulted in a maximum difference between true and measured range of 0.7 % over that range. Below these ranges the percentage difference between the two detected signals was increasing due to angular misalignments which affected the distribution of the emitted light. The misalignments calculated for a mirror target were 0.3^0 and for matt white paper 0.05^0. Calibrations with such small misalignments are considered very stringent and although such accuracies are not necessary for the successful operation of the sensor, if they are achieved they will assure large operational ranges with a relatively shorter starting range and very high accuracy (< 1 %).

The symmetry in the emission distribution from the emitting fibre was tested by arranging the three fibres with X_0 = 0 mm and rotating the emitting fibre. The results showed that the balance between the two detecting fibres varied as the emitting fibre was rotated. Both kinds of target arrangements (mirror and matt white paper) were shown to be affected by the rotation of the emitting fibre. This rotation provided a means of balancing the two detected signals to the highest level.

Target alignment exposed very stringent tolerances for the arrangement where a mirror was used as a target (1.2 %/^{0}). The arrangement with matt white paper as target resulted in much less stringent tolerances (0.06 %/^{0}) making it a very attractive option.

Seven (7) POFs were also used in the sensor arrangement in order to overcome the misalignment problems that may be present and also obtain better light detection. 6 detecting fibres were positioned in a coaxial arrangement with the emitting fibre in the middle and the detecting ones in an alternating configuration around it. The improvement obtained using this arrangement was better detection of the reflected light from the target but the response was not linear. Rotation of the emitting fibre did not offer any improvements on the linearity of response. The best sensor head arrangement is therefore the one with the three POFs.

Operation of the sensor under dc conditions was detrimentally affected by ambient illumination. By changing the dc operating circuitry to an ac one, desensitisation of the sensor from ambient effects was demonstrated resulting in an operational range between 25 mm and 85 mm with a 1 % accuracy for matt white paper.

The software controlled automated version of the sensor was used under ambient illumination conditions and a matt white paper as target and resulted in a linear response between 25 mm and 40 mm with average accuracy of 1 %. The spread of the points (50 repeated measurements), however, resulted in an increasing error as range increased.

For static displacement measurements, the sensor has been shown to be a very usable device and the extend of the achievable operational range depends on the control electronics. When the data was measured using two DMMs and processed manually, it resulted in very long and accurate operational ranges (R > 85 mm). When two ADCs were used, due to their higher noise contribution, it resulted in shorter operational ranges (~ 15 mm).

Comparing this novel sensor with the ones surveyed in the literature (see Section 3.5 and Table 3.3), it can be concluded that for static displacement measurements this sensor offers a superior arrangement/performance combination. Performancewise it has a linear operational range in excess of 85 mm when used with matt white paper with 1 % accuracy and better than 0.5 % resolution. Dimensionwise this sensor has a transverse size which can vary between 6.6 mm and 10 mm, depending on the arrangement used, which is indeed a very compact size offering great flexibility. The other sensors surveyed deliver an operational range which can vary between 0.2 mm and 100 mm. Most of them had a linear response whereas others did not. The sensor with the longest linear operational range (100 mm) is the one by Lahteenmaki *et al* (1989) which uses a triangulation arrangement which consequently makes the sensor size relatively large resulting in the sensor not being flexible enough when is required to operate in difficult locations. The same holds for the arrangement by Brenci *et al* (1988) which has a non linear operational range of 90 mm. This arrangement also requires expensive GRIN lenses. The arrangement employed by Regtien (1990) has an operational range of 100 mm and although similar to the one investigated in this thesis it does not have a linear response resulting in two ranges having the same value of relative response and the overall dimensions involved in the fibre positioning result again in a large size (a minimum of 35 mm transverse dimension).

The automated version of the displacement sensor presented in this thesis has been arranged to measure single degree vibrations using the cap of the cone of the bass driver of a loudspeaker as target. A linear operational range of 6 mm has been defined with accuracy of ± 4 %. Information about the displacement of the cone and its frequency of vibration were then obtained. The sensor can determine the motion of the cone of the bass driver of a loudspeaker as long as the motion of the cone is kept above a minimum displacement corresponding to the resolution of the sensor (estimated to be better than 0.5 % of range for this arrangement). The target used was able to vibrate above this minimum displacement up to the frequency of 150 Hz. Given a displacement larger than 0.15 mm and considering a minimum of 10 samples per cycle then the sensor should be able to measure vibrational frequency of up to 750 Hz with the present arrangement.

The measurements performed on the bass driver revealed several features about the behaviour of its cone. The cone displacement was measured and compared to the displacement at higher frequencies. At low frequencies the cone was displaced to a higher value whereas as the frequency increases the displacement of the cone became smaller. The suspension and spider holding the cone was established to have different levels of flexibility causing unequal displacements of the cone which may result in distorted sound produced if the cone was vibrated with displacements larger than 2 mm.

The sensor investigated in this thesis has been arranged to monitor vibrations in an application which required a maximum displacement range of 6 mm with a maximum accuracy of ± 4 % although it can be arranged to monitor vibrations with displacements of much larger amplitude. From the survey performed on vibration sensors it is noted that the maximum displacement of vibration monitored is that by Lin and Chang (1994) who reported a 2 mm maximum displacement. The fact is that not all amplitudes of vibration that need monitoring are in the sub-millimetric region. Also, some authors (Conforti *et al*, 1989, Toba *et al*, 1991, Chitnis *et al*, 1994, Dinev, 1995) claim the accurate monitoring of displacement, yet they have a non-referenced arrangement and have not elaborated on how the sensor will be affected by any intensity fluctuations and ageing of the source used. These sensors, clearly, can still be useful in measuring the frequency of vibration but their long term accuracy in monitoring the amplitude of these vibrations could be in doubt. These disadvantages have been shown not to exist in the sensor described in this thesis, which also has the potential of measuring vibration amplitudes considerably greater than the demonstrated 6 mm.

It is believed that a very useful and versatile displacement sensor has been developed using a novel proposed sensing technique and very low cost optoelectronic components. There is promising scope to develop this into a commercial system provided that some aspects are addressed which will assure the successful long term operation of the sensor and also its adaptation to other applications.

9.2. SUGGESTIONS FOR FUTURE WORK

The experimental work has shown that this displacement sensor can indeed perform static displacement and vibration measurements successfully. There are, however, several improvements that should be made.

Starting from the hardware of the sensor, the SMA connectors used so far should be changed to ST ones which offer keying connection. This sort of connection will make sure that the POFs are connected to their active elements always in the same way. Such an operation will improve the repeatability of the connections, especially if the active element of the opto-electronic components used is not positioned on the optical axis of the POFs, thus resulting in differing levels of intensity detected every time a POF is disconnected and reconnected.

Another very important area is the polishing of the POFs. At present the effects of angular misalignment due to inadequate polishing may be corrected if the emitting POF is rotated in order to achieve the required balance between the two detectors. Automated polishing will offer a repeatable polishing with a known angular misalignment, if any, which although it may not be as accurate as required in order to avoid the operation of rotating the emitting POF, it will at least create a pattern which can be followed when positioning the POFs in the sensor head thus avoiding the long procedure of trial and error in order to achieve the necessary balance between the two detectors so as to maximise the operational range of the sensor.

The choice of wavelength to be used in the sensor was based on the second lowest transmission window of POF which is in the region of 660 nm and where the attenuation is 150 dB/km. LEDs operating at this wavelength are powerful and fast. Considering, however, the spectrum of daylight it can be noticed that it is at its maximum intensity around this region resulting in very high levels of interference from background radiation which can affect the operation of the sensor. The continuum of the daylight spectrum weakens whilst moving away from this wavelength weather towards the infrared or ultraviolet. As an example, the intensity of the daylight spectrum at 950 nm is 90 % less than that for 660 nm which will result in much less effect on the operation of the sensor. Thus, the wavelength chosen for the sensor should be investigated considering the intensity of the daylight spectrum at the suggested wavelength, the attenuation of POF at this wavelength along with what other spectra exist around the suggested wavelength of interest aiming for the optimum wavelength for use with the sensor.

Investigation on the behaviour of the sensor with regards to other targets especially of other colour is very important. This should be combined with the chosen wavelength of the emitted light from the LED. This will show whether the operation of the sensor is sensitive to the colour of various targets and by how much.

The POFs in the experimental sensor head were left uncovered thus allowing for the uncertainties due to scratching or damage if they were to come in contact with another object. Dust could also accumulate on the tips of the POFs if they are uncovered thus affecting the amount of light entering the core. Some sort of cover should be employed which would not stop the sensor from operating. Figure 9.1 shows a possible arrangement with a glass cover which although itself would need cleaning every now and then to remove the dust it will, however, protect the POFs.

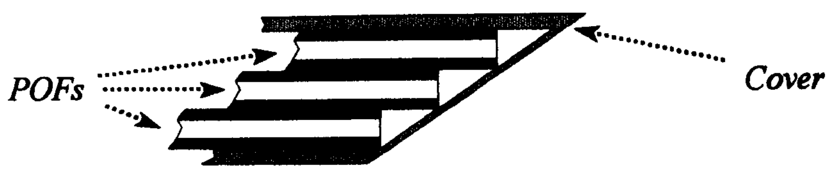

Fig. 9.1: The suggested protective cover for the POFs in the sensor head

The front cover could be clear so as not to block any light although an optical filter may be used to block light of unwanted wavelengths. The front cover should be tilted and be touching the end corners of the jacket of the POFs as shown in the figure in order to block any light which may be reflected from the part of the glass covering the emitting POF from reaching the front detecting POF. It is however noted that such a cover would modify the light transmitted through it via refraction. Further investigation on such an effect must be performed.

The ADC cards used in order to convert the analogue output from the detecting circuits to digital were existing designs which were modified to accommodate the needs of the sensor. The components used had excessive offset voltage figures which affected the accuracy of the S response. They were also arranged to measure the detected signals one after the other thus creating another uncertainty. Tailor-made ADC cards should either be designed or bought with the requirements of the sensor in mind. They should also be made to measure the detected signals simultaneously and not one after the other.

A way of improving the sensor performance could be through the electronic circuitry which could be arranged in such a way so as to perform the transfer function under analogue conditions, and then convert the S value to digital for further signal processing. In this way, the resolution of the ADCs will not affect the detected signals, as it does with the present arrangement, but only the final S value thus assisting in extending the linear operational range of the sensor.

The resultant signals from the vibration measurements could be improved if Fourier analysis were performed to extract their frequency and displacement content. With such an approach, the present operational frequency range of the sensor would be extended. Also, the use of a faster PC would also increase the frequency response of the sensor.

The sensor can also be arranged to measure other variables related to displacement such as pressure, force or liquid level. It will require, however, mechanical devices which will move or undergo structural changes under strain caused by the measurand. Such devices may be diaphragms, bellows, coil springs or others whose shape may change linearly under the influence of the measurand. As a pressure sensor it will require a bellows or a diaphragm. A bellows seems to be a very attractive device to use as target since it is intended for conversion of pressure into a linear displacement. This linear displacement can be accurately monitored by this displacement sensor and be related to the pressure applied on the bellows.

As a force sensor it could be made to quantitatively measure the force applied on a surface which moves linearly under force. Such a surface can be positioned on a coil spring which will be operated in its linear range. By measuring the displacement (d) of a coil spring with a known coefficient (k) then the compressing or expanding force (F) can be determined ($F = d / k$).

As a level sensor it will require some sort of a float which will follow the level of the liquid in a tank. The displacement sensor will be positioned fixed on the tank monitoring the displacement of the lever of the float close to its base where the range is not excessive. At present floats are used in tanks mostly to open or close the liquid incoming valve when necessary. The suggested arrangement will be able to monitor the liquid level at any instance as well as to allow the incoming of liquid when necessary.

Theoretical investigation on matt white paper as target suggested that the slope of the linear response would depend only on the X_0 separation between the three POFs and experimental work proved this point. This held true when the diameter of the target was larger than the effective diameter of the cone of emission on the target at any point in the range. But suspicions were raised over the fact that when the diameter of the target was smaller than the effective diameter of the cone of emission on the target then a lower slope would result. This is an effect caused by the lower levels of signal detected which affects the signal to noise ratio of the detectors. In this case, up to the point where the diameter of the target becomes equal to the effective diameter of the cone of emission on the target the resultant slope would be the one predicted. But for ranges beyond this point the slope of the S response changed becoming more horizontal. This effect will have to be further investigated in view of determining whether it could result in the displacement sensor being able to measure rotation. This will require the attachment of matt white paper shaped as shown in Figure 9.2 around a rotating rod. Apart from the frequency of rotation the monitoring of the angular position of the rod will be possible enabling the rod to be stopped at a particular angle. An arrangement such as this will be preferred when compared with other optical rotating sensing arrangements which rely in the positioning of the rod in an off axis arrangement or the eccentrical fitting of a cam onto a rotating spindle (Mignani, et al 1994) which is bound to produce vibrational resonances at some frequencies of rotation. Such an application could find use in the robotics industry.

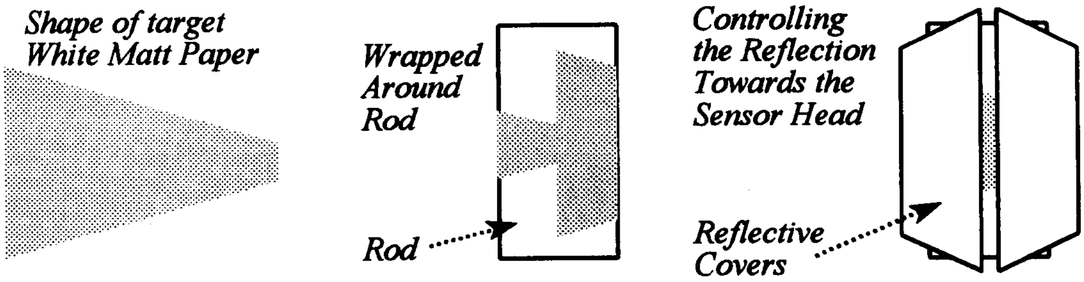

Fig. 9.2: The target arrangement for rotation measurements

Most of the work carried out with this sensor was to develop it to the point of demonstrating convincingly its usefulness for the measurement of some physical parameters such as static displacement or single degree vibration. Further work could now aim to improve the sensor as a system and investigate its adoption to new applications. This would indeed be a very logical step forward.

Appendix A
Computer Programs
(Turbo C)

A. CONTENTS

A.1. PARTLY REFLECTIVE / PARTLY DIFFUSIVE SURFACED TARGETS AND LAMBERTIAN SOURCE EMISSION

```
/* A PROGRAM IN C TO SIMULATE THE BEHAVIOUR OF THE SENSOR */
/* ASSUMING LAMBERTIAN DISTRIBUTION */
/* THREE POFs, POF DETECTION LIMITS */
/* A PARTLY REFLECTIVE / PARTLY DIFFUSIVE SURFACED TARGET */
/* FILENAME: PARTLY */

# include <stdio.h>
# include <math.h>
# include <dos.h>

void main (void)

{
float R;            /* RANGE */
float RMAX;         /* MAXIMUM RANGE */
float XD;           /* DISTANCE FROM E TO TARGET ON OPTICAL AXIS */
float XD2;          /* SQUARE OF X */
float XAD;          /* DISTANCE FROM TARGET TO D1 ON OPTICAL AXIS */
float XBD;          /* DISTANCE FROM TARGET TO D2 ON OPTICAL AXIS */
float XAD2;         /* SQUARE OF XA */
float XBD2;         /* SQUARE OF XB */
float XAR;          /* DISTANCE FROM E TO D1 ON OPTICAL AXIS */
float XBR;          /* DISTANCE FROM E TO D2 ON OPTICAL AXIS */
float XAR2;         /* SQUARE OF XAR */
float XBR2;         /* SQUARE OF XBR */
float b;            /* SOLID ANGLE FOR TARGET CELLS */
float b1;           /* SOLID ANGLE FOR D1 */
float b2;           /* SOLID ANGLE FOR D2 */
float x1;           /* SEPARATION BETWEEN ENDS OF D1 AND E */
```

```
float x2;           /* SEPARATION BETWEEN ENDS OF D2 AND E */
float y1;           /* HEIGHT BETWEEN AXIS OF E AND AXIS OF D1 */
float y2;           /* HEIGHT BETWEEN AXIS OF E AND AXIS OF D2 */
float z1;           /* DISPLACEMENT OF AXIS OF D1 IN Z-DIRECTION */
float z2;           /* DISPLACEMENT OF AXIS OF D2 IN Z-DIRECTION */
float ys;           /* HEIGHT OF DETECTING POF CELLS, Y-DIRECTION */
float ysR;          /* HEIGHT OF DET. POF CELLS, Y-DIRECTION - REFL */
float zs;           /* HEIGHT OF DETECTING POF CELLS, Z-DIRECTION */
float zsR;          /* HEIGHT OF DET. POF CELLS, Z-DIRECTION - REFL */
float ys2;          /* SQUARE VALUE OF ys */
float ysR2;         /* SQUARE VALUE OF ysR */
float zs2;          /* SQUARE VALUE OF zs */
float zsR2;         /* SQUARE VALUE OF zsR */
int yt;             /* HEIGHT OF TARGET CELLS, Y-DIRECTION */
int yt2;            /* SQUARE VALUE FOR yt */
int zt;             /* HEIGHT OF TARGET CELLS, Z-DIRECTION */
int zt2;            /* SQUARE VALUE FOR zt */
float h;            /* RADIUS OF DETECTING POFs */
int r;              /* RADIUS OF ILLUMINATION ON TARGET */
double w;           /* DIRECT DISTANCE BETWEEN AXIS OF E AND EACH
                           CELL ON DIFFUSE TARGET */
double wR1;         /* DIRECT DISTANCE BETWEEN AXIS OF E AND EACH
                           CELL OF D1 */
double wR12;        /* wR1 * wR1 */
double wR2;         /* DIRECT DISTANCE BETWEEN AXIS OF E AND EACH
                           CELL OF D2 */
double wR22;        /* wR2 * wR2 */
double ww;          /* w * w */
double w1;          /* DIRECT DISTANCE BETWEEN EACH CELL OF TARGET
                           AND EACH CELL (ys and zs) OF D1 */
double w12;         /* w1 * w1 */
```

```
double w2;          /* DIRECT DISTANCE BETWEEN EACH CELL OF TARGET
                           AND EACH CELL (ys and zs) OF D2 */
double w22;         /* w2 * w2 */
double ws1;         /* ww * w12 */
double ws2;         /* ww * w22 */
float p;            /* EMISSION POWER TOWARDS TARGET - COS VALUE */
float p1;           /* EMISSION POWER TOWARDS D1 POF */
float p2;           /* EMISSION POWER TOWARDS D2 POF */
float pR1;          /* EMISSION POWER TOWARDS D1 POF - REFL */
float pR2;          /* EMISSION POWER TOWARDS D2 POF - REFL */
float a;            /* AREA OF DETECTING CELLS */
float c1;           /* CALIBRATION CONSTANT FOR S1 */
float c2;           /* CALIBRATION CONSTANT FOR S2 */
float ac1;          /* a * c1 */
float ac2;          /* a * c2 */
double sD1;         /* SIGNAL DETECTED FROM D1 - DIFFUSE */
double sD2;         /* SIGNAL DETECTED FROM D2 - DIFFUSE */
double sR1;         /* SIGNAL DETECTED FROM D1 - REFLECTIVE */
double sR2;         /* SIGNAL DETECTED FROM D2 - REFLECTIVE */
float alfa;         /* +VE HEIGHT OF EFFECTIVE TARGET */
float beta;         /* -VE HEIGHT OF EFFECTIVE TARGET */
float gamma;        /* +/- WIDTH OF EFFECTIVE TARGET */
float delta;        /* INCREASE OF RANGE STEPS */
float rad;          /* COS RAD VAL OF POF ACC. ANGLE +/- 28 DEGREES */
float lambda;       /* TAN 28 DEGREES */
float rc;           /* REFLECTIVITY COEFFICIENT FROM 0 TO 1 */
float em;           /* EMISSIVITY COEFFICIENT FROM 0 TO 1 */
char ch[15];        /* FILENAMES CAN ACCEPT UP TO 15 CHARACTERS */
FILE *fp;
clrscr();
printf  ("\a\a\a\nENTER THE REFLECTIVITY COEFFICIENT VALUE :\n\t");
scanf   ("%f", &rc);
```

```
if (rc > 1)
        {
        printf ("\nTHE REFLECTIVITY COEFFICIENT VALUE MUST NOT BE
                        LARGER THAN ONE !\n\t");
        getch();
        }
else
        {
printf ("\nENTER THE MAXIMUM RANGE VALUE :\n\t");
scanf ("%f", &RMAX);
printf ("\nENTER THE x1 VALUE :\n\t");
scanf ("%f", &x1);
printf ("\nENTER THE x2 VALUE :\n\t");
scanf ("%f", &x2);
printf ("\nENTER THE y1 VALUE :\n\t");
scanf ("%f", &y1);
printf ("\nENTER THE y2 VALUE :\n\t");
scanf ("%f", &y2);
printf ("\nENTER THE FILENAME FOR RANGE, S1 AND S2 VALUES :\n\t");
scanf ("%s", &ch);
if ((fp = fopen (ch, "w"))==NULL)
        {
        printf ("\aCANNOT OPEN DATAFILE FOR RANGE, S1 AND S2 VALUES\n");
        exit(1);
        }
a = 0.01;               /* AREA OF EACH DETECTING ELEMENT */
c1 = 1;                 /* CALIBRATION CONSTANT FOR D1 */
c2 = 1;                 /* CALIBRATION CONSTANT FOR D2 */
ac1 = a * c1;
ac2 = a * c2;
r = 54;                 /* RADIUS OF ILLUMINATED TARGET AT RMAX = 100 */
rad = 0.8829;           /* COS RAD VAL OF POF ACC. ANGLE +/- 28 DEGREES */
```

```
lambda = 0.5317;        /* TAN 28 DEGREES */
em = 1 - rc;            /* EMISSIVITY COEFFICIENT */
clrscr();
printf ("\a\a\a\n\n\n\n\n\t\t\tD O  N O T  D I S T U R B");
printf ("\n\n\t\t\tI' M  W O R K I N G . . .");
printf ("\n\n\n\t\t\tK E E P  A W A Y  ! ! !\n\n\n\n\n");
for (R=0; R<=RMAX; R=R+delta)           /* FOR 1 */
        {
        delta = R > 10 ? 1:0.1;
        printf ("RANGE = %6.1f\n", R);
        XAR = 2*R + x1;
        XBR = 2*R + 2*x1 + x2;
        XAR2 = XAR * XAR;
        XBR2 = XBR * XBR;
        XD = R + x1;
        XAD = R;
        XBD = R + x1 + x2;
        XD2 = XD * XD;
        XAD2 = XAD * XAD;
        XBD2 = XBD * XBD;
        alfa = 2.2 + XBD * lambda;              /* +VE HEIGHT OF EFCTVE TARGET */
        beta = -2.2 - (XAD * lambda);           /* -VE HEIGHT OF EFCTVE TARGET */
        gamma = XBD * lambda;                   /* RADIUS/WIDTH OF EFCTVE TRGT */
        sD1 = sD2 = sR1 = sR2 = 0;

/*R E F L E C T I V E   T A R G E T*/

if(rc > 0)
        {
for (ysR=0.5; ysR>=-0.5; ysR=ysR-0.01)          /* FORR 1 */
        {
        ysR2 = ysR * ysR;
```

```
for (zsR=-0.5; zsR<=0.5; zsR=zsR+0.01)              /* FORR 2 */
        {
        zsR2 = zsR * zsR;
if (0.25 >= ysR2 + zsR2)                   /* IFR 1 */
        /* IF h LESS THAN OR EQUAL TO THE RADIUS OF POF CARRY ON */
        {
        wR12 = (XAR2 + (y1+ysR)*(y1+ysR) + zsR2);
        wR22 = (XBR2 + (y2+ysR)*(y2+ysR) + zsR2);
        wR1 = sqrt (wR12);
        wR2 = sqrt (wR22);
        pR1 = XAR / wR1;
        pR2 = XBR / wR2;
if (pR1 > rad)                             /* IFR 2 */
        /* IF RECEPTION ANGLE LESS THAN ACC. ANGLE OF D1 THEN */
        {
        sR1 = ((rc * ac1 * pR1 * pR1) / wR12) + sR1;
        }                                  /* IFRC 2 */
if (pR2 > rad)                             /* IFR 3 */
        /* IF RECEPTION ANGLE LESS THAN ACC. ANGLE OF D2 THEN */
        {
        sR2 = ((rc * ac2 * pR2 * pR2) / wR22) + sR2;
        }                                  /* IFRC 3 */
        }                                  /* FORRC 2 */
        }                                  /* FORRC 1 */
        }
        }


/* D I F F U S I V E   T A R G E T */


if (em > 0)
        {
for (yt = alfa; yt >= beta; yt--)          /* FOR 2 */
```

```
        {
        yt2 = yt * yt;
for (zt = -gamma; zt <= gamma; zt++)              /* FOR 3 */
        {
        zt2 = zt * zt;
if (r >= lambda * XD)                       /* IF 1 */
        {
        ww = ( XD2 + yt2 + zt2 );
        w = sqrt (ww);
        p = (XD / w);                       /* SOLID ANGLE - p IS A COS VALUE */
if (p > rad)                                /* IF 2 */
        {
for (ys = 0.5; ys >= -0.5; ys -= 0.05)            /* FOR 4 */
        {
        ys2 = ys * ys;
for (zs =- 0.5; zs <= 0.5; zs += 0.05)            /* FOR 5 */
        {
        zs2 = zs * zs;
if (0.25 >= ys2 + zs2)                      /* IF 3 */
        /* IF h^2 LESS THAN OR EQUAL TO THE RADIUS^2 OF POF THEN */
        {
        w12 = ( XAD2 + (y1+ys) * (y1+ys) + zs2 );
        w22 = ( XBD2 + (y2+ys) * (y2+ys) + zs2 );
        w1 = sqrt (w12);
        w2 = sqrt (w22);
        p1 = (XAD / w1);                /* SOLID ANGLE - p1 IS A COS VALUE */
        p2 = (XBD / w2);                /* SOLID ANGLE - p2 IS A COS VALUE */
        ws1 = w12 * ww;                 /* MULTIPLICATION OF DISTANCE BY S1 */
        ws2 = w22 * ww;                 /* MULTIPLICATION OF DISTANCE BY S2 */
if (p1 > rad)                           /* IF RECEPTION ANGLE LESS THAN
                                           ACCEPTANCE ANGLE OF D1 THEN */
```

```
        {
        sD1 = ( (em * ac1 * p * p1 * p * p1) / ws1 ) + sD1;
        }
if (p2 > rad)                      /* IF RECEPTION ANGLE LESS THAN
                                      ACCEPTANCE ANGLE OF D2 THEN */
        {
        sD2 = ( (em * ac2 * p * p2 * p * p2) / ws2 ) + sD2;
        }
        }                             /* IF 3 */
        }                             /* FOR 5 */
        }                             /* FOR 4 */
        }                             /* IF 2 */
        }                             /* IF 1 */
        }                             /* FOR 3 */
        }                             /* FOR 2 */
        }
fprintf (fp,"%6.1f %12.10e %12.10e %12.10e %12.10e\n", R, sR1, sR2, sD1, sD2);
                        /* PRINT R, s1 and s2 VALUES INTO DATAFILE */
        }                             /* FOR 1 */
fclose  (fp);                         /* CLOSE THE DATAFILE */
printf  ("\a\a\a\t\t\tF I N I S H E D   ? ! ? !");
getch();
}
}
```

A.2. EXPERIMENTAL DISPLACEMENT MEASUREMENTS USING A STATIONARY / VIBRATING TARGET

```
/* STATIC OR DYNAMIC (ac) DISPLACEMENT MEASUREMENTS */
/* A PROGRAM TO RUN THE LED, READ THE TWO 12-BIT ADC CARDS */
/* PROCESS AND STORE THE READ DATA INTO A DATAFILE */
/* FILENAME: ACPASSIVE */

# include <stdio.h>
# include <dos.h>
# define portA 0x01B0
# define portB 0x01B1
# define portC 0x01B2
# define ADCS1 0x1200
# define ADCS2 0x1202
# define MAX 2902          /* MAX VALUE MUST BE A MULTIPLE OF 2 */
                           /* 5502 FOR VIBRATION */
# define MIN 2802          /* MIN VALUE FOR DATA RECORDING & ...
                              ... CAPACITOR SETTLING TIME */
                           /* 2 FOR VIBRATION */

void main (void)

{
int k, l, R, F, x1[MAX], x2[MAX], S1A, S1B, S2A, S2B, S1, S2;
long int i;
float S;
char ch[15];               /* FILENAME: UP TO 15 CHARACTERS */
FILE *fp;
clrscr();
printf  ("\nENTER THE RANGE VALUE :\n\t");
scanf  ("%d", &R);         /* F FOR VIBRATION */
```

```
printf  ("\nENTER THE DATAFILE NAME :\n\t");
scanf  ("%s", &ch);
fp = fopen (ch, "a");            /* APPEND DATA INTO EXISTING DATAFILE */
if (!fp)                         /* IF DATAFILE DOES NOT EXIST OPEN IT */
        {
        fp = fopen (ch, "w");
        }
outportb (0x01B3, 0x81);         /* SET OUTPUT PIN PB7 OF I/O BOARD 8255 */
i = 0;
l = 0;
/* for (;;) */                   /* FOR CALIBRATION PURPOSES */
        do
        {
        outportb (portB, 0x80);          /* SWITCH LED ON */
        x1[l] = inport (ADCS1);          /* DELAY BY READING ADCS1 */
        x2[l] = inport (ADCS2);          /* DELAY BY READING ADCS2 */
        x1[l] = inport (ADCS1);          /* DELAY BY READING ADCS1 */
        x2[l] = inport (ADCS2);          /* DELAY BY READING ADCS2 */
        x1[l] = inport (ADCS1);          /* READ ADCS1 */
        x2[l] = inport (ADCS2);          /* READ ADCS2 */
        i++;
        outportb (portB, 0x00);          /* SWITCH LED OFF */
        x1[l] = inport (ADCS1);          /* DELAY BY READING ADCS1 */
        x2[l] = inport (ADCS2);          /* DELAY BY READING ADCS2 */
        x1[l] = inport (ADCS1);          /* DELAY BY READING ADCS1 */
        x2[l] = inport (ADCS2);          /* DELAY BY READING ADCS2 */
        x1[l] = inport (ADCS1);          /* READ ADCS1 */
        x2[l] = inport (ADCS2);          /* READ ADCS2 */
        i++;
        }while (i <= 120000);
 k = 0;
        do
```

```
{
outportb (portB, 0x80);          /* SWITCH LED ON */
                        /* 0x88 TO SWITCH TIMER ON FOR VIBRATION */
x1[l] = inport (ADCS1);          /* DELAY BY READING ADCS1 */
x2[l] = inport (ADCS2);          /* DELAY BY READING ADCS2 */
x1[l] = inport (ADCS1);          /* DELAY BY READING ADCS1 */
x2[l] = inport (ADCS2);          /* DELAY BY READING ADCS2 */
x1[k] = inport (ADCS1);          /* READ ADCS1 */
x2[k] = inport (ADCS2);          /* READ ADCS2 */
k++;
outportb (portB, 0x00);          /* SWITCH LED OFF */
                /* 0x08 TO SWITCH LED OFF ONLY  FOR VIBRATION */
x1[l] = inport (ADCS1);          /* DELAY BY READING ADCS1 */
x2[l] = inport (ADCS2);          /* DELAY BY READING ADCS2 */
x1[l] = inport (ADCS1);          /* DELAY BY READING ADCS1 */
x2[l] = inport (ADCS2);          /* DELAY BY READING ADCS2 */
x1[k] = inport (ADCS1);          /* READ ADCS1 */
x2[k] = inport (ADCS2);          /* READ ADCS2 */
k++;
}while (k <= MAX);
outport (portB, 0x00);       /* SWITCH TIMER OFF FOR VIBRATION */
k = MIN;
do                           /* COPY THE DATA INTO THE DATAFILE */
{
S1A = S1B = S2A = S2B = S = 0;
S1A = x1[k] & 0x0fff;
S2A = x2[k] & 0x0fff;
k++;
S1B = x1[k] & 0x0fff;
S2B = x2[k] & 0x0fff;
k++;
S1 = S1A - S1B;
```

```
        S2 = S2A - S2B;
/*      S = (((S1 - S2) * 1.0) / (S1 * 1.0)) * 100;*/  /* % DIFF. WHEN Xo = 0 */
        S = (S1 + S2) / ((S1 - S2) * 1.0);             /* S WHEN Xo > 0 */
fprintf (fp,"%d %d %d %d %d %d %d %6.2f\n", R, S1A, S2A, S1B, S2B, S1, S2, S);
printf  ("%d %d %d %d %d %d %d %6.2f\n", R, S1A, S2A, S1B, S2B, S1, S2, S);
        }while (k < (MAX-2));
fclose  (fp);                                  /* CLOSE THE DATAFILE */
getch();
}
```

Appendix B

Components Used

B. CONTENTS

B.1. TRANSLATION STAGE

UT 100

The UT 100 stages are microdisplacement translators consisting of a slide frame which supports a mobile carriage. The guides consist of track linear ball bearings which are preloaded to eliminate play .

The methods of driving the stage are as follows :

- direct manual drive by knurled knob
- differential manual drive incorporating direct drive and 1/10 reduction
- DC motor
- stepping motor : 1 step = 0.1 µm, 1 µm or 10 µm depending on the model.

The drive commands are transmitted to the system by means of a leadscrew and nut. The pitch of the leadscrew is 1 mm per rotation, 2 mm for 10 µm step.

The travel of the stage is limited by positive mechanical stops. In motorized systems, these stops are augmented by limit switches which cut the power to the motor before the carriage has reached its mechanical limit of travel.

The position of the carriage is given by a mobile index which is read against a millimetre scale. Finer indication of position is available through any of the following :

- graduated scale engraved on the drive knob (type MS)
- numerical readout in conjunction with a vernier scale (type MN)
- incremental encoder (type GS)
- potentiometer
- stepping motor

UT 100 PP stages with stepping motors can be optionally equipped with an electromechanical origin search device.

specification

- On axis accuracy : 4 µm
- Repeatability : 0.8 µm
- Hysteresis : 2.5 µm
- Resolution : 10 µm,1 µm or 0.1 µm depending on model
- Straightness of trajectory :
  pitch αy 50 x 10^{-6} rad
  yaw αz 30 x 10^{-6} rad
- Weight : 2.5 to 3 kg

micro-controle

in France

Head office - Sales department
Research laboratories
Department Nachet
7, rue Jean Mermoz
Z. I. St Guénault BP 144
91005 Evry Cedex
Tel.: (1) 64 97 98 98
Telex: 601 105 F
Fax: 33 1 60 79 45 61

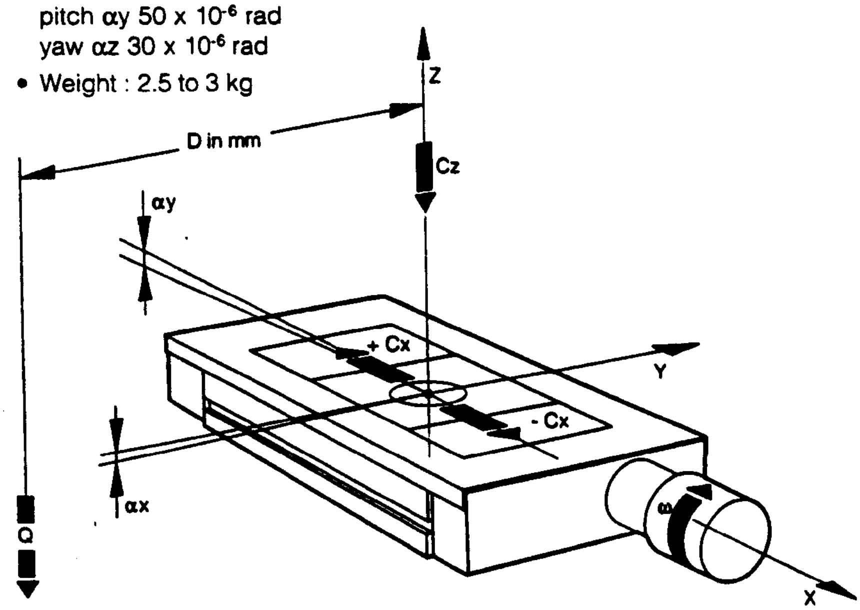

load capacity

C = Q (1 + 0.02 D) must be ≤ Cz, with :

Cz = nominal load capacity equivalent to the vertical load capacity	200 N
C = load capacity (N) Q = actual load (N) D = distance from centre of carriage (mm)	
transversal rigidity (roll), αx	1.5. 10^{-7} rad./Ncm
longitudinal rigidity (pitch), αy	10^{-7} rad./Ncm
load capacity + Cx direction	50 N
load capacity - Cx direction	10 N
flexion torque ω = 3 (1 + Qx) cmN. with : (Qx = axial load)	

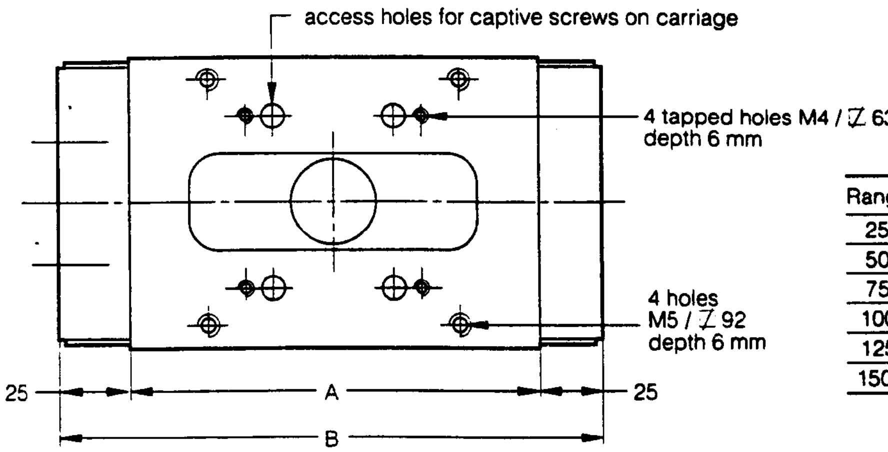

Range	A	B	Weight (kg)
25	105	155	2
50	130	180	2.2
75	155	205	2.4
100	180	230	2.6
125	205	255	2.8
150*	230	280	3

* actual travel : 152.4 mm (6")

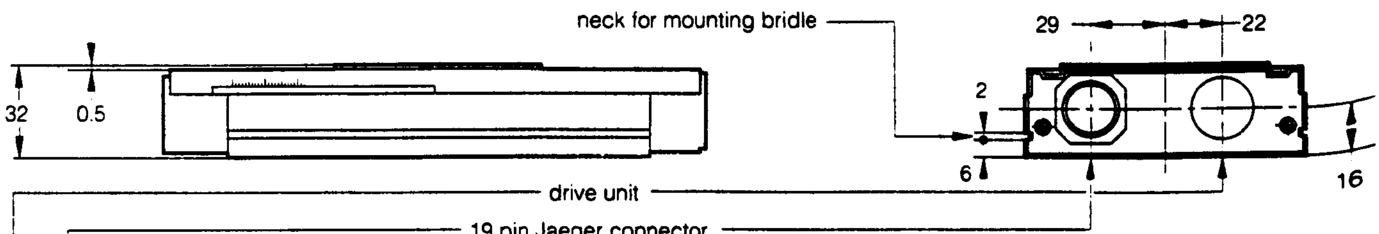

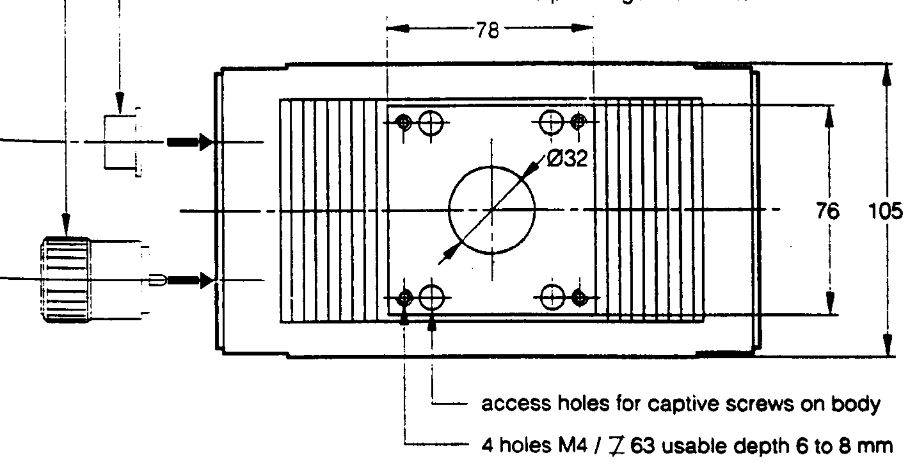

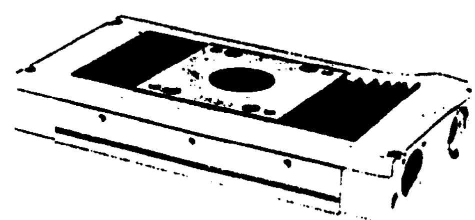

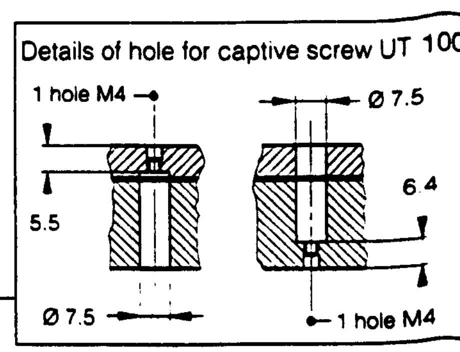

UT 100. - - MS + GS

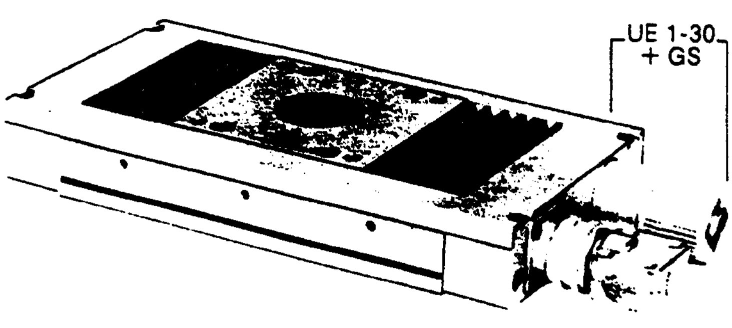

- Manually driven with incremental encoder
- 1 increment = 1 µm or 0.1 µm

	1 µm	0,1 µm
UT 100.25 MS + GS	**354 444**	**354 344**
UT 100.50 MS + GS	**354 445**	**354 345**
UT 100.75 MS + GS	**354 446**	**354 346**
UT 100.100 MS + GS	**354 447**	**354 347**
UT 100.125 MS + GS	**354 448**	**354 348**
UT 100.150 MS + GS	**354 449**	**354 349**

B.2. LED AND PHOTODIODE

SMA Emitters and Detectors

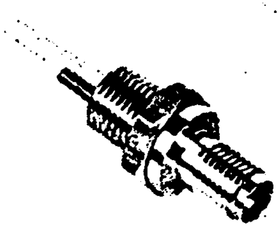

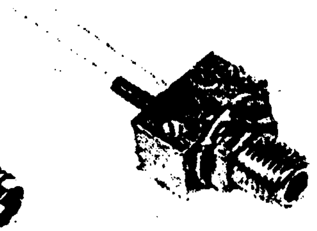

Panel, Rear Fitting
Body overall L = 20.6
Nut = 11 A/F

PCB
Body overall L = 16.3, W = 12.7
2 holes drilled
and tapped 2.56 UNC

FIBRE DATA

Panel cut-out

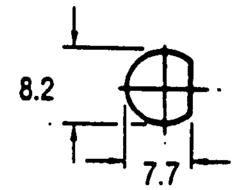

Single hole type

PCB type recommended panel hole size = 2.3 dia. 2 holes on 9.5 fixing centres. Lead length = 21

Connections: Emitters: Red sleeve – Anode. Detectors: Black sleeve – Anode.

Universal 9mm FSMA emitters and detectors are suitable for use with both 1mm polymer fibre and 200/250μm glass fibre cables. This enables low cost polymer cable to be used over shorter distances with the same emitters and detectors as used with 200/250μm cable over longer distances.

The PIN diode photodetectors have 1mm square active area permitting collection of light with high efficiency for all fibres up to 1000μm (1mm) core size, and can be used for frequencies up to and in excess of 100MHz. The spectral range of sensitivity is 400 to 1100nm.

The emitters and detectors are both available in a choice of mounting styles with SMA connection. All have full epoxy primary encapsulation.

Emitters

Launch power (typ.) @ 50mA dc	900μW into 1mm polymer 60μW into 200/250μm
Peak emission wave length	660nm @ 20mA dc
Response time	70ns (typ.)
Forward voltage drop	1.6V
Reverse voltage (max.)	5V
Forward current (max.)	50mA
Operating temperature	–20°C to +70°C

Detectors

Responsivity (typ.) @ 850nm	0.6A/W
Dark current (typ.) @ 5V	1nA
Capacitance (typ.) @ 5V	3.5pF
Response time	2ns typ, 4ns max.
Reverse voltage (max.)	30V
Power dissipation	100mW
Operating temperature	–40°C to +80°C

Link performace of emitter/detector pairs
200m @ 20kBd, 100m @ 10MBd with 1mm polymer cable
800m @ 10MBd with 200/250μm cable

Mftrs. List No.	Order Code	Mftrs. List No.	Order Code
H3E-2000BHR	179-126	H3R-880IR	179-130
H22E-2000BHR	179-128	H22R-880IR	179-132

B.3. S1336 - 44BQ, HAMAMATSU PIN PHOTODIODE

Type No.	Dimensional Outline (P.38-42)/ Window Material*	Package (mm)	Active Area Size (mm)	Effective Active Area (mm^2)	Spectral Response Range (nm)	Peak Sensitivity Wavelength λp (nm)	Photo Sensitivity S (A/W) λp Typ.	200nm Min.	200nm Typ.	He-Ne Laser 633nm Typ.	GaAs LED 930nm Typ.	Short Circuit Current Isc 100 lx Min. (μA)	Short Circuit Current Isc 100 lx Typ. (μA)
S1336 Series (Metal Package)													
S1336-18BQ	❶/Q	TO-18	1.1×1.1	1.2	190 to 1100	960	0.5	0.08	0.1	0.33	0.5	1	1.2
S1336-18BK	❶/K				320 to 1100			—	—				
S1336-5BQ	❽/Q	TO-5	2.4×2.4	5.7	190 to 1100			0.08	0.1			4	5
S1336-5BK	❽/K				320 to 1100			—	—				
S1336-44BQ	❽/Q		3.6×3.6	13	190 to 1100			0.08	0.1			8	10
S1336-44BK	❽/K				320 to 1100			—	—				
S1336-8BQ	⓬/Q	TO-8	5.8×5.8	33	190 to 1100			0.08	0.1			22	28
S1336-8BK	⓬/K				320 to 1100			—	—				

(Ta=25℃)

Dark Current ID V_R=10mV Max. (pA)	Temperature Dependence of ID Typ. (times/℃)	Rise Time tr V_R=0V R_L=1kΩ (μs)	Terminal Capacitance Ct V_R=0V f=10kHz Typ. (pF)	Shunt Resistance Rsh V_R=10mV Min. (GΩ)	Shunt Resistance Rsh V_R=10mV Typ. (GΩ)	NEP Typ. ($W/Hz^{1/2}$)	Absolute Maximum Ratings Reverse Voltage V_R Max. (V)	Operating Temperature Topr (℃)	Storage Temperature Tstg (℃)	Type No.
20	1.15	0.1	20	0.5	2	5.8×10^{-15}	5	−20 to +60	−55 to +80	S1336-18BQ
								−40 to +100	−55 to +125	S1336-18BK
25		0.2	65	0.4	1	8.1×10^{-15}		−20 to +60	−55 to +80	S1336-5BQ
								−40 to +100	−55 to +125	S1336-5BK
50		0.5	160	0.2	0.6	1.1×10^{-14}		−20 to +60	−55 to +80	S1336-44BQ
								−40 to +100	−55 to +125	S1336-44BK
100		1	370	0.1	0.4	1.3×10^{-14}		−20 to +60	−55 to +80	S1336-8BQ
								−40 to +100	−55 to +125	S1336-8BK

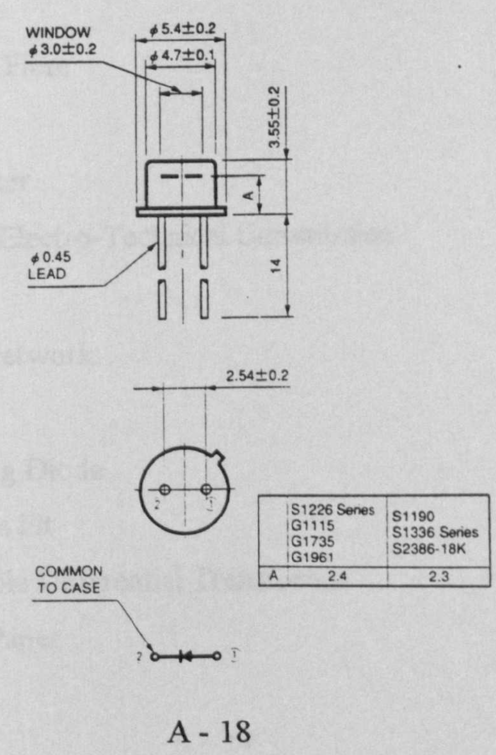

Glossary

ADC	Analogue to Digital Converter
APD	Avalanche Photodiode
ATR	Attenuated Total Reflection
C	Interception with S-axis, Constant
CALC	Calculated
CCW	Counter Clockwise
COMP	Computed
CW	Clockwise
DMM	Digital Multi-Meter
DR	Diffuse Reflective
EMI	Electro-Magnetic Interference
FDM	Frequency Division Multiplexing
FSR	Full Scale Reading
FTIR	Frustrated Total Internal Reflection
F/B	Feedback
GI	Graded Index
GOF	Glass Optical Fibre
GRIN	Graded Index
HPF	High Pass Filter
IEC	International Electro-Technical Commission
I/O	Input/Output
LAN	Local Area Network
LD	Laser Diode
LED	Light Emitting Diode
LSF	Least Squares Fit
LVDT	Linear Variable Differential Transformer
MWP	Matt White Paper

NA	Numerical Aperture
OFST	Offset
PBS	Polarized Beam Splitter
PC	Personal Computer
PCB	Printed Circuit Board
PE	Polyethylene
PMMA	Polymethyl Methacrylate
POF	Plastic Optical Fibre
PSD	Position Sensitive Detector
PZT	Piezoelectric Element
P/D	Photodiode
RC	Resistor and Capacitor
RI	Refractive Index
SI	Step Index
SNR	Signal-to-Noise Ratio
SPKR	Speaker
TDM	Time Division Multiplexing
THEO	Theoretical
VLM	Visible Laser Module
WDM	Wavelength Division Multiplexing

References

Allocca, J.A. and Stuart, A., (1984) *Transducers, Theory and Applications*, Reston Publishing Company, ISBN 0-8359-7796-X.

Anderson, J.S. and Bratos-Anderson, M., (1993) *Noise: Its Measurement, Analysis, Rating and Control*, Avebury Technical, ISBN 0-291-39794-8.

Ashpole, R.S., Hall, S.R. and Luker, P.A., (1990) "Polymer Optical Fibres - A Case Study", *GEC Journal of Research*, Vol. 8, No. 1, pp 32 - 41.

Berthold, J.W., (1994) "Historical Review of Microbend Fibre Optic Sensors", *SPIE, 10th Optical Fibre Sensors Conference*, Vol. 2360, pp 182 - 186.

Billings, A.R., (1993) "Optical Sensors", *Optics, Opto-electronics and Photonics: Engineering Principles and Applications*, Prentice Hall, Ch. 10, pp 313 - 332, ISBN 0-13-709115-X.

Brenci, M., Conforti, G., Mignani, A.G. and Scheggi, A.M., (1988) "Fibre Optic Position Sensor Array", *Optical Fibre Sensors '88, Technical Digest Series*, Vol. 2, pp 141 - 144.

Bolton, W., (1996) "Position and Motion Measurements", *Measurement and Instrumentation Systems*, Newnes, Ch. 11, pp 276 - 302, ISBN 0-7506-3114-7.

Chitnis, V.T., Kumar, S. and Sen, D., (1989) "Optical Fibre Sensor for Vibration Amplitude Measurement", *Journal of Lightwave Technology*, Vol. 7, No. 4, pp 687 - 691.

Clarke, T., (1998) "Simple Scanners Reveal Shape, Size and Texture", *Opto & Laser Europe*, Issue 52, April, pp 29 - 32.

Cockshott, C.P. and Pacaud, S.J., (1989) "Compensation of an Optical Fibre Reflective Sensor", *Sensors and Actuators*, 17, pp 167 - 171.

Conforti, G., Brenci, M., Mencaglia, A. And Mignani, A.M., (1989) "Fibre Optic Vibration Sensor for Remote Monitoring in High Power Electric Machines", *Applied Optics*, Vol. 28, No. 23, pp 5158 - 5161.

Dally, J.W., Riley, W.F. and McConnell, K.G., (1993) "Sensors for Transducers", *Instrumentation for Engineering Measurements*, 2nd Ed., John Wiley & Sons, Inc., Ch. 5, pp 124 - 158, ISBN 0-471-60004-0.

Daum, W., Brockmeyer, A. and Goehlich, L., (1992) "Environmental Qualification of Polymer Optical Fibres for Industrial Applications", *1st Int. Conf. POF and Applications*, Paris, pp 91 - 95.

Dinev, P.D., (1995) "A Two-Dimensional Fibre-Optical Vibration Sensor", *Measurement, Science and Technology, 6*, pp 1395 - 1398.

Farnell Components, (Oct. 1996 - Mar. 1997) *Commercial Cataloque*, Section 20, p 833.

Felgenhauer, R., Haack, A. and Streuf, M., (1993) "Fibre Optic Distance Sensor with POF", *2nd Int. Conf. POF and Applications*, Hague, pp 171 - 173.

Figliola, R.S. and Beasly, D.E., (1991) "Metrology, Displacement and Motion Measurements", *Theory and Design for Mechanical Measurements*, John Wiley and Sons, Ch. 10, pp 417 - 446, ISBN 0-471-54441-8.

Fraden, J., (1997) *Handbook of Modern Sensors: Physics, Designs and Applications*, 2nd Ed., AIP Press, ISBN 1-56396-538-0.

Fuhr, P.L., Feener, H.C. and Spillman, W.B.Jr, (1989) "Fibre Optic Linear Displacement Sensor Based on Matched Interference Filters", *SPIE, Fibre Optic and Laser Sensors VII*, Vol. 1169, pp 461 - 472.

Giles, I.P., McNeill, S. and Culshaw, B., (1985) "A Stable Remote Intensity Based Optical Fibre Sensor", *J. Phys. E: Sci. Instrum.*, Vol. 18, pp 502 - 504.

Grandke, T. and Ko, W.H., (1989) "Preface", *Sensors: A Comprehensive Survey*, T. Grandke, W.H. Ko (Vol. Eds), W. Göpel, J. Hesse and J.N.Zemel (Series Eds), Vol. 1, ISBN 3-527-26767-0 (VCH, Weinheim).

Gregory, B.A., (1981) "Transducers", *An Introduction to Electrical Instrumentation*, The Macmillan Press Ltd, Ch. 5, pp 234 - 276, ISBN 0-333-29394-3.

Halliwell, N.A., (1993), "Laser Vibrometry", *Optical Methods in Engineering Metrology*, Williams, D.C. (Ed.), Chapman and Hall, Ch. 6, pp 179 - 211, ISBN 0-412-39640-8.

Haslam, J.A., Summers, G.R. and Williams, D., (1981) "Transducers", *Engineering Instrumentation and Control*, Edward Arnold, Ch. 3, pp 27 - 50, ISBN 0-7131-3431-3.

Hoss, R.J., (1990) "Fibre Optic Component Specification", *Fibre Optic Communications: Design Handbook*, Prentice Hall Int. Inc., Ch. 3, pp 66 - 140, ISBN 0-13-313321-4.

Hughes, E., (1977) "Efficiency of D.C. Machines" *Electrical Technology*, 5th Ed., Longman Group Limited, Ch. 9, pp 251 - 265, ISBN 0-582-41144-0.

Inoue, M., (1990) "Vibration-Induced Intensity Modulation in Multimode fibre", *Japanese Journal of Applied Physics*, Vol. 29, No. 12, pp 2741 - 2743.

Ishigure, T., Nihei, E., Yamazaki, S., Kobayashi, K. and Koike, Y., (1995) "2.5Gbit/s 100m Data Transmission Using Graded Index Polymer Optical Fibre and High Speed Laser Diode at 650nm Wavelength", *Electronics Letters*, Vol. 31, No. 6, pp 467 - 469.

Johnson, C., (1993) "Mechanical Sensors", *Process Control Instrumentation Technology*, 4th Ed., Prentice Hall, Ch. 5, pp 182 - 230, ISBN 0-13-016585-9.

Jones, B.E., Medlock, R.S. and Spooncer, R.C., (1989) "Intensity and Wavelength-Based Sensors and Optical Actuators", *Optical Fibre Sensors: Systems and Applications*, Brian Culshaw and John Dakin (eds), Vol. 2, Ch. 12, pp 431 - 473, ISBN 0-89006-376-1.

Kalymnios, D., (1993) "Linear and Scalable Optical Sensing Technique for Displacement", *Sensors VI, Technology, Systems and Applications*, Sensors Series, KTV Grattan and AT Augusti (eds), pp 291 - 293.

Kalymnios, D., (1994) "Plastic Optical Fibres (POF) - Characteristics, Metrology and Applications", *Trends in Optical Fibre Metrology and Standards*, O.D.D. Soares (Ed.), NATO ASI Series, Series E: Applied Sciences - Vol. 285, ISBN 0-7923-3402-7.

Karim, D.P., (1991) "Bandwidth Measurements of Polymer Optical Fibres", *SPIE, Plastic Opitical Fibres*, Vol. 1592, pp 31 - 41.

Keiser, G., (1991) "Optical Fibres: Structures, Waveguides and Fabrication", *Optical Fibre Communications*, 2nd Ed., McGraw Hill Int. Eds, Ch. 2, pp 16 - 85, ISBN 0-07-100785-7.

Krohn, D.A., (1986) "Intensity Modulated Fibre Optic Sensors - Overview", *SPIE, Fibre Optic and Laser Sensors IV*, Vol. 718, pp 2 - 11.

Lahteenmaki, V., Kopola, H., Myllyla, R. and Wierzba, H., (1989) "A Two-Detector Fibre Optic Sensor for Industrial Conditions", *SPIE, Optical Fibres and their Applications*, Vol. 1085, pp 480 - 483.

Libo, Y. and Anping, Q., (1991) "Fibre Optic Diaphragm Pressure Sensor with Automatic Intensity Compensation", *Sensors and Actuators A*, 28, pp 29 - 33.

Libo, Y., Jian, P., Tao, Y. and Guochen, H., (1993) "Analysis of the Compensation Mechanism of a Fibre Optic Displacement Sensor", *Sensors and Actuators A*, 36, pp 177 - 182.

Lin, C.S. and Chang, R.S., (1994), "Fibre Optic Displacement Sensors for the Measurement of a Vibrating Object", *Precision Engineering,* Vol. 16, No. 4, pp 302 - 306.

Lion, K.S., (1969) "Transducers: Problems and Prospects", *IEEE Trans. Industr. Electron. Contr. Instrum.*, Vol. IECI-16, pp 2 - 5.

Loughlin, C., (1989) "Distance Sensing: Making Light Work", *Sensor Review,* 9 (3), pp 131 - 136.

Loughlin, C., (1989) "Ultrasonic Measurement: Keeping your Distance", *Sensor Review,* 9 (2), pp 85 - 89.

Marcou, J., Boutinaud, G., Faugeras, P., Etourneau, K., Roblin, G., Roger, G., Dequenne, M., Dugas, J. and Zimmermann, P., (1995) "Study of the POF Behavior under Mechanical and Thermal Constrains", *4th Int. Conf. POF and Applications,* Boston, pp 105 - 110.

McComb, G., Evans, A.J. and Evans, E.J., (1991) "Introduction - of Sound and Speakers", *Building Speaker Systems,* 2nd Ed., Master Publishing, Inc., Ch. 1, pp 1 - 12.

Medlock, R.S., (1986) "Review of Modulating Techniques for Fibre Optic Sensors", *Journal of Optical Sensors,* Vol. 1, No. 1, pp 43 - 68.

Melles Griot, (1990) "Detectors", *Optics Guide 5,* Ch. 22, pp 22_1 - 22_40.

Mignani, A.G., Mencaglia, A. and Brenci, M. (1994) "Using Fiber-Optic Proximity Sensors to Control Spindle Stop Position in Robot Applications", *10th Optical Fiber Sensors Conference,* pp 489 - 492.

Morris, N.M., (1991) "Transducers", *Control Engineering,* 4th Ed., McGraw-Hill, Ch. 2, pp 14 - 26, ISBN 0-07-707284-7.

Murtaza, G. and Senior, J.M., (1995) "Schemes for Referencing of Intensity-Modulated Optical Sensor Systems", *Optical Fibre Sensor Technology,* K.T.V. Grattan and B.T. Meggitt (Eds.), Chapman & Hall, London, Ch. 12, pp 383 - 407, ISBN 0 412 59210 X.

Murphy, M.M. and Jones, G.R., (1994) "A Variable Range Extrinsic Optical Fibre Displacement Sensor", *Pure Applied Optics,* 3, pp 361 - 369.

Nelson, D.F., Kleinman, D.A. and Wecht, K.W., (1977) "Vibration-Induced Modulation of Fibreguide Transmission", *Applied Physics Letters,* Vol. 30, No. 2, pp 94 - 96.

Nyfors, E. and Vainikainen, P., (1989) "Microwave Sensors", *Industrial Microwave Sensors,* Artech House, Inc., Ch. 1, pp 1 - 39, ISBN 0-89006-397-4.

Philp, W.R., Booth, D.J., Shelamoff, A. and Linthwaite, M.J., (1992) "A Simple Fibre Optic Sensor for Measurement of Vibrational Frequencies", *Measurement, Science and Technology, 3*, pp 603 - 606.

Pinnock, R.A., Extance, P., Hazelden, R.J., Pacaud, S.J. and Cockshott, C.P., (1987) "Colour Modulation Optical Displacement Sensors", *SPIE, Fibre Optics '87: Fifth Int. Conf. on Fibre Optics and Opto-Electronics*, Vol. 734, pp 238 - 244.

Ramsay, D.C., (1981) "Transducers", *Engineering Instrumentation and Control*, Stanley Thornes (Publishers) Ltd, Ch. 2, pp 26 - 51, ISBN 0-85950-439-5.

Regtien, P.P.L., (1990) "Accurate Optical Proximity Detector", *IEEE Instrumentation & Measurements, Tech. Conf.*, San Jose, 13 - 15 Feb., pp 141 - 143.

Ryder, G.H. and Bennett, M.D., (1992) "Vibrations of Single-Degree-of-Freedom Systems", *Mechanics of Machines*, 2nd Ed., The Macmillan Press Ltd, Ch. 13, pp 262 - 281, ISBN 0-333-53703-7.

Senior, J.M., Murtaza, G., Stirling, A.I. and Wainwright, G.H., (1992) "Single LED Based Dual Wavelength Referenced Optical Fibre Sensor System using Intensity Modulation", *Optics & Laser Technology*, Vol. 24, No 4, pp 187 - 192.

Seippel, R. G., (1983) "Vibration: Acceleration, Displacement, and Velocity" *Transducers, Sensors, and Detectors*, Reston Publishing Company, Inc., Ch. 4, pp 92 - 114, ISBN 0-8359-7797-8.

Sincerbox, G.T. and Gordon (II), J.G., (1981) "Modulating Light by Attenuated Total Reflection", *Laser Focus*, November, pp 55 - 58.

Toba, E., Shimosaka, T. and Shimazu, H., (1991) "Non-Contact Measurements of Microscopic Displacement and Vibration by Means of Fiber Optics Bundle", *SPIE, Fiber Optic and Laser Sensors IX*, Vol. 1584, pp 353 - 363.

Toray Plastic Optical Fibre, *PF/PG Series Data Sheet*, Commercial Literature.

Turner, R.P. and Gibilisco, S., (1991) *The Illustrated Dictionary of Electronics*, 5th Ed., McGraw-Hill, Inc., ISBN 0-8306-3345-6.

Udd. E., (1992) "Optical Fibre Sensors", *Fibre and Integrated Optics*, Vol. 11, pp 319 - 336.

Usher, M.J. and Keating, D.A., (1996) "Transducers for Length", *Sensors and Transducers*, 2nd Ed., Macmillan Press Ltd, Ch. 5, pp 52 - 92, ISBN 0-333-60487-3.

Whitaker, G. and Zarian, J., **(1995)** "Large Core Plastic Optical Fibre: New Innovations for the Signage Industry", *4th Int. Conf. POF and Applications*, Boston, pp 210 - 215.

Wilson, J. and Hawkes, J.F.B., **(1989)** "Noncommunication Applications of Fibres", *Optoelectronics: An Introduction*, 2nd Ed., Prentice Hall, Ch. 10, pp 408 - 437, ISBN 0-13-638461-7.

Young, P.H., **(1991)** "Fibre Optic Communication", *Electronic Communication Techniques*, 2nd Ed., Macmillan Publishing Company, Ch. 18, pp 775 - 812, ISBN 0-02-946312-2.

Publications

Ioannides, N., Kalymnios, D. and Rogers, I.W., (1993) "Experimental and Theoretical Investigation of a POF based Displacement Sensor", *Proc. of the 2nd Int. Conf. POF and Applications*, The Hague, pp 162 - 165, ISBN 3 905084 33 3.

Ioannides, N., Kalymnios, D. and Rogers, I.W., (1994) "Plastic Optical Fibre (POF) Displacement Sensor", *Trends in Optical Fibre Metrology and Standards*, O.D.D. Soares (Ed.), NATO ASI Series, Series E: Applied Sciences - Vol. 285, pp 827 - 828, ISBN 0-7923-3402-7.

Ioannides, N., Kalymnios, D. and Rogers, I.W., (1995) "A POF based Displacement Sensor for Use Over Long Ranges", *Proc. of the 4th Int. Conf. POF and Applications*, Boston, pp 157 -161.

Ioannides, N., Kalymnios, D. and Rogers, I.W., (1996) "An Optimised Plastic Optical Fibre Displacement Sensor", *Proc. of the 5th Int. Conf. POF and Applications*, Paris, pp 251 - 255, ISBN 3 905084 49 X.

Ioannides, N., Kalymnios, D. and Rogers, I.W., (1998) "A Plastic Optical Fibre (POF) Vibration Sensor", *Proc. of the Appl. Opt. Div. Conf. of IOP in Applied Optics and Optoelectronics 1998*, K.T.V. Grattan (Ed.), pp 163 - 168, Brighton, March, ISBN 0 7503 0456 1.

35

Experimental and theoretical investigation of a POF based displacement sensor.

N. Ioannides, D. Kalymnios, I.W. Rogers, University of North London (London, GB)

Abstract

A novel optoelectronic displacement sensor is described and results are presented from both experimental and analytical investigations of such a sensor. These results indicate that such a sensor should have a linear response over a useful distance range.

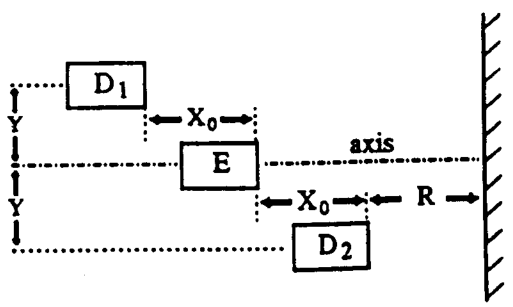

Figure 1

Introduction

In many industrial applications accurate measurements of linear displacements need to be made rapidly, the range of the displacement varying from the submicron region to many millimetres. Of the possible techniques available, an optical, non-contact method is often preferred. Many fire-optic displacement measurement techniques have been reported in the literature. Some are suitable for ranges of 10 mm or less[1-3] whilst others are for longer ranges[4-9].

The sensor described here, and shown schematically in Figure 1, is based upon the inverse square law and is suitable for the longer range applications. It consists of an optical emitter E and 2 optical detectors D_1 and D_2 displaced from each other parallel to the axis of the detector by a distance X_0, and perpendicular to this axis by an amount y, both X_0 and y being of the order of millimetres. This arrangement was chosen since a simplified theoretical treatment[10] showed that when the output signal S is defined by

$$S = \frac{S_1 + S_2}{S_1 - S_2}$$

where S_1 and S_2 are the outputs from the detectors D_1 and D_2 respectively, then S is expected to be a linear function of the range R for $R > 4X_0$. At the same time sensor performance is expected to be independent of any temporal variations in the output of the emitter. Initial experimental results using an infrared LED as the emitter and PIN diode detectors confirmed this behaviour for $4X_0 < R < 10X_0$ but showed a marked deviation from the theoretical curve at greater ranges, this deviation being ascribed to an observed asymmetry in the far-field pattern of the emitter relative to the axis of the detector.

Although successful, the sensor as constructed had the disadvantage that a great deal of care would be required in the selection of the emitter to ensure maximum isotropy of output. It would also be of limited use in electrically noisy environments since the active components (the emitter and PIN diodes) need to be close to the surface whose displacement is to be measured. In order to overcome both of these problems a new sensor has been constructed using plastic optical fibre (POF) both to take the light from the emitter to the position of E in Figure 1, and to collect the reflected light at positions D_1 and D_2 and guide it to the PIN diodes. Since the output from such a fibre is symmetrical about the axis it was expected that this would remove the problem associated with asymmetry. Also, by using

Papers presented at POF '93 the Second Annual Conference, held in the Hague, June 28–29, 1993.
The European Institute for Communications and Networks, Geneva.
POF '93, Secretariat: P.O. Box 6, CH-4002 Basel, Switzerland. Telephone ++41 61 691 51 11; Telefax ++41 61 691 81 89

POF the active components can be placed some metres away from the surface to be measured and the problems associated with electrical noise would be much reduced. A further advantage is a reduction in physical size of the sensor at the measurement location.

This paper presents some of the results of an analytical investigation of the expected sensor properties and a comparison with the initial results obtained experimentally.

Experimental Arrangement

In the sensor used to make the measurements reported here the plastic optical fibres carrying the optical signals were held in a jig such that the separation of the centres (y in Figure 1) was 3 mm and X_o = 3 mm. Each fibre had a core diameter of 960 μm, a cladding thickness of 20 μm and a length of 5 m. Typical attenuation along these fibres was 0.2 dB m^{-1}. The emitter used was a red LED coupled into the emitter fibre. The detectors were reverse biassed PIN diodes, the outputs being measured across load resistors using digital multimeters. Using a plane mirror as the reflecting surface the signals obtained from the detectors varied from a maximum of 820 mV at the shortest range to 6.5 mV at a range of 60 mm.

Analytical treatment

In order to obtain an accurate analytical description of the expected behaviour of the sensor under different conditions e.g. variation in X_o, y etc., a computer program has been developed which calculates, by numerical integration, the light incident upon each of the detectors taking into account the polar diagram for the emitter and the orientation and shape of the detector fibre end surfaces. The data from this program can then be modified to allow for inequalities in the performance of the complete detector system i.e. the combination of fibre, PIN diode and measuring instrument.

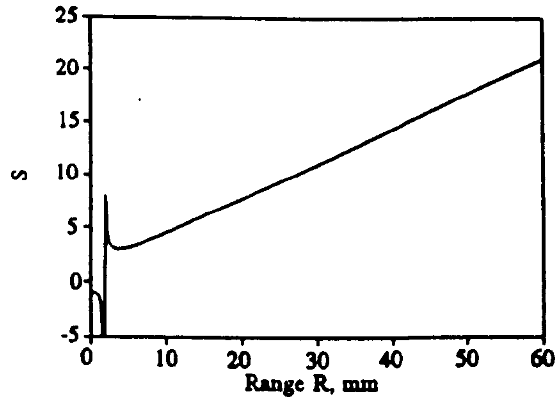

Figure 2

Figure 2 shows the variation of the calculated S value as a function of range, R, for the values of X_o and y used experimentally i.e. X_o = 3 mm and y = 3 mm.

The major points to note in this figure are:-

1. At ranges of < 5 mm the sensor response is extremely non-linear, showing a discontinuity at a range of approximately 3 mm. This result is readily understood in terms of the finite numerical aperture of the emitting fibre, the output beam having an angular width of 32°. Consider Figure 3 in which the sensor behaviour is represented in terms of the images of the detectors in the reflecting surface of Figure 1. For a small emitter-detector separation such as x1 no light would be collected by either of the detectors and so $S_1 = S_2 = 0$. If the distance is increased to x2, D_2 collects light over the whole of its surface whilst D_1 is

only partially illuminated. Under these circumstances $S_1 < S_2$ and so $S < 0$. Ultimately, at large distances e.g. x3, both detectors are fully illuminated and, as a result of the inverse square law effect, $S_1 > S_2$ and so $S > 0$. The predicted variations in S_1 and S_2 are shown in Figure 4.

Note: At a distance of approximately 2 mm, $S_1 = S_2$ and so $S = \infty$.

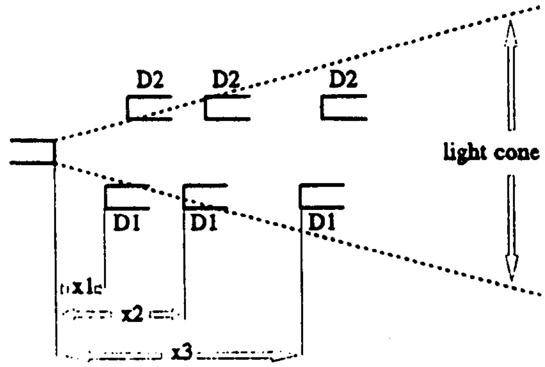

Figure 3

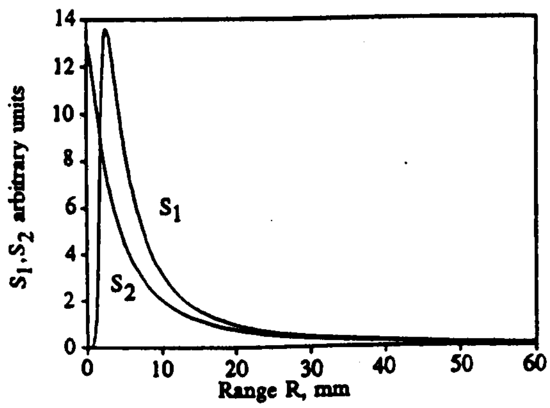

Figure 4

2. At ranges $R > 10$ mm the relationship between S and R is a linear one, the slope being 0.33. This is in agreement with the simplified theory which predicts a slope of X_o^{-1} at $R > 4X_o$.

<u>Comparison with experimental measurements</u>

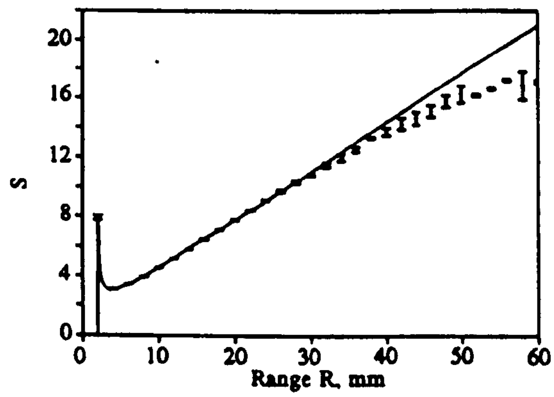

Figure 5

The graph of Figure 5 presents a comparison between the experimental results and analytical predictions for the sensor used. In this graph the errors shown for the experimental points represent the standard deviation from a number of repeated measurements. The important points to note from this graph are:-

1. There is excellent agreement between experiment and theory for ranges up to 30 mm, including the point at the range of 2 mm i.e. at the discontinuity in the analytical curve.
2. Over the range $10 \text{ mm} < R < 30 \text{ mm}$ the experimental points lie on a straight line. Using a least squares fit routine it is found that this line is represented by

   $$S = (0.323 \pm 0.002)\,R + (1.324 \pm 0.052)$$

   Taking the inverse of this since in practice the sensor would be used to determine the range R from a measured value of S, the relationship is

   $$R = (3.10 \pm 0.02)\,S - (4.09 \pm 0.16)$$
3. Beyond R = 30 mm the experimental S values deviate from the analytical curve, the deviation increasing as the range increases. At this time there is no clearcut explanation for this deviation but two possibilities have been investigated analytically:

   (a) In deriving the analytical curve it

is assumed that the signals from the two detectors will be identical for identical illumination of the fibre end i.e. both complete detector systems are identically calibrated. To determine the possible effect of mis-calibration the signal from the sensor was redefined as

$$S = \frac{k_1S_1 + k_2S_2}{k_1S_1 - k_2S_2}$$

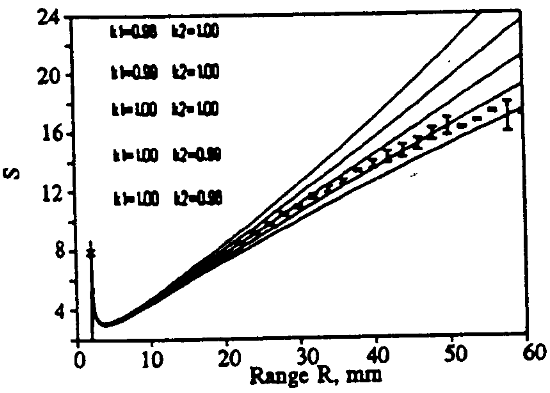

Figure 6

where k_1 and k_2 represent calibration factors. For ideal calibration $k_1 = k_2 = 1$. Figure 6 shows the analytical curves obtained for a range of combinations of k_1 and k_2 values, the maximum difference being 2%, compared with the experimental results. From this it can be seen that even a small mis-calibration could lead to major errors at large ranges.

(b) The possibility exists that one of the detector outputs contained a dc offset voltage. The effect of this has been investigated analytically with the result shown in Figure 6 where the lower curve was obtained for an offset in the output of D_2 of 0.1 mV, the upper curve being the ideal. It can be seen that such an offset would go a long way towards explaining the deviation of the experimental results from the analytical predictions.

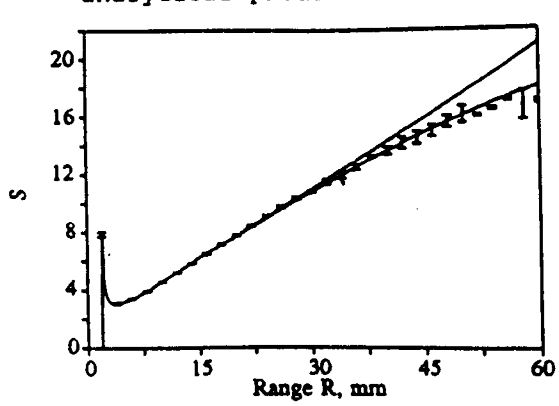

Figure 7

Conclusions

From the analytical studies it is clear that the proposed sensor arrangement would give a linear response for ranges greater than 10 mm but that in order to achieve linearity over a large range of distances e.g. up to 60 mm, a great deal of care would be needed to ensure that both detectors were calibrated equally over the whole of the proposed distance range and that no offsets existed. At the same time the experimental results indicate that even with the simple system used, linearity of response can be obtained over a useful range of distances.

Work on the sensor is continuing since it is believed that an exclusively POF displacement sensor of this type should find many useful applications. The continuing work is aimed in particular at extending both the linear range and the reproducibility of the sensor performance.

References

1. A.M. Scheggi et al : 'Optical Fibre Displacement Sensor'. SPIE, vol 798 Fiber Optic Sensors II(1987) pp72-74.
2. M. Brenci et al : 'Fibre Optic Position Sensor Array'. Optical Fibre Sensors 1988, Technical Digest Series, vol 2 (Optical Society of America, Washington DC 1988) pp141-144.
3. E. Bois et al : 'Loss Compensated Remote Fiber Optic Displacement Sensor for Industrial Applications'. Proc. EFOC/LAN 88, June 29-July 1 1988, pp246-250.
4. C.A. Wade et al : 'Optical Fibre Displacement Sensor based on Electrical Subcarrier Interferometry using a Mach-Zender configuration'. SPIE, vol 586, Fibre Optic Sensors (1985) pp223-229.
5. G.I. Frank et al : 'General Purpose Position Sensor'. SPIE, vol 586, Fibre Optic Sensors (1985) pp238-243.
6. S. Ramakrishan et al : 'Line Loss Independent Fibreoptic Displacement Sensor with Electrical Subcarrier Phase Encoding'. Optical Fibre Sensors 1988. Technical Digest Series, vol 2 pp133-136.
7. H. Hosokawa et al : 'Integrated Optic Microdisplacement Sensor using a Y Junction and a Polarization Maintaining Fibre'. Optical Fibre Sensors 1988. Technical Digest Series, vol 2 pp137-140.
8. G. Murtaza et al : 'Intensity Modulated Optical Fibre Sensor System for measuring up to 20mm of linear displacement'. IEE Colloquium, 'Fibre-optic Sensor Technology', May 1992. Digest no. 1992/128.
9. K. Iwamoto and I Kamata : 'Liquid-level Sensor with Optical Fibers'. Appl. Optics, vol 31, no. 1 1992, pp51-54.
10. D. Kalymnios : 'Linear and Scalable Optical Sensing Technique for Displacement', Submitted: Sensors and their Applications VI, Manchester 12-17 Sept. 1993.

PLASTIC OPTICAL FIBRE (POF) DISPLACEMENT SENSOR

N. IOANNIDES, D. KALYMNIOS and I.W. ROGERS
SECEAP, University of North London, Holloway Road
London N7 8DB, United Kingdom

Abstract

In many industrial applications accurate measurements of linear displacements need to be made rapidly, the range of the displacement varying from the submicron region to many millimetres. Of the possible techniques used an optical, non contact method is often preferred.

The sensor shown schematically in figure 1 is based on the inverse square law and is suitable for the longer ranges.

This novel optical method for measuring displacement gives an output which varies linearly with displacement and with a simple adjustment to the sensor dimensions can be used to cover a number of different ranges from a few millimetres to many centimetres.

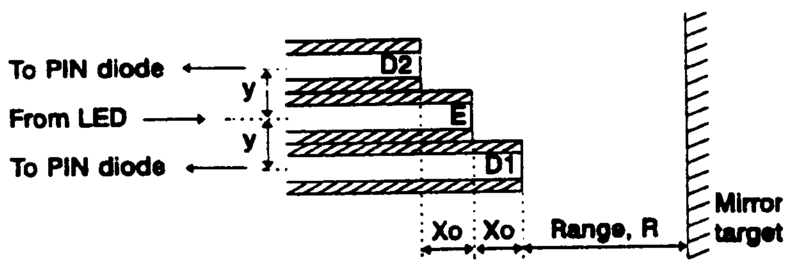

Figure 1

This arrangement was chosen since a simplified theoretical treatment showed that when the output signal S is defined by:

$$S = (S1+S2) / (S1-S2)$$

where S1 and S2 are the outputs from the two detectors D1 and D2 respectively then S varies linearly with the range R for R > 4Xo. Using a least squares fit routine over the useful measured S and by taking the inverse of this, the range R could be determined.

The sensor is using Plastic instead of Glass Optical Fibres for the reason that Plastic Optical Fibres have a fibre diameter of 1mm and so there is no need for any kind of lenses or any other optics to assist in collecting enough light.

Three 5 m long PMMA fibres, with their protective sheath are used one emitting (E) and two receiving (D1, D2), displaced from each other parallel to the axis of the detector by a scale factor Xo and perpendicular to this axis by an amount Y, both Xo and Y being of the order of millimetres. The three fibres are held side by side in the

O. D. D. Soares (ed.), *Trends in Optical Fibre Metrology and Standards*, 827–828.

same plane using a simple holder. The emitting fibre is coupled to a red LED and emits about 400 μW on to a target. The detecting fibres are coupled to two 13 mm^2 active area PIN photodiodes with transimpedance amplifiers.
From the experimental results obtained by using a reflective target and by having the Xo and Y separations set at 3mm and 2.2mm respectively, acceptable linearity was confirmed over the range 10mm < R < 80mm for a temperature range of 20°C < T < 35°C. Figure 2 shows experimental results. Each experimental point shown represents the spread of S values from 9 independent runs. The sensor performance remained unchanged when the current through the LED was varied from 80 mA down to 8 mA and also when the op amp power supply was varied from ± 18 V down to ± 10 V.
Experimental results were also obtained by using diffuse targets (Al beadblasted plate and white matt paper). Acceptable linearity was confirmed for the range 10mm < R < 50mm (figure 3).
The slope of the experimental points taken by using diffuse targets was exactly half the slope of the points when using reflective targets for this particular Xo separation as was predicted theoretically.

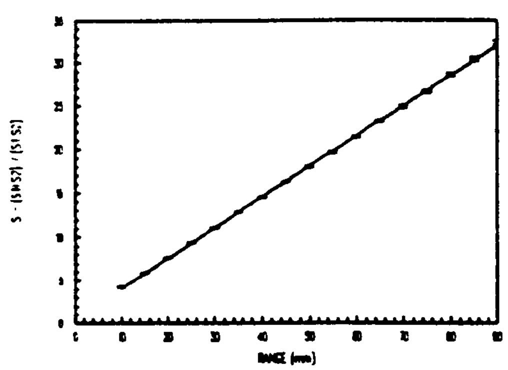

Figure 2

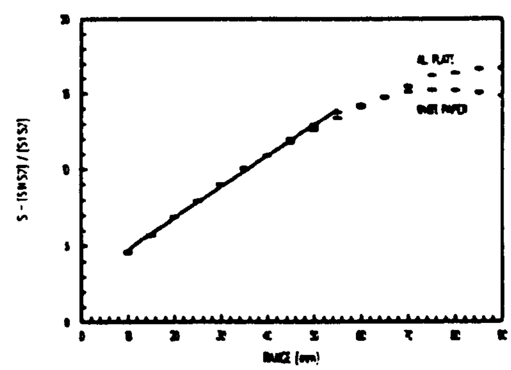

Figure 3

The conclusions from both experimental and theoretical results are that a displacement sensor based upon this principle could be constructed which would be both linear and scalable, the maximum measurable displacement being set by the available power from the emitter and the limiting signal to noise ratios of the detectors.
Work is continuing since it is believed that an exclusively POF sensor of this type, could find many useful applications.

References:

1. Kalymnios, D. (1993) Linear and scalable optical sensing technique for displacement, Sensors series, Sensor VI, KTV Grattan and AT Augousti, pp 291 - 3.

2. Ioannides, N., Kalymnios, D., and Rogers, I.W. (1993) Experimental and theoretical investigation of a POF based displacement sensor, 2nd international conference in plastic optical fibres and applications, The Hague, June 28 - 29.

A POF-BASED DISPLACEMENT SENSOR FOR USE OVER LONG RANGES

N. Ioannides, D. Kalymnios & I. Rogers

SECEAP, University of North London, 166-220 Holloway Road, London N7 8DB, UK.

Summary

In this paper we present recent results obtained using a novel design of Plastic Optical Fibre (POF) based displacement sensor and show that it has a linear response, it is accurate, repeatable and temperature stable for a range of distances from 10 mm to 80 mm.

Introduction

In a previous report[1] a novel optical method for measuring displacement was described. This method, based upon the inverse square law, uses a combination of a single emitter and two detectors (Figure 1) displaced relative to each other along the direction of the displacement to be measured. Defining the transfer function as:

$$S = \frac{S1 + S2}{S1 - S2}$$

where S1 and S2 are the signals from D1 and D2 respectively, then S is expected to be a linear function of the range R and the use of two detectors will compensate for any variations in the intensity of the LED. The method was said to be suitable for both 'opto-electronic sensors' (where the active elements are within the sensor head) and 'fibre-optic sensors' (where the active elements are remote from the sensor head, information being transferred between these elements and the sensor head along fibre optic cables). Results from an analytical treatment of the sensor and experimental results from a prototype fibre-optic sensor were the subject of a later report[2] and supported the validity of the method and indicated that such a sensor should have a linear response and a scalable range. Following this work has continued upon the development of a sensor with some or all of the characteristics shown in Table 1.

Table 1

Range:	10 - 100 mm
Accuracy:	better than 1%
Resolution:	better than 1%
Response:	linear
Temperature stability:	0.1% °C^{-1}
Operating frequency:	5 - 10 kHz

The displacement sensor

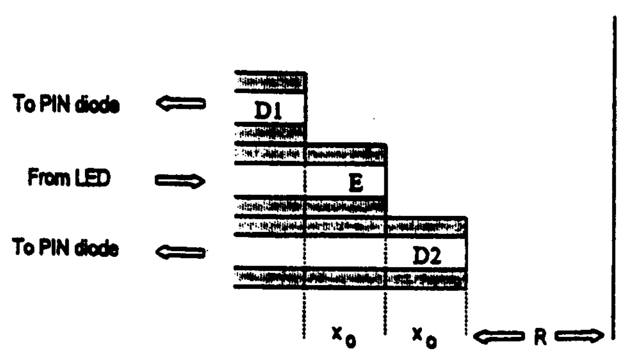

Figure 1: Schematic of the displacement sensor.

In the fibre-optic sensor used for the measurements reported here, three 5 m long, 1 mm core PMMA fibres are used complete with their protective sheaths. At the sensor head, shown schematically in Figure 1, these are held side by side in the same plane using a simple mechanical holder, with the ends of the fibres displaced relative to each other by a distance $x_0 = 2$ mm in the direction of the fibres. The central, emitting fibre (E) is coupled to a red LED which results in the emission of ~ 400 μW on to the mirror target. The two outer, detecting fibres (D1 and D2) are each coupled to a 3.6 mm^2 active area PIN photodiode with an associated transimpedance amplifier. Under these conditions the outputs from the detectors range from 6 V for a sensor to target distance, R = 10 mm, down to 80 mV for R = 100 mm. At present the outputs from the amplifiers are measured using digital multimeters and the analysis of the data is performed manually. Once the sensor has been fully characterized it is intended to develop the circuitry necessary to perform this analysis automatically.

Sensor linearity and accuracy

In the previous report[2] it was shown that S is expected to be a linear function of range, R, for ranges greater than $4x_0$. Below this range the response is extremely non-linear because of the non-isotropic distribution of the light from the emitting fibre.

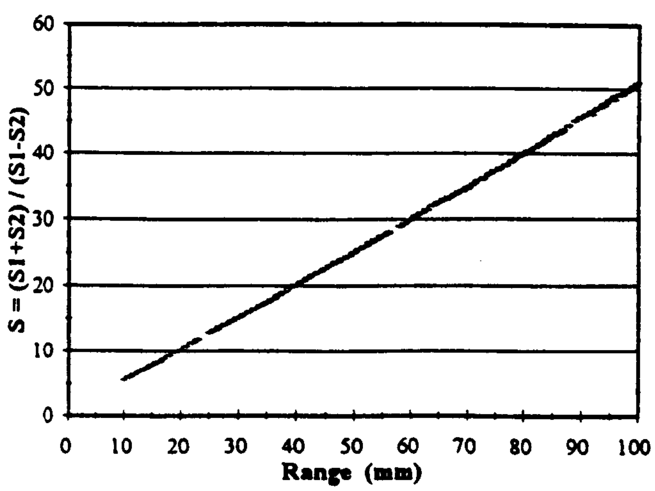

Figure 2: Variation of S with range, R.

Figure 2 shows the experimental variation of S for 500 randomly selected points with R over the range from R = 10 mm to R = 100 mm measured at a temperature of 25°C. The least squares fit equation to the experimental points of this line is:

$$S = 0.493R + 0.465$$

with R in mm, over a useful range of 15 mm < R < 80 mm. The slope of this line is in very good agreement with the expected slope[1] of $| x_0 |^{-1} = 0.5$.
By rearranging the equation of the least squares fit line it is possible to define the calibration curve as:

$$R_{exp} = (S - 0.465) / 0.493$$

where R_{exp} is the range obtained from the measured S value.

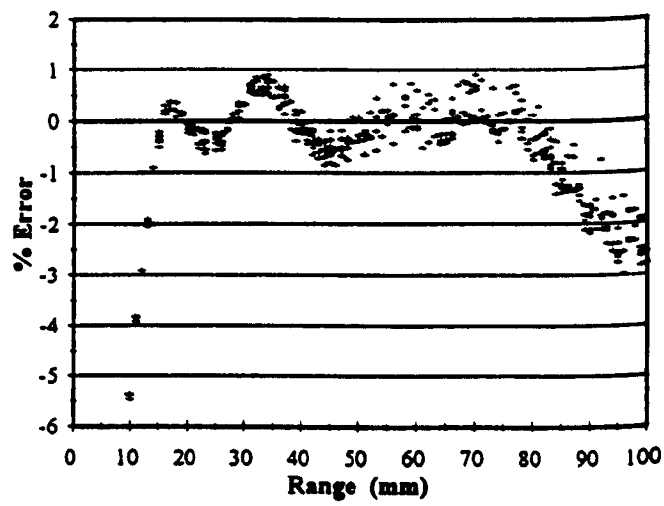

Figure 3: Percentage error in measured range as a function of true range.

Figure 3 shows the variation with range of the percentage error in measured range defined by:

$$\% \text{ Error} = [(R - R_{exp}) \times 100] / R$$

where R is the true range, obtained by applying this calibration to the measured S values for the data of Figure 2. From this it can be seen that the sensor gives an error in the range with a magnitude of less than 1%

for ranges between 15 mm and 80 mm. Allowing for the observed fluctuations in S, typical errors are (0.0 ± 0.2) % at 20 mm corresponding to (0 ± 40) μm, (-0.6 ± 0.4) % at 45 mm corresponding to (−270± 180) μm, and (0.5 ± 0.5) % at 70 mm corresponding to (350 ± 350) μm.

The sensor performance remained unaltered when the LED intensity was decreased by 40 % thus confirming the compensation expected from the use of two detectors.

Temperature stability

In order to check the temperature stability of the sensor measurements were made of S vs R for temperatures of 25 °C, 33 °C, 40 °C and 50 °C with the results shown in Figure 4.

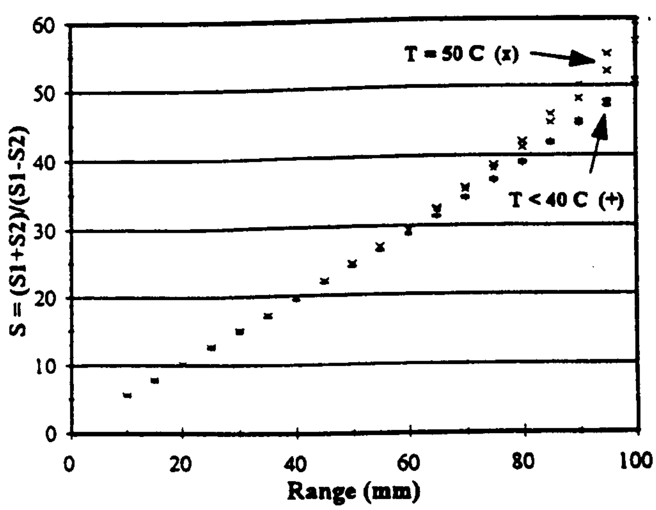

Figure 4: S vs R at different temperatures.

From this figure it can be seen that there is very little variation with temperature for the whole dynamic range of the sensor (15 mm < R < 80 mm) up to 40 °C. The sensor becomes temperature sensitive at higher temperatures (i.e. 50 °C).

Figure 5 shows the ratio of the signals from each diode at temperatures 33 °C, 40 °C and 50 °C over the signals detected at 25 °C. As the temperature increases, the output of the detecting circuits decreases due to a decrease in LED intensity. From the range R = 15 mm to R = 50 mm both diodes behave in a similar fashion leading to no variation in S with temperature. At ranges R > 50 mm the behaviour of the diodes diverges, the relative output of D2 increasing with range when compared with that of D1, leading to an increase in the overall S value at these ranges. This is believed to be a dark current effect, the dark current from D2 being more temperature sensitive than that from D1.

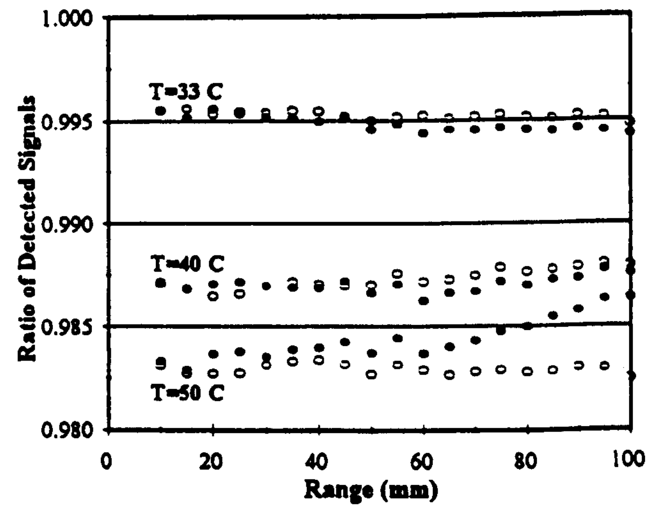

Figure 5: Ratio of detected signals for each detector: O D1, ● D2.

These results indicate that the range over which the sensor can be made insensitive to temperature could be increased by either using better matched PIN photodiodes or by increasing the LED output such that the individual signals from the diodes at large ranges are much greater than the dark current.

Resolution

The attainable resolution for this sensor will depend upon the accuracy with which the individual values of S1 and S2 can be measured and any inherent fluctuations (noise) in these and the resultant S value. With the existing arrangement where S1 and S2 are measured using digital multimeters the accuracy is ± 0.01 mV in a minimum of 80 mV and so lack of accuracy is not a limiting factor.

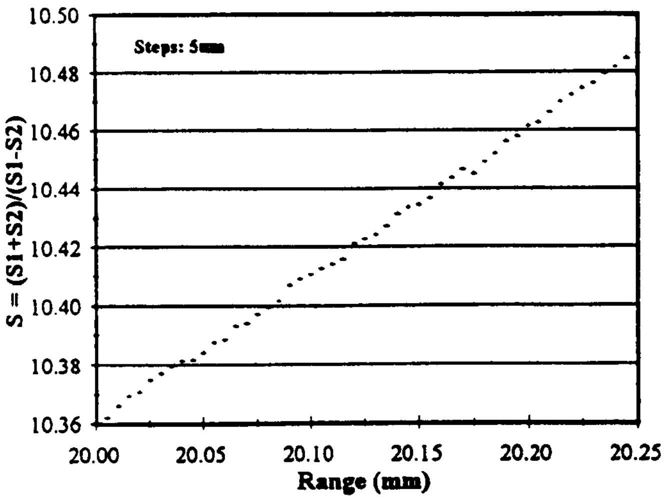

Figure 6: Resolution measurements at close ranges.

Figure 6 shows experimental results taken at steps of 5 μm. Resolution of 10 μm (0.05 %) at 20 mm is realizable. At R = 70 mm the sensor can resolve changes of 70 μm (0.1 %). These figures have been obtained under the best possible conditions. In practice any fluctuations in the measured signals are expected to result in a lower attainable resolution.

Operating frequency

Up to the present time no attempt has been made to determine the operating frequency of the sensor as this will depend, among other factors, upon the design of the processing circuitry and on the requirements of any application that the sensor may be used for.

Using a diffuse target

The report[1] which described this novel method for measuring displacement also considered the use of diffuse point targets, to be realised with collimated beams. The simple theory in that report showed that a linear response should still be realizable with a slope of $|2x_0|^{-1}$, in this case 0.25.

To investigate the performance of the sensor with diffuse targets the mirror target used during the previous measurements was replaced by a matt white paper disc of radius 5 mm.

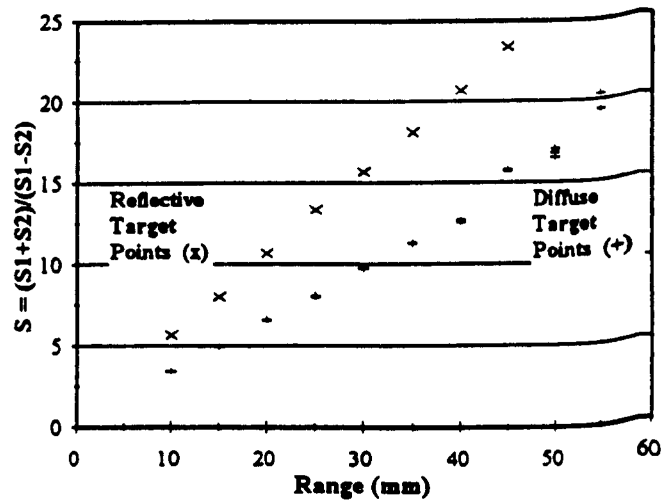

Figure 7: S vs R for two kinds of target, a diffuse and a reflective.

Figure 7 shows the experimental variation of S with R over the range from R = 10 mm to R = 55 mm for three runs taken at a temperature of 25 °C. Also shown for comparison are the results for a reflecting target. It can be seen that a linear response exists over the range 10 mm < R < 40 mm, the equation for the best fit straight line being:

$$S = 0.308R + 0.4$$

Although the slope of this line does not agree with the expected slope[1] of $|2x_0|^{-1} = 0.25$ predicted by the simple theory, it is clear that no matter what surface a target has (reflective or diffuse) a linear response is still realizable.

Rearranging the equation of the least squares fit line the calibration curve is defined as:

$$R_{exp} = (S - 0.4) / 0.308$$

where R_{exp} is the range obtained from the measured S value.

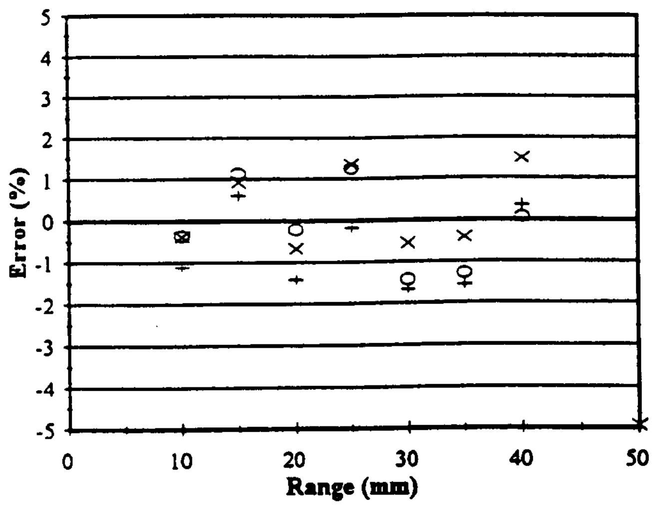

Figure 8: Percentage error in measured range as a function of true range for a diffuse target.

Figure 8 shows the variation with range of the percentage error in measured range obtained by applying this calibration to the measured S values for the data of Figure 7. From this it can be seen that the sensor gives an error with a magnitude of less than 2 % for ranges between 10 mm and 40 mm.

Discussion

From the results presented it is clear that the sensor is a usable device if the ranges to be measured lie between 15 mm and 80 mm. It offers accuracy better than 1 %, and resolution of 10 µm at short ranges and 70 µm at long ranges. It can operate up to a temperature of 40 °C without any problems for the whole range and up to 50 mm for even higher temperatures. Any variations / fluctuations in the intensity of the LED will leave the sensor unaffected. The nature of the target will determine the slope of the linear response with the diffuse target giving a slope which is nearly half that of a reflective target.
Future work will be aimed at improving the performance of the sensor with particular emphasis upon the reduction of both the fluctuations in the measured S values and the temperature effects. The control electronics for the sensor will also be modified to operate under ac rather than dc conditions. At the same time the application of the sensor to specific measurement situations will be investigated.

References

1. Kalymnios D., 1993, 'Linear and scalable optical sensing technique for displacement', Sensors VI, Technology Systems and Applications, pp 291-294.

2. Ioannides N. et al., 1993, 'Experimental and theoretical investigation of a POF-based displacement sensor', Proc. 2nd Int. Conf. POF and Applications, The Hague, pp 162-165.

3. Murphy M. M. and Jones G. R., 1994, 'A variable range extrinsic optical fibre displacement sensor', Pure Appl. Opt. 3, pp 361-369.

4. Libo Y. and Anping Q., 1991, 'Fibre optic diaphragm pressure sensor with automatic intensity compensation', Sensors and Actuators A, 28, pp 29-31.

5. Cockshot C. P. and Pacaud J., 1989, 'Compensation of an optical fibre reflective sensor', Sensors and Actuators, 17, pp 167-171.

6. Felgenhauer R., et. al., 1993, 'Fibre optic distance sensor with POF', Proc. 2nd Int. Conf. POF and applications, The Hague, pp 171-173.

7. Hadjiloucas S., et. al., 1994, 'Plastic optical fibres for measuring leaf water potential', Proc. 3rd Int. Conf. POF and Applications, pp 64 - 68.

44
An optimised, plastic optical fibre (POF) displacement sensor

N. Ioannides, D. Kalymnios, I.W. Rogers, University of North London (London, UK)

Summary.

A new, improved, more reliable, automated version of this displacement sensor has been implemented. This new version employs circuitry which allows for operation under ambient illumination conditions. The photodiode outputs are processed using 12-bit ADCs linked to a PC. Data collection is performed under software control and the value of the transfer function and the equivalent measured range are displayed in real time. The results obtained with the new set up are compared with the previous ones obtained under dark room conditions.

Introduction.

At the Boston conference we presented results obtained from a POF based displacement sensor [1]. This sensor, shown schematically in figure 1, employs three 5 m long, 1 mm core diameter PMMA fibres complete with their protective sheaths which are held side by side in the same plane by a simple mechanical holder. The middle POF (E) emits towards a mirror target and the other two (D1 and D2) receive the reflected light.

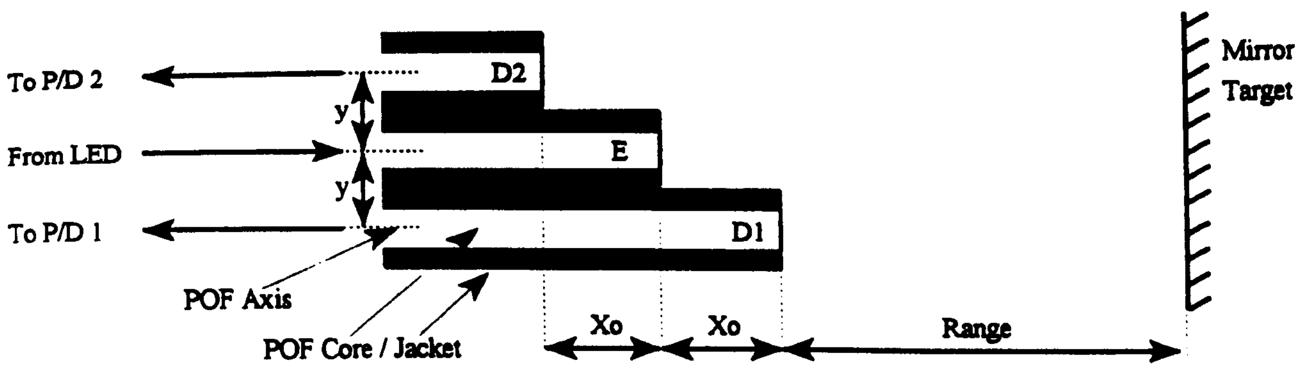

Figure 1: The sensor head arrangement.

The sensor is based upon the inverse square law. It has been shown both theoretically and experimentally that the transfer function, S, defined by:

$$S = (S1 + S2) / (S1 - S2)$$

where S1 and S2 are the signals from the two detectors D1 and D2 respectively, is very close to being a linear function of the range, R. Those results indicated that when operated under ideal conditions i.e. with no external illumination, and using high accuracy DVMs to measure S1 and S2, the sensor, which had the X_0 separation set at 2 mm, had a usable range from 15 mm to 80 mm with an accuracy of 1%. Since then the work has been aimed towards producing a practical sensor which can be used under conditions of variable ambient illumination and under computer control.

Operation of the Sensor under dc Conditions.

In order to produce a sensor system that could operate under computer control, two 12-bit ADCs were used to link the dc circuitry with a PC. The X_0 separation was set at 5 mm. Measurements were performed initially under dark room conditions with the detected signals recorded simultaneously by both the high accuracy DVMs and the ADCs for comparison purposes. The same measurements were then repeated but under ambient illumination conditions. The results of these measurements are shown in figure 2. The ellipses show the response of the sensor when monitoring using the DVMs and the triangles the response with the ADCs. The solid markers show the response of the sensor under dark room conditions and the open ones under ambient illumination.

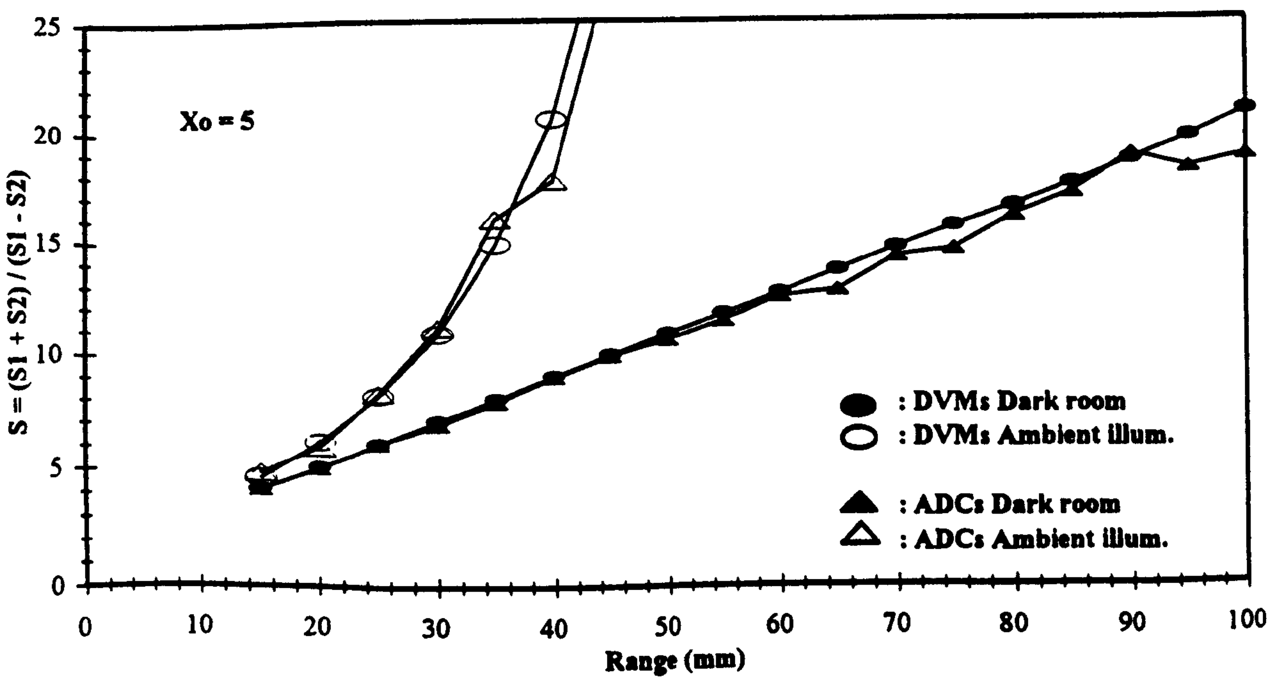

Figure 2: The response of the sensor under dc operation.

Under dark room conditions the response of the DVMs and the ADCs is linear. The response recorded by the DVMs extends towards the longer ranges due to their high accuracy offering a dynamic range of 85 mm, from 15 mm up to 100 mm, with an accuracy of 1%. The least squares fit equation to the experimental points of this line is:

$$S = 0.193R + 1.426$$

By rearranging the equation of the least squares fit line the calibration curve is defined as:

$$R_{exp} = (S - 1.426) / 0.193$$

where R_{exp} is the range obtained from the measured S value.

The response recorded by the ADCs offers linearity over a shorter range than the one recorded by the DVMs. At longer ranges the linearity of response of the sensor is greatly affected as a result of quantization error. A dynamic range of 40 mm, from 20 mm up to 60 mm with an accuracy of 1.5% was obtained. The least squares fit equation to the experimental points of this line is:

$$S = 0.187R + 1.556$$

The calibration curve is defined as:

$$R_{exp} = (S - 1.556) / 0.187$$

The slopes of these two lines are in very good agreement with the expected slope [2] of $| X_0 |^{-1} = 0.2$.

Under ambient illumination conditions, as the open points show in figure 2, linearity of response breaks down completely (both DVMs and ADCs agree). The amount of non-linearity varies with the level of ambient illumination.

The similarity of the results obtained when operating with the DVMs and the ADCs under dark room and ambient illumination conditions, show that computer controlled operation of the sensor is possible.

Operation of the Sensor under ac Conditions.

To remove the sensitivity to variations in ambient illumination the sensor has been converted to ac operation by driving the LED with an 8.5 kHz square wave. A detecting circuit that would respond to the LED and would offer filtering facilities was built. This detecting circuit was then linked to the PC via the same 12-bit ADCs. Measurements were performed under dark room conditions and variable ambient illumination. The results of these measurements are shown in figure 3. The solid blocks show the response of the sensor under dark room conditions and the open ones under ambient illumination.

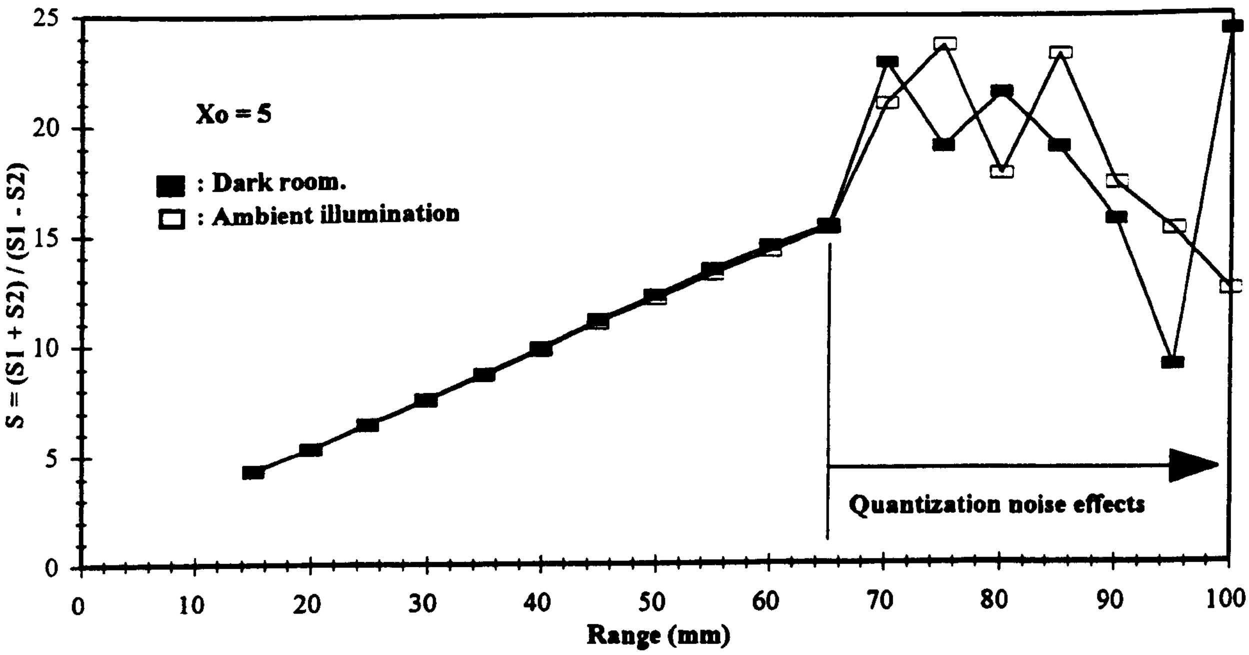

Figure 3: The response of the sensor with the new ac operating circuitry.

As shown in figure 3 the response of the sensor with the new ac circuitry remains linear under both dark room and ambient illumination conditions. The response recorded offers linearity over a similar range as the one recorded under dark room conditions using the ADCs but with the dc method.
A dynamic range of 45 mm, from 20 mm up to 65 mm (limited due to quantization error) with an accuracy of 1% was obtained. The least squares fit equation to the experimental points of the line under dark room conditions is:

$$S = 0.228R + 0.675$$

The calibration curve is defined as:

$$R_{exp} = (S - 0.675) / 0.228$$

The least squares fit equation to the experimental points of the line under ambient illumination conditions is:

$$S = 0.224R + 0.744$$

The calibration curve is defined as:

$$R_{exp} = (S - 0.744) / 0.224$$

The similarity of response of the two attempts, under dark room and ambient illumination, using the ac method clearly shows that the new version of the sensor can operate under any level of ambient illumination.

Conclusions and Further Work.

The greatest limitation of the displacement sensor, its sensitivity to variations in ambient illumination, has been overcome by changing the mode of operation of the sensor from dc to ac. Under ideal conditions (no external illumination and using high accuracy DVMs to measure S1 and S2) the dc operating circuitry performed excellently, producing linearity of response over a dynamic range of 85 mm (15 mm < R_{exp} < 100 mm) with accuracy of 1%. Computer control, lowered the dynamic range down to 40 mm (20 mm < R_{exp} < 60 mm) due to quantization noise of the ADCs, with accuracy of 1.5%. This dc version of the sensor was extremely unreliable under variable ambient illumination conditions with a complete breakdown of linearity.

The new version of the sensor operates under ac conditions and computer control. Effects caused by any ambient illumination conditions have been removed and a practicable sensor for such conditions has become feasible. Linearity of operation was obtained over a dynamic range of 45 mm (20 mm < R_{exp} < 65 mm) with accuracy of 1%.

Work is continuing in extending the dynamic range of the sensor. To do so, improvement of the processing electronics and higher bit accuracy ADCs will be necessary. The adoption of the sensor for applications of dynamic variables is considered. Vibration, pressure, acceleration, etc. are a few examples.

References.

1. **Ioannides, N., Kalymnios, D. and Rogers, I.W. (1995)** "A POF based Displacement Sensor for use over long ranges", Proc. 4th Int. Conf. Plastic Optical Fibres and Applications, pp 157 - 161, Boston.
2. **Kalymnios, D. (1993)** "Linear and Scalable Optical Sensing Technique for Displacement", in K.T.V. Grattan and A.T. Augousti (eds), Sensors VI, IOP Publishing Ltd., Great Yarmouth, pp 291 - 293.

Other References.

Cockshott, C.P. and Pacaud, S.J., (1989) "Compensation of an Optical Fibre Reflective Sensor", *Sensors and Actuators*, 17, pp 167 - 171.

Cook, R.O. and Hamm, C.W., (1979) "Fibre Optic Lever Displacement Transducer", *Applied Optics*, Vol. 18, No. 19, pp 3230 - 3240.

Kalymnios, D., (1994) "Plastic Optical Fibres (POF)", *Trends in Optical Fibre Metrology and Standards*, O.D.D. Soares (Ed.), NATO ASI Series, Series E: Applied Sciences - Vol. 285, ISBN 0-7923-3402-7.

Krohn, D.A., (1986) "Intensity Modulated Fibre Optic Sensors - Overview", *SPIE, Fibre Optic and Laser Sensors IV*, Vol. 718, pp 2 - 11.

Libo, Y. and Anping, Q., (1991) "Fibre Optic Diaphragm Pressure Sensor with Automatic Intensity Compensation", *Sensors and Actuators A*, 28, pp 29 - 33.

Murtaza, G. and Senior, J.M., (1994) "Referenced Intensity-based Optical Fibre Sensors", *Int. Journal of Optoelectronics*, Vol. 9, No. 4, pp 339 - 348.

Regtien, P.P.L., (1990) "Accurate Optical Proximity Detector", *IEEE Instrumentation & Measurements. Tech. Conf.*, San Jose, 13 - 15 Feb., pp 141 - 143.

A Plastic Optical Fibre (POF) Vibration Sensor

Ioannides, N., Kalymnios, D. and Rogers, I.W.

University of North London, School of Communications Technology and Mathematical Sciences, 166 - 220 Holloway Road, London N7 8DB, England.

Abstract: An optical method for measuring vibration is described. It uses a non contact displacement sensor which has a linear response and a scalable range. Single degree vibrations with peak displacement in the millimeter range can be monitored. The displacement and frequency of vibration of the vibrating surface can be determined.

1. Introduction

The monitoring and control of vibration is very important in many industrial applications. If it remains uncontrolled it can degrade the performance and safety of machines in motion or machines that have rotating members. Sensors used to monitor vibration include strain gauges, potentiometric, capacitive, piezoresistive, optical, etc. Optical vibration sensors employing optical fibres are very desirable since they allow for remote operation free from electromagnetic interference. Fibre optic vibration sensors arranged in an extrinsic configuration offer non contact and non destructive operation. Various such sensors have been reported [1 - 5]. This paper describes the use of an extrinsic sensor [6 - 8] to monitor vibrations with amplitudes up to several millimetres.

2. The Fibre Optic Sensor

The fibre optic sensor used to measure vibrations is shown schematically in Figure 1. It employs three 5 m long, 1 mm core diameter Plastic Optical Fibres (POF), complete with their protective sheaths, held side by side in the same plane using a simple mechanical holder. The POFs are displaced from each other parallel to the axis of the sensor head by a scale factor X_0 (mm), and are separated perpendicular to this axis by an amount y (mm). The middle POF, coupled to a red LED, emits light onto a target and each outer fibre receives the reflected light from the target and guides it to a silicon PIN photodiode which is connected via a passive RC high pass filter in order to reject ambient illumination, to a voltage amplifier.

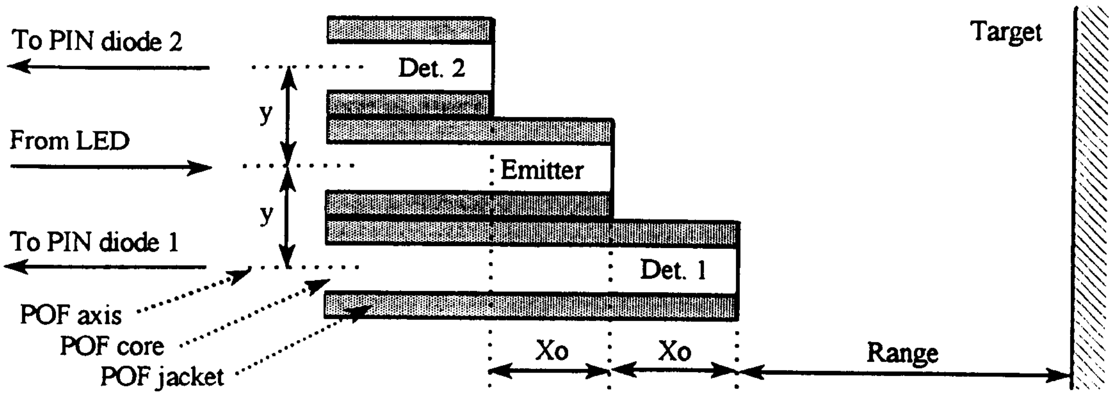

Fig. 1: The sensor head arrangement

The outputs from the two detecting circuits were connected to a 10 MHz 286 PC via two 12-bit ADC cards. The emitting circuit was also connected to the same PC via an Input/Output port. A block diagram of the electronics involved in this automated version of the sensor is shown in Figure 2. A C++ program controlled the operation of the sensor system. The LED was modulated at a frequency of 6.6 kHz with the two ADC cards converting the signal detected twice for every period, i.e. once when the LED was on and once when it was off, in sequence. The frequency of modulation of the LED was limited by the 10 MHz clock speed of the PC. With a faster PC the modulation frequency could be increased. However, the use of this PC was concidered adequate for demonstrating the use of this simple and inexpensive sensor for vibration measurements.

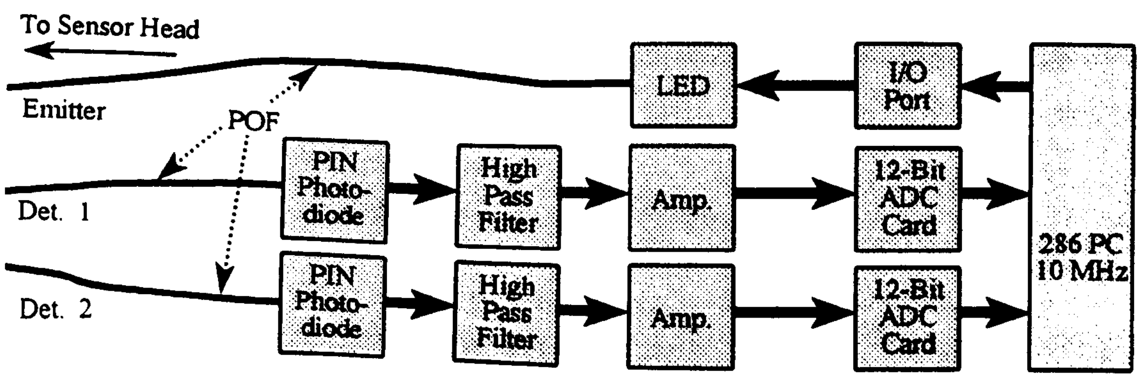

Fig. 2: The emitting and the two identical detecting circuits

Operation of the sensor is based upon the inverse square law. It has been shown both theoretically and experimentally that the transfer function, S, defined by:

$$S = (S1 + S2)\ /\ (S1 - S2) \qquad \textbf{Eq. (1)}$$

where S1 and S2 are the signals from the two detectors Det. 1 and Det. 2 respectively, is very close to being a linear function of the range, R.

Theoretical investigation performed with various targets, each having a surface with different reflectivity coefficient, and lambertian source emission showed that extreme non linearities in the form of a spike appeared in the very short ranges caused by the finite numerical aperture of the POFs [7]. This makes the sensor unusable at close ranges. Linearity of response was obtained from around a minimum range of 12 mm. The slopes of the linear responses depended on the X_0 separation and the reflectivity coefficient of the surface of the target. The extend of the linear operational range was a function of the level of calibration between the two detectors, the possible offset voltage in the preamplifiers, errors in the detected signals and the X_0 separation which can also offer scalable response, i.e. control the maximum operational range.

Experimental results for static displacements using a mirror target [7-8] under dark room conditions confirmed the long linear operational range of the sensor which can be between 15 mm and 90 mm, with $X_0 = 5$ mm. Further results [9] showed that with white matt paper as target one can get a range up to 100 mm or more. White matt paper is a better option to use as target since it has less stringent alignment requirements than a mirror target.

3. Vibration Measurements

In order to perform vibration measurements the sensor head was positioned in front of and facing the dust cap of the cone of the bass driver of a loudspeaker. This was a curved target with cross-sectional diameter of 70 mm and radius of curvature of 35 mm which was sprayed white to increase its diffuse reflectivity coefficient. Initial experimental measurements were performed without exciting the loudspeaker, i.e. static displacement measurements, by moving the loudspeaker (positioned on a translation stage) in order to obtain the calibration curve of the sensor arrangement. For this test the sensor was not optimised for maximum linear operational range as an operational range in the order of 6 mm (19 mm < R < 25 mm) was considered adequate. The calibration curve obtained was:

$$S = (0.821 \pm 0.006)R - (13.500 \pm 0.209) \qquad \textbf{Eq. (2)}$$

The estimated average accuracy of the static displacement measurement was ± 0.5 % with a scatter of individual experimental points in the order of ± 4 %. The maximum displacement recorded at 27 mm has an estimated accuracy of 4 % with a scatter of ± 4 %. The scatter is caused by the presence of high frequency noise attributed to the electronics used.

Following the above arrangement the sensor was positioned at a stand off distance from the dust cap of 22 mm. The cone, which was excited sinusoidally directly by a function generator, vibrated at a nominal driver setting of 77 Hz and approximately 750 sets of measurements were recorded corresponding to about 100 samples per period. The signals detected (S1 and S2) were substituted into the transfer function of the sensor. The calibration curve was used to derive the displacement of the bass driver with respect to time. The maximum displacement, D, was found to be 1 mm from its position of rest with an accuracy of ± 4 %. The frequency of vibration was determined as 77.5 Hz with an accuracy of ± 0.5 % which is very close to the nominally set frequency. S1, S2 and S, and the displacement graph are shown in Figure 3. The positive values on the displacement graph show the motion of the cone moving away from the sensor.

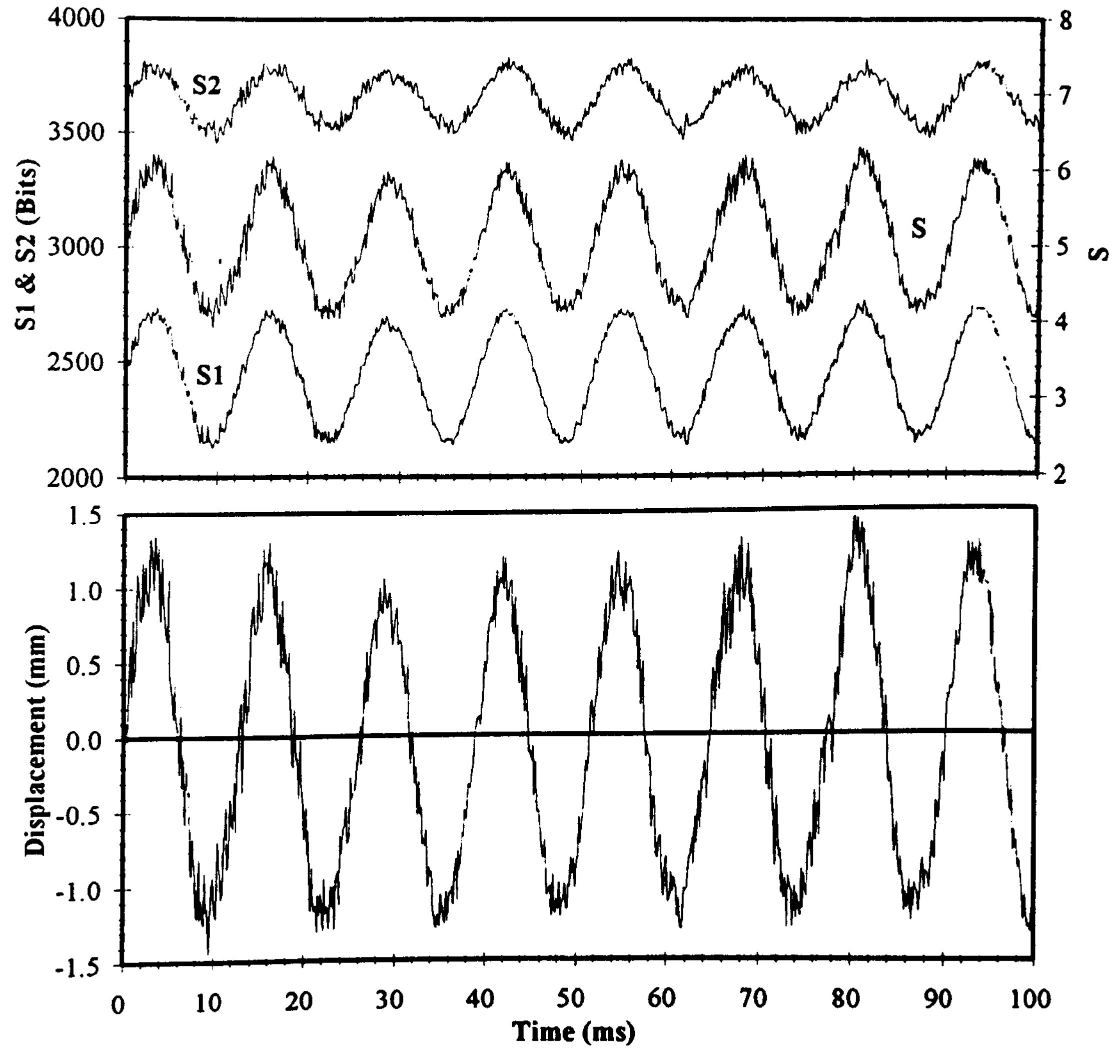

Fig. 3: S1, S2 and S, and Displacement graphs for f = 77.5 Hz

Another set of measurements was performed for an increasing frequency exciting the cone. The frequency was varied from around 15 Hz up to 150 Hz. The resulting S1, S2 and S are shown in Figure 4 along with the graph of displacement.

As expected, the detected signals, S1 and S2, reproduced the motion of the cone showing that as the frequency of vibration increases the cone amplitude of displacement decreases. On the displacement graph it can be clearly seen that when $D < 2$ mm the motion of the cone is fairly symmetrical but when $D > 2$ mm the cone does not move symmetrically. The displacement of the cone at $t = 9$ ms seems to be at its maximum suggesting that at this point the suspension and spider of the cone cannot be stretched any more thus holding it back. This is not the case at $t = 40$ ms where the cone is moving towards the magnet suggesting that the suspension and spider can be stretched more freely in this direction. Thus, if this bass driver were to be used to produce sounds with $D > 2$ mm then distortion of the sound would occur.

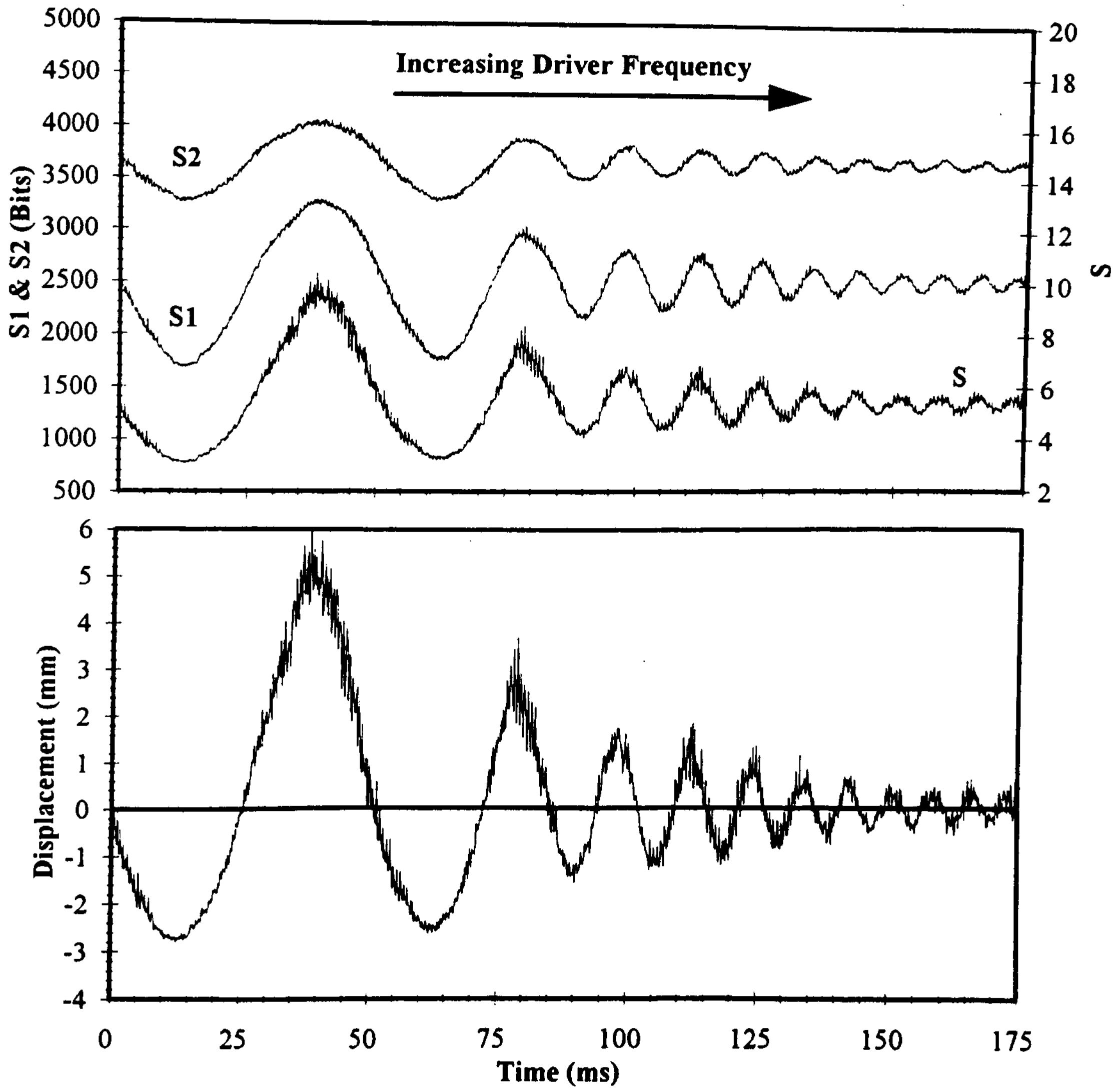

Fig. 4: S1, S2 and S, and Displacement graphs for 15 Hz < f < 150 Hz

4. Summary

The vibration sensor presented in this paper has been shown to measure single degree vibrations using the cap of the cone of the bass driver of a loudspeaker as target. Peak to peak displacements of 6 mm have been measured with a worst case accuracy of ± 4 %. Other vibration sensors reported in the literature [1 - 5] make reference to a maximum vibrational displacement of 2 mm. When the cone was driven sinusoidally, its displacement and frequency of vibration could be determined. The accuracy with which these parameters can be determined depends on the target vibrating above a minimum level of displacement consistent with the resolution of the sensor (estimated to be better than 1 % of range). The target used was able to vibrate above this minimum displacement up to a frequency close to 150 Hz. However, if the cone could vibrate with a higher displacement amplitude then, with some improvements to the detection electronics, i.e. less noise, one would be able to determine vibration parameters accurately up to around 600 Hz with the presently used PC and assuming having 10 samples per cycle of the maximum frequency of vibration. A faster PC would allow for even higher frequencies of vibration to be measured, provided the amplitude of vibration is satisfactorily longer than the resolution of the sensor.

5. References

[1] Chitnis, V.T., Kumar, S. and Sen, D., (1989) "Optical Fibre Sensor for Vibration Amplitude Measurement", *Journal of Lightwave Technology*, Vol. 7, No. 4, pp 687 - 691.

[2] Conforti, G., Brenci, M., Mencaglia, A. and Mignani, A.M., (1989) "Fibre Optic Vibration Sensor for Remote Monitoring in High Power Electric Machines", *Applied Optics*, Vol. 28, No. 23, pp 5158 - 5161.

[3] Dinev, P.D., (1995) "A Two-Dimensional Fibre-Optical Vibration Sensor", *Measurement, Science and Technology, 6*, pp 1395 - 1398.

[4] Lin, C.S. and Chang, R.S., (1994), "Fibre Optic Displacement Sensors for the Measurement of a Vibrating Object", *Precision Engineering*, Vol. 16, No. 4, pp 302 - 306.

[5] Toba, E., Shimosaka, T. and Shimazu, H., (1991) "Non-Contact Measurements of Microscopic Displacement and Vibration by Means of Fiber Optics Bundle", *SPIE, Fiber Optic and Laser Sensors IX*, Vol. 1584, pp 353 - 363.

[6] Kalymnios, D., (1993) "Linear and Scalable Optical Sensing Technique for Displacement", *Sensors VI. Technology, Systems and Applications*, Sensors Series, KTV Grattan and AT Augusti (eds), pp 291 - 293.

[7] Ioannides, N., Kalymnios, D. and Rogers, I.W., (1993) "Experimental and Theoretical Investigation of a POF based Displacement Sensor", *2nd Int. Conf. POF and Applications*, The Hague, pp 162 - 165.

[8] Ioannides, N., Kalymnios, D. and Rogers, I.W., (1996) "An Optimised Plastic Optical Fibre Displacement Sensor", *5th Int. Conf. POF and Applications*, Paris, pp 251 - 255.

[9] Ioannides, N., (1997) PhD Thesis: "Novel Opto-Electronic and Plastic Optical Fibre Sensors", Under Preparation.